

Université Mohamed Khider – Biskra
Faculté des Sciences et de la technologie
Département: Génie électrique
Ref :.....



جامعة محمد خيضر بسكرة
كلية العلوم و التكنولوجيا
قسم: الهندسة الكهربائية
المرجع:.....

Thèse présentée en vue de l'obtention
Du diplôme de

Doctorat en sciences

Option : Commande et Réseaux Electriques

Contribution à la Commande Neuro-Floue de la Machine Asynchrone à Double Alimentation Utilisé dans un Système Eolien

Présentée par :

Abdelhak DIDA

Soutenue publiquement le : 14/05/2017

Devant le jury composé de :

Dr. Kamel SRAIRI	Professeur	Président	Université de Biskra
Dr. Djilani BENATTOUS	Professeur	Rapporteur	Université d'El Oued
Dr. Arezki MENCER	Professeur	Examineur	Université de Biskra
Dr. Med Toufik BENCHOUIA	Professeur	Examineur	Université de Biskra
Dr. Azeddine CHAIBA	M.C.A	Examineur	Université de Sétif
Dr. Laid ZELLOUMA	M.C.A	Examineur	Université d'El Oued

Mohamed Khider University – Biskra

Faculty of Science and Technology

Department : Electrical Engineering

Ref :.....



جامعة محمد خيضر بسكرة

كلية العلوم و التكنولوجيا

قسم: الهندسة الكهربائية

المرجع:.....

A thesis submitted for the fulfillment of the degree of

Doctor of Science on: Electrical Engineering

Option: Control and Power System

Entitled

Contribution to the Neuro-Fuzzy Control of Wind Turbine Driven Doubly-Fed Induction Generator

*Towards Improving the Efficiency, Stability and Robustness of Variable Speed Operation Mode
under Faulty Operating Conditions*

Presented by:

Abdelhak DIDA

Lecturer in the Ferhat Abbas University, Setif-1

Exposed in public at: 14/05/2017

In front of the jury composed by:

Dr. Kamel SRAIRI

Dr. Djilani BENATTOUS

Dr. Arezki MENCER

Dr. Med Toufik BENCHOUIA

Dr. Azeddine CHAIBA

Dr. Laid ZELLOUMA

Professor

Professor

Professor

Professor

M.C.A

M.C.A

President

Supervisor

Examiner

Examiner

Examiner

Examiner

University of Biskra

University of El Oued

University of Biskra

University of Biskra

University of Setif

University of El Oued

Abstract

This thesis deals with the analysis, modeling, and control of the doubly-fed induction generator (DFIG) used in a wind power generation system (WPGS). A state review about the WPGS is discussed in order to give a historical overview and indicate our location in this area. Conventional vector control strategies for both rotor-side and grid-side converters of the DFIG-WPGS has been carried out. The standard Field Oriented Control (FOC) schemes usually used to control DFIGs comprise proportional-integral (PI)-controlled cascaded current and power loops, the system transient performance degrades when the actual values of the DFIG parameters deviate from those choose during the design the control system. In this framework, several alternative high dynamic performance power control schemes of DFIGs are being proposed in this thesis. Intelligent Fuzzy and Neuro-Fuzzy controllers (FLC, NFC) have been proposed as alternative of the PI control which is usually used in the machine power control, MPPT algorithms and the pitch angle control. In order to add robustness to our controllers, many data sets are collected with different PI controllers and different operating conditions. Operator experience plays an important role in the choice of the most adequate data sets and to find the most accurate scaling factors of the inputs and outputs signals of the fuzzy controllers.

Keywords: DFIG, WPGS, FOC, DPC, FLC, NFC, Multilevel converters.

Acknowledgments

In the name of Allah, the most beneficent, the most merciful, and all praise is due to Allah, God of the worlds, and the pray and the salaam be upon the lord of the messengers and the seal of the prophets, our lord the prophet Muhammad, and his family and companions and all those who follow his path until the day of resurrection.

Firstly, I would like to express my deep and sincere gratitude to my god, the great, the powerful and the merciful, who gave me life, health and willpower to finish my assignment in spite of everything.

I would like to express my sincerely appreciation to my supervisor, Prof. Djilani BENATTOUS, for his supervision, guidance and encouragement throughout my period of study and research.

I would like also to express my sincere appreciation to my examiners, Prof. Kamel SRAIRI, Prof. Arezki MENCER, Prof. Mohamed Toufik BENCHOUIA, Dr. Azeddine CHAIBA and Dr. Laid ZELLOUMA for their time dedicated to examine and review my work and also for their valuable feedback, as well as useful suggestions that helped to improve this thesis.

I would like to thank everyone who has helped me materiality or morally throughout my graduate study.

Finally, I am deeply grateful to my wife, my parents, my brother and sisters for their belief, patience, love and encouragement.

Biskra, Mars 16, 2016

Abdelhak DIDA

To the most precious persons to my heart, my mother and my father, thank you very much

To my wife for her support, understanding, and especially for her love

To the mystery of my happiness, my lovely daughters and my precious son

To my dear brothers and my dear sisters

To my entire family

To my entire friends

To my entire co-workers

I dedicate this modest work

Table of Contents

Abstract	I
Acknowledgments	II
Dedication	III
Table of Contents	IV
List of Figures	VII
List of Tables	X
List of Acronyms and Symbols	XI

General Introduction	01
----------------------------	----

Chapter 1: Wind Power Generation System: State of the Art

1.1. Introduction	14
1.2. Historical Facts about Wind Power	14
1.3. Development of Wind Power Generation	15
1.4. Components of Modern Wind Turbines	17
1.5. State-Of-The-Art of Currently Used Generator Systems	18
1.5.1. Fixed Speed WTs Concept	19
1.5.2. Variable Speed WTs Concept with Geared-Drive and Partial-Rated Power Converter.....	21
1.5.3. Variable Speed WTs Concept with Geared-Drive and Fully-Rated Power Converter.....	22
1.5.4. Variable Speed WTs Concept with Direct-Drive and Fully-Rated Power Converter	23
1.5.5. Conclusion on Currently Used Generator Systems	24
1.6. Development Trends to Reduce the Weight and Volume of the WTS	25
1.6.1. Brushless DFIG (BDFIG)	25
1.6.2. Continuously Variable Hydrostatic Gearbox (CVHG)	27
1.6.3. Magnetic Gearbox (MG)	28
1.6.4. Continuously Variable Magnetic Gearbox (CVMG)	28
1.6.5. Magnetic Pseudo DD Generator (PDD)	29
1.6.6. High-Temperature Superconducting (HTS) generator-based system	30
1.6.7. Transformer-Less WTGS using a Multilevel Converter	30
1.6.8. Multi-Coil Generator based Medium Voltage Converter	31
1.6.9. Multiple Generators based Medium Voltage Converter	32
1.6.10. Medium-Frequency Magnetic Link-based MV Converter	33
1.6.11. Matrix Converter based MV Converter	34
1.6.12. Medium-voltage DC converter	35
1.6.13. Medium Frequency Transformer based System	35
1.7. Conclusion	36
1.8. References of Chapter 1	37

Chapter 2: Modeling and Control of the DFIG based WPGS

2.1. Introduction.....	40
2.2. Modeling of the Global WPGS	40
2.2.1. Wind Speed Model	42
2.2.2. Wind Turbine Model.....	43
• Blade Pitch Angle Model	45
2.2.3. Two-Mass Drive Train Model	46
2.2.4. DFIG Model	47
2.2.5. Back-to-Back Power Electronic Converters Model	49
2.2.6. Grid-Interfaced Inductance Filter Model	50

2.2.7. DC-Link Capacitor Model	51
2.3. Power flow in Wound-Rotor Induction Machine	52
2.4. Control Schemes of Grid Connected DFIG	54
3.4.1. DC-link Capacitor Charging using GSC Current Control	55
3.4.2. Generation of Electrical Power	56
2.5. Simulation Results	59
2.6. Conclusion	63
2.7. References of Chapter 2	64

Chapter 3: Power Maximization and Pitch Angle Control using Fuzzy and Neuro-Fuzzy Controllers

3.1. Introduction	67
3.2. Maximum Power Point Tracking Algorithms	68
3.2.1. Optimal Torque Algorithm	69
• Simulation Results	70
• Discussion	71
3.2.2. Power Signal Feedback Algorithm	71
3.2.3. Optimum TSR Algorithm	72
A. TSR Algorithm using PI and FLC as Rotational Speed Controller	72
• Simulation Results	73
• Discussion	75
B. Sensorless TSR based MPPT Algorithm using a FLC	76
• Rotational Speed Estimation	76
• Wind Speed Estimation	78
• Simulation Results	78
• Discussion	80
3.2.4. Maximum Power Curve Searching Algorithm	81
• Simulation Results	84
• Discussion	86
3.2.5. Perturb and observe Algorithm using a FLC	86
• Simulation Results	89
• Discussion	91
3.3. Blade Pitch Angle Control	91
3.3.1. Blade Pitch Angle Control using Neuro-Fuzzy Controllers	91
• Simulation Results	92
• Discussion	93
3.3.2. Blade Pitch Control and MPPT Algorithm using ANFIS	94
• Simulation Results	98
• Discussion	100
3.4. Conclusion	101
3.5. References of Chapter 3	102

Chapter 4: Direct Power Control of Grid-Connected Doubly-Fed Induction Machine, Review

4.1. Introduction	104
4.2. Control Strategies of the DFIG	104
4.2.1. Field Oriented Control law of the DFIG	105
4.2.2. Direct Power Control Law of the DFIG	106
4.2.3. Sliding Mode Control Law of the DFIG	109
4.2.4. Fuzzy Logic Control Law of the DFIG	111
4.3. Simulation Results	112
4.3.1. The Normal Operating Conditions Test (Test N ⁰ 1)	112
4.3.2. The Machine Parameter Variations Test (Test N ⁰ 2)	113
4.3.3. The Faulty Grid Voltage Test (Test N ⁰ 3)	113

• <i>Discussion of Normal Operating Condition</i>	115
• <i>Discussion of Machine Parameters Variation Condition</i>	117
• <i>Discussion of Grid Voltage Unbalance and Distortion Condition</i>	117
• <i>Discussion of Switching Frequency</i>	118
4.4. Further Decoupled Direct Power Control Laws of DFIG	119
4.4.1. Vector Control with RST or LQG Regulators	119
4.4.2. Nonlinear Input-Output Feedback Linearization control	120
4.4.3. Second-Order Sliding-Mode Control.....	120
4.4.4. Adaptive Back-stepping Control.....	120
4.4.5. Model-Based Predictive Control.....	120
4.4.6. Deadbeat Control	121
4.4.7. Model Reference Adaptive Control	121
4.4.8. Robust H_{∞} Control	121
4.4.9. Adaptive Neural Network control	121
4.4.10. Fuzzy Logic control	122
4.4.11. Adaptive Neuro-fuzzy control	122
4.5. Conclusion	122
4.6. References of Chapter 4	123
Chapter 5: Modeling and Control of Back-to-Back Multilevel Converters based DFIG using Neuro-Fuzzy Controllers	
5.1. Introduction	125
5.2. Multilevel converters	125
5.3. Five-Level NPC Converter Model	126
• <i>Connection Functions</i>	128
• <i>Complementary Control</i>	128
5.4. Modulation Strategy for Five-Level NPC Converter	129
5.5. Comparison between 3L, 5L and 7L NPC Converter	131
5.6. DC-Bus Balancing using a Clamping Bridge Circuit in the 5L	133
5.7. Fuzzy Gain Tuner of PI Controller	135
5.8. Adaptive Neuro-Fuzzy Inference System	136
• <i>Input Node (Layer 1)</i>	138
• <i>Rule Nodes (Layer 2)</i>	138
• <i>Average Nodes (Layer 3)</i>	138
• <i>Consequent Nodes (Layer 4)</i>	138
• <i>Output Node (Layer 5)</i>	138
5.9. Training process of the NFCs of stator power and rotor currents	139
5.10. Simulation Results	141
5.10.1. Normal Operation of the WPGS-DFIG	141
5.10.2. Robustness of the NFC against the Parameters Variations	144
5.10.3. Robustness of the NFC against the Grid Disturbances	145
5.11. Conclusion	147
5.12. References of Chapter 5	148
General Conclusion and Suggestions	150
Appendices.....	152
Vita	162

List of Figures

Figure Intr.01 Block diagram of the two types of FISs: (a) <i>Mamdani</i> FIS (b) <i>TSK</i> FIS.	04
Figure Intr.02 Cooperative NFS model.	05
Figure Intr.03 Concurrent NFS model.	05
Figure Intr.04 <i>Mamdani</i> neuro-fuzzy system.	06
Figure Intr.05 <i>TSK</i> neuro-fuzzy system.	06
Figure Intr.06 Block diagram of inverse control method using ANFIS.	06
Figure Intr.07 Flow chart of training methodology of ANFIS system.	07
Figure 1.01 Famous Dutch windmills.	14
Figure 1.02 Early WT designs, including horizontal and vertical axis turbines.	15
Figure 1.03 Global cumulative installed wind power capacity from 1999 to 2020.	16
Figure 1.04 Distribution of WT market share by the manufacturers in 2012.	16
Figure 1.05 Evolution of WT size and the power electronics seen from 1980 to 2018 (estimated).	17
Figure 1.06 Basic components of a modern, horizontal-axis WT with a gearbox.	17
Figure 1.07 Component costs distribution for typical 2MW WT.	18
Figure 1.08 Scheme of a fixed speed WT with SCIG.	20
Figure 1.09 Pole-changeable concept with SCIG.	20
Figure 1.10 Limited variable speed concept with WRIG.	21
Figure 1.11 Scheme of a variable speed concept with DFIG.	21
Figure 1.12 Picture of wounded rotor used in the DFIG.	21
Figure 1.13 Scheme of a variable-speed WT with SC IG and GFC.	22
Figure 1.14 Scheme of a variable-speed WT with PM SG and GFC.	23
Figure 1.15 Variable-speed WT with DD EE SG and GFC.	23
Figure 1.16 Gearless nacelle, in this case of an Enercon E-66 DD WT.	24
Figure 1.17 WT configurations installed in Germany between 1990 and 2008.	24
Figure 1.18 Cascaded BDFIG.	25
Figure 1.19 Self-cascaded BDFIG.	26
Figure 1.20 BDFIG with nested rotor with six loops.	26
Figure 1.21 Hydrostatic gearbox for WTSs.	27
Figure 1.22 MG in series with a PM or EE SG.	28
Figure 1.23 CVMG gear in series with a PM SG.	29
Figure 1.24 Integrated magnetically geared PM SG.	29
Figure 1.25 Main components of a HTS multi-pole generator.	30
Figure 1.26 Single phase converter circuit diagram: (a) 3-level NPC, (b) 3-level FC, (c) 5-level MMC.	31
Figure 1.27 SliM-based MV converter topology.	31
Figure 1.28 Multi-coil generator based WTGS.	32
Figure 1.29 Large diameter DD generator of Sway Turbine. Source: Sway Turbine.	32
Figure 1.30 Multiple generators based WT system: single-phase layout.	33
Figure 1.31 MF magnetic-link-based MV converter: single phase layout.	33
Figure 1.32 Scheme of MF magnetic-link MV converter-based WTGS.	34
Figure 1.33 SPMC MV converter based WTGS.	34
Figure 1.34 WT with segmented stator generator and MC	35
Figure 1.35 WT with PM generator and MF Transformer.	36
Figure 1.36 WT with MC and multi-generation system.	36
Figure 2.01 Main components of a typical WPGS.	40
Figure 2.02 General scheme of the DFIG based WTS.	41
Figure 2.03 Control block diagram of DFIG wind turbine.	42
Figure 2.04 Generation of wind speed by ARMA model in MATLAB/Simulink.	43
Figure 2.05 Sample wind speed obtained using ARMA model (mean speed being 12 m/s).	43
Figure 2.06 Maximum power curve (MPC).	44

Figure 2.07 Maximum efficiency coefficient curve (MECC).	45
Figure 2.08 hydraulic blade pitch control system.	45
Figure 2.09 Bloc diagram of the blade pitch angle system.	46
Figure 2.10 Two-mass drive train model.	47
Figure 3.11 Equivalent circuit of the DFIG in d-q coordinates.	48
Figure 3.12 AC/DC/AC bidirectional power converter.	49
Figure 3.13 Pulse width modulator for a three-phase inverter.	50
Figure 3.14 DC/AC Grid-Interfaced converter.	51
Figure 2.15 Operating quadrants of the WRIM.	52
Figure 2.16 Power flow in the DFIG system.	53
Figure 2.17 Block diagram of three-phase PLL control.	55
Figure 2.18 Grid voltage oriented control scheme of the GSC.	56
Figure 2.19 Block diagram of DFIG system used for control.	58
Figure 2.20 Stator flux oriented control scheme of the DFIG	59
Figure 2.21 Detailed model of the DFIG based WPGS in Matlab/SimPowerSystems environment.	60
Figure 2.22 Detailed simulation of different operating modes of the DFIG based WPGS.	62
Figure 3.01 Power curve of a variable speed WT.	67
Figure 3.02 Detailed scheme of the DFIG control with back-to-back converters in the rotor circuit.	68
Figure 3.03 Block diagram of OT control based MPPT method.	69
Figure 3.04 Dynamic responses of WPGS in the VSOM with and without MPPT algorithm.	71
Figure 3.05 Block diagram of PSF control based MPPT method.	72
Figure 3.06 Block diagram of the TSR based MPPT control system.	73
Figure 3.07 FLC structure of the rotational speed control loop.	73
Figure 3.08 Dynamic responses of WPGS in the VSOM using TSR-FLC algorithm.	75
Figure 3.09 Schematic blocks of the MRAS based DFIG rotor speed observer.	77
Figure 3.10 Structure of FLC for rotational speed MRAS observer.	77
Figure 3.11 Inputs and output MFs of the FLC based MRAS observer.	77
Figure 3.12 Structure of the wind speed estimator.	78
Figure 3.13 Dynamic responses of WTS in the VSOM using sensorless TSR algorithm.	80
Figure 3.14 Working principle of MPCs approach.	82
Figure 3.15 FLC structure of the mechanical power control loop.	82
Figure 3.16 Membership functions of Fuzzy-MPCS controller.	83
Figure 3.17 Block diagram of the MPCs based MPPT control system.	84
Figure 3.18 Dynamic responses of the fuzzy-MPCS algorithm in the VSOM.	85
Figure 3.19 Comparison study of dynamic response between OT and MPCs control techniques.	86
Figure 3.20 Adaptive P&O approach working principle.	87
Figure 3.21 Structure of FLC for P&O based MPPT algorithm.	87
Figure 3.22 Membership functions of Fuzzy-P&O algorithm.	88
Figure 3.23 Block diagram of P&O based MPPT control system.	89
Figure 3.24 Dynamic responses of the fuzzy-P&O algorithm in VSOM.	90
Figure 3.25 Pitch angle control scheme using two NFCs.	92
Figure 3.26 Dynamic responses of the WPGS in the constant speed operation mode using ANFIS.	93
Figure 3.27 Training process of the ANFIS based MPPT.	95
Figure 3.28 Training process of the ANFIS based blade pitch angle control.	97
Figure 3.29 MPPT and Pitch angle control scheme of the WPGS using ANFIS.	97
Figure 3.30 Dynamic responses of the proposed algorithm in the largely variable WS.	100
Figure 4.01 Different control schemes for power converters and drives.	105
Figure 4.02 Closed loop stator active power control using PI controller.	105
Figure 4.03 Block diagram of the overall FOC scheme of the DFIG.	106
Figure 4.04 Stator and rotor flux vectors in rotor reference frame.	108
Figure 4.05 Stator flux angle referred to rotor reference frame and correspond sector.	108
Figure 4.06 Global diagram of the conventional lookup table based DPC strategy for DFIG.	109
Figure 4.07 Block diagram of the overall SMC scheme of the DFIG.	111
Figure 4.08 Structure of fuzzy logic controller for stator active power control loop.	112
Figure 4.09 Membership functions of the adopted fuzzy logic controller.	112

Figure 4.10 Variation of the rotational speed of the DFIG.	113
Figure 4.11 Grid voltage unbalance and distortion.	113
Figure 4.12 Decoupled stator powers control of DFIG under normal operating conditions.	115
Figure 4.13 Decoupled power control of DFIG under parameters variations operating conditions.	116
Figure 4.14 Decoupled stator powers control of DFIG under unbalanced and disturbed utility grid.	117
Figure 4.15 Switching frequency of each control law of the DFIG.	118
Figure 5.01 Topologies and phase voltages of the conventional two-level and multilevel VSIs.	126
Figure 5.02 Topology of the 5L NPC converter.	127
Figure 5.03 Different configurations of the 5L NPC converter.	127
Figure 5.04 Classification of the most common modulation techniques for power converters.	129
Figure 5.05 Proposed PWM strategy for the 5L NPC converter.	131
Figure 5.06 PWM strategy for 2L, 3L, 5L, and 7L converters.	133
Figure 5.07 Imbalance minimization between the DC-link voltages.	134
Figure 5.08 Clamping bridge structure.	134
Figure 5.09 Control scheme of the 5L NPC GSC.	135
Figure 5.10 Cascade control structure of the GSC using FGT.	135
Figure 5.11 FGT of the DC-link voltage controller.	136
Figure 5.12 NFC structure for the stator active power control loop.	137
Figure 5.13 Indirect vector control of the DFIG using the RSC.	139
Figure 5.14 Membership Functions of the TS-FLC inputs.	139
Figure 5.15 RMSE of the active power NFC.	140
Figure 5.16 NFC test with training and checking data sets.	140
Figure 5.17 Reference tracking characteristics of the DFIG based WPGS.	143
Figure 5.18 Parameters variation rejection by using the NFC.	145
Figure 5.19 Grid voltage disturbance rejection by using NFC.	146
Figure 5.20 Average DC-link voltage response using PI and FGT.	147
Figure A.1 Bloc diagram of the PI controller.	155
Figure A.2 Topology of the three phase 3L NPC converter.	156
Figure A.3 One phase Level-Shifted PWM strategy for the 3L NPC converter.	156
Figure A.4 One phase output voltage of the 3L NPC converter.	157
Figure A.5 Topology of the three phase 5L NPC converter.	157
Figure A.6 One phase Level-Shifted PWM strategy for the 5L NPC converter.	158
Figure A.7 One phase output voltage of the 5L NPC converter.	158
Figure A.8 Three phases PWM of the 5L NPC converter and its model.	159
Figure A.9 Topology of the three phase 7L NPC converter.	160
Figure A.10 One phase Level-Shifted PWM strategy for the 7L NPC converter.	161
Figure A.11 One phase output voltage of the 7L NPC converter.	161

List of Tables

Table Intr.1: Comparison between neural networks and fuzzy inference systems	04
Table 1.1: Top 10 WT manufacturers of 2012, currently used generator concepts and power ranges	19
Table 3.1: Rule table for the fuzzy logic rotor speed controller	73
Table 3.2: Rules table of the FLC used for rotor speed estimator	77
Table 3.3: Rule table of the Fuzzy-MPCS controller	83
Table 3.4: Rule table of Fuzzy-P&O controller	89
Table 4.1: Optimal lookup table for stator flux based DPC law	109
Table 4.2: Rule table for the fuzzy logic controller	112
Table 4.3: Parameters variation of the 1.5MW DFIG	113
Table 4.4: Brief comparison study of various direct power control laws of DFIG	119
Table 5.1: Electrical magnitude of each configuration of arm k	128
Table 5.2: V_{KM} and switch order control B_{ks}	130
Table 5.3: Comparison between 2L, 3L, 5L and 7L NPC converters	133
Table 5.4: Rule table for DC-link voltage fuzzy K_p tuner	136
Table 5.5: Rule table for DC-link voltage fuzzy K_i tuner	136
Table A.1: Parameters of DFIG and the WTS in the per-unit system used in chapters N ^o : 3 and 4	152
Table A.2: K_p , K_i gains of the PI controllers used in chapters N ^o : 3 and 4	152
Table A.3: Parameters of DFIG and the WTS used in chapters N ^o : 5 and 6	153
Table A.4: K_p , K_i gains of the PI controllers used in chapters N ^o : 6	153
Table A.5: Parameters of DPC methods of the DFIG used in chapter N ^o : 5	153
Table A.6: Base value definition	154

List of Acronyms and Symbols

Acronym	Description
WPGS	Wind Power Generation System
WTGS	Wind Turbine Generation System
WT	Wind Turbine
WTS	Wind Turbine System
DFIG	Doubly-fed Induction Generator
WRIM	Wound Rotor Induction Machine
WRIG	Wound Rotor Induction Generator
BDFIG	Brushless DFIG
IG	Induction Generator
CSIG	Constant Speed Induction Generator
SG	Synchronous-Generator
EE	Electrical Excitation
PM	Permanent-Magnet
GFC	Variable Speed, Gearbox, Full Converter
DD	Direct-Drive
RSC	Rotor-Side Converter
GSC	Grid-Side Converter
AI	Artificial Intelligent
FIS	Fuzzy Inference System
FLC	Fuzzy Logic Controller
ANN	Artificial Neural Networks
NNC	Neural Networks Control
TSK	Takagi, Sugeno, and Kang
NFS	Neuro-Fuzzy Systems
NFC	Neuro-Fuzzy Controller
MFs	Membership Functions
ANFIS	Adaptive-Network-Based FIS
GSST	Grid Side Step-up Transformer
CVT	Continuously Variable Transmissions
CVHG	CVT based Hydrostatic Gearbox
MG	Magnetic Gearbox
CVMG	Continuously Variable Magnetic Gearbox
PDD	Pseudo Direct-Drive Generator
HTS	High-Temperature Superconducting
NPC	Neutral Point Clamped
FC	Flying Capacitor
CHB	cascaded H-bridge
MMC	Modular Multilevel Cascaded
MC	Matrix Converter
PLL	Phase Locked Loop
VCO	Voltage Controlled Oscillator
IGBT	Insulated Gate Bipolar Transistor
VSC	Voltage Source Converters
VSI	Voltage Source Inverters
VSOM	Variable Speed Operation Mode
TSR	Tip Speed Ratio
MPC	Maximum Power Curve
MECC	Maximum Efficiency Coefficient Curve
MPPT	Maximum Power Point Tracking
OT	Optimal Torque
PSF	Power Signal Feedback
MPCS	Maximum Power Curve Searching
HCS	Hill-Climb Searching
P&O	Perturb and Observe
HSS	High-Speed Shaft
LSS	Low-Speed Shaft
EMF	Electromagnetic Force
PI	Proportional-Integral
FOC	Field Oriented Control
DPC	Direct Power Control
DTC	Direct Torque Control
SMC	Sliding Mode Control
MPC	Model Predictive Control
RMSE	Root Mean Squared Error
FGT	Fuzzy Gain Tuner
MRAS	Model Reference Adaptive System
ARMA	Autoregressive Moving Average
LQG	Linear Quadratic Gaussian
GW	Giga-Watt
MW	Mega-Watt
MV	Medium-Voltage
HV	High-Voltage
MF	Medium-Frequency
HF	High-Frequency
AC	Alternating Current
DC	Direct Current
HVDC	High-Voltage Direct Current
GFRT	Grid-Fault Ride-Through
abc/d-q	Park's Transformation
abc/α-β	Clark's Transformation
GA	Genetic Algorithm
PSO	Particle Swarm Optimization
ACO	Ant Colony Optimization
BCA	Bee Colony Algorithm
FFO	Firefly Optimization
PWM	Pulse Width Modulator
SVM	Space Vector Modulation
THD	Total Harmonic Distortion

Symbol	Description
V_w	Wind Speed (m/s)
V_{mean}	Mean Wind Speed Part (m/s)
V_{turb}	Turbulent Wind Speed Part (m/s)
E_w	Wind Kinetic Energy (J)
ρ	Mass Density of Air (Kg/m ³)
A	Frontal Area of the WT (m ²)
R	Rotor Radius of WT (m)
β	Pitch Angle of Rotor Blades (deg)
J_β, d_β	Inertia Moment and Friction Coefficient Respectively of Pitch System (kg.m ²)
T_β, T_r	Blade Orientation System and the Wind Resistance Torques (N.m)
$\tau_{d\beta}$	Time Constant of Blade Orientation System (s)
C_p	Power Efficiency Coefficient of the WT
C_{pmax}	Optimal Power Efficiency Coefficient of the WT
λ	Tip Speed Ratio
λ_{opt}	Optimal Tip Speed Ratio
ω_t, ω_m	Turbine Rotor and Generator Rotor Mechanical Angular Velocities Respectively (rad/s)
$\omega_{t_opt}, \omega_{m_opt}$	Optimal Rotational Speed of the WT and the Generator Respectively (rad/s)
$\omega_g, \omega_s, \omega_e, \omega_r$	Grid Side, Stator Side, Rotor and Slip Electrical Angular velocities Respectively (rad/s)
f	Grid Frequency (Hz)
s	Slip or the Laplace Operator as Evident
J_t, J_g	Turbine Rotor and Generator Moment of Inertia Respectively (kg.m ²)
T_t	Aerodynamic Torque of the WT (N.m)
T_{lss}	Low-Speed Shaft Torque of the Gearbox (N.m)
T_{hss}	High-Speed Shaft Torque of the Gearbox (N.m)
T_{em}	Electromagnetic Torque of the Generator (N.m)
N_g	Ratio of the Gearbox
K_{stiff}	Torsional Stiffness Coefficient of the Low Speed Shaft (N.m/rad)
D_{damp}	Torsional Damping Coefficient of the Low Speed Shaft (N.m.s/rad)
b	Damping coefficient of the generator (N.m.s/rad)
θ_t, θ_m	Turbine Rotor and Generator Rotor Angular Positions Respectively (rad)
$\theta_g, \theta_s, \theta_{\phi_s}$	Grid Voltage, Stator Voltage and Stator Flux Vectors Positions Respectively (rad)
V_g, V_s, V_r	Grid, Stator and Rotor Voltage Vectors Respectively (V)
i_s, i_r, i_g, i_{out}	Stator, Rotor, GSC Output and Total Output Current Vectors Respectively (A)
i_{gDC}, i_{rDC}, i_{DC}	DC output current of the GSC, DC input current of RSC, DC-Link Capacitor Current (A)
Φ_s, Φ_r	Stator and Rotor Flux Vectors Respectively (Web)
i_{ms}	Stator Magnetizing Current Vector (A)
R_s, R_r	Stator, Rotor Winding Resistances Respectively (Ω)
L_s, L_r, L_m	Stator, Rotor Winding Leakage Inductance, Mutual Inductance (H)
R_g, L_g	Grid Side Filter Resistance and Leakage Inductance Respectively (Ω, H)
σ	Leakage Factor
p	Number of Pole Pairs
C_{DC}	DC-Bus Capacitance (F)
P_m	Mechanical Power of the WT (W)
$P_{loss,GB}$	Gearbox Mechanical Losses (W)
P_{rated}	Rated power of the DFIG(W)
P_s, P_r, P_g, P_{DC}	Stator Active Power, RSC Active Power, GSC Active Power, DC-link Active Power (W)
Q_s, Q_r, Q_g	Stator Reactive Power, RSC Reactive Power, GSC Reactive Power (VAR)
$S_{out}, P_{out}, Q_{out}$	Apparent, Active and Reactive Output Powers of the Generator (VA, W, VAR)
T_s	Sampling Period (s)
N_k	Sector Number

Subscripts	Description
$\alpha\text{-}\beta$	α -axis and β -axis component of the stationary reference frame
$D\text{-}Q$	D-axis and Q-axis component of the rotor reference frame
$d\text{-}q$	d-axis and q-axis component of the synchronous reference frame
$^*, \text{ref}$	Reference value
\cdot	derivation
$s = d/dt$	differential operator (Laplace Operator)
g, s, r	Grid, Stator and rotor-side value respectively
$\text{max}, \text{min}, \text{opt}$	Maximum, minimum and optimal

General Introduction

General Introduction

- **Backgrounds**

Wind power, as a clean and sustainable energy, has obtained highly concentrations during the past decade [1-2]. Research and development of renewable energy has gained tremendous momentum in the past decade as the cost of conventional electrical power generation continuously escalate due to the limited fuel resources, and the general public becomes increasingly concerned of the environmental impacts caused by the thermal and nuclear generation. Among many technologies promising green power, the utilization of wind energy via wind power generation system (WPGS) is one of the most mature and well developed. Across the world, the total capacity of wind generation has already exceeded the giga-watt (GW) rating and larger wind farms are constantly being planned and commissioned [3-4-5].

The main components of a WPGS include the turbine rotor, gearbox, generator, transformer, and possible power electronics. The turbine rotor converts the fluctuating wind energy into mechanical energy, which is converted into electrical power through the generator, and then transferred into the grid through a transformer and transmission line. Wind turbines capture the power from the wind by means of aerodynamically designed blades and convert it to rotating mechanical power. The number of blades is normally three and the rotational speed decreases as the radius of the blade increases. For mega-watt range wind turbines, the rotational speed will be 10-15 rpm. The efficient way to convert the low-speed, high-torque power to electrical power is to use a gearbox and a generator with standard speed. The gearbox adapts the low speed of the turbine rotor to the high speed of the generator. The gearbox may be not necessary for multi-pole generator systems [6].

The generator converts the mechanical power into electrical energy, which is fed into a grid through a power electronic converter, and a transformer with circuit breakers and electricity meters. The connection of wind turbines to the grid is possible at low voltage, medium voltage, high voltage, and even at the extra high voltage system since the transmittable power of an electricity system usually increases with increasing the voltage level. While most of the turbines are nowadays connected to the medium voltage system, large offshore wind farms are connected to the high and extra high voltage level [6].

Doubly fed induction generators (DFIG) based wind turbines (DFIG-WT), a typical employed WPGS, have been widely used to achieve the maximum power conversion, smaller capacity of power electronic devices and full controllability of active and reactive power of the DFIG [6], due to their characteristics such as varying speed operation. The stator circuit of the DFIG is connected to the grid directly, while the rotor circuit is fed via a back-to-back power converter. The back-to-back converter consists of two converters, i.e., rotor-side converter (RSC) and grid-side converter (GSC), which are connected “back-to-back”. Between the two converters a DC-link capacitor is placed, as energy storage, in order to keep the voltage variations (or ripple) in the DC-link small.

- **Challenges & Problems**

The DFIG-WT is a dynamic system with strong nonlinear coupled characteristics and time varying uncertain inputs. The aerodynamic of wind turbine introduces strong nonlinearities and uncertainties [7]. Objectives of the wind-turbine controller depend upon the operating area defined via wind speed [8]. For moderate wind speeds, it is more important to maximize wind power capture while it is recommended to limit power production and rotor speed above the rated wind speed to protect the mechanical part of the WPGS. The power regulation of the wind turbine is a highly nonlinear system as the plant, actuation and control objectives are all strong nonlinear [9].

As an induction machine, the DFIG is also a typical nonlinear system as induction motor, which has been used widely as a test benchmark for nonlinear control system design. With the time-varying and intermittent wind power input, DFIG-WT is required to operate at an operation envelope with a wide range rather than one operation point. Moreover, during voltage sags due to grid load disturbances or grid faults, DFIG-WT will operate far away from its normal operation point. During the grid fault period and post-fault period, terminal voltage normally dropped close to the ground and cause a strong dynamics in the stator and rotor currents, and such that stator-flux will not be remained as constant as well. This will destroy the condition of the mostly used vector control schemes for DFIG-WTs and dynamic of the active and reactive power of the DFIG are still coupled during the transient period of stator flux or stator-voltage. As all vector control schemes depend upon the assumptions of constant voltage and flux to realize asymptotical decoupling control of the active and the reactive power, it can expect that their performance will be degraded during voltage sags and grid faults. On the other side, unlike the vector control of induction motor in which the rotor flux is controlled directly, stator-flux of the DFIG normally is not one of the controlled variables and thus not controlled directly [6].

The control function within the vector control scheme has commonly been performed by using PI (proportional-integral) controllers. One challenge is how to tune the parameters of the PI control loops to provide optimal performance around one special operation point and cope with the time-varying operation points. For examples, many results have been done to automatically tune the PI controller's parameters, such as using genetic algorithm [10] and particle swarm optimization [11]. Automatic tuning based on artificial intelligence and gain schedule technique have been proposed to provide optimal performance for a varying operation condition. Input/output linearization has been proposed to fully decoupling control of induction motor [12-13]. When the wind turbine operates at varying speed to achieve the maximum wind power conversion, rotor speed will travel between the sub-synchronous to super-synchronous speed and other state variables of the DFIG, including stator and rotor currents and the rotor voltages, are dynamic variables so as to inject different value of active power. However, because the system is highly nonlinear, it is difficult to find one set of parameters, which can provide a consistent optimal response when the operation point changes. Moreover, in some worst cases, unstable mode may exist because of one set of PI parameters [14].

- **Motivations**

The performance of DFIG-WT depends heavily upon the controllers applied on the generator side and the wind turbine side. The DFIG-WT is usually controlled via a cascaded structure including an inner fast-loop for power regulation of the DFIG and an outer relative slow loop for the speed control of drive train. The reference of active power of the DFIG is determined based on the maximum energy conversion, which is defined as maximum power point tracking (MPPT), when wind speed is below the rated value; while constant reference is given when wind speed is above the rated value. The wind turbine also employs pitch angle control to regulate the extracted power from wind source by wind turbine for wind speed above the rated value, while pitch angle is fixed when wind speed below the rated value [6].

The artificial intelligent (AI) control algorithms are well known for their ability in handling the non-linearities and uncertainties in a system. They need a simple and less intensive mathematical design for the effective control or modeling of a highly non-linear system with lot of uncertainties. Therefore, the AI algorithms can be very advantageous in handling a system like variable speed DFIG based WPGS, where the operating conditions change very rapidly due to the intermittent nature of wind [15]. The AI controllers imitate the human decision-making process and can often be implemented in complex systems with more success than conventional control techniques. Artificial intelligence can be classified into expert systems, Fuzzy Inference System (FIS), Artificial Neural Networks (ANN) and genetic algorithms. With the exception of expert systems, these techniques are

based on *soft-computing* methods. The result is that they are capable of making approximations and ‘intelligent guesses’ where necessary, in order to come out with a ‘good enough’ result under a given set of constraints. Intelligent control systems may use one or more AI techniques in their design [16].

The most commonly used architectures for fuzzy system development are *Mamdani* fuzzy system [17-18] and TSK (*Takagi, Sugeno, and Kang*) fuzzy system [19-20-21], as shown in Figure Intr.1. Both of them consist of three blocks: fuzzification, fuzzy rules, and defuzzification/normalization. Each of the blocks could be designed differently.

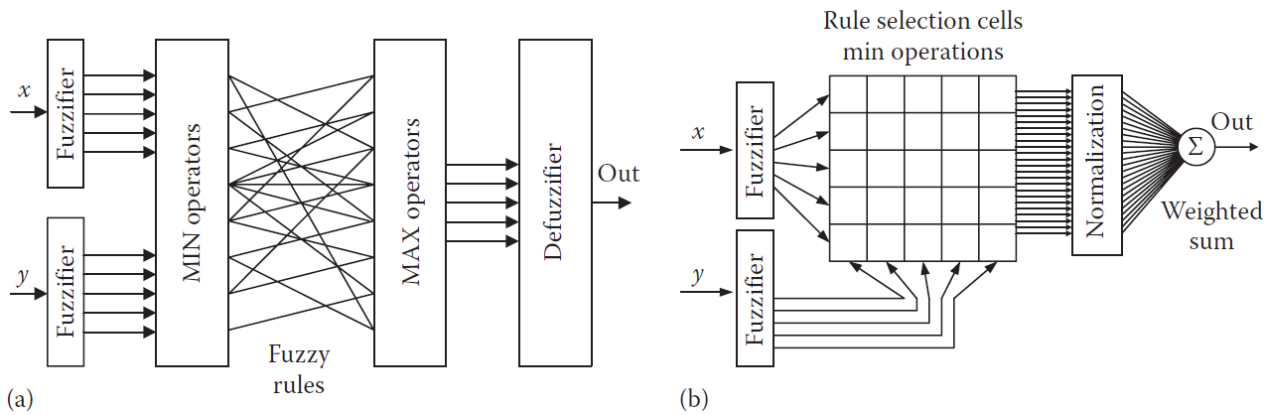


Figure Intr.1 Block diagram of the two types of FISs: (a) *Mamdani* FIS and (b) *TSK* FIS [22].

Note: With the same membership function, TSK fuzzy systems perform more accurate calculation than *Mamdani* fuzzy system [22].

A simple FIS controller has a narrow operating range and needs much more manual adjustments by trial and error for higher performance. On the other hand, it is extremely difficult to create a series of training data for ANN that can perform under different operating conditions [15]. Table 1.1 summarizes the comparison between ANNs and FIS [23]. To a large extent, the drawbacks pertaining to these two approaches seem complementary. Therefore, it seems natural to consider building an integrated system combining the concepts of FIS and ANN modeling.

Table Intr.1: Comparison between neural networks and fuzzy inference systems [23]

Artificial Neural Network	Fuzzy Inference System
Difficult to use prior rule knowledge	Prior rule-base can be incorporated
Learning from scratch	Cannot learn (linguistic knowledge)
Black box	Interpretable (if-then rules)
Complicated learning algorithms	Simple interpretation and implementation
Difficult to extract knowledge	Knowledge must be available

• Neuro-Fuzzy Systems

In the recent years, the researchers have tried to combine the advantages of both FIS and ANN in a new form, known as Neuro-Fuzzy Systems (NFS). The NFS utilizes the linguistic representation of fuzzy system with the learning capability of ANN. However, most of the NFS's use large numbers of membership functions and rule bases, which causes lot of computational burden and hence are not suitable for practical industrial application [15]. There are several works related to the integration of ANNs and FISs [24-25-26-27-28-29-30-31-32-33-34-35-36-37], it could be formulated into three main categories: cooperative, concurrent and integrated neuro-fuzzy models [23].

In the simplest way, a cooperative model can be considered as a preprocessor wherein ANN learning mechanism determines the FIS membership functions or fuzzy rules from the training data as shown in Figure Intr.2. In a concurrent model shown in Figure Intr.3, ANN assists the FIS continuously (or vice versa) to determine the required parameters especially if the input variables of the controller cannot be measured directly. Such combinations do not optimize the fuzzy system but only aids to improve the performance of the overall system [23].

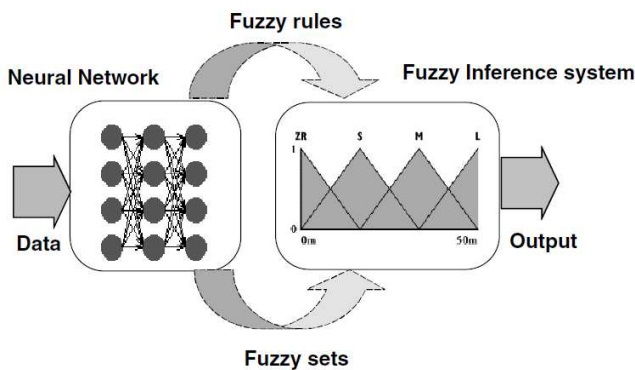


Figure Intr.2 Cooperative NFS model

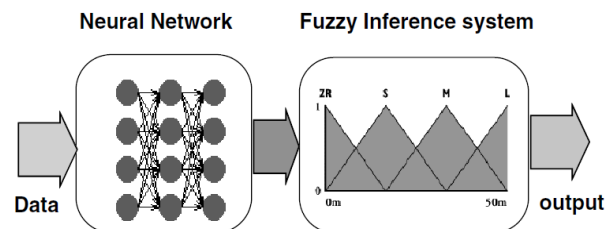


Figure Intr.3 Concurrent NFS model

As evident, both cooperative and concurrent models are not fully interpretable due to the presence of neural network (black box concept). Whereas an integrated NFS model is interpretable and capable of learning in a supervised mode, the architecture of *Mamdani* NFS and TSK NFS are illustrated in Figure Intr.4 and Figure Intr.5 respectively [23].

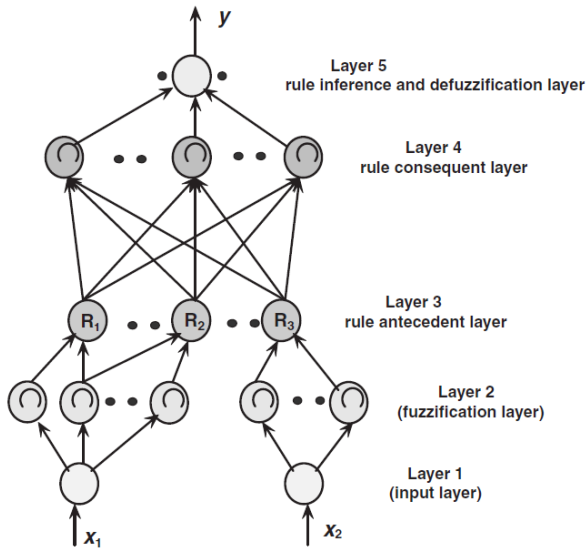


Figure Intr.4 Mamdani neuro-fuzzy system

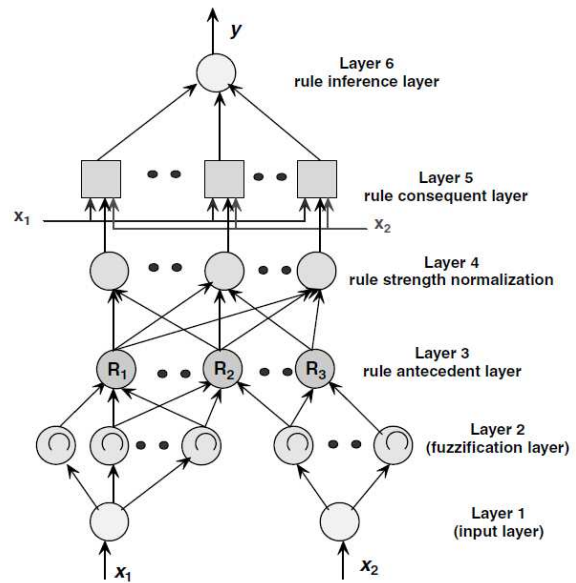


Figure Intr.5 TSK neuro-fuzzy system

There are different integrated NFS models that make use of the complementarities of neural networks and fuzzy inference systems implementing a *Mamdani* or *TSK* FIS. Some of the major works in this area are GARIC [38], FALCON [32], ANFIS [39], NEFCON [40], NEFCLASS [41], NEFPROX [34], FUN [42], SONFIN [43], FINEST [44], EFuNN [45], dmEFuNN [46], EvoNF [47], and many others [48-49-50].

The adaptive-network-based fuzzy inference system (ANFIS) is used for controlling and parameter estimation purpose. Some of the advantages of ANFIS are fast convergence due to hybrid learning and ability to adjust the shape of input membership functions. It has better tracking and adaptive capabilities than any other controller. The ANFIS generally utilizes the TSK fuzzy rule-based systems, as they require less computation than *Mamdani* methods [51-52-15]. Most of the time, the ANFIS controller mimicked another working controller, the controller being mimicked is an experienced human operator who can control the plant satisfactorily. Another scheme for obtaining desired control action is the inverse control method shown in Figure Intr.6 [53].

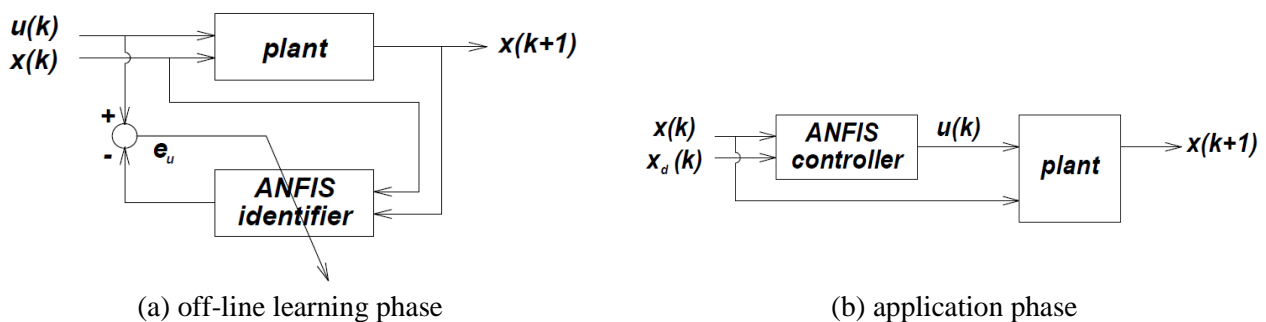


Figure Intr.6 Block diagram of inverse control method using ANFIS [53].

In symbols, we have: $x(k+1) = f(x(k), u(k))$ (Plant)
 $u(k) = g(x(k))$ (Controller)

The flow chart of proposed training methodology of ANFIS system is shown in Figure Intr.7. The modeling process starts by obtaining a data set (input-output data pairs) and dividing it into training and checking data sets. Training data constitutes a set of input and output vectors. The data is normalized in order to make it suitable for the training process. This normalized data was utilized as the inputs and outputs to train the ANFIS. To avoid the over fitting problems during the estimation, the data set were randomly split into two sets: a training set (70% of the data), and a checking set (30% of the data). When both checking data and training data were presented to ANFIS, the FIS was selected to have parameters associated with the minimum checking data model error. In other words, two vectors are formed in order to train the ANFIS, input vector and the output vector (Figure Intr.7). The process is terminated when the error becomes less than the threshold value [54].

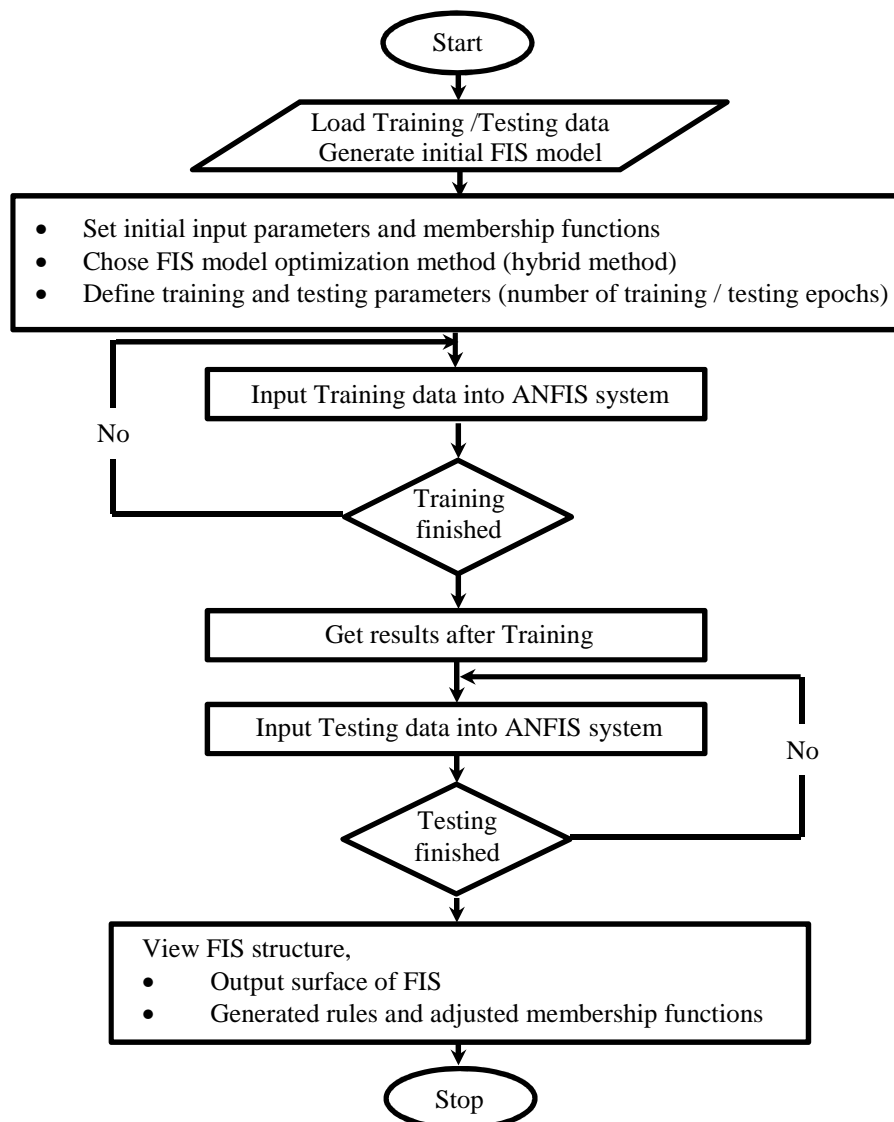


Figure Intr.7 Flow chart of training methodology of ANFIS system [54].

The main purpose of this thesis is to develop intelligent fuzzy and neuro-fuzzy control strategies for DFIG-WT to improve efficiency, robustness and the transient dynamics, by considering nonlinear dynamics, uncertain wind power inputs and grid faults. Simulation studies of the proposed control algorithms in each chapter are carried out based on Matlab/Simulink or Simpowersystem.

• Thesis Outline

The rest of this thesis is organized as follows:

- Chapter 1 presents a state of the art of the WPGS and the different WT concepts in order to give an overview of the history and the future of the WPGSs, and to indicate our location in this world of renewable energy conversion.
- Chapter 2 presents the modeling of a DFIG based variable-speed WT, including dynamic model of WT, pitch orientation system, drive train, DFIG and power electronic converters. For the controllers design, the dynamic model of DFIG is obtained under the d-q rotating reference frame, and the conventional vector control using PI controllers is employed in the RSC and the GSC.
- Chapter 3 reviews state of the art of MPPT algorithms using fuzzy logic controller (FLC). A comparison has been made between the different MPPT algorithms in regard of various speed responses and ability to achieve the maximum energy yield. In the high wind speed condition, a blade pitch control law using a neuro-fuzzy controller (NFC) is proposed as alternative of the PI (proportional and integral) control in order to improve the stability of the system; in the high wind speed condition.
- Chapter 4 gives a comparison between four different concepts of directly control of stator active and reactive powers of the DFIG, vector control using PI controller, look-up table based direct power, sliding mode control and finally fuzzy logic control. Robustness against machine parameters variations and grid fault are discussed.
- Chapter 5 presents a neuro-fuzzy control law for the DFIG-WT connected to a five-level back-to-back converter in the rotor circuit. The modeling of the five-level converter and the structure of the ANFIS are presented. The PI controllers of the cascade two stages control loops (speed, stator powers and rotor currents) are replaced by a trained ANFIS controller using an appropriate data collection from the studied system in different operating modes.
- Finally we present the final conclusion of the thesis with some perspectives and future projects.

• List of Published Papers

This thesis is based in some part on the work contained in the following papers, referred to in the text:

➤ Publications

1. A. Dida and D. Benattous. Fuzzy logic control of grid connected DFIG system using back-to-back converters, *International Journal of Systems Assurance Engineering and management*. Vol. 8, No. 1, 2017.
2. A. Dida and D. Benattous. Doubly-Fed Induction Generator Drive based WECS using Fuzzy Logic Controller, *Frontier of energy*. Vol. 9, No. 3, 2015.
3. A. Dida and D. Benattous. Doubly-Fed Induction Generator Drive System Based on Maximum Power Curve Searching using Fuzzy Logic Controller, *International Journal of Power Electronics and Drive System*, Vol. 5, No. 4, 2015.
4. A. Dida and D. Benattous. Modeling and Control of DFIG through Back-to-Back Five levels Converters based on Neuro-Fuzzy Controller, *Journal of Control, Automation and Electrical Systems*, Vol. 26, No. 5, 2015.
5. A. Dida and D. Benattous. Adaptive hill-climb searching method for MPPT algorithm based DFIG system using fuzzy logic controller, *International Journal of Systems Assurance Engineering and management*, Vol. 8, No. 1, 2017.
6. A. Dida and D. Benattous. A Complete Modeling and Simulation of DFIG based Wind Turbine System using Fuzzy Logic Control, *Frontier of energy*. Vol. 10, No. 2, 2016.

➤ Communications

1. A. Dida and D. Benattous. Fuzzy Logic Control of Grid Connected DFIG Using Back-to-Back Five-level NPC Converters for WECS, *5th International Conference on Electronics Engineering (ICEE 2013)*, 20 & 21 November 2013, Oran, Algeria.
2. A. Dida and D. Benattous. Fuzzy Logic Control of Grid Connected DFIG using Back-to-Back Converters for WECS, *International Conference of Modeling and Simulation*, September 21- 23, 2014, Khemis Miliana, Algeria.
3. F. Merah and A. Dida, D. Benattous. Control of Wind Energy Conversion System Using Neuro-Fuzzy Based Five-Level NPC Converters, *6th AUN/SEED-Net regional conference on electrical engineering*, 4 & 5 March 2014, Malaya, Malaysia.
4. A. Dida and D. Benattous. Neuro-Fuzzy Control of Grid Connected DFIG via Five-Level NPC Converter for WECS, *2nd International Conference on Electrical Energy and Systems*, October 28-30, 2014, Annaba, Algeria.

5. A. Dida and D. Benattous. Adaptive P&O Control for MPPT Algorithm in DFIG System using Fuzzy Logic Controller, *3rd International Conference on Information Processing and Electrical Engineering, (ICIPEE'14)*. November 24-25, 2014, Tebessa, Algeria.
6. A. Dida and D. Benattous. Fuzzy Logic based Sensorless MPPT Algorithm for Wind Turbine System Driven DFIG, *3rd IEEE International Conference on Control, Engineering & Information Technology (CEIT'2015)*, May 25-27, 2015, Tlemcen, Algeria.
7. A. Dida and D. Benattous. Modeling and Control of DFIG via Back-to-Back Multilevel Converters using Fuzzy Logic Controller, *3rd IEEE International Conference on Control, Engineering & Information Technology (CEIT'2015)*, May 25-27, 2015, Tlemcen, Algeria.

• References of General Introduction

- [1] R. Swisher, C. R. De Azua, J. Clendenin, Strong winds on the horizon: wind power comes of age, *IEEE Proceedings, American Wind Energy Assoc.*, Washington, DC, USA, Vol. 89, No. 12, pp. 1757-1764, Dec. 2001.
- [2] S. Heier, *Grid integration of wind energy conversion systems*, John Wiley and Sons, New York, 1998.
- [3] M. Ahlstrom, L. Jones, R. Zavadil, and W. Grant, The future of wind forecasting and utility operation, *IEEE Power and Energy Magazine*, Vol. 3, No. 6, pp. 57-64, Nov./Dec. 2005.
- [4] R. Piwko, D. Osborn, R. Gramlich, G. Jordan, D. Hawkins, and K. Porter, Wind energy delivery issues, *IEEE Power and Energy Magazine*, Vol. 3, No. 6, pp. 47-56, Nov./Dec. 2005
- [5] J. Ekanauake, L. Holdsworth, and N. Jenkins, Control of DFIG wind turbines, *IEEE Power Engineer*, vol. 17, pp. 28-32, Feb. 2003.
- [6] Lei Wang, *Advanced control of variable speed wind turbine based on doubly-fed induction generator*, Phd Thesis, University of Liverpool, Sep. 2012.
- [7] W. E. Leithead and B. Connor, Control of variable speed wind turbines: dynamic models, *International Journal of Control*, Vol. 73, No. 13, pp. 1173-1188, Sep. 2000.
- [8] J. Lopez, P. Sanchis, X. Roboam and L. Marroyo, Wind turbines based on doubly fed induction generator under asymmetrical voltage dips, *IEEE Trans. on Energy Conversion*, Vol. 23, No. 1, pp. 321-330, Mar. 2008.
- [9] W. E. Leithead and B. Connor, Control of variable speed wind turbines: design task, *International Journal of Control*, Vol. 73, No. 13, pp. 1189-1212, Sep. 2000.
- [10] J. P. A. Vieira, M. N. A. Nunes and U. H. Bezerra, Design of optimal PI controllers for doubly fed induction generators in wind turbines using genetic algorithm, *IEEE Power and Energy Society General Meeting*, pp. 1-7, Pittsburgh, Jul. 2008.
- [11] W. Qiao, G. K. Venayagamoorthy and R. G. Harley, Design of optimal control PI controllers for doubly fed induction generators driven by wind turbines using particle swarm optimization, *International Joint Conference on Neural Networks*, pp. 1982-1987, Canada, Jul. 2006.
- [12] R. Marino, S. Peresada and P. Valigi, Adaptive input-output linearising control of induction motor, *IEEE Transactions on Automatic Control*, Vol. 38, No. 2, pp. 208-221, Feb. 1993.
- [13] A. F. Payam, An adaptive input-output feedback linearization controller for doubly-fed induction machine drives, *Serbian Journal of Electrical Engineering*, Vol. 5, No. 1, pp. 139-154, May 2008.
- [14] X. P. Zhang, K. Godfrey and P. Ju, Small signal stability analysis and optimal control of a wind turbine with doubly fed induction generator, *IET Generation, Transmission & Distribution*, Vol. 1, No. 5, pp. 751-760, Sep. 2007.
- [15] M. Singh, *Adaptive network-based fuzzy inference systems for sensorless control of PMSG based wind turbine with power quality improvement features*, Phd thesis, Superior Technology school, Montreal, 16 July 2010.
- [16] M.N. Cirstea, A. Dinu, J.G. Khor, M. McCormick, *Neural and fuzzy logic control of drives and power systems*, Newnes publications, Elsevier Science Linacre House, Jordan Hill, Oxford OX2 8DP 225 Wildwood Avenue, 2002.
- [17] E. H. Mamdani, Application of fuzzy algorithms for control of simple dynamic plant, *IEEE Proceedings, Institution of , Queen Mary College, London, UK*, Vol. 121, No. 12, pp. 1585–1588, 1974.
- [18] M. McKenna and B. M. Wilamowski, Implementing a fuzzy system on a field programmable gate array, *International Joint Conference on Neural Networks (IJCNN'01)*, Washington DC, pp. 189–194, July 15–19, 2001.
- [19] T. Takagi and M. Sugeno, Fuzzy identification of systems and its application to modeling and control, *IEEE Trans. on System, Man, Cybernetics*, Vol. 15, No. 1, pp. 116–132, 1985.
- [20] M. Sugeno and G. T. Kang, Structure identification of fuzzy model, *Fuzzy Sets and Systems*, Vol. 28, No.1, 15–33, 1988.
- [21] B. M. Wilamowski and J. Binfet, Do fuzzy controllers have advantages over neural controllers in microprocessor implementation, *2nd International Conference on Recent Advances in Mechatronics—ICRAM'99*, Istanbul, Turkey, pp. 342–347, May 24–26, 1999.
- [22] T. Xie, H. Yu, and B. Wilamowski, Replacing fuzzy systems with neural networks, *Rzeszow, Poland*, May, 13-15, 2010.

- [23] A. Abraham, Adaptation of fuzzy inference system using neural learning, *StudFuzz* 181, pp. 53–83, Springer-Verlag Berlin Heidelberg, 2005.
- [24] A. Abraham, *Neuro-Fuzzy Systems: State-of-the-Art Modeling Techniques, Connectionist Models of Neurons, Learning Processes, and Artificial Intelligence*, Springer-Verlag Germany, Jose Mira and Alberto Prieto (Eds.), Granada, Spain, pp. 269–276, 2001.
- [25] A. Abraham, *Intelligent Systems: architectures and perspectives, recent advances in intelligent paradigms and applications*, Abraham A., Jain L. and Kacprzyk J. (Eds.), *Studies in Fuzziness and Soft Computing*, Springer Verlag Germany, Chap. 1, pp. 1–35, 2002.
- [26] A. Abraham and M.R. Khan, *Neuro-Fuzzy paradigms for intelligent energy management, innovations in intelligent systems: design, management and applications*, Abraham A., Jain L. and Jan van der Zwaag B. (Eds.), *Studies in Fuzziness and Soft Computing*, Springer Verlag Germany, Chap. 12, pp. 285–314, 2003.
- [27] F. De Souza, M.M.R. Vellasco, M.A.C. Pacheco, *The hierarchical Neuro-Fuzzy BSP model: an application in electric load forecasting, connectionist models of neurons, learning processes and artificial intelligence*, Jose Mira et al (Editors), LNCS 2084, Springer Verlag Germany, 2001.
- [28] R. Fuller, *Introduction to Neuro-Fuzzy Systems*, studies in fuzziness and soft computing, Springer Verlag, Germany, 2000.
- [29] J. Hollatz, *Neuro-Fuzzy in legal reasoning*, IEEE International Conference on Fuzzy Systems, pp. 655–662, 1995.
- [30] E. Khan and P. Venkatapuram, *Neufuz: Neural network based fuzzy logic design algorithms*, IEEE International Conference on Fuzzy Systems, pp. 647–654, 1993.
- [31] W. Li, *Optimization of a fuzzy controller using neural network*, IEEE International Conference on Fuzzy Systems, pp. 223–227, 1994.
- [32] C.T. Lin and C.S.G. Lee, *Neural network based fuzzy logic control and decision system*, IEEE Trans. on Computing. Vol. 40, No.12, pp. 1320–1336, 1991.
- [33] A. Lotfi, *Learning fuzzy inference systems*, Phd Thesis, Department of Electrical and Computer Engineering, University of Queensland, Australia, 1995.
- [34] D. Nauck D. and R. Kruse, *Neuro-Fuzzy Systems for Function Approximation*, *Fuzzy Sets and Systems*, Vol. 101, pp. 261–271, 1999.
- [35] S.K. Pal and S. Mitra, *Neuro-Fuzzy pattern recognition: methods in soft computing*, John Wiley & Sons, Inc, USA, 1999.
- [36] H. Takagi, *Fusion technology of fuzzy theory and neural networks – Survey and Future Directions*, 1st International Conference on Fuzzy Logic & Neural Networks, pp. 13–26, 1990.
- [37] R.R. Yager, *On the Interface of Fuzzy Sets and Neural Networks*, International Workshop on Fuzzy System Applications, pp. 215–216, 1988.
- [38] H.R. Berenji and P. Khedkar, *Learning and tuning fuzzy logic controllers through reinforcements*, IEEE Trans. on Neural Networks, Vol. 3, pp. 724–740, 1992.
- [39] R. Jang, *Neuro-Fuzzy modeling: architectures, analyses and applications*, Phd Thesis, University of California, Berkeley, 1992.
- [40] D. Nauck and R. Kruse, *NEFCON-I: An X-Window based simulator for neural fuzzy controllers*, IEEE International Conference on Neural Networks, Orlando, pp. 1638–1643, 1994.
- [41] D. Nauck and R. Kruse, *NEFCLASS: A Neuro-Fuzzy approach for the classification of data*, acm symposium on applied computing, George K et al (Eds.), Nashville, ACM Press, pp. 461–465, 1995.
- [42] S.M. Sulzberger, N.N. Tschicholg-Gurman, S.J. Vestli, *FUN: Optimization of fuzzy rule based systems using neural networks*, IEEE Conference on Neural Networks, San Francisco, pp. 312–316, 1993.
- [43] J.C. Feng and L.C. Teng, *An online self constructing neural fuzzy inference network and its applications*, IEEE Trans. on Fuzzy Systems, Vol. 6, No.1, pp. 12–32, 1998.
- [44] S. Tano, T. Oyama and T. Arnould, *Deep combination of fuzzy inference and neural network in fuzzy inference*, *Fuzzy Sets and Systems*, Vol. 82, No. 2, pp. 151–160, 1996.
- [45] N. Kasabov, *Evolving fuzzy neural networks – algorithms, applications and biological motivation*, In Yamakawa T and Matsumoto G (Eds), *Methodologies for the Conception, Design and Application of Soft Computing*, World Scientific, pp. 271–274, 1998.

- [46] N. Kasabov and S. Qun, Dynamic evolving fuzzy neural networks with m-out-of-n activation nodes for on-line adaptive systems, Technical Report TR99/04, Department of information science, University of Otago, New Zealand, 1999.
- [47] A. Abraham, EvoNF: A framework for optimization of fuzzy inference systems using neural network learning and evolutionary computation, 17th IEEE International Symposium on Intelligent Control, ISIC'02, IEEE Press, pp. 327–332, 2002.
- [48] A. Kandel, Q.Y. Zhang and H. Bunke, A Genetic Fuzzy Neural Network for Pattern Recognition, IEEE Trans. on Fuzzy Systems, pp. 75–78, 1997.
- [49] M. Mizumoto, S. Yan, A new approach ofneurofuzzy learning algorithm, intelligent hybrid systems: fuzzy logic, neural networks, and genetic algorithms, Ruan D (Ed.), Kluwer Academic Publishers, pp. 109–129, 1997.
- [50] Q.Y. Zhang, A. Kandel, Compensatory Neuro-fuzzy systems with fast learning algorithms, IEEE Trans. on Neural Networks, Vol. 9, No. 1, pp. 83–105, 1998.
- [51] M. A Denai, F. Palis, A. Zeghib, ANFIS based modelling and control of non-linear systems : a tutorial, IEEE International Conference on Systems, Man and Cybernetics, Vol. 4, pp. 3433-3438, 2004
- [52] J-S R. Jang, ANFIS: adaptive-network-based fuzzy inference system, IEEE Transactions on Systems, Man and Cybernetics, Vol. 23, No 3, p. 665-685. 1993
- [53] J-S R. JANG, C-T SUN, Neuro-Fuzzy modeling and control, Proceedings of the IEEE, Vol. 83, No. 3, March 1995.
- [54] Azar, Ahmad Taher (2010). Adaptive Neuro-Fuzzy Systems, Fuzzy Systems, Ahmad Taher Azar (Ed.), ISBN: 978-953-7619-92-3, InTech, Available from: <http://www.intechopen.com/books/fuzzy-systems/adaptive-neurofuzzy-systems>.

Chapter 1:

Wind Power Generation System: State of the Art

Chapter 1: Wind Power Generation System: State of the Art

1.1. Introduction

This chapter gives an overview of the current wind turbine systems (WTSs) and describes some future trends. After discussing some recent statistics, it describes the currently used wind generation systems, and then possible future generators and drive train systems are reviewed, to overcome the drawbacks of the conventional multi-stage gearbox and the grid side step-up transformer (GSST), some ideas of enhanced electrical machine, torque converter and power electronic grid interfaces are presented.

1.2. Historical Facts about Wind Power

Wind energy has been used for thousands of years by humans. Ancient Persians used wind energy to pump water before the birth of Christ [1]. Propulsion of sailboats, pumping water and grinding corn were the earliest application areas. Recently, Denmark was the first country to use the wind for generation of electricity. The Danes were using a 23 m diameter WT in 1890 to generate electricity. By 1910, several hundred units with capacities of 5 to 25 kW were in operation in Denmark [2]. The famous design of Dutch windmills is presented in Figure 1.1.



Figure 1.1 Famous Dutch windmills.

In the international scale, interest in renewable energy has been increasing since the first oil crisis in 1973 and the renewable energy industry has made significant advances since the protocol of Kyoto (Japan, 1997) where collective reductions in greenhouse gas emissions were agreed and various developments were encouraged by governments around the world [3].

In the 1970s and 1980s, a variety of onshore WT configurations were investigated, including both horizontal and vertical axis designs (see Figure 1.2). Gradually, the horizontal axis design with three-blade came to dominate [4].

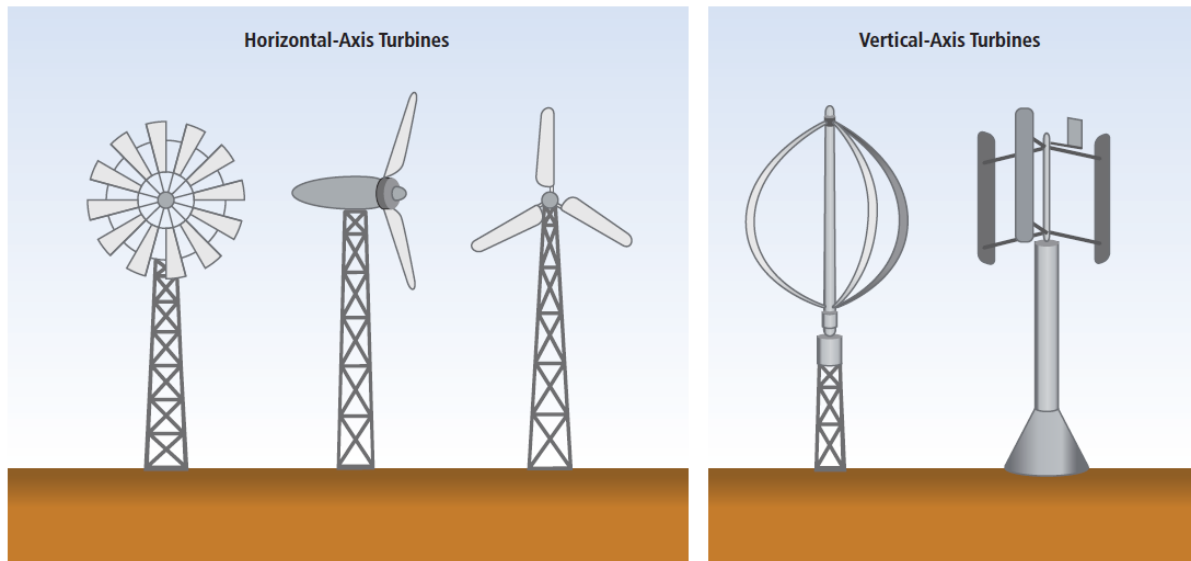


Figure 1.2 Early WT designs, including horizontal and vertical axis turbines.

1.3. Development of Wind Power Generation

The cumulative wind power capacity from 1999 to 2020 is shown in Figure 1.3, and it can be seen that the wind power has grown fast to a capacity of 283 GW with ~45 GW installed only in 2012, and this number is expected to achieve 760 GW in 2020 on moderate scenario [5]. Wind power grows more significant than any other renewable energy sources and is becoming really an important player in the modern energy supply system. For example, Denmark has a high penetration by wind power and today >30% of the electric power consumption is covered by wind. This country has even the ambition to achieve 100% non-fossil based power generation system by 2050 [6].

Regarding the markets and manufacturers, the U.S. became the largest markets with over 13.1 GW capacity installed in 2012, together with China (13 GW) and the EU (11.9 GW) sharing around 87% of the global market. The Danish company *Vestas* first gives out the top position among the largest manufacturers since 2000, while GE catches up to the first because of the strong U.S. market in 2012. Figure 1.4 summarizes the worldwide top suppliers of WTs in 2012. It is seen that there are four Chinese companies in the top 10 manufacturers with a total market share of 16.6%, which is a significant drop compared with the 26% in 2011 [5,7].

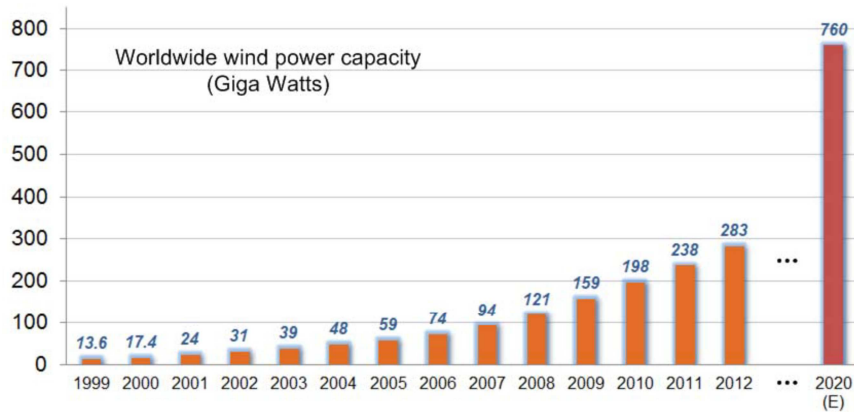


Figure 1.3 Global cumulative installed wind power capacity from 1999 to 2020.

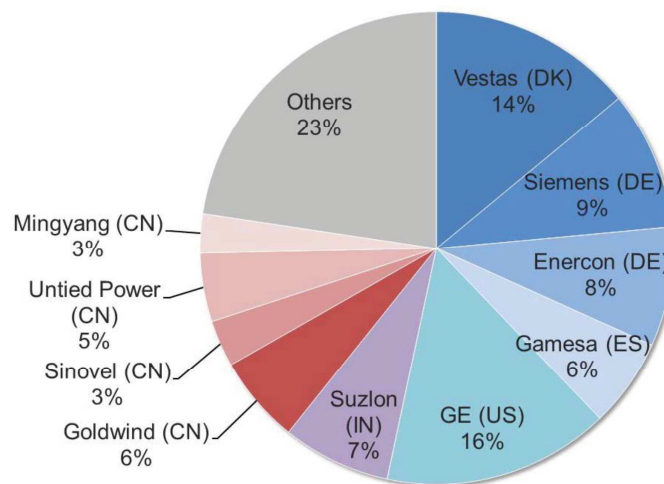


Figure 1.4 Distribution of WT market share by the manufacturers in 2012.

In addition to the quick growth in the total installed capacity, the size of individual WT is also increasing dramatically to obtain a reduced price per generated kilowatt hour. In 2012, the average turbine size delivered to the market was 1.8-MW, among which the average offshore turbine has achieved a size of 4-MW. The growing trends of emerging turbine size between 1980 and 2018 are shown in Figure 1.5, where the development of power electronics in the WTS (rating coverage and function role) is also shown. It is noted that the cutting-edge 8-MW WTs with a diameter of 164 m have already shown up in 2012 [8]. Right now most of the turbine manufacturers are developing products in the power range 4.5–8 MW, and it is expected that more and more large WTs even up to 10-MW will appear in 2018, will be present in the next decade [7].

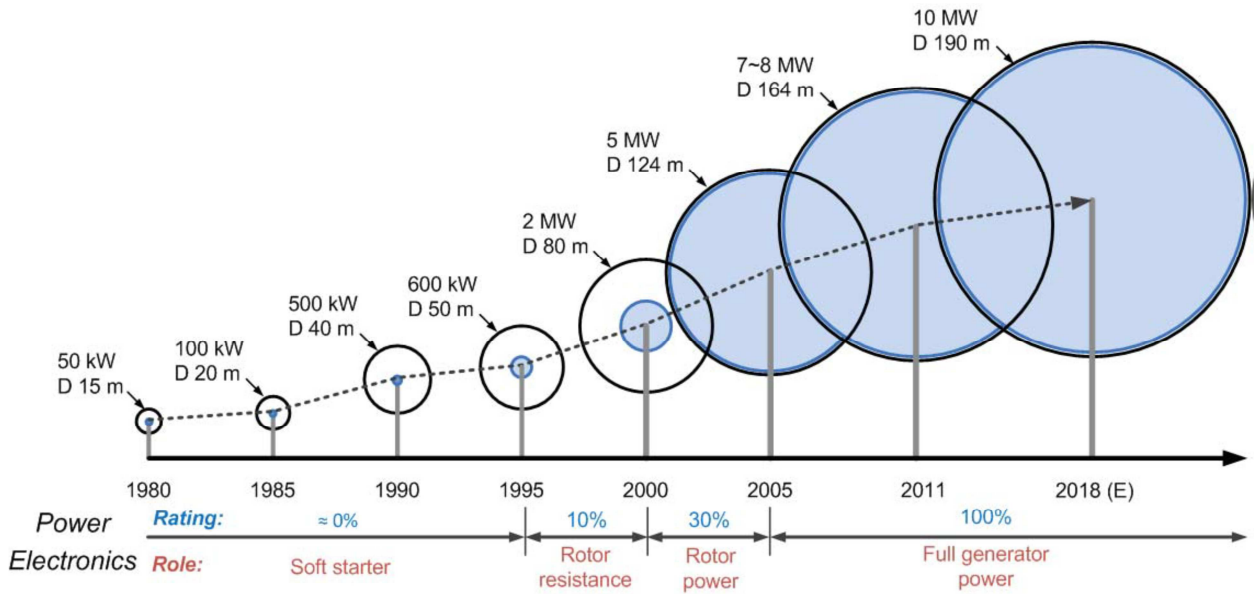


Figure 1.5 Evolution of WT size and the power electronics seen from 1980 to 2018 (estimated). Blue circle: the power coverage by power electronics.

1.4. Components of Modern Wind Turbines

Not all of the components described here will be found in every type and size of WT but the main components of a typical one are illustrated in Figure 1.6.

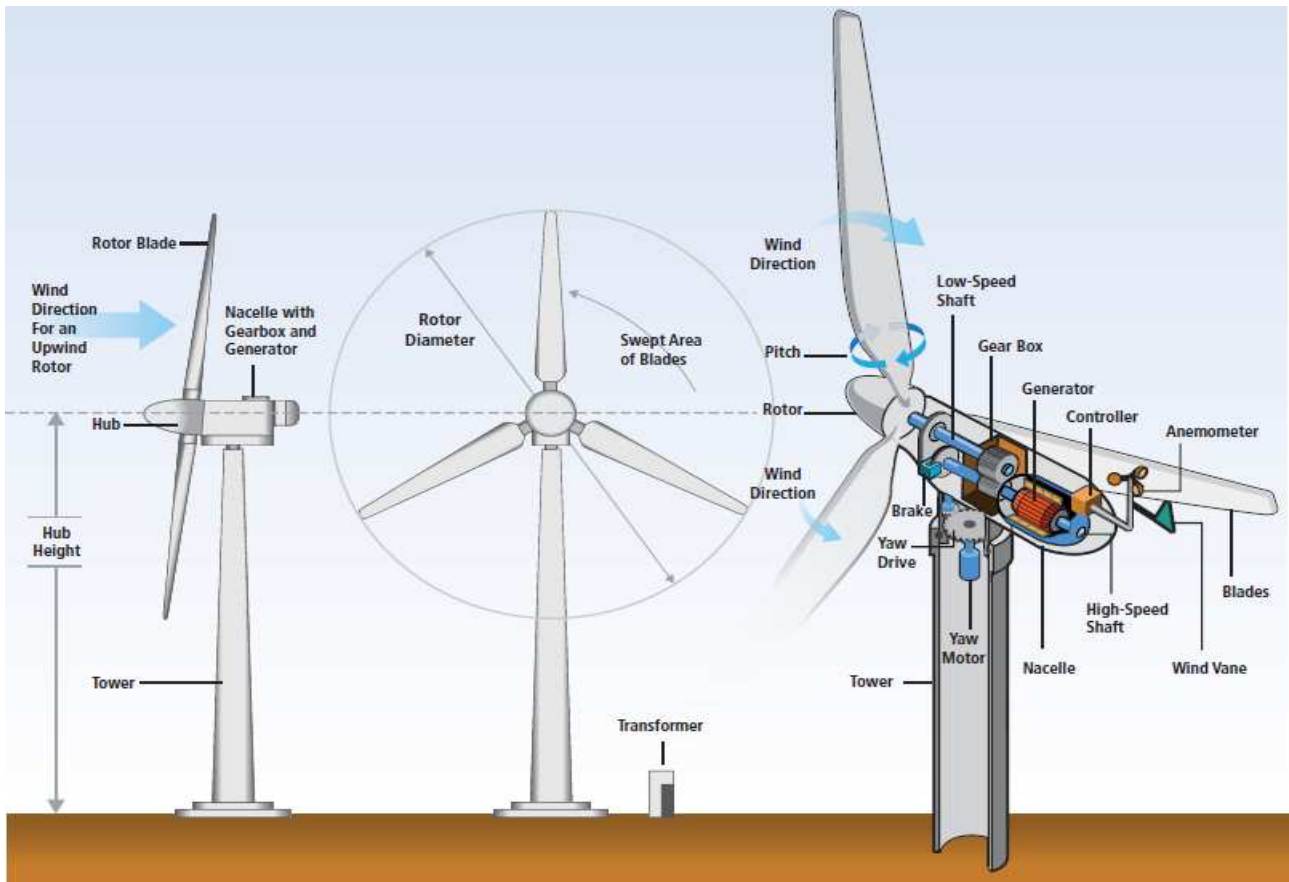


Figure 1.6 Basic components of a modern, horizontal-axis WT with a gearbox (Design by the National Renewable Energy Laboratory (NREL)).

Driven by the wind, the blades (connected to the rotor by the hub) transmit the mechanical energy via the low speed shaft through the gearbox to the high speed shaft that is attached to the generator. The low speed shaft is supported by the main bearing, and the gearbox adjusts this speed, some WT configurations use a converter to match the grid connection [3].

Alignment to the direction of the wind is controlled by a yaw system that rotates the nacelle (housing) at the top of a tower mounted on a bedplate or foundation. The pitch system (mounted in each blade) controls the amount of power going to the WT as well as acting as an aerodynamic brake; there will also be a hydraulic brake mounted on the high speed shaft to stop the WT. A meteorological unit may provide weather data (e.g. wind speed and direction) for the control of the pitch, brake and yaw systems, etc.

The costs of all these components in different types and sizes of WT will vary. For example, the costs of both converters and generators will differ depending on the configuration and some WTs do not have a gearbox at all, Figure 1.7 shows the component cost distribution for a typical 2MW WT [9,3].

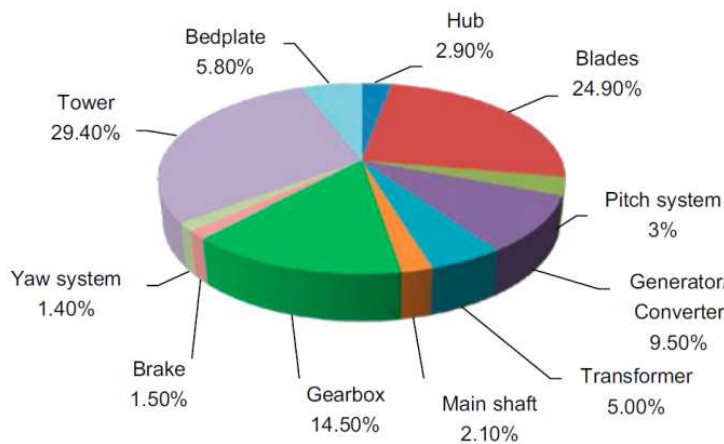


Figure 1.7 Component costs distribution for typical 2MW WT.

1.5. State-Of-The-Art of Currently Used Generator Systems

WTs can operate with either fixed speed or variable speed. The actual rotational speed of a WT is quite low and not fixed in nature. Therefore, the turbine speed must be adjusted to suit the electrical frequency. This can be done in two ways: either with a gearbox or with the number of pole pairs of the generator. The pole pair sets the mechanical speed of the generator with respect to the electrical frequency and the gearbox adjusts the rotor speed of the turbine to the mechanical speed of the generator. The gearbox-based system has shorter life time and requires frequent maintenance. The efficiency and armature diameter of an induction machine depend on the number of poles. The increase in the number of poles may decrease the efficiency and increase the magnetizing currents [10].

Depending on the types of generator, power electronics, speed controllability, gearbox or direct-drive (DD), and the way in which the aerodynamic power is limited the WT designs can generally be categorized into several concepts [11]. Next, the four most commonly used generator systems applied in WTs concepts are going to be presented. Table 2.1 lists the top 10 WT manufacturers of 2012 with the power levels of their products and the generator systems they use [12].

Table 1.1: Top 10 WT manufacturers of 2012, currently used generator concepts and power ranges [13]–[14]

Manufacturer	Concept	Rotor diameter	Power range
Vestas (Denmark)	DFIG	80 – 100 m	1.8 – 3 MW
	GFC PM	112 – 164 m	1.8– 8 MW
General Electric (US)	DFIG	77 – 120 m	1.5 – 2.85 MW
	DD PM	113 m	4.1 MW
Sinovel (China)	DFIG	60 – 113 m	1.5 – 5 MW
Enercon (Germany)	DD EE	48 – 126 m	0.8 – 7.5 MW
Goldwind (China)	DD PM	70 – 109 m	1.5 – 2.5 MW
Gamesa (Spain)	DFIG	52 – 114 m	0.85 – 2 MW
	GFC PM	128 m	4.5 MW
Guodian United Power (China)	DFIG	77 – 100 m	1.5 – 3 MW
	DD PM	100 m	3MW
Suzlon/REpower (India)	CSIG	52 – 88 m	0.6 – 2.1 MW
	DFIG	95 – 97m	2.1 MW
Siemens (Germany/ Denmark)	GFC IG	82 – 120 m	2.3 – 3.6 MW
	DD PM	101 – 154 m	3 – 6 MW
MingYang (China)	DFIG	77 – 83 m	1.5 MW
	GFC PM	92 – 108 m	2.5 – 3MW

where:

CSIG: constant speed with gearbox and induction generator, possibly with extended slip or two speeds.

DFIG: variable speed with gearbox, doubly-fed induction generator and partly rated converter.

DD EE: variable speed with direct-drive synchronous generator with electrical excitation and full converter.

DD PM: variable speed with direct-drive permanent-magnet generator and full converter.

GFC PM: variable speed with gearbox, permanent-magnet generator and full converter.

GFC IG: variable speed with gearbox, induction generator and full converter.

1.5.1. Fixed Speed WTs Concept

During the last decades of the last century, most WT manufacturers mainly built constant speed WTs with power levels increasing to ~ 1.5 MW. This constant speed system consists of a three-stage gearbox and a SCIG directly connected to the utility grid. This system (shown in Figure 1.8) is also referred to as the Danish concept [12].

Above the rated wind speed, the power is mostly limited using the classic stall principle: if the wind speed increases above the rated wind speed, the power coefficient reduces, so that the power produced by the turbine remains approximately equal to the rated power. Sometimes active stall is used: negative pitch angles are used to limit the power.

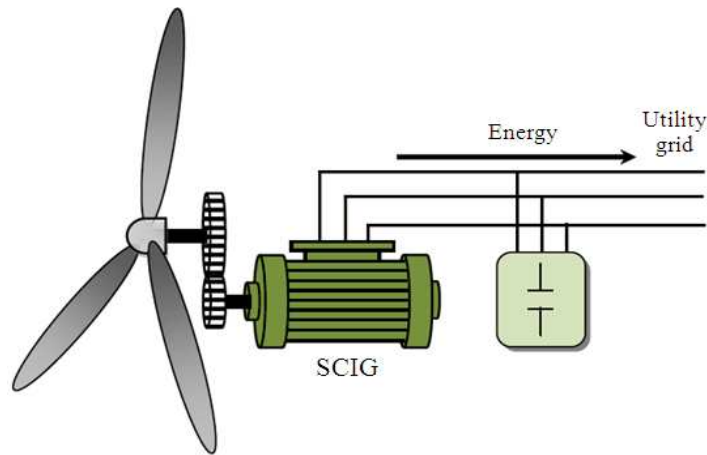


Figure 1.8 Scheme of a fixed speed WT with SCIG.

The main strength of this system is that it consists of simple off-the-shelf components and that, therefore, it is cheap. Two variants of this system have been used to overcome some of its drawbacks.

- Pole-changeable SCIGs (shown in Figure 1.9) have two stator windings with different numbers of pole pairs so that the turbine can operate at two constant speeds to increase energy yield and reduce audible noise.

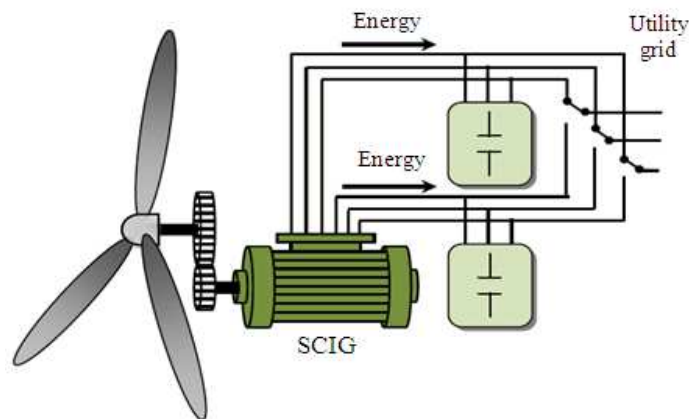


Figure 1.9 Pole-changeable concept with SCIG.

- The limited variable speed (slip $\leq +10\%$) WT has a wound rotor induction generator (WRIG) with an electronically variable rotor resistance (shown in Figure 1.10). This enables larger speed variations and reduces mechanical loads and power quality problems. This system is sometimes mentioned as a separate generator system [13].

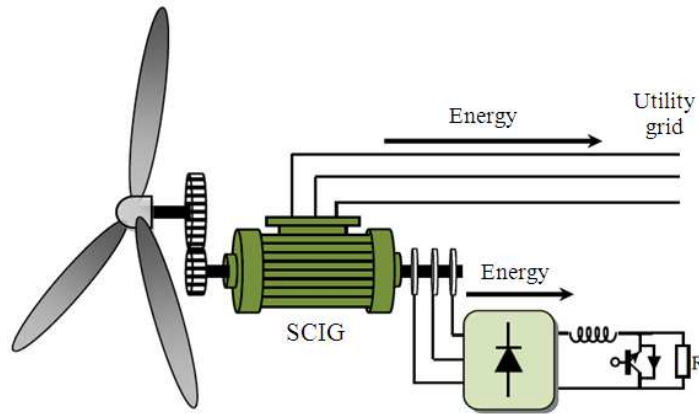


Figure 1.10 Limited variable speed concept with WRIG.

1.5.2. Variable Speed WTs Concept with Geared-Drive and Partial-Rated Power Converter

After 1996, many WT manufacturers changed to a variable speed WTS with DFIG and power levels above roughly 1.5-MW (shown in Figure 1.11). This system consists of a multi-stage gearbox, a relatively low cost standard DFIG and a partly rated power electronic converter feeding the rotor winding shown in Figure 1.12. Pitch control limits the output power to rated power at wind speeds above rated [12]. The power rating of the converter is ~25% of the rated power, enabling a speed range from roughly 60% to 110% of the rated speed. This is sufficient for a good energy yield because the tip speed ratio can be kept optimal for a large part of the operating range.

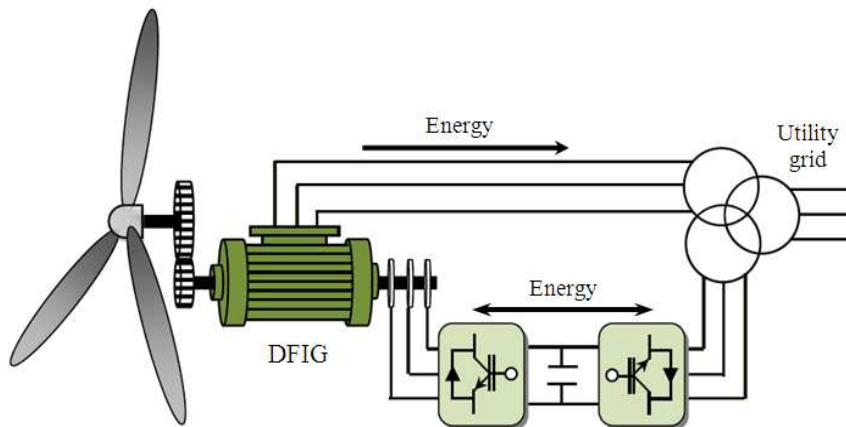


Figure 1.11 Scheme of a variable speed concept with DFIG.



Figure 1.12 Wounded rotor used in the DFIG.

Compared with the constant speed system, this system enables a more flexible match with requirements considering audible noise, mechanical loads, power quality, and energy yield. An important disadvantage of this system appeared when the grid codes of the power system operators prescribed grid-fault ride-through (GFRT) capabilities [15]. This was not possible with the standard DFIG system, and therefore a lot of work has been done to enable GFRT [16, 17]. This work has been so successful that general electric (GE), after changing to gear and full converter (GFC) systems around 2005, changed back to DFIG in 2012.

1.5.3. Variable Speed WTs Concept with Geared-Drive and Fully-Rated Power Converter

Since around 2005, several large manufacturers have developed variable speed WTs with a gearbox, a brushless generator, and a converter for the full rated power. Pitch control limits the output power to rated power at wind speeds above rated. This system is mainly used to obtain better GFRT characteristics than the DFIG and to avoid the maintenance and the failures of the brushes of the DFIG. However, a fully rated converter has more losses than a partly rated converter as in the case of a DFIG [12].

There are quite a number of variants of this system on the market because different generator types and different gearboxes are used. Several manufacturers use PM SG (shown in Figure 1.14), but SCIGs are also used as shown in Figure 1.13 (Table 2.1). The number of gear stages in this system may vary from one to three. According to [12], a lower number of gear stages implies a larger generator, but the resulting system may be more efficient and more reliable because of the omission of the high speed stage of the gearbox [18].

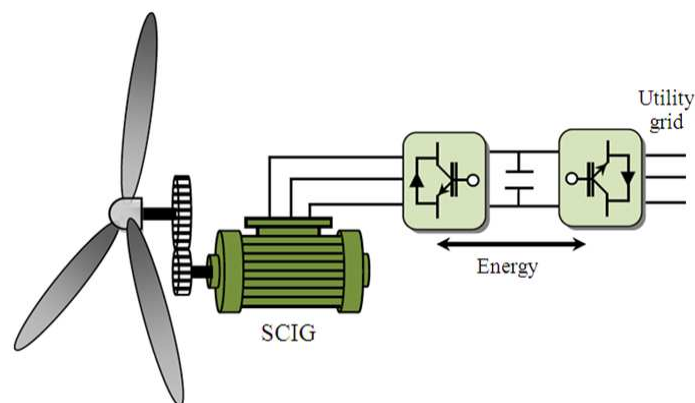


Figure 1.13 Scheme of a variable-speed WT with SC IG and GFC.

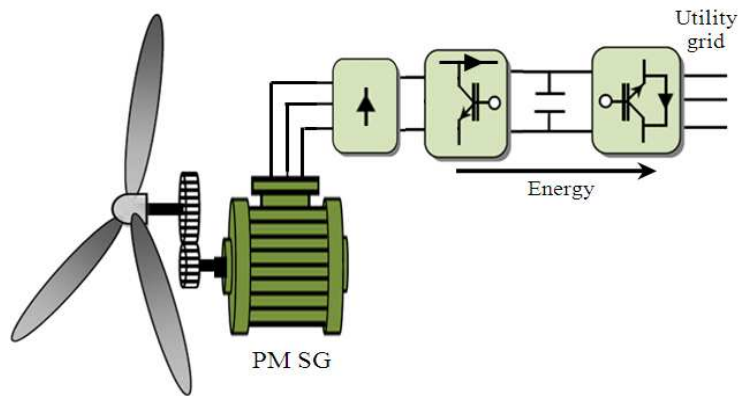


Figure 1.14 Scheme of a variable-speed WT with PM SG and GFC.

1.5.4. Variable Speed WTs Concept with Direct-Drive and Fully-Rated Power Converter

Since 1992, there have also been WT manufacturers using gearless generator systems with DD generators as shown in Figure 1.15. The generator is an electrical excitation (EE) synchronous machine. A fully-rated power converter is necessary for the grid connection.

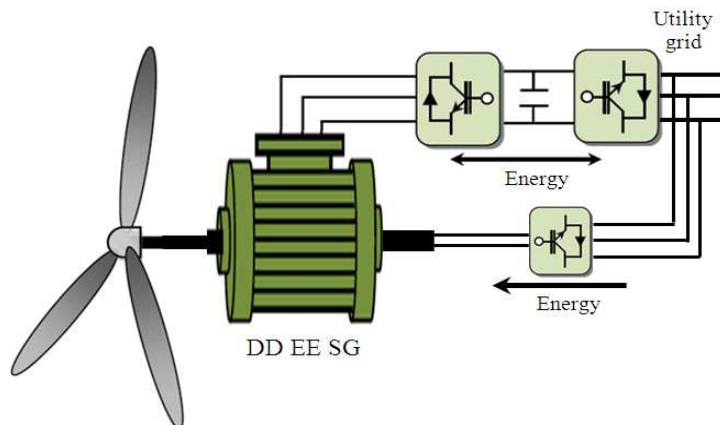


Figure 1.15 Variable-speed WT with DD EE SG and GFC.

In the nineties, DD generators mainly had EE, because PMs were too expensive. When the price of PMs decreased, the focus shifted to PM SGs. The high magnet prices around the year 2011 have again increased the interest in alternatives for PMs [12]. For a long time, *Enercon* has been the only large successful DD manufacturer (shown in Figure 1.16), although there were several smaller DD manufacturers. However, also other large WT manufacturers have started producing DD WTs.

The main reason for using DD systems is to increase reliability by avoiding the maintenance and the failures of the gearbox and by reducing the number of turbine parts. However, it has yet to be proven that the reliability of DDs is really better than that of geared systems [19]. The main drawbacks of the DD generator are that the low-speed high-torque generator is a large, heavy [12], and expensive and that low speed generators are less efficient than high speed generators. Therefore, a lot of research has been done to optimize these machines. The electromagnetic and thermal limitations of the iron cored radial flux generators as applied in the industry are described in [20].

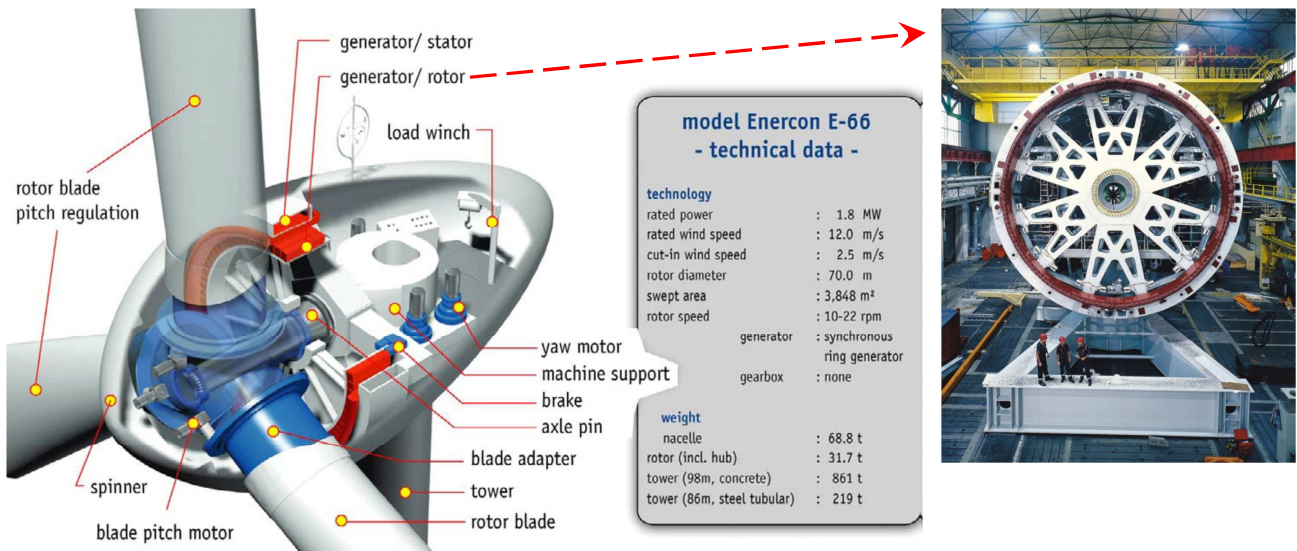


Figure 1.16 Gearless nacelle, in this case of an Enercon E-66 DD WT.

Source: Bundesverband WindEnergie e.V.

1.5.5. Conclusion on Currently Used Generator Systems

It is clear that the constant speed system is disappearing. However, the configuration of DFIG equipped with partial-scale power converter is dominating on the market, but in very near future the configuration with SG with full scale power converter is expected to take over. Actually, the solutions with full-scale power converter are becoming the preferred technology choices in the best selling power ranges of the WTs [21, 8].

Figure 1.17 shows how the numbers and configurations of onshore installations have changed over time so as to increase the power generated in Germany [22, 3] (which had approximately 34% of the total WTs of the world in 2003 [23])

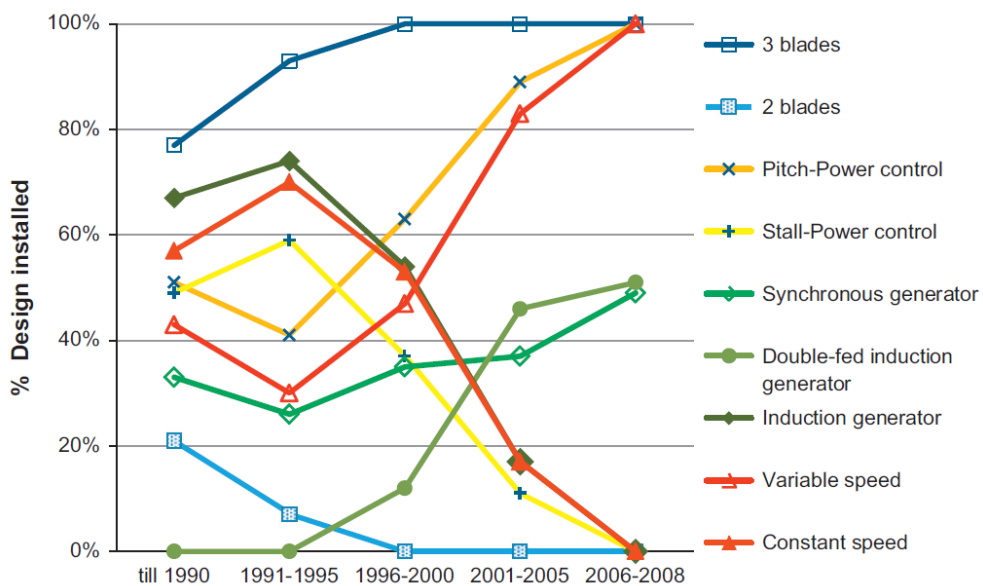


Figure 1.17 WT configurations installed in Germany between 1990 and 2008.

1.6. Development Trends to Reduce the Weight and Volume of the WTS

The turbine nacelle with traditional wind turbine generation system (WTGS) is heavy, especially in offshore applications due to the large mass of the GSST operated at 50 or 60Hz, and copper conductor generator. For example, the weight and volume of a 0.69/33kV 2.6MVA transformer are typically in the range of 6–8 t and 5–9 m³, respectively. The weight for a 10MW DD PM generator is about 300t. These penalties significantly increase the tower construction, and turbine installation and maintenance costs [10]. This section covers the research and development trends on generators, power converters and GSSTs to reduce the weight and volume, and increase the reliability of the WTGSs.

1.6.1. Brushless DFIG (BDFIG)

The BDFIG was reported in the literature by *Hunt* and *Creedy* in the early years of the 20th century [24–25]. Some basic aspects of the BDFIG were also discussed in 1967 [26]. The first implementations of BDFIGs used two DFIGs affixed to the same shaft with their rotor windings connected as shown in Figure 1.18. This topology is known as the Cascaded BDFIG [24,27]. An improvement to the implementation of cascaded DFIGs is the “self-cascaded” BDFIG which is reported in [28, 29]. In this machine two separate windings are located on the stator, sharing the same magnetic circuit. The main advantage of this topology is that only one machine, with two stators, is required instead of two machines affixed to the same shaft as shown in Figure 1.19 [30].

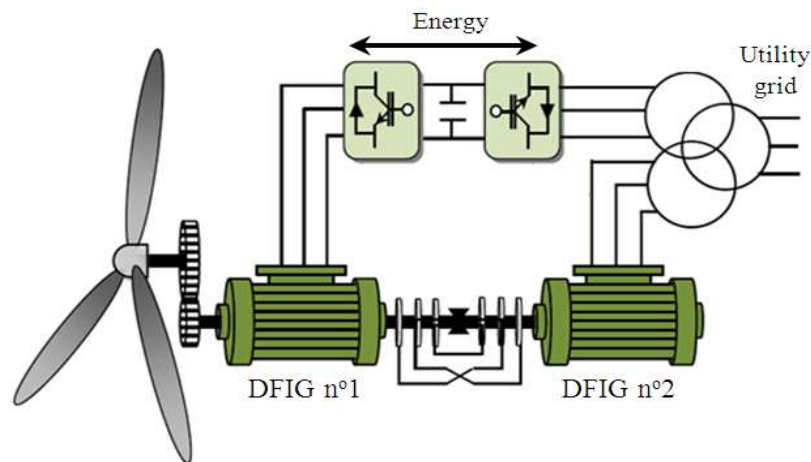


Figure 1.18 Cascaded BDFIG.

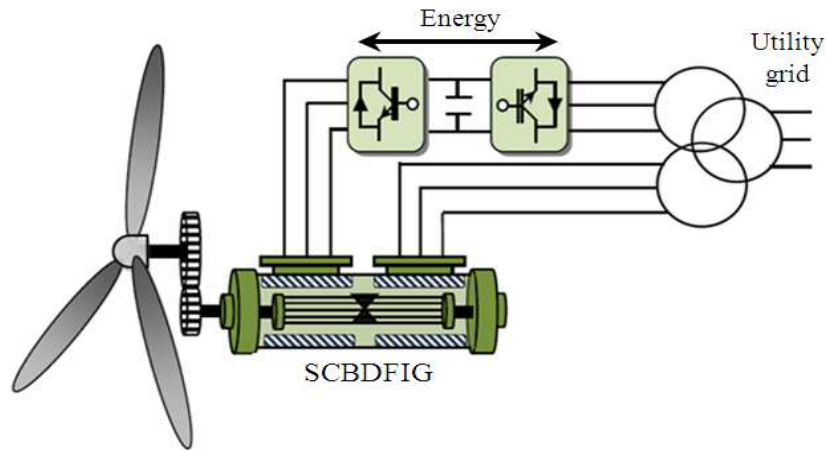


Figure 1.19 Self-cascaded BDFIG.

In [31]–[32], it has been proposed to use the BDFIG as a generator for use in WTSs. The proposed BDFIG has two stator windings, one of which is connected to the grid (known as power winding) and the other (known as control winding) is supplied via a converter, in the same manner as a DFIG. The machine has two principal fields, associated with the two stator windings, of different pole numbers which cross couple via the rotor. The rotor has a short-circuited winding consisting of so-called nested loops as shown in Figure 1.20. The machine operates in a synchronous mode with a fixed ratio between shaft speed and the two stator frequencies, again like the DFIG [12].

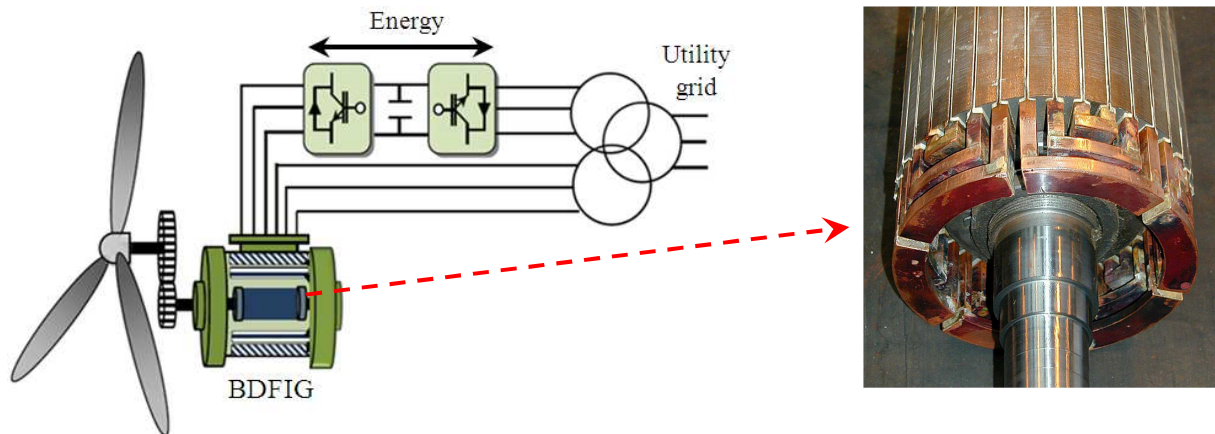


Figure 1.20 BDFIG with nested rotor with six loops.

BDFIG shares with the DFIG the benefits of low cost construction in that no PMs materials are used and only a fractionally rated converter need be employed. Simultaneously, the absence of brush-gear avoids one of the main failure modes of the DFIG. Use of the BDFIG therefore gives a low cost but reliable option [31]. The BDFIG also has a significantly improved GFRT performance compared with an equivalent DFIG, further reducing system cost and complexity.

1.6.2. Continuously Variable Hydrostatic Gearbox (CVHG)

Continuously variable transmissions (CVTs) allow the gear ratios to vary smoothly between a certain range. There are a number of advantages of using a CVT over fixed speed gearbox. First it allows variable speed turbine operation without the use of power electronics. This is a great advantage from the cost of energy perspective since removing the power electronics systems will decrease the capital cost of turbine and increase the reliability of the drivetrain. Second it allows the WT to operate at peak aerodynamic efficiency for a larger wind speed range compared to conventional variable speed machines and this leads to increase in annual energy production [33].

Hydrostatic transmissions on the other hand use fluid flow generated by positive displacement pump to transmit power as shown in Figure 1.21. CVHGs have the highest power density (power to weight) among all transmission technologies. This makes it compact and lighter compared to mechanical gearbox or other drivetrain of similar rating. The flexible nature of the CVHG makes it possible to place the motor and generator assembly of a WT at the base of the tower while the pump remains in the nacelle. This reduces both the nacelle weight and the operation and maintenance costs by not having to use a crane to service the generator and associated electronics in the nacelle [33].

The CVHG is controlling the rotor speed without the need for a frequency converter, and with the use of a synchronous generator with an electrical voltage in the 10 kV range which eliminates the need for a GSST, so the down time related to the mechanical gearboxes and power converters are eliminated [34]. One disadvantage of commercially available hydrostatic drives is the low efficiency. This decreases the annual energy production although decreases the production costs.

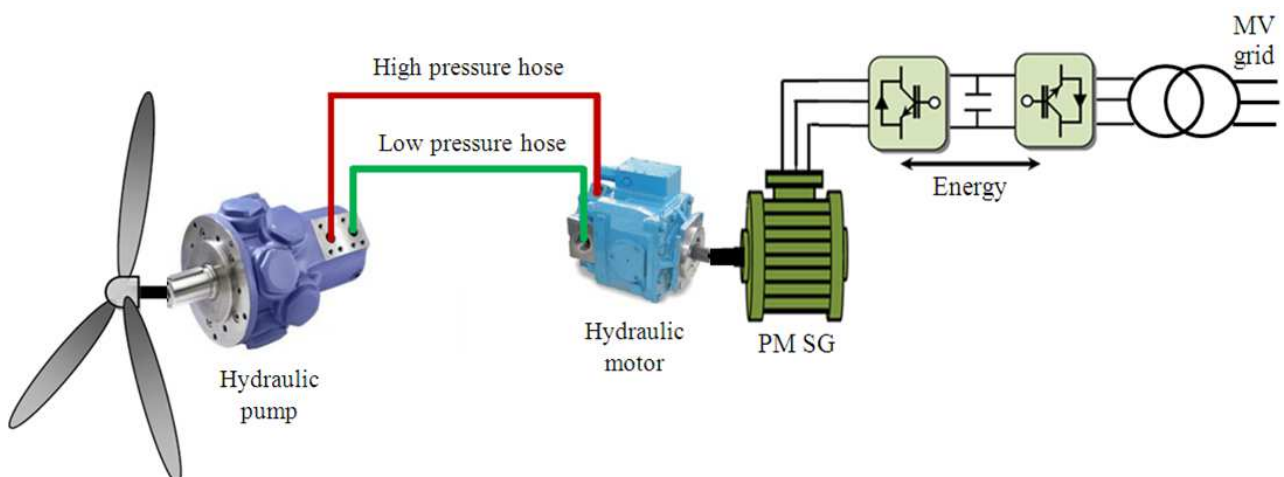


Figure 1.21 Hydrostatic gearbox for WTSS.

1.6.3. Magnetic Gearbox (MG)

In 2001, *Atallah* and *Howe* proposed the coaxial MG as shown in Figure 1.22, which was completely different from the converted MGs. It employs PMs on both outer and inner rotors, and has ferromagnetic pole-pieces between the two rotors. Its operation relies on the use of the ferromagnetic pole-pieces to modulate the magnetic fields produced by each of the PM rotors [35, 36]. Due to the contribution of all PMs to the torque transmission, it exhibits a high torque density, namely $50\text{-}150\text{kNm/m}^3$. The advantages of MGs over mechanical gears are:

- Higher reliability with lower maintenance and no lubrication
- Physical isolation between input and output shafts.
- Very significant torque per volume.
- Very low acoustic noise and vibration
- Compliant transmission eliminates drivetrain pulsations

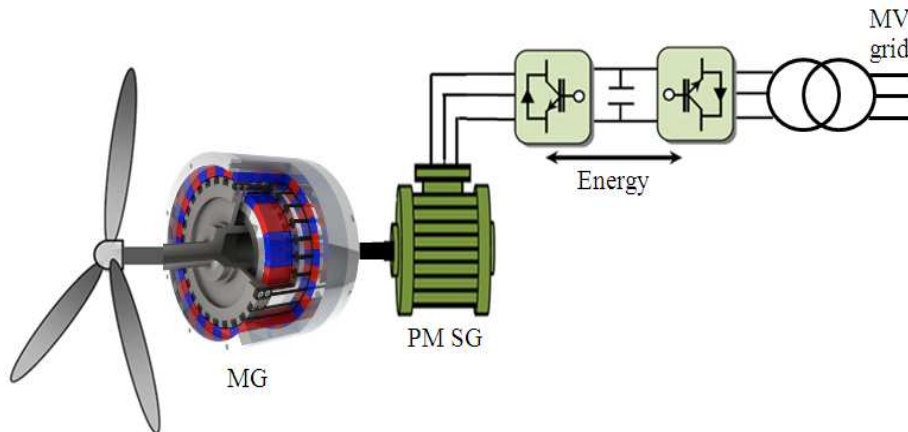


Figure 1.22 Magnetic gearbox in series with a PM or EE SG.

1.6.4. Continuously Variable Magnetic Gearbox (CVMG)

If the outer rotor of the MG is controlled with a stator winding then the variable input speed, can be converted into a constant output speed, by actively controlling the rotor mechanical frequency. An example of a continuously variable magnetic gearbox (CVMG) is shown in Figure 1.23 [37, 38]. The advantages of the CVMG are:

- Controllable gear ratio
- High efficiency
- Compact
- No lubrication
- Power split operation
- Matches fixed-speed prime mover to variable load

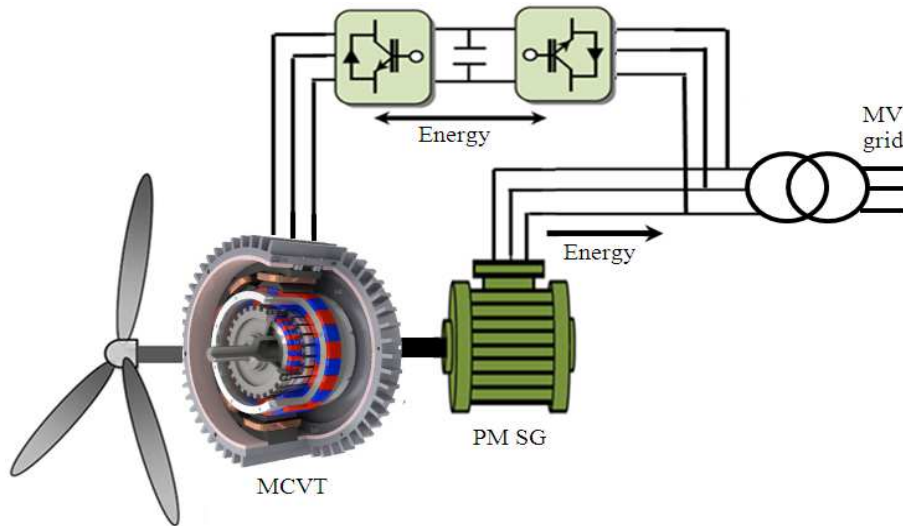


Figure 1.23 CVMG gearbox in series with a PM SG.

1.6.5. Magnetic Pseudo DD Generator (PDD)

A MG may be combined with an electrical machine to realise a high torque density magnetically geared drive in various ways. Figure 1.24 shows a PDD electrical machine, where the magnetic gear and the electrical machine are mechanically as well as magnetically integrated [39,40]. The fundamental flux density component of the PMs on the high-speed rotor couples with the stator winding to produce torque, while the asynchronous space harmonic resulting from the modulation by the ferromagnetic pole pieces of the magnetic field of the high-speed rotor PMs couples with the PMs on stator to transmit torque at fixed gear ratio [12].

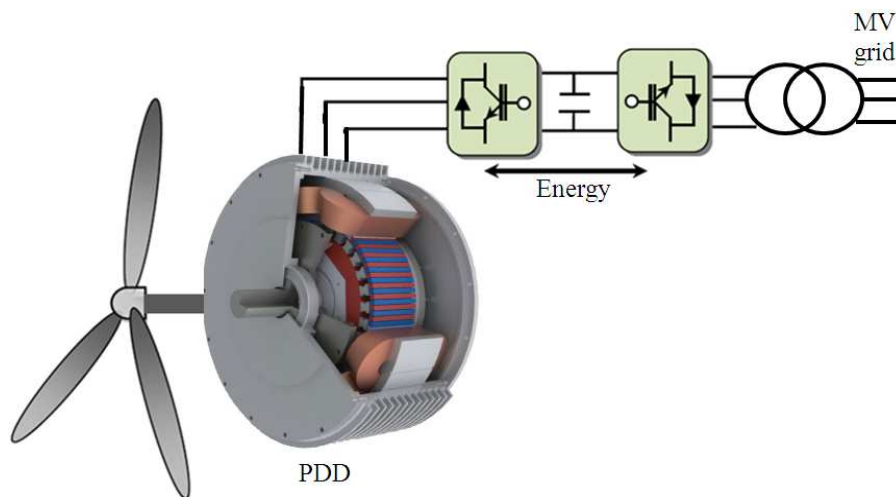


Figure 1.24 Integrated magnetically geared PM SG.

1.6.6. High-Temperature Superconducting (HTS) generator-based system

The current densities of the superconductors are over 100 times higher than those in conventional copper conductors. Therefore, a superconductor based compact and light weight generator may reduce the weight of WT power generation systems. The optimum weight for a 10MW DD PM SG is about 300t, whereas the projected weight of a 10MW HTS generator is approximately 150–180t [41]. There are several successful tests of the first generation models and the prototypes of motors and generators using HTS [42]. Recently, Sway Turbine and Windtec Solutions have been developing a 10MW WT generator, which is called the *SeaTitan* and this is considered to be the world's most powerful turbine [43].

The *SeaTitan* WT design employs an HTS generator, which is significantly smaller and lighter and expected to be commercially available by 2015 [44]. There are several challenges, like the price of superconducting wires and cooling technology, which must be addressed before large scale utilization can be obtained. The main components of the HTS machine are illustrated in Figure 1.25.

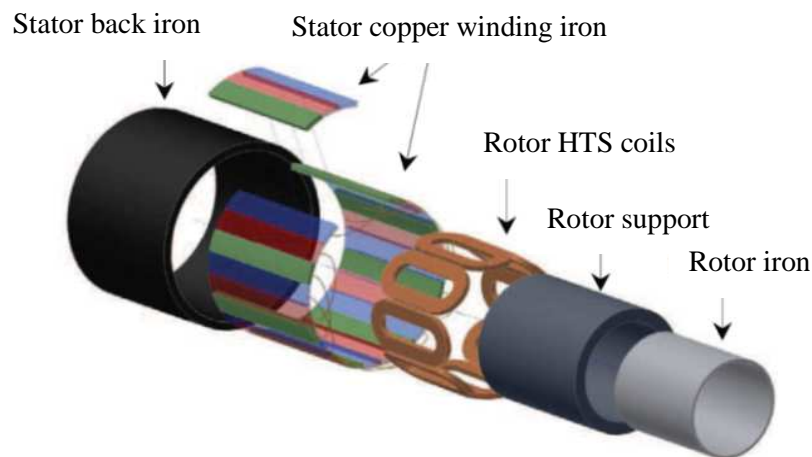


Figure 1.25 Main components of a HTS multi-pole generator [45].

1.6.7. Transformer-Less WTGS using a Multilevel Converter

Elimination of heavy and large GSST from the nacelle means significant reduction of weight and size of WTS. Medium-voltage (MV) power converters like multi-level converter and modular matrix converter topologies have been gaining the popularity to eliminate the GSSTs in recent years.

With the arrival of new high-power semiconductor devices, new power converter structures are conceived to meet the needs of future MV or high-voltage (HV) converter systems. In this highly active area, neutral point clamped (NPC), flying capacitor (FC) and modular multilevel converter (MMC) topologies and circuits as shown in Figure 1.26 have found their application in low- voltage applications [46]. For medium or high-voltage applications, the selection of multilevel converter topology is very critical. According to [10], the MMC topology is the feasible choice for MV converter applications.

The high number of levels means that MV attainability is possible with lower-voltage devices to connect the WT to the MV network directly and also possibility to improve the output power quality. The component number and control complexity increases linearly with the increase of level number.

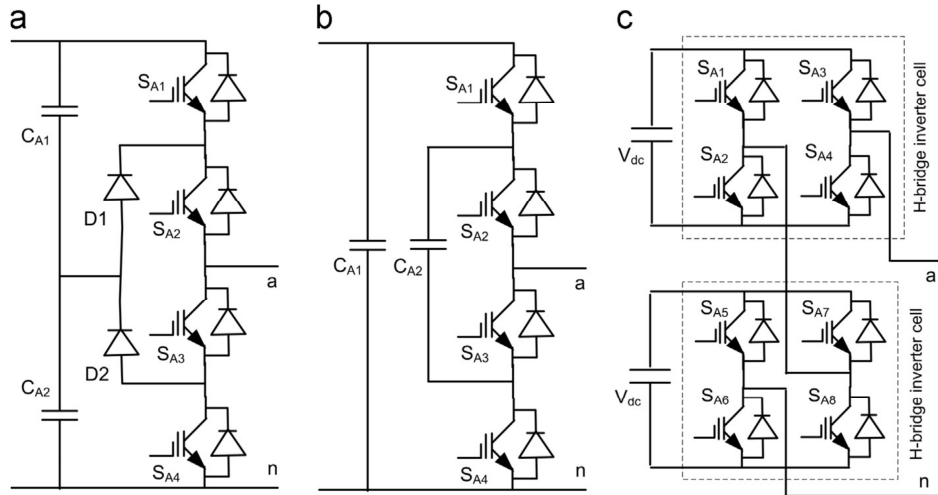


Figure 1.26 Single phase converter circuit diagram: (a) 3-level NPC, (b) 3-level FC, and (c) 5-level MMC.

1.6.8. Multi-Coil Generator based Medium Voltage Converter

A new type of lightweight ironless-stator modular DD generator, known as the spoked lightweight machine (SLiM) was proposed in 2005 for DD WTGSs [47]. This is a PM SG with a large number of magnets placed on the steel rotor rim. Copper coils are accommodated on the non-iron inner stator rim. The ironless stator and gearbox free operation allow a lightweight structure but still require a GSST. In 2006, a study was carried out to eliminate the GSST from the SLiM-based WTGS [48]. Pair of generator coils of SLiM were used to generate multiple sources for the MMC converter as shown in Figure 1.27. A multi-coil generator-based WTS is shown in Figure 1.28.

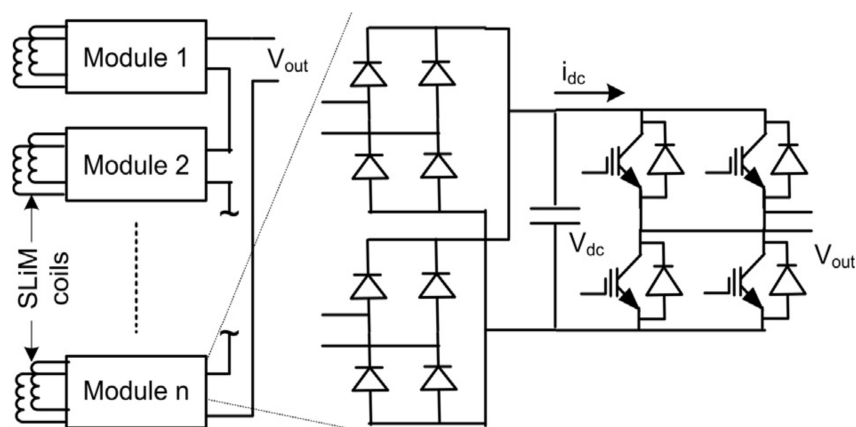


Figure 1.27 SLiM-based MV converter topology.

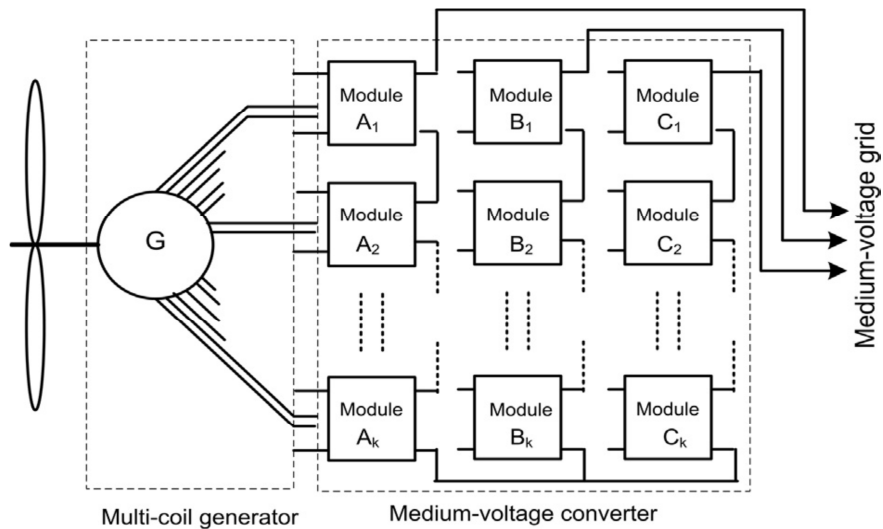


Figure 1.28 Multi-coil generator based WTGS.

The idea to use large diameter generators with an air core to remove the attractive force between stator and rotor [20]–[49] has been adopted by, for example, Sway Turbine [50] (shown in Figure 1.29), and Boulder Wind Power [51]. Such constructions make it possible to use less electromagnetically active and structural material. However, protection of the windings and the magnets against the aggressive environment with humidity and salt is an issue.



Figure 1.29 Large diameter DD generator of Sway Turbine. Source: Sway Turbine.

1.6.9. Multiple Generators based Medium Voltage Converter

A transformer-less WTGS structure with several parallel six-phase PM SGs placed in the turbine nacelle has been proposed in [52]. A multiple generators-based WTS is shown in Figure 1.30. All the generators are driven by the same WT and each stator winding generates an isolated source for an H-bridge inverter cell of the MMC converter. The MMC converter generates MV AC output, which can be connected to the MV network directly.

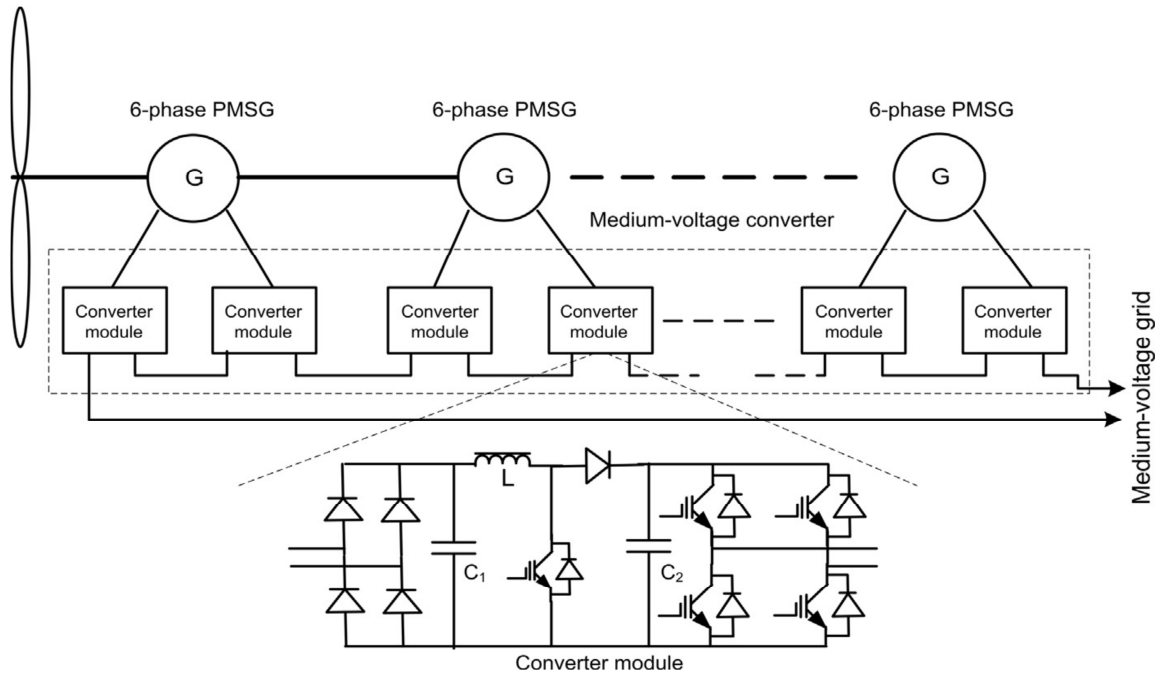


Figure 1.30 Multiple generators based WT system: single-phase layout.

1.6.10. Medium-Frequency Magnetic Link-based MV Converter

Compared with the conventional transformers operated at the power frequency, the medium-frequency (MF) (in the range of a few kHz to MHz) transformers have much smaller and lighter magnetic cores and windings, and thus much lower costs. A medium frequency magnetic-link-based novel MV MMC converter system was proposed as shown in Figure 1.31, to eliminate the GSST, which is desirable for both onshore and offshore WTGS [53].

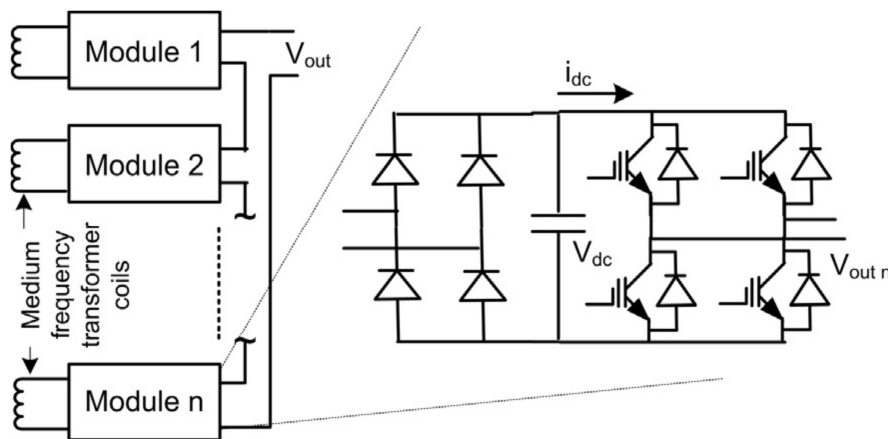


Figure 1.31 MF magnetic-link-based MV converter: single phase layout.

This MF magnetic-link-based MV converter eliminates the GSST without changing the design of traditional generators. A three phase MV converter based WTGS is shown in Figure 1.32 [10].

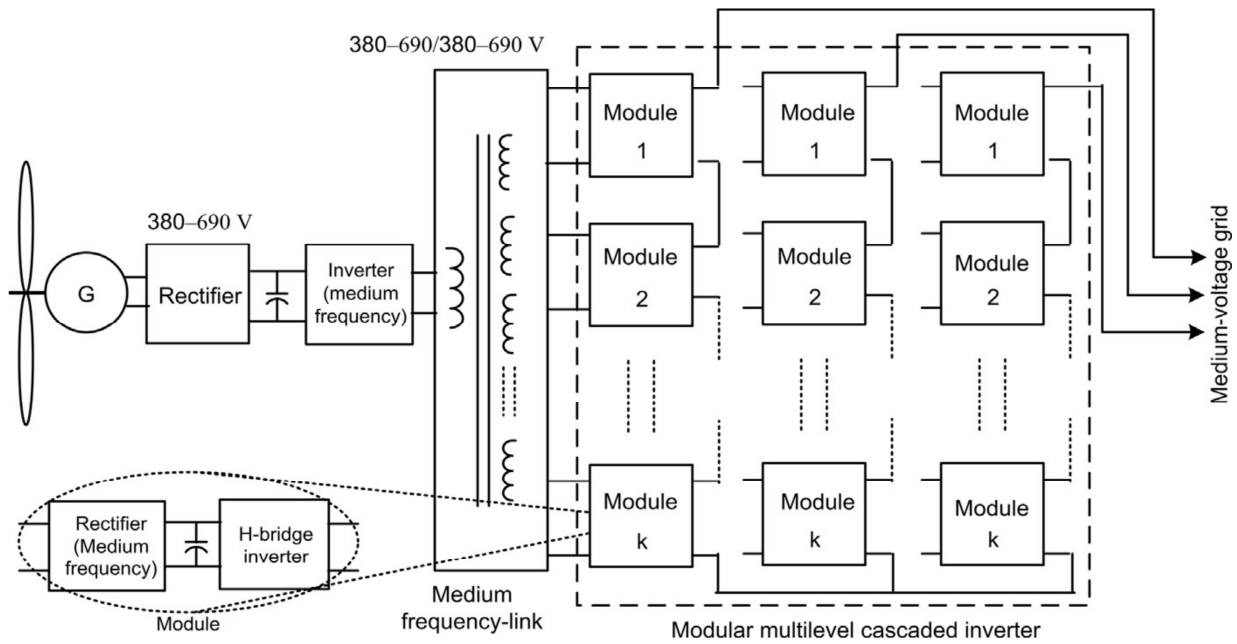


Figure 1.32 Scheme of MF magnetic-link MV converter-based WTGS.

1.6.11. Matrix Converter based MV Converter

In 2007, the first multi-winding phase-shifted transformer-based MV multi-modular MC (matrix converter) topology was proposed in [54]. In 2011, single-phase output MC (SPMC)-based MV WTS was proposed in [55]. The converter topology is shown in Figure 1.33. Split winding PM SG WT generators based modular MC was also investigated in [56] to eliminate the GSST from the WTGSs. Although this design does not require special machine, it needs several generators.

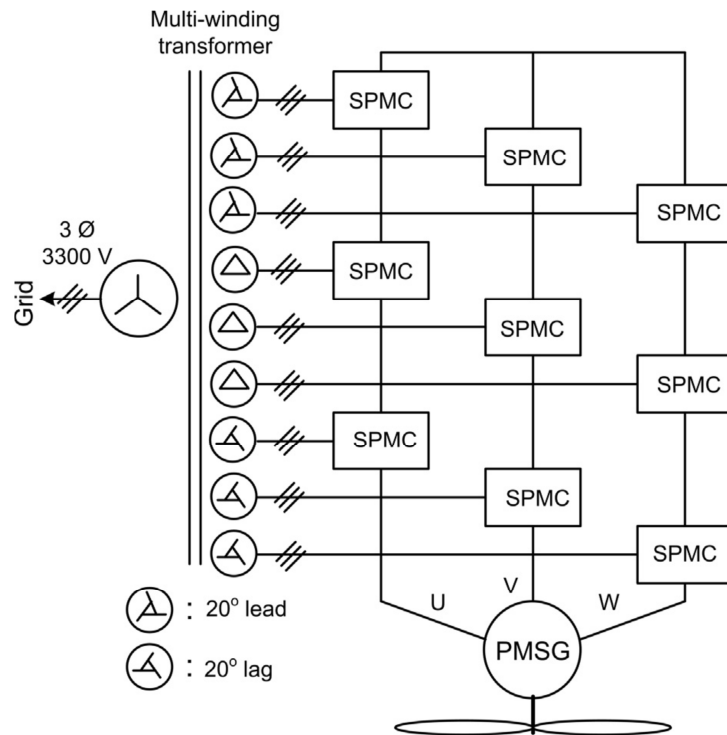


Figure 1.33 SPMC MV converter based WTGS.

1.6.12. Medium-voltage DC converter

Recently, a transformer-less generator-converter concept has been introduced for lightweight HVDC WTGS [57]. The iron-less stator generator with several stator segments and modular AC/DC converters was used in the proposed system as portrayed in Figure 1.34. In 2012, a minimum weight dual active bridge converter was proposed to reduce the weight of WTGS [58].

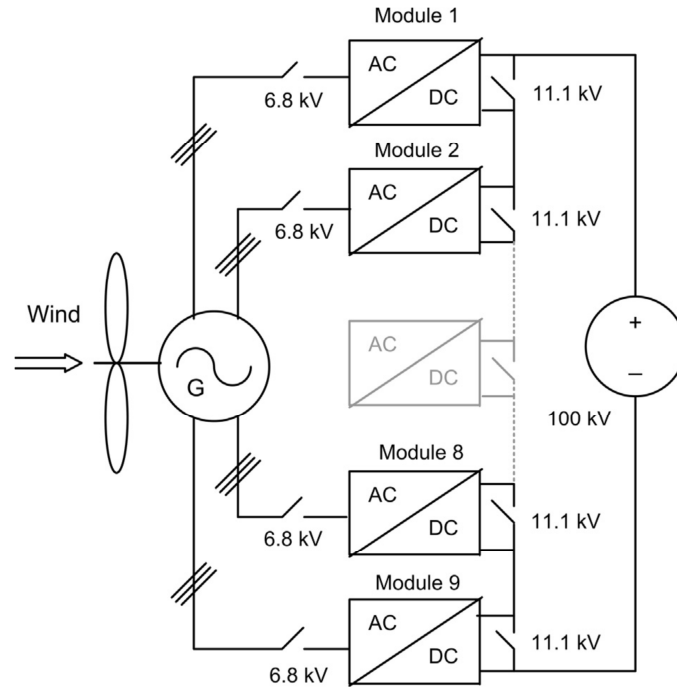


Figure 1.34 WT with segmented stator generator and MC.

1.6.13. Medium Frequency Transformer based System

Increasing the operation frequency can greatly reduce the physical volume of the transformer, which has been widely used in switched mode power supplies. Operated at 1.2 kHz, the weight and size of a 3 MW transformer can be less than 8% of an equivalent 50 Hz unit [59]. For high-power applications, a new type of transformer employing new magnetic materials with higher saturation flux density levels and lower core losses, and efficient semiconductor devices with fast switching possibilities, high blocking capabilities, and higher power densities, known as the power electronic transformer, was investigated in [60]. A new HVDC wind farm with MF transformer was introduced in [59] as shown in Figure 1.35. Design considerations of a 3MW MF transformer for offshore wind farms were proposed in [61]. A multi- generation turbine and MC-based HVDC system has been proposed in [62]. That proposed system consists of MCs, high-frequency (HF) transformers and full bridge rectifiers as shown in Figure 1.36.

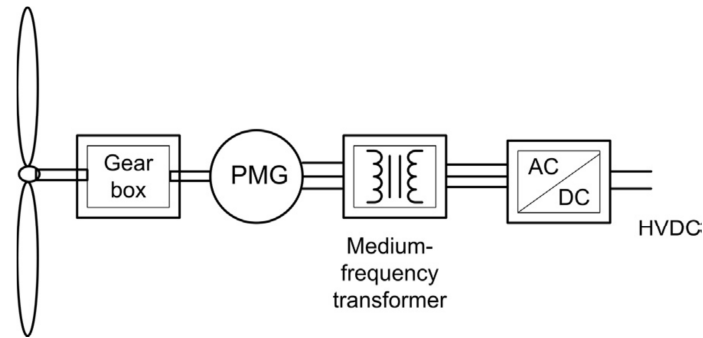


Figure 1.35 WT with PM generator and MF Transformer.

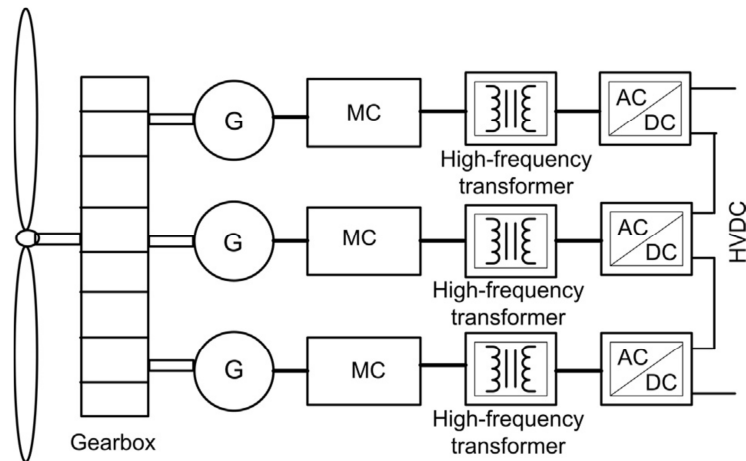


Figure 1.36 WT with MC and multi-generation system.

1.7. Conclusion

In this chapter, an overview of electric generator topologies for wind energy systems has been presented, as conclusion, there is no trend toward a single WT generator system, but instead the diversity of WT generator systems is growing. The three currently used variable speed systems (with gearbox and DFIG, with gearbox and full converter and DD) are expected to remain for the coming years. Several development trends to reduce the weight and volume of the WTS have been proposed in the last years, this development trends are focused on the elimination of the heaviest and the most broken down components of the nacelle, the mechanical drive train and the GSST. As final conclusion, there is no definitive solution, each new WTS has some advantages and drawbacks, High-Temperature Superconducting WTS is one of the most competitive, smaller, lighter, DD and compact WTGS, with successful developed 10MW WT generator.

1.8. References of Chapter 1

- [1] National Resources Canada. (Jul. 2000). The history of wind energy. [Online], Available: <http://www.canren.gc.ca/>
- [2] G. L. Johnson. Wind energy systems. Manhattan, KS. October 10, 2006.
- [3] J. M. P. Pérez , F. P. G. Márquez, A. Tobias, M. Papaalias, Wind turbine reliability analysis, Renewable and Sustainable Energy Reviews, Vol. 23, pp: 463–472, 2013.
- [4] Wiser, R., Z. Yang, M. Hand, O. Hohmeyer, D. Infield, P. H. Jensen, V. Nikolaev, M. O'Malley, G. Sinden, A. Zervos, 2011: Wind Energy. In IPCC Special Report on Renewable Energy Sources and Climate Change Mitigation [O. Edenhofer, R. Pichs-Madruga, Y. Sokona, K. Seyboth, P. Matschoss, S. Kadner, T. Zwickel, P. Eickemeier, G. Hansen, S. Schlomer, C. von Stechow (eds)], Cambridge University Press, Cambridge, United Kingdom and New York, NY, USA.
- [5] (2012, Jun.). REN21—Renewables 2012 global status report [Online]. Available: <http://www.ren21.net>
- [6] (2010, Sep.). Green Energy—The road to a danish energy system without fossil fuels [Online]. Available: <http://www.klimakommissionen.dk/en-US/>
- [7] F. Blaabjerg, Ke Ma. Future on power electronics for wind turbine systems, IEEE Journal of Emerging and Selected Topics in Power Electronics, Vol. 1, No. 3, Sep. 2013
- [8] Vestas Wind Power, Aarhus, Denmark. (2011, Apr.). Wind Turbines Overview [Online]. Available: www.vestas.com/
- [9] PROTEST (Procedures for Testing and measuring wind energy systems). Deliverable D1: State-of-the-Art-Report. FP7-ENERGY-2007-1-RTD; 2009.
- [10] M. R. Islam, Y. Guo, J. Zhu, A review of offshore wind turbine nacelle: Technical challenges, and research and developmental trends, Renewable and Sustainable Energy Reviews, Vol. 33, pp. 161–176, 2014.
- [11] P. Tavner, Offshore wind turbines: reliability, availability and maintenance, Stevenage, U.K.: IET, 2012.
- [12] H. Polinder, J. A. Ferreira, B. B. Jensen, A. B. Abrahamsen, K. Atallah, R. A. McMahon. Trends in Wind Turbine Generator Systems, IEEE Journal of Emerging and Selected Topics in Power Electronics, Vol. 1, No. 3, Sep 2013.
- [13] A. D. Hansen, F. Iov, F. Blaabjerg, and L. H. Hansen, Review of contemporary wind turbine concepts and their market penetration, Wind Eng., Vol. 28, No. 3, pp. 247–263, 2004.
- [14] H. Polinder, S. W. H. de Haan, M. R. Dubois, and J. G. Slootweg, Basic operation principles and electrical conversion systems of wind turbines, EPE J., Vol. 15, No. 4, pp. 43–50, Dec. 2005.
- [15] M. Tsili and S. Papathanassiou, A review of grid code technical requirements for wind farms, IET Renew. Power Generat., vol. 3, no. 3, pp. 308–332, 2009.
- [16] Z. Chen, J. M. Guerrero, and F. Blaabjerg, A review of the state of the art of power electronics for wind turbines, IEEE Trans. Power Electron, vol. 24, no. 8, pp. 1859–1975, Aug. 2009.
- [17] L. G. Meegahapola, T. Littler, and D. Flynn, Decoupled-DFIG fault ride-through strategy for enhanced stability performance during grid faults, IEEE Trans. Sustain. Energy, Vol. 1, No. 3, pp. 152–162, Oct. 2010.
- [18] H. Polinder, F. F. A. van der Pijl, G. J. de Vilder, and P. Tavner, Comparison of direct-drive and geared generator concepts for wind turbines, IEEE Trans. Energy Convers., Vol. 21, No. 3, pp. 725–733, Sep. 2006.
- [19] H. A. Hoseynabadi, P. J. Tavner, and H. Oraee, Reliability comparison of direct-drive and geared drive wind turbine concepts, Wind Energy, Vol. 13, No. 1, pp. 62–73, 2010.
- [20] M. Mueller and A. Zavvos, Electrical generators for direct drive systems: A technology overview, in Electrical Drives for Direct Drive Renewable Energy Systems, M. Mueller and H. Polinder, Ed. Oxford, U.K.: Woodhead, 2013, pp. 1–29.
- [21] F. Blaabjerg, M. Liserre, and K. Ma, Power electronics converters for wind turbine systems, IEEE Trans. Ind. Appl., Vol. 48, No. 2, pp. 708–719, Mar./Apr. 2012.
- [22] Fraunhofer (IWES). (<http://windmonitor.iwes.fraunhofer.de>).

- [23] J.G. McGowan, R.W. Hyers, K.L. Sullivan, J.F. Manwell, S.V. Nair, McNiff B, et al. A review of materials degradation in utility scale wind turbines, *Energy Materials*, Vol. 2, No. 1, pp: 41–64, 2007.
- [24] L.J. Hunt, A new type of induction motor, *Journal of the Institute of Electrical Engineers*, Vol. 39, pp: 648–667, 1907.
- [25] F. Creedy, Some developments in multispeed cascade induction motors, *Journal of IEE (London)*, Vol. 59, pp: 511–532, 1927.
- [26] B.H. Smith, Synchronous behavior of doubly fed twin stator induction, *IEEE Trans. on Power Apparatus and Systems*, Vol. 86, pp: 1227–1234, 1967.
- [27] B. Hopfensperger, D.J. Atkinson, R.A. Lakin, Combined magnetizing flux oriented control of the cascaded doubly-fed induction machine, *IEE Proceedings –Electric Power Applications*, Vol. 148, pp.354–362, 2001.
- [28] A.R.W. Broadway, L. Burbridge, Self-cascaded machine: a low-speed motor or high-frequency brushless alternator, *Institute of Electrical Engineers*, Vol.117, pp. 1277-1290, 1970.
- [29] A.K. Wallace, R. Spee, G.C. Alexander, The brushless doubly-fed machine: its advantages, applications and design methods, *Sixth International Conference on Electr. Mach. and Drives*, pp. 511–517, 1993.
- [30] R. Cárdenasa, R. Pena, P. Wheeler, J. Clare, A. Muñoz, A. Sureda, Control of a wind generation system based on a Brushless Doubly-Fed Induction Generator fed by a matrix converter, *Electric Power Systems Research*, Vol. 103, pp. 49– 60. 2013.
- [31] R. A. McMahon, P. C. Roberts, X. Wang, and P. J. Tavner, Performance of BDFM as generator and motor, *IEE Proc. Electr. Power Appl.*, Vol. 153, No. 2, pp. 289–299, Mar. 2006.
- [32] P. C. Robert, R. A. McMahon, P. J. Tavner, J. M. Maciejowski, and T. J. Flack, Equivalent circuit for the brushless doubly fed machine (BDFM) including parameter estimation and experimental verification, *IEE Proc. Electr. Power Appl.*, Vol. 152, No. 4, pp. 933–942, Jul. 2005.
- [33] R. Dutta, Modeling and Analysis of Short Term Energy Storage for Mid-Size Hydrostatic Wind Turbine, Master of Science from the University of Minnesota, August, 2012.
- [34] K.E. Thomsen, O.G. Dahlhaug, M.O.K. Niss, S.K. Haugset, Technological advances in hydraulic drive trains for wind Turbines, *Energy Procedia*, Vol. 24, pp.76-82, 2012.
- [35] K. Atallah and D. Howe, A novel high-performance magnetic gear, *IEEE Trans. on Magnetics*, Vol. 37, No. 4, pp. 2844-2846, 2001.
- [36] K. Atallah, S. D. Calverley, D. Howe, Design, analysis and realization of a high-performance magnetic gear, *IEE Proc. | Electr. Power Appl.*, Vol. 151, No. 2, pp. 135-143, 2004.
- [37] P. Padmanathan and J. Z. Bird, A continuously variable magnetic gear performance comparison, presented at *IEEE International Magnetics Conference (INTERMAG)*, Dresden, Germany, 2014.
- [38] P. Padmanathan, Design of a continuously variable magnetic gear, M.S. Thesis, *Elect. and Comp. Eng.*, Univ. North Carolina at Charlotte, Charlotte, USA, Dec. 2013.
- [39] K. Atallah, J. Rens, S. Mezani, and D. Howe, A novel ‘pseudo’ direct drive brushless permanent magnet machine, *IEEE Trans. Mag.*, Vol. 44, No. 11, pp. 4349–4352, Nov. 2008.
- [40] L. Jian, K. T. Chau, and J. Z. Jiang, A magnetic-gear outer-rotor permanent-magnet brushless machine for wind power generation, *IEEE Trans. Ind. Appl.*, Vol. 45, No. 3, pp. 954–962, May./Jun. 2009.
- [41] Li H, Chen Z, Polinder H. Optimization of multibrid permanent-magnet wind generator systems. *IEEE Trans Energy Convers*; Vol. 24, pp. 82–92. 2009.
- [42] D. Aized, BB. Gamble, AS. Yekhlef, JP. Voccio, DI. Driscoll, DA. Shoykhet, et al. Status of the 1000HP HTS motor development. *IEEE Trans. Appl Supercond*; Vol. 9, pp.1197–1200. 1999.
- [43] AMSC.SeaTitan10MWwindturbine.Availableonline: (<http://www.amsc.com>) [accessed 10.03.13].
- [44] G. Snitchler, B. Gamble, C. King, P. Winn. 10MW class superconductor wind turbine generators. *IEEE Trans Appl Supercond*, Vol. 21, pp.1089–1092. 2011.
- [45] Wenping Cao (2011). High-Temperature Superconducting Wind Turbine Generators, *Wind Turbines*, Dr. Ibrahim Al-Bahadly (Ed.), ISBN: 978-953-307-221-0, InTech, Available from: <http://www.intechopen.com/books/wind-turbines/high-temperature-superconducting-wind-turbine-generators>

- [46] J.S.Lai, FZ.Peng. Multilevel converters-a new breed of power converters. IEEE Trans. IndAppl, Vol. 32: pp.509–17. 1996.
- [47] E. Spooner, P. Gordon, J.R. Bumby, C.R. French. Lightweight ironless-stator PM generators for direct-drive wind turbines. IEE Proc Electr Power Appl; Vol.152, pp.17–26. 2005.
- [48] M.A. Parker, C.H. Ng, L. Ran, P. Tavner, E. Spooner. Power control of direct drive wind turbine with simplified conversion stage & transformerless grid inter-face. 41stInternational Universities Power Engineering Conference, pp.65–68, 2006.
- [49] M. J. Kamper, J. H. J. Potgieter, J. A. Stegman, and P. Bouwer, Comparison of air-cored and iron-cored non-overlap winding radial flux permanent magnet direct drive wind generators, in Proc. ECCE, pp. 1620–1627, Sep. 2011.
- [50] (2013, Apr. 30) [Online]. Available: <http://www.swayturbine.com/>
- [51] (2013, Apr. 30) [Online]. Available: <http://www.boulderwindpower.com/>
- [52] F. Deng, Z. Chen. A new structure based on cascaded multilevel converter for variable speed wind turbine. 36th annual conference on IEEE Industrial Electronics Society, pp.3167–72. 2010.
- [53] M.R. Islam, YG. Guo, JG. Zhu. A transformer-less compact and light wind turbine generating system for offshore wind farms. IEEE International Conference on Power and Energy, pp: 605–10. 2012.
- [54] Y. Ueda, M. Ikeda, R. Suenaga, K. Imanishi, E. Masuda, E. Watanabe. Development of medium voltage matrix converter. IEEJ Annual Meeting; 2007.
- [55] J. Kang, N. Takada, E. Yamamoto, E. Watanabe. High power matrix converter for wind power generation applications. IEEE 8thInternational Conference on Power electronics (ECCE Asia), pp. 1331–6. 2011.
- [56] S.D.G. Jayasinghe, D.M. Vilathgamuwa. A modular matrix converter for transformer-less PMSG wind generation systems. IEEE 9thInternational Conference on Power Electronics and Drive Systems (PEDS), pp.474–479. 2011.
- [57] S.S. Gjerde, P.K. Olsen, T.M. Undeland. A transformer-less generator-converter concept making feasible a 100kV low weight offshore wind turbine Part II – the converter. IEEE Energy Conversion Congress and Exposition (ECCE), pp.253–60. 2012.
- [58] R.A.Friedemann, F.Krismer, J.W.Kolar. Design of a minimum weight dual active bridge converter for an Airborne Wind Turbine system. 27th annual IEEE Applied Power Electronic Conference and Exposition (APEC), pp.509–516, 2012.
- [59] A.Prasai, JS.Yim, D. Divan, A. Bendre and K. Sul. A new architecture for offshore wind farms. IEEE Trans. Power Electron, Vol. 23, pp. 1198–204. 2008.
- [60] M. Sabahi, AY. Goharzi, SH. Hosseini, MBB.Sharifian, GB.Gharehpetian. Flexible power electronic transformer. IEEE Trans. Power Electron; Vol.25, pp. 2159–69. 2010.
- [61] S. Meier, T. Kjellqvist, S. Norrga, H.P. Nee. Design considerations for medium-frequency power transformers in offshore wind farms. 13th European conference on power electronics and applications. pp. 1–12, 8-10 sep 2009.
- [62] A. Garcés, M. Molinas. High frequency wind energy conversion from the ocean. International power electronics conference (IPEC); pp.2056–61, 2010.

Chapter 2:

Modeling and Control of the DFIG based WPGS

Chapter 2: Modeling and Control of the DFIG based WPGS

2.1. Introduction

Wind energy is one of the most important and promising sources of renewable energy all over the world, mainly because it is considered to be non-polluting and economically viable. At the same time, there has been a rapid development of related WT technology [1-2]. The main components of a grid-connected WTS are presented in Figure 2.1.

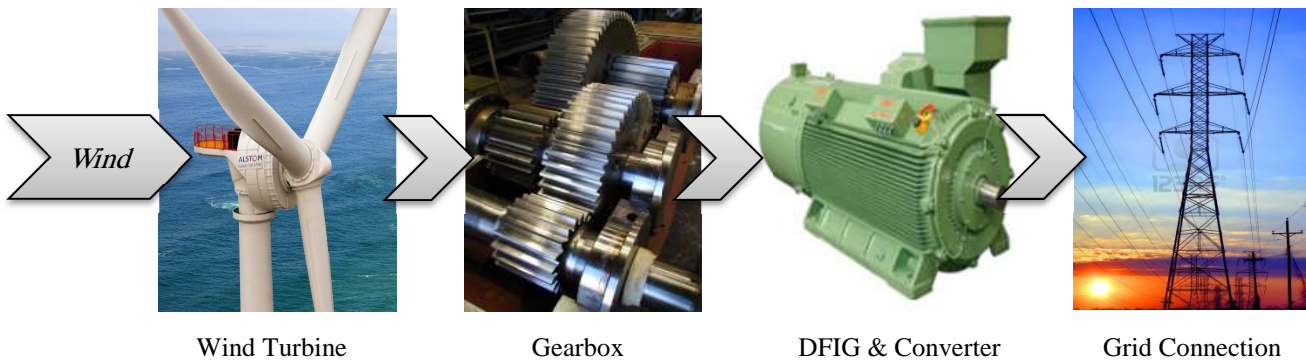


Figure 2.1 Main components of a typical WPGS.

This chapter is dedicated to give the mathematical modeling and the control schemes of the DFIG based WPGS.

2.2. Modeling of the Global WPGS

DFIGs are widely used in modern WTSs due to their variable speed operation mode (VSOM), four-quadrant active and reactive power controllability, low-converter cost, and reduced power losses compared to other machines such as constant speed induction generators and synchronous generators with fully rated converters [3]. DFIG reduces acoustic noise and stresses of the mechanical structure [4]. Another benefit of the DFIGs system is their power electronic converter system which is connected between the utility grid and the rotor winding circuit, are sized only for a part of the full power of the generator. The WTGSs can harvest the maximum wind power available at various wind speed by adjusting correctly the speed of the rotating shaft [5].

The blocks marked as RSC and GSC in Figure 2.2, refer to the Rotor-Side Converter and the Grid-Side Converter respectively. As can be judged from the wound-rotor induction generator symbol, marked as WRIG, the RSC is connected to the rotor windings while the GSC is connected via the inductance filter and the transformer to the grid, hence the name. A three-winding transformer allows independent rated voltage on the stator and the rotor [6]. The converters share a DC-link formed by the capacitor that allows bi-directional power flow between the machine's rotor circuit and the grid since the converters are IGBT based. Together these three components namely the RSC, the DC-link and the GSC form a back-to-back converter. Since the DFIG is essentially a rotating transformer, the fundamental frequency of the current and the voltage in the rotor circuit changes with its speed. The DC-link thus provides the decoupling between the two alternative current sides, which are at different frequencies. The inductance filter mitigates the harmonics in the current, due to the switching converter, and provides the impedance over which energy can be exchanged. The stator windings are connected directly to the grid via the transformer [7].

The mathematical modeling of the WTGS presented in Figure 2.2 starts from the input kinetic power of the wind and finishes in the output electrical power (from the left to the right). The general control structure as connectionism between the WTS components is shown in Figure 2.3. A model of a DFIG-WT basically consists of (1) a generator and drive train, (2) a turbine rotor model, (3) a GSC and DC-link capacitor, (4) a pitch controller, and (5) a rotor-side controller that controls the active and reactive power of the generator [9].

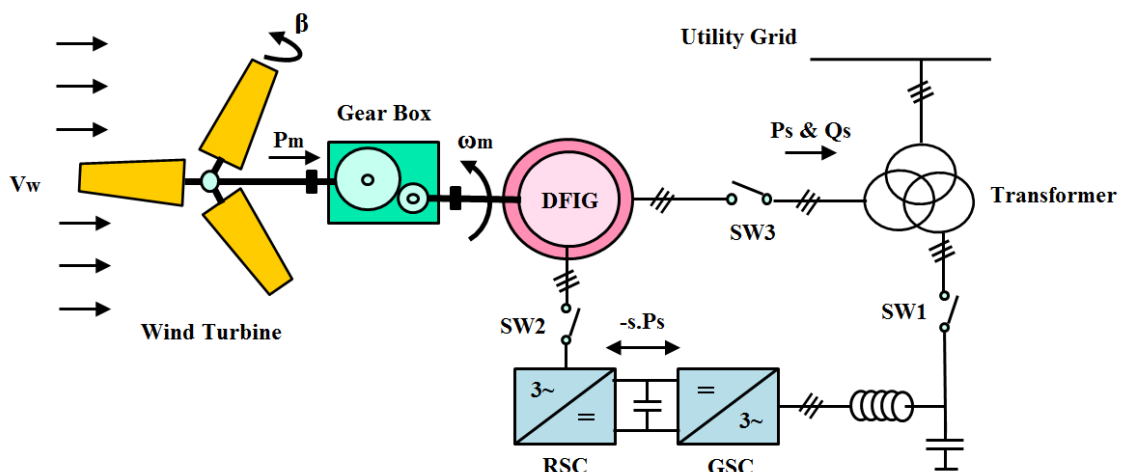


Figure 2.2 General scheme of the DFIG based WTS [8].

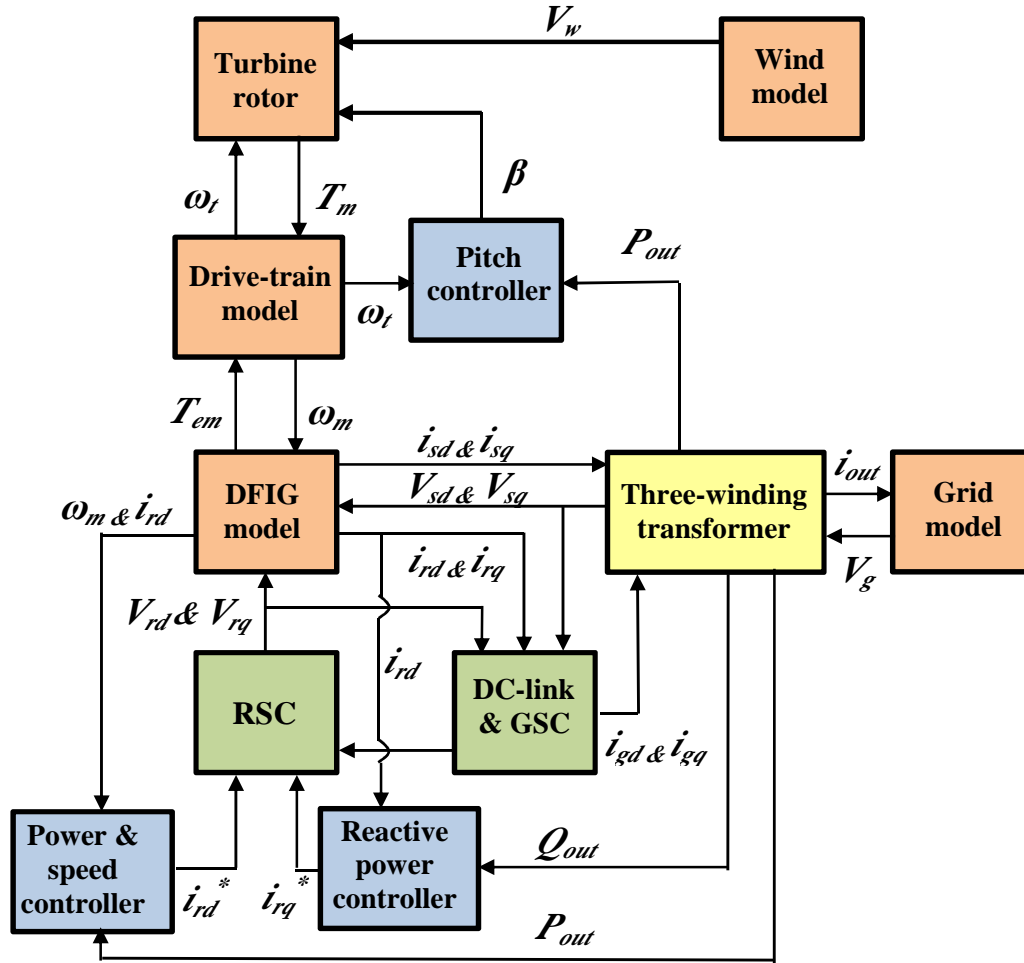


Figure 2.3 Control block diagram of DFIG wind turbine.

2.2.1. Wind Speed Model

A wind speed signal generated by an autoregressive moving average (ARMA) model described in [10], and its development is described here. The wind speed $V_w(t)$ has two constituent parts expressed as [10]:

$$V_w(t) = V_{mean} + V_{turb}(t) \quad (2.01)$$

where V_{mean} is the mean wind speed at hub height and V_{turb} is the instantaneous turbulent part, whose linear model is composed by a first-order filter excited by Gaussian noise [10]:

$$\dot{V}_{turb}(t) = -\frac{1}{T_w}V_{turb}(t) + \alpha_{turb} \quad (2.02)$$

where T_w is the time constant and α_{turb} is the white noise process with zero mean. The white noise is smoothed by a signal shaping filter, thereby transforming it to colored noise V_{turb} , as shown in Figure 2.4.

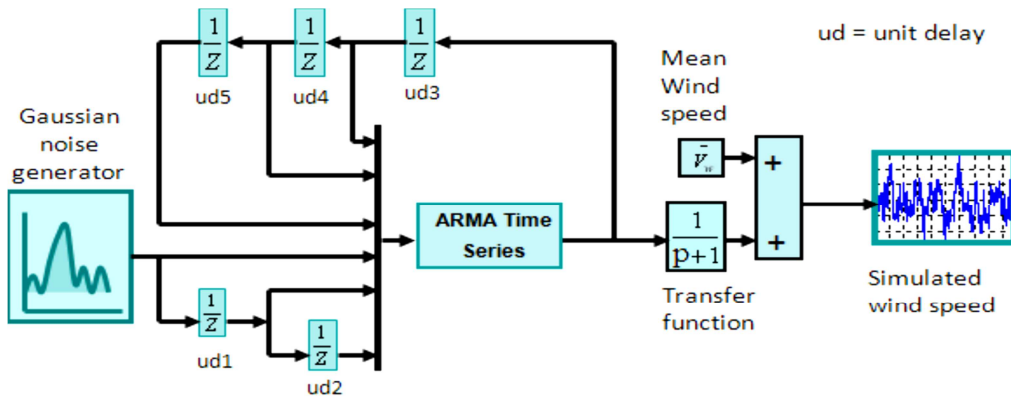


Figure 2.4 Generation of wind speed by ARMA model in MATLAB/Simulink [10].

The instantaneous turbulence component of wind speed is obtained as [10]:

$$V_{turb}(t) = \alpha_{turb} V_{turb} \tag{2.03}$$

where α_{turb} is the standard deviation, V_{turb} is the ARMA time series model, which is given by [10]:

$$V_{turb}(t) = aV_{turb_1} - bV_{turb_2} + cV_{turb_3} + \alpha_{turb} - d\alpha_{turb_1} + e\alpha_{turb_2} \tag{2.04}$$

where a , b , and c are the autoregressive parameters and d and e are moving average parameters whose values being: $a = 1.7901$, $b = 0.9087$, $c = 0.0948$, $d = 1.0929$ and $e = 0.2892$. The wind profile obtained by the ARMA model is presented in Figure 2.5.

2.2.2. Wind Turbine Model

The turbine is the prime mover of WTS that enables the conversion of kinetic energy of wind E_w into mechanical power (P_m) and eventually into electrical power [11].

$$P_m = \frac{\partial E_w}{\partial t} C_p = \frac{1}{2} \rho A C_p(\lambda, \beta). V_w^3 \tag{2.05}$$

where V_w is the wind speed at the center of the rotor (m/s), ρ is the air density (Kg/m^3), $A = \pi R^2$ is the frontal area of the WT (m^2) and R is the rotor radius (m). Figure 2.6 illustrates the triple relationship between the mechanical power, turbine speed and wind speed ($P_m(\omega_t, V_w)$).

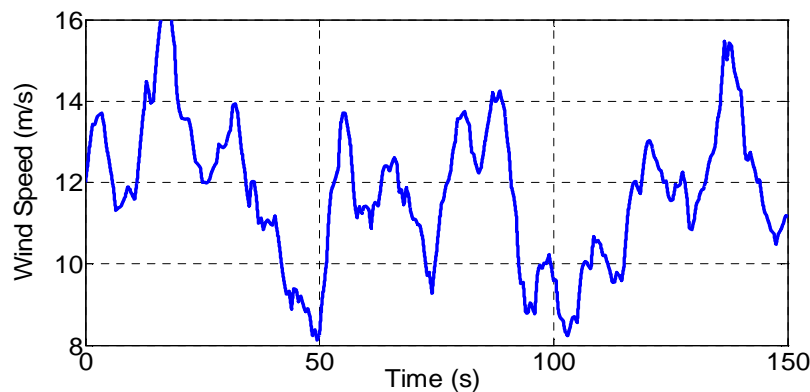


Figure 2.5 Sample wind speed obtained using ARMA model (average speed being 12 m/s).

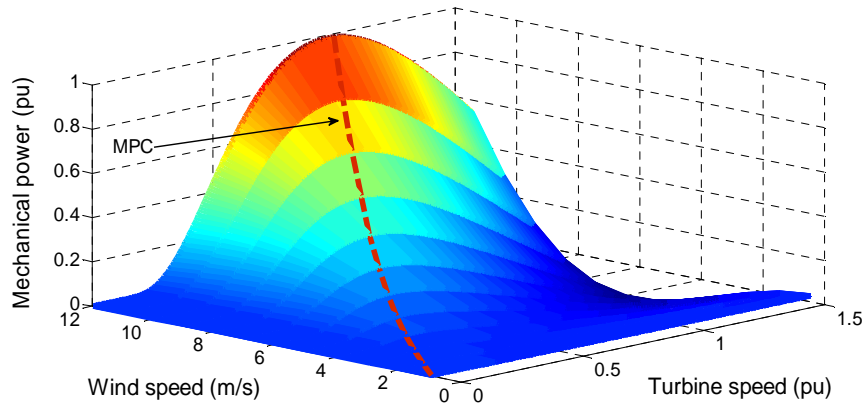


Figure 2.6 Maximum power curve (MPC) of the WTS.

The TSR (Tip Speed Ratio) is the ratio of the linear speed of the blade tip ($\omega_t \times R$) and the wind speed. It is given as:

$$\lambda = \frac{\omega_t R}{V_w} \quad (2.06)$$

The efficiency coefficient $C_p(\lambda, \beta)$, as indicated, is a function of the blade angle called the pitch angle and denoted by β , and the TSR denoted by λ , this triple relationship is presented in Figure 2.7. One way to define the efficiency coefficient is by using a look-up table, another way is by approximating the efficiency coefficient using a non-linear function. The second method gives more accurate results and it's faster in simulation as given by [12]:

$$C_p(\lambda, \beta) = 0.22 \left(\frac{116}{\lambda_i} - 0.4\beta - 5 \right) e^{-\frac{12.5}{\lambda_i}} \quad (2.07)$$

where:
$$\frac{1}{\lambda_i} = \frac{1}{\lambda + 0.08\beta} - \frac{0.035}{\beta^3 + 1}$$

From the plot shown in Figure 2.6, it can be stated that the optimal operating point is ($\beta=0^\circ$, $\lambda_{opt}=10$ and $C_{pmax}=0.5$). So, if the WTS is running at a particular speed that corresponds to wind speed in such a way that the TSR remains optimal ($\lambda=\lambda_{opt}$), then we can extract the maximum available power from the available wind speed ($C_p=C_{pmax}$).

the optimal rotational speed has to be taken as reference to get the MPPT purpose which given by:

$$\omega_{t_opt} = \frac{\lambda_{opt} V_w}{R} \quad (2.08)$$

then, the maximum mechanical power extracted from the wind is obtained by:

$$P_{m_max} = \frac{1}{2} \rho \pi R^2 C_{pmax} V_w^3 = \frac{1}{2} \rho \pi R^5 \frac{\omega_t^3}{\lambda_{opt}^3} C_{pmax} \quad (2.09)$$

Moreover, the optimal driving torque of the wind turbine is defined by: $T_{t_opt} = P_{m_max} / \omega_{t_opt}$

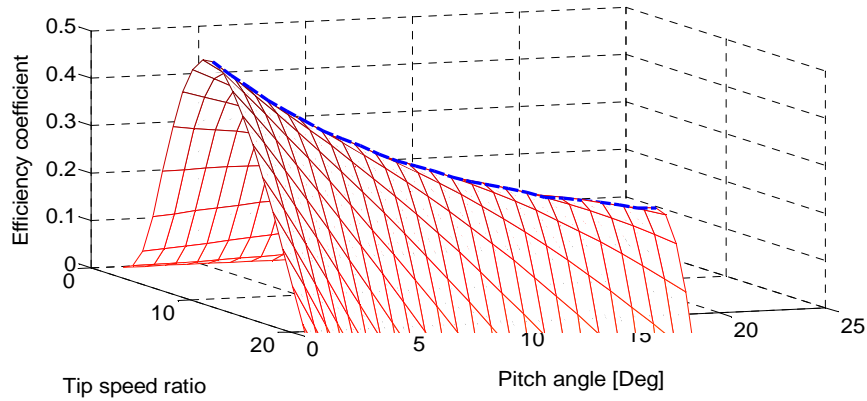


Figure 2.7 Maximum efficiency coefficient curve (MECC).

- **Blade Pitch Angle Model**

In case of wind speeds above the rated wind speed usually the pitch control is activated. The pitch control by changing the angle of blades around their longitudinal axis (see Figure 2.8) reduces the mechanical power and thus, keeps the output power around its nominal value and minimizes the mechanical stress [13], in the blade pitch angle control we have two options, the collective and the individual blade orientation systems.

Few papers discuss the modeling of the blades orientation system around their axes. In general a first-order system model can be found in [15]:

$$\frac{\dot{\beta}}{T_{\beta} - T_r} = \frac{1}{J_{\beta}s - d_{\beta}} \quad (2.10)$$

where J_{β} and d_{β} are the moment of inertia and the friction coefficient respectively, and T_{β} and T_r are the blade orientation system and the wind resistance torques.



Figure 2.8 Hydraulic blade pitch control system [14].

The mechanism of blade orientation system has two loops, the inner one controls the speed variation of $\dot{\beta}$, and the outer one controls β . In fact, lots of torques interferes in the dynamical study of the blade orientation control system [16]. The representation of these torques demand the modeling of the dynamical structure of the blades, also the wind behavior around the blades with taking into account the friction of the rotor hub. Moreover, the control of RS of the blades around their axes with band-pass larger than that of the pitching angle. Bearing in mind these two last observations, we decide to approximate the control loop of the pitch angle variation speed by a first-order linear system contain the principal dynamic system defined by the time constant $\tau_{d\beta}$ [17].

Pitch angle orientation system is then modeled by a proportional controller which generates the variation speed reference of pitch angle, then a first-order system gives the dynamical behavior of the pitch variation speed system, the pitch angle is given by integrating the speed [17]. As security precautions, the pitch angle speed has to be limited, so we take $|\dot{\beta}| \leq 10^\circ / \text{sec}$, and the pitch angle is limited to the interval $[0-30^\circ]$. The overall pitch angle orientation system is presented in Figure 2.9.

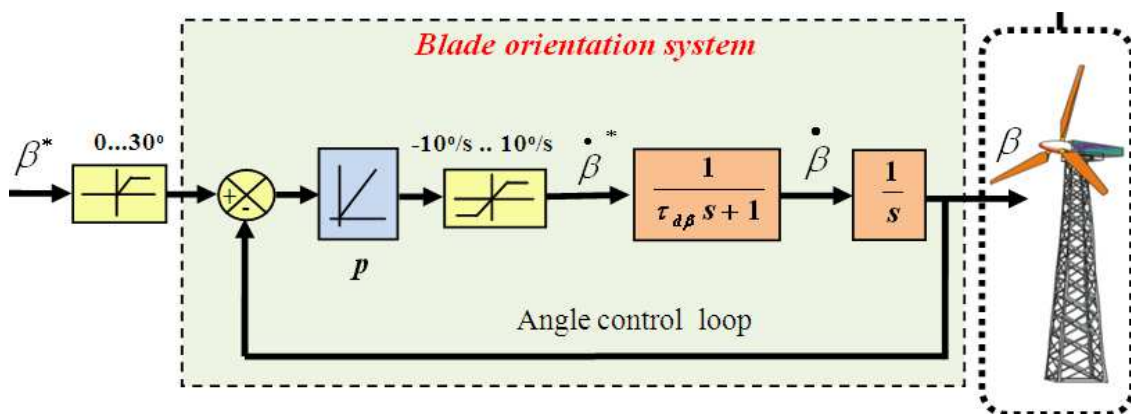


Figure 2.9 Bloc diagram of the blade pitch angle system.

Generally, if the wind speed is below the rated value, the WTS operates in the VSOM, the C_p is kept at its maximum and the pitch control system is deactivated. If the wind speed is above the rated value, the pitch control system is activated in order to reduce the aerodynamic power.

2.2.3. Two-Mass Drive Train Model

Three different drive-train models (one, two, and three-mass models) usually used to model the drive-train [18]. The so-called two-mass model (shown in Figure 2.10) is simple and sufficient with reasonable accuracy for the transient stability analysis of WTGS especially the interaction with the grid [19-20]. The aerodynamic torque T_t causes the turbine speed ω_t , which gives by the following dynamic equation [21-13]:

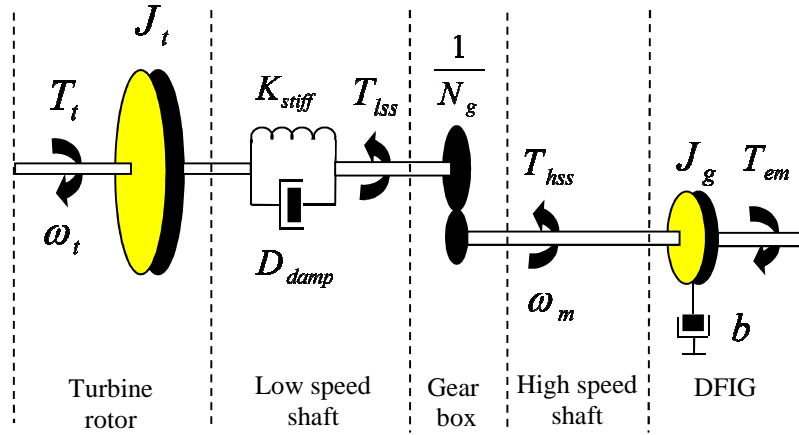


Figure 2.10 Two-mass drive train model [19-20].

$$J_t \frac{d\omega_t}{dt} = T_t - T_{lss} \quad (2.11)$$

Here, the low-speed shaft torque T_{lss} acts as a braking torque, it is obtained by:

$$\begin{cases} T_{lss} = K_{stiff} \left(\theta_t - \frac{\theta_m}{N_g} \right) + D_{damp} \left(\omega_t - \frac{\omega_m}{N_g} \right) = N_g T_{hss} \\ \omega_m = N_g \omega_t \\ \dot{\theta}_t = \omega_t \text{ and } \dot{\theta}_m = \omega_m \end{cases} \quad (2.12)$$

The generator inertia J_g is driven through the high-speed shaft, the high-speed shaft torque T_{hss} is braked by generator electromagnetic torque T_{em} , its dynamic system is described by:

$$J_g \frac{d\omega_m}{dt} = T_{hss} - T_{em} - b \omega_m \quad (2.13)$$

where: T_t and T_g : aerodynamic torque of turbine and generator electromagnetic torque respectively,

J_t and J_g : turbine rotor and generator moment of inertia respectively,

ω_t and ω_m : turbine and generator rotational speed respectively,

K_{stiff} and D_{damp} : shaft torsional stiffness and torsional damping coefficients respectively

N_g : ratio of the gearbox.

2.2.4. DFIG Model

The DFIG model has been implemented with motor convention on the rotor side and generator convention on the stator side [22-23-24], or motor convention on both rotor side and stator side [25-26-27-17]. Application of Park's transformations [24] to the three-phase model of the DFIG, with motor convention on both rotor and stator sides allows writing the dynamic voltages and fluxes equations in the arbitrary d-q reference frame are given by [28]:

$$\begin{cases} V_{sd} = R_s i_{sd} + \frac{d\Phi_{sd}}{dt} - \omega_s \Phi_{sq} \\ V_{sq} = R_s i_{sq} + \frac{d\Phi_{sq}}{dt} + \omega_s \Phi_{sd} \\ V_{rd} = R_r i_{rd} + \frac{d\Phi_{rd}}{dt} - \omega_r \Phi_{rq} \\ V_{rq} = R_r i_{rq} + \frac{d\Phi_{rq}}{dt} + \omega_r \Phi_{rd} \end{cases} \quad (2.14)$$

where R_s and R_r are respectively the resistance of the stator and rotor windings, ω_s and ω_r are the rotational speed of the synchronous reference frame, and the rotor reference frame respectively, which are related by the following relation: $\omega_r = \omega_s - p\omega_m = \omega_s - \omega_e$.

The stator and rotor flux are given by:

$$\begin{cases} \Phi_{sd} = L_s i_{sd} + L_m i_{rd} = (L_{sl} + L_m) i_{sd} + L_m i_{rd} = L_{sl} i_{sd} + L_m i_{ms} \\ \Phi_{sq} = L_s i_{sq} + L_m i_{rq} = (L_{sl} + L_m) i_{sq} + L_m i_{rq} = L_{sl} i_{sq} + L_m i_{ms} \\ \Phi_{rd} = L_r i_{rd} + L_m i_{sd} = (L_{rl} + L_m) i_{rd} + L_m i_{sd} = L_{rl} i_{rd} + L_m i_{ms} \\ \Phi_{rq} = L_r i_{rq} + L_m i_{sq} = (L_{rl} + L_m) i_{rq} + L_m i_{sq} = L_{rl} i_{rq} + L_m i_{ms} \end{cases} \quad (2.15)$$

where L_s and L_r are respectively the inductances of the stator and rotor windings, L_{ls} and L_{lr} are respectively the leakage inductances of the stator and rotor windings, and L_m is the mutual inductance.

The equivalent circuit of the DFIG in d-q reference frame is shown in Figure 2.11.

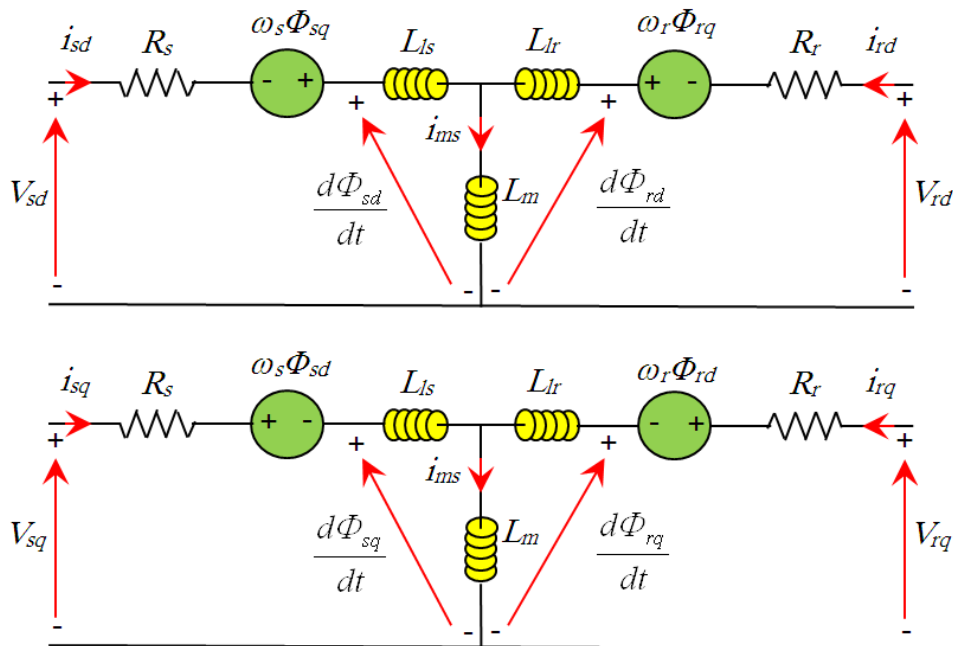


Figure 2.11 Equivalent circuit of the DFIG in the d-q coordinates [29].

The electromagnetic torque can be written as a function of rotor currents and stator fluxes as:

$$T_{em} = p \frac{L_m}{L_s} (\Phi_{sq} i_{rd} - \Phi_{sd} i_{rq}) \quad (2.16)$$

The stator active and reactive powers are expressed as:

$$\begin{cases} P_s = V_{sd} i_{sd} + V_{sq} i_{sq} \\ Q_s = V_{sq} i_{sd} - V_{sd} i_{sq} \end{cases} \quad (2.17)$$

2.2.5. Back-to-Back Power Electronic Converters Model

The main power circuit of three-phase two-level pulse width modulator (PWM) back-to-back VSCs (voltage source converters) employed in the current study is shown in Figure 2.12. The power rating of the RSC is determined by two factors, namely maximum slip power and reactive power control capability [30]. The RSC can be seen as a current controlled VSC.

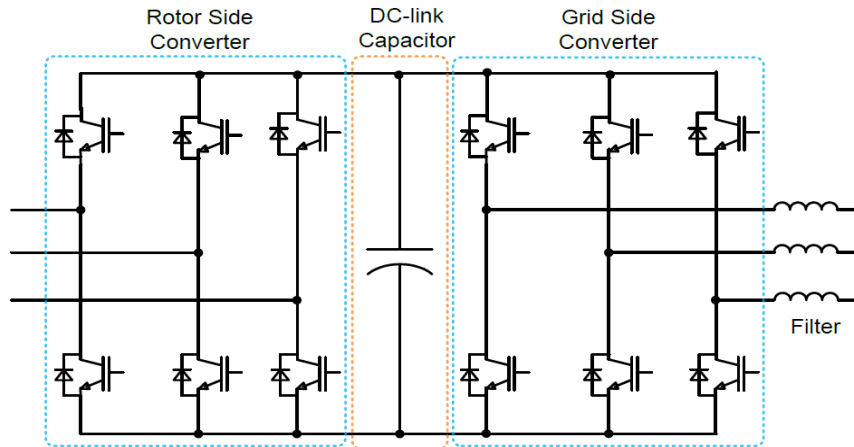
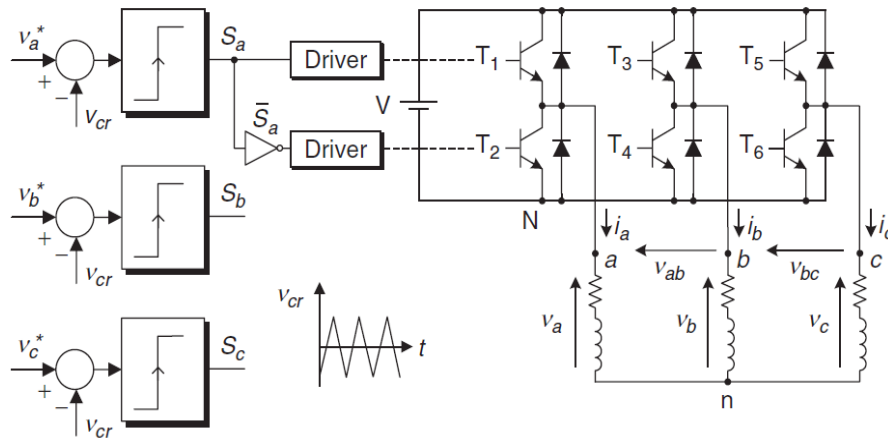


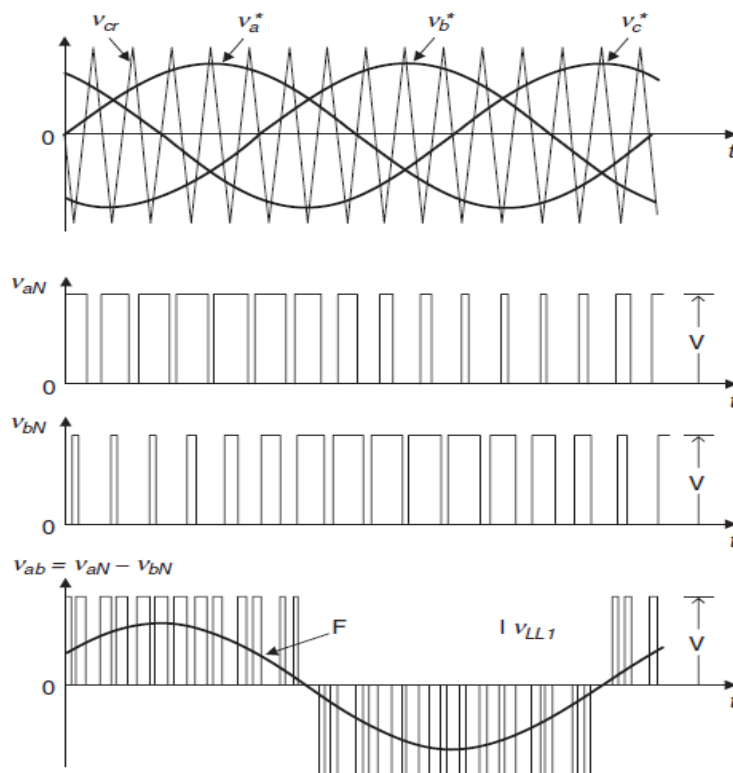
Figure 2.12 AC/DC/AC bidirectional power converter [31].

The control objective of RSC is to regulate the stator side active power (or rotational speed) and the stator side reactive power independently. The power rating of the GSC is mainly determined by maximum slip power since it usually operates at a unity power factor to minimize the losses in the converter [31]. The GSC is normally dedicated to controlling the DC-link voltage only. The converter can also be utilized to support grid reactive power during a fault [32]. The GSC can also be used to enhance grid power quality [33].

In this chapter, only linear PI control schemes with PWM have been used in the three-phase back-to-back VSCs. The reference voltage of each phase is compared to the triangular waveform, generating the switching states for each corresponding inverter leg, as shown in Figure 2.13. Output voltages for phases a and b , v_{aN} and v_{bN} , and line-to-line voltage v_{ab} are also shown in this figure [34].



(a) Pulse width modulator of VSC



(b) Output voltages for phases *a* and *b*

Figure 2.13 Pulse width modulator for a three-phase inverter [34].

The vector control system based on Park’s transformation is used in the back-to-back VSCs, it provides two orthogonal channels *d* and *q* to each converter thereby allowing decoupled control of active and reactive power. This is equivalent to the control of a DC machine where this decoupling is achieved through machine construction [35].

2.2.6. Grid-Interfaced Inductance Filter Model

Figure 2.14 presents the schematic diagram of the GSC and the DC-link system. The voltage equation across the inductors is [37]:

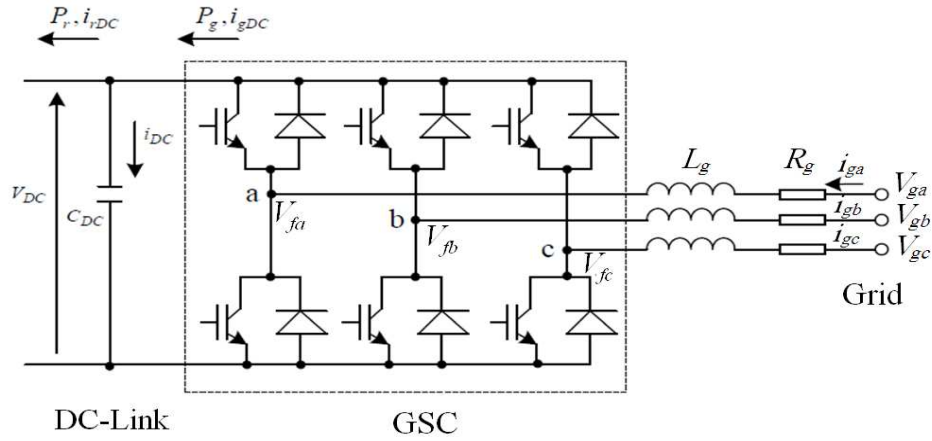


Figure 2.14 DC/AC grid-interfaced converter [36].

$$\begin{bmatrix} V_{ga} \\ V_{gb} \\ V_{gc} \end{bmatrix} = R_g \begin{bmatrix} i_{ga} \\ i_{gb} \\ i_{gc} \end{bmatrix} + L_g \frac{d}{dt} \begin{bmatrix} i_{ga} \\ i_{gb} \\ i_{gc} \end{bmatrix} + \begin{bmatrix} V_{fa} \\ V_{fb} \\ V_{fc} \end{bmatrix} \quad (2.18)$$

Apply the Park transformation to Equation (2.18), we obtain the following voltage equations in the d-q frame rotating at grid voltage frequency ω_g :

$$\begin{cases} V_{gd} = R_g i_{gd} + L_g \frac{di_{gd}}{dt} - \omega_g L_g i_{gq} + V_{fd} \\ V_{gq} = R_g i_{gq} + L_g \frac{di_{gq}}{dt} + \omega_g L_g i_{gd} + V_{fq} \end{cases} \quad (2.19)$$

The active and reactive powers exchanged between the grid and the GSC are:

$$\begin{cases} P_g = V_{gd} i_{gd} + V_{gq} i_{gq} \\ Q_g = V_{gq} i_{gd} - V_{gd} i_{gq} \end{cases} \quad (2.20)$$

2.2.7. DC-Link Capacitor Model

We assume the back-to-back converter is lossless and neglect the losses in the inductor resistance, then the DC-link is modeled as [36-37]:

$$P_{DC} = V_{DC} \cdot i_{DC} \quad (2.21)$$

$$P_g = V_{DC} \cdot i_{gDC} \quad (2.22)$$

$$P_r = V_{DC} \cdot i_{rDC} \quad (2.23)$$

$$P_{DC} = P_g - P_r \quad (2.24)$$

$$i_{DC} = i_{gDC} - i_{rDC} \quad (2.25)$$

$$i_{DC} = C_{DC} \frac{dV_{DC}}{dt} \quad (2.26)$$

2.3. Power flow in Wound-Rotor Induction Machine

Stator side always feeds active power to the grid in the generator operating mode and vice-versa for the motor operating mode, whereas active power is fed into or out of the rotor depending on the operating condition of the drive. For example, if the WRIM works as a generator, in the super-synchronous operating mode, power flows from the rotor via the converter to the grid, whereas it flows in the opposite direction in the sub-synchronous operating mode as shown in the Figure 2.15.

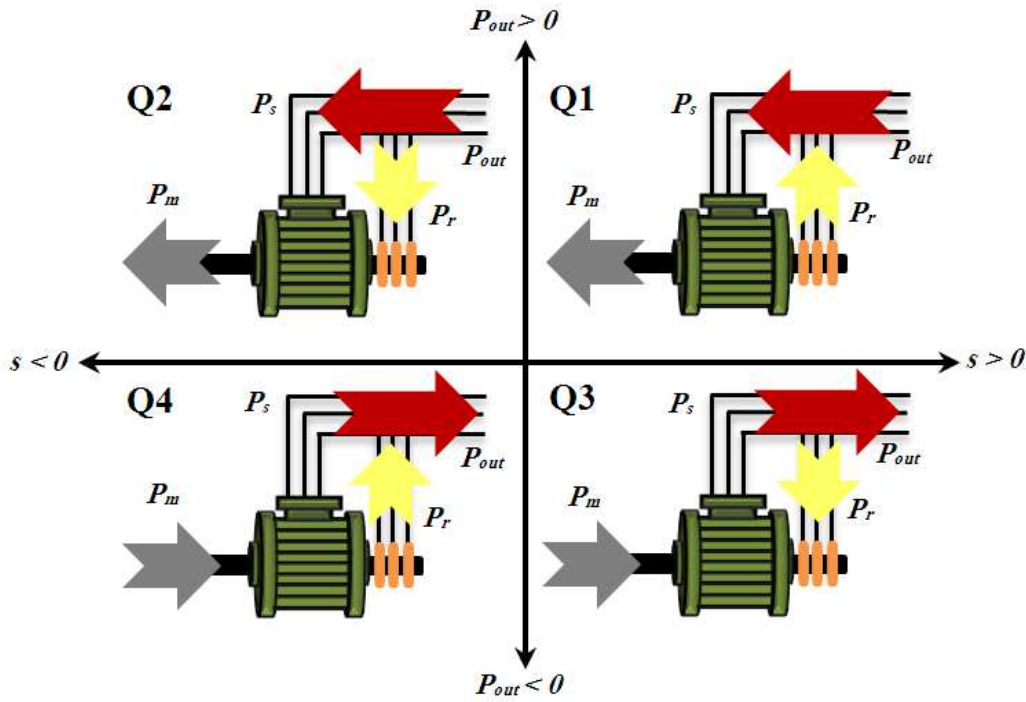


Figure 2.15 Operating quadrants of the WRIM [26].

- where, in quadrant:
- **Q1:** the WRIM is a motor in the sub-synchronous operating mode.
 - **Q2:** the WRIM is a motor in the super-synchronous operating mode.
 - **Q3:** the WRIM is a generator in the sub-synchronous operating mode.
 - **Q4:** the WRIM is a generator in the super-synchronous operating mode.

In steady-state at fixed rotor speed for a lossless DFIG system we have $T_m \approx T_{em}$, the mechanical power from the wind turbine applied to the shaft is given by $P_m = P_s + P_r$. It follows that [38]:

$$P_r = P_m - P_s = T_m \omega_e - T_{em} \omega_s = -T_m \left(\frac{\omega_s - \omega_e}{\omega_s} \right) \omega_s = -T_m s \omega_s = -s P_s \quad (2.27)$$

where s is defined as the slip of the WRIG: $s = (\omega_s - \omega_e) / \omega_s$

Therefore if the maximum slip is limited, say to 0.3, the rotor winding converters can be rated as a fraction of the induction generator rated power. This is typically around $\pm 30\%$ for WRIG in WPGSs gives a slip range of ± 0.3 . This is one key advantage of the DFIG system over fully-rated power electronic systems.

From the above relationships, the stator and rotor power are:

$$P_s = P_m / (1 - s) \quad \text{and} \quad P_r = -sP_m / (1 - s) \quad (2.28)$$

To consider the mechanical power change during different rotor speeds, the following analysis is carried out with all terms in per unit values. The slip is assumed to vary from a sub-synchronous value of +0.35 to a super-synchronous value of -0.35. Figure 2.16 shows how the rotor and stator power vary as the rotor slip changes from sub- to super-synchronous modes. The speed of the rotor has to change as wind speed changes in order to track the maximum power point of the aerodynamic system. Slip, s , therefore is related to incident wind speed. In this case, a slip of -0.2 occurs with rated wind speed (12m/s). As wind speed drops, slip has to increase and in this case has a maximum value of 0.35 [38].

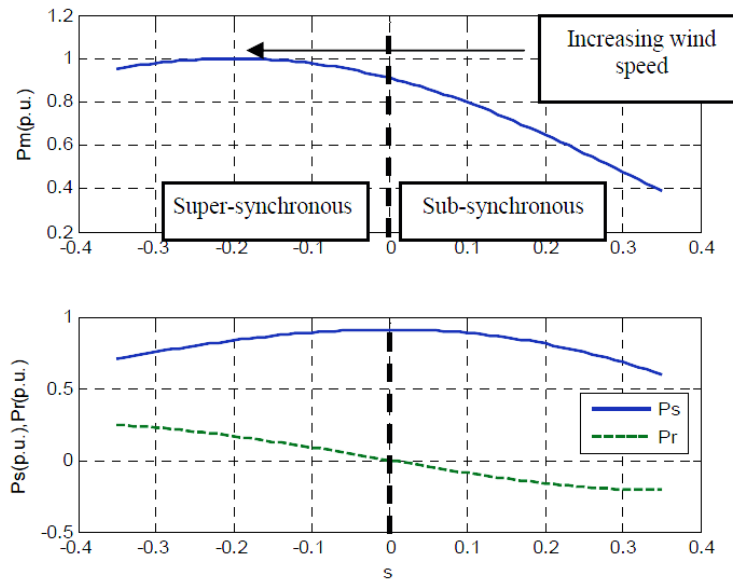


Figure 2.16 Power flow in the DFIG system [38].

It is clear that the mechanical power, P_m , reaches its peak at super-synchronous speed when $s = -0.2$. When rotating at the synchronous speed ($s = 0$), the DFIG supplies all the power via the stator winding, with no active power flow in the rotor windings and their associated converters. Note that at $s=0$, the stator power is maximum. As the wind speed increases, the rotational speed must also increase to maintain optimum tip-speed ratios. In such circumstances, the machine operates at super-synchronous speeds ($s < 0$). The mechanical power flows to the grid through both the stator windings and the rotor windings and their converter. For example, at $s=-0.2$, P_s is 0.8pu and P_r is 0.2pu giving a total generated power of 1pu. At lower wind speeds, the blades rotate at a sub-synchronous speed ($s > 0$). In such circumstances, the rotor converter system will absorb power from the grid connection to provide excitation for rotor winding. For example, at $s=0.2$, P_s is 0.8pu but P_r is -0.2pu giving a total generated power of 0.6pu.

With such a control scheme it is possible to control the power extracted from the aerodynamic system such that the blade operates at the optimum aerodynamic efficiency (thereby extracting as much energy as possible) by adjusting the rotation speed according to the incident wind speed [38].

2.4. Control Schemes of Grid Connected DFIG

The DFIG has to be synchronized and connected to the grid before any power can be produced. Typically, when the generator rotational speed exceeds a certain threshold value, it is assumed that the wind is strong enough to generate electric power profitably, and the global control system produces an order of connecting the DFIG stator to the grid [39].

2.4.1. DC-link Capacitor Charging using GSC Current Control

The GSC as mentioned earlier has two tasks. It has to maintain the DC-link voltage and exchange reactive power with the grid if required. At the start-up stage of the DFIG system, it is the GSC that has to bring the DC-link voltage to the level required for the operation of the system after which the RSC control can be enacted [40] [41]. During normal operation, the GSC maintains the DC-link voltage by exchanging the active power of the RSC with the grid.

The d-axis of the rotating reference frame is aligned with the grid voltage vector, so we have [36-42]:

$$V_{gd} = V_g \quad \text{and} \quad V_{gq} = 0 \quad (2.29)$$

Phase, amplitude and frequency of the grid voltage are critical information for the operation of the grid-connected inverter systems. A simple way to get information about the phase angle is to use the angle of the voltage vector in the α - β reference frame:

$$\theta_g = \int \omega_g dt = \arctan \frac{V_{g\beta}}{V_{g\alpha}} \quad (2.30)$$

Using \arctan of the voltage ratio works well with an ideal grid without disturbances, if the signals are distorted, the output of this method will also be distorted. Therefore, a Phase Lock Loop (PLL) is implemented in the software, the function of the PLL is to keep track of the phase angle under any condition. The most common PLL technique applied to three phase grid-connected systems is based on an algorithm implemented in synchronous reference frame (d-q). The structure of the employed PLL algorithm is presented in Figure 2.17

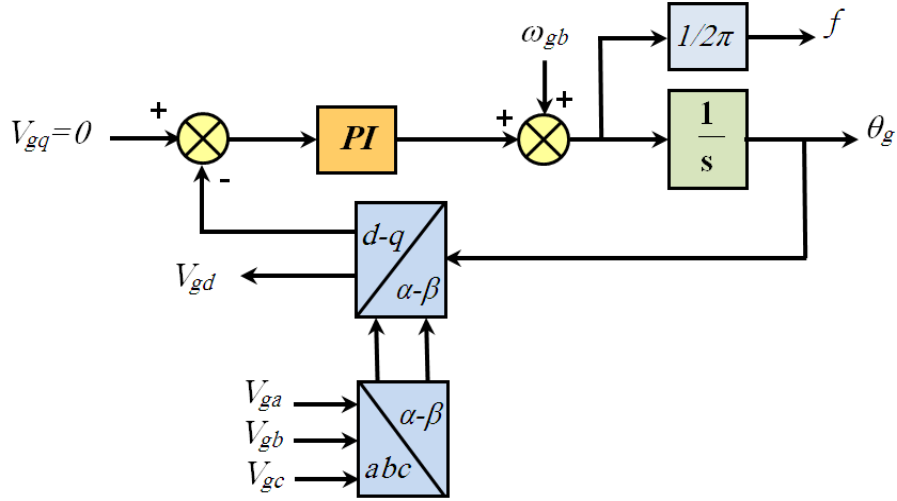


Figure 2.17 Block diagram of three-phase PLL structure [43].

Thus, we can rewrite the active and reactive power equations of the GSC as:

$$\begin{cases} P_g = V_{gd} i_{gd} \\ Q_g = -V_{gd} i_{gq} \end{cases} \quad (2.31)$$

Now, it can be clearly seen that active and reactive powers are proportional to i_{gd} and i_{gq} respectively. Therefore we can achieve the decoupled control of the active and reactive powers through i_{gd} and i_{gq} .

We assume that harmonics due to the switching can be neglected, the GSC and the inductor resistance are lossless, then based on the DC-link model (Equations (2.21, ..., 2.26)), we have:

$$i_{DC} = C_{DC} \frac{dV_{DC}}{dt} = i_{gDC} - i_{rDC} \quad (2.32)$$

$$\begin{cases} P_g = V_{DC} i_{gDC} = V_{gd} i_{gd} \\ V_{gd} = \frac{m_{GSC}}{2} V_{DC} \\ i_{gDC} = \frac{m_{GSC}}{2} i_{gd} \end{cases} \quad (2.33)$$

where m_{GSC} is the modulation index of the GSC. We consider i_{rDC} as disturbance, and apply Laplace transform to Equation (2.32) then we can obtain transfer function of V_{DC} as function of i_{gd} [36]:

$$V_{DC} = \frac{m_{GSC}}{2C_{DC} \cdot s} i_{gd} \quad (2.34)$$

where s is the Laplace operator.

control between the stator active and reactive power, we choose a d-q representation of the DFIG with the d-axis oriented along the stator-flux vector position [39]. The stator flux angle is given by:

$$\begin{cases} \Phi_{s\alpha} = \int V_{s\alpha} - R_s i_{s\alpha} dt \\ \Phi_{s\beta} = \int V_{s\beta} - R_s i_{s\beta} dt \end{cases} \Rightarrow \theta_{\Phi_s} = \arctan \left(\frac{\Phi_{s\beta}}{\Phi_{s\alpha}} \right) \quad (2.37)$$

where θ_s is the stator-flux vector position.

Since the stator is connected to the grid, we could make the following assumptions [37]:

- The stator resistance R_s can be neglected (usually justified in machines with a rating over 10kW).
- The stator magnetizing current space phasor \vec{i}_{ms} is constant in magnitude and phase.
- Frequency of the power supply on the stator is constant, i.e. $\omega_s = \text{constant}$.

Under those assumptions, it implies that:

$$\begin{cases} \Phi_{sd} = \Phi_s = L_s i_{sd} + L_m i_{rd} = L_m i_{ms} \\ \Phi_{sq} = 0 = L_s i_{sq} + L_m i_{rq} \\ \Phi_{rd} = L_r i_{rd} + L_m i_{sd} = \frac{L_m^2}{L_s} i_{ms} + \sigma L_r i_{rd} \\ \Phi_{rq} = L_r i_{rq} + L_m i_{sq} = \sigma L_r i_{rq} \end{cases} \quad (2.38)$$

where σ is the leakage factor: $\sigma = 1 - L_m^2 / L_s L_r$. The stator and rotor voltage can be written as:

$$\begin{cases} V_{sd} = 0 = R_s i_{sd} + \frac{d\Phi_{sd}}{dt} - \omega_s \Phi_{sq} \\ V_{sq} = V_s = R_s i_{sq} + \frac{d\Phi_{sq}}{dt} + \omega_s \Phi_{sd} \approx \omega_s L_m i_{ms} \\ V_{rd} = R_r i_{rd} + \sigma L_r \frac{di_{rd}}{dt} - \omega_r \sigma L_r i_{rq} \\ V_{rq} = R_r i_{rq} + \sigma L_r \frac{di_{rq}}{dt} + \omega_r \left(\frac{L_m^2}{L_s} i_{ms} + \sigma L_r i_{rd} \right) \end{cases} \quad (2.39)$$

The relation $\omega_s \Phi_s = V_s$ confirms that stator-flux vector and stator-voltage vector are turning in same angular speed, but stator-flux vector is in advance to stator-voltage vector with $\pi/2$ rad. This gives us another way to calculate the stator-flux vector position [26,44]:

$$\theta_{\Phi_s} = \theta_s - \frac{\pi}{2} = \tan^{-1} \left(\frac{V_{s\beta}}{V_{s\alpha}} \right) - \frac{\pi}{2} \quad (2.40)$$

Then, from Equation (2.39), the following voltage components are applied to the DFIG rotor during the running stage:

$$\begin{cases} V_{rd}^* = V_{rd}' - \omega_r \sigma L_r i_{rq} \\ V_{rq}^* = V_{rq}' + \omega_r \left(\frac{L_m^2}{L_s} i_{ms} + \sigma L_r i_{rd} \right) \end{cases} \quad (2.41)$$

where V_{rd}' and V_{rq}' are the output of the inner rotor currents controllers.

Now, we rewrite the stator active and reactive power equations:

$$\begin{cases} P_s = V_{sq} i_{sq} = -V_{sq} \frac{L_m}{L_s} i_{rq} \\ Q_s = V_{sq} i_{sd} = V_{sq} (\Phi_{sd} - L_m i_{rd}) / L_s = V_{sq} \frac{L_m}{L_s} \left(\frac{V_{sq}}{\omega_s L_m} - i_{rd} \right) = V_{sq} \frac{L_m}{L_s} (i_{ms} - i_{rd}) \end{cases} \quad (2.42)$$

the electromagnetic torque equation as:

$$T_{em} = p \frac{L_m}{L_s} (\Phi_{sq} i_{rd} - \Phi_{sd} i_{rq}) = -p \frac{L_m}{L_s} \Phi_{sd} i_{rq} = -p \frac{L_m^2}{L_s} i_{ms} i_{rq} \quad (2.43)$$

Then, from Equations (2.39) and (2.42), the resulting block diagram of the DFIG is presented in Figure 2.19.

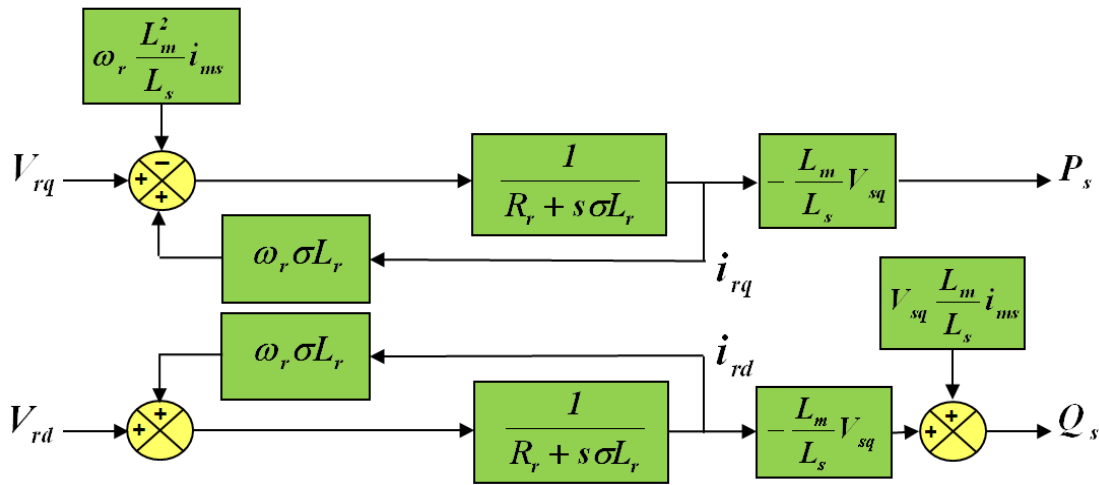


Figure 2.19 Block diagram of DFIG system used for control.

From Equations (2.42) and (2.43), it can be seen that the stator active power (and the electromagnetic torque) depends only on the q-axis rotor current. The stator reactive power only depends on the d-axis rotor current. Therefore, the decoupled control of stator active and reactive powers has been achieved in the stator-flux reference frame using the indirect vector control of the stator power as presented in Figure 2.20, there are two control loops, the inner one consist of the rotor current loop, while the outer one is the stator power control loop. PI control is typically used and can satisfy the control requirement under normal operating conditions, the PI controllers terms are calculated with a pole-compensation method as presented in Appendix C.

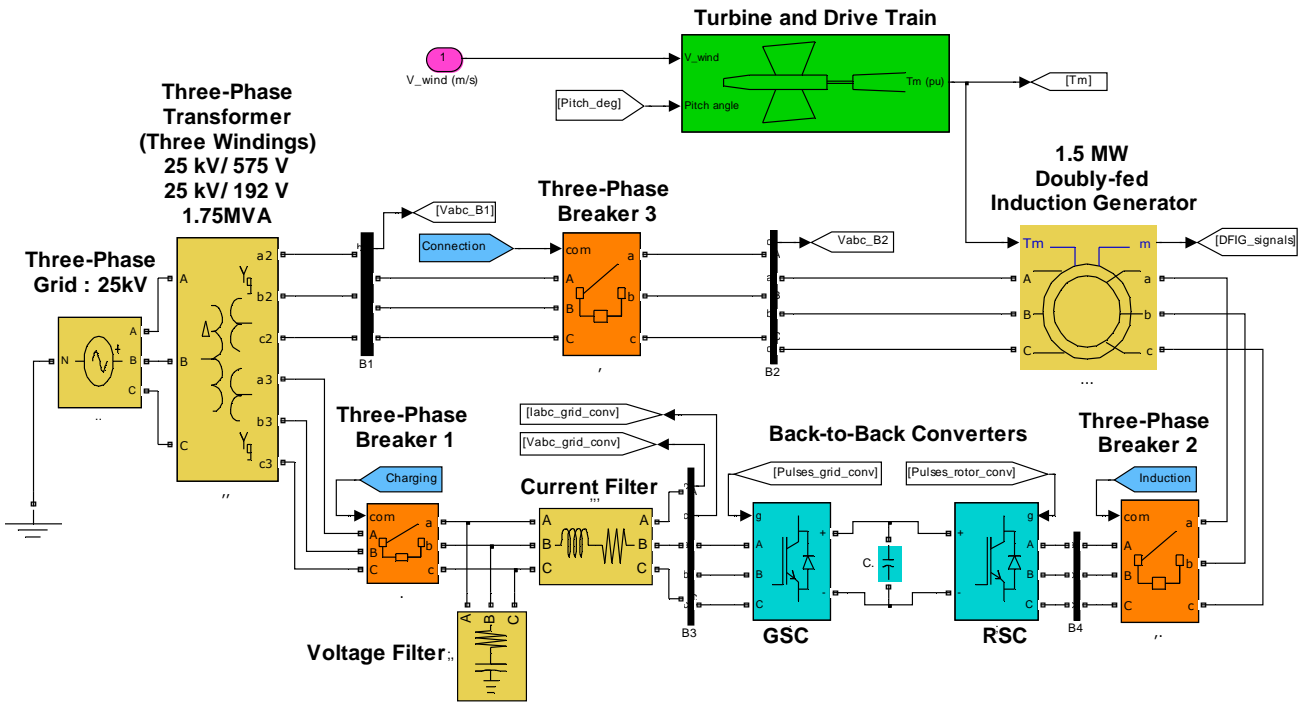
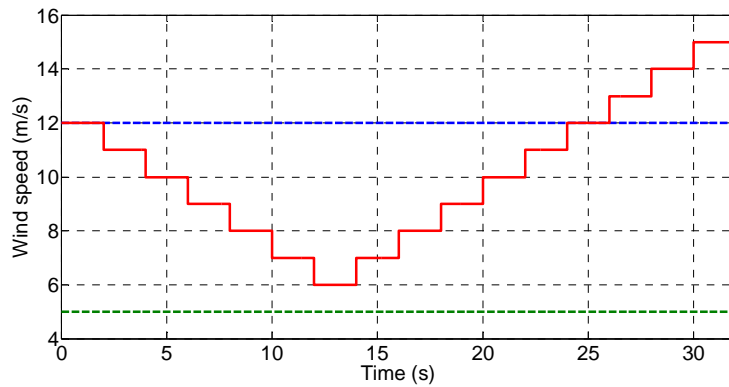
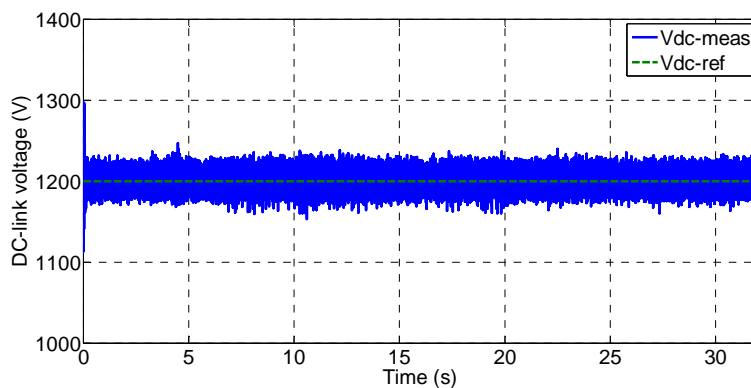


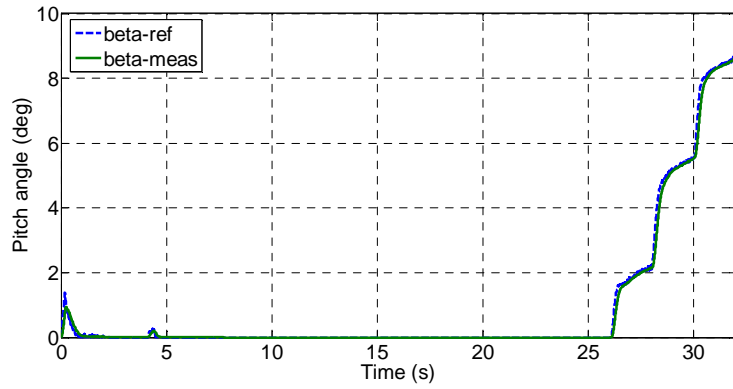
Figure 2.21 Detailed model of the DFIG based WPGS in Matlab/SimPowerSystems environment.



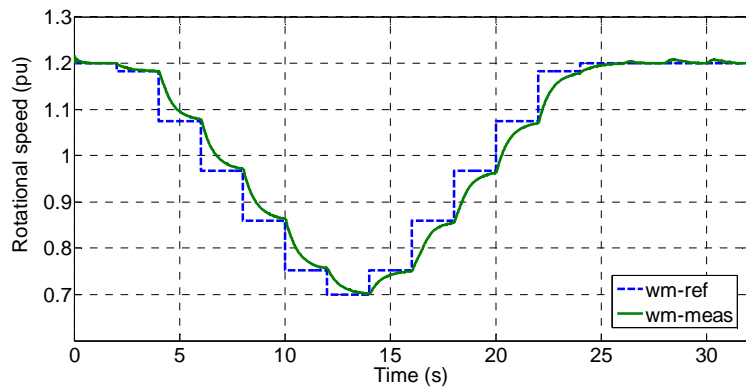
(a) Wind speed profile employed.



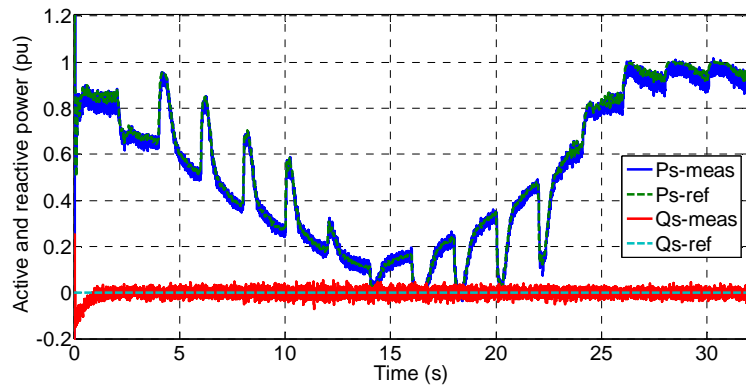
(b) Control of the DC-link voltage.



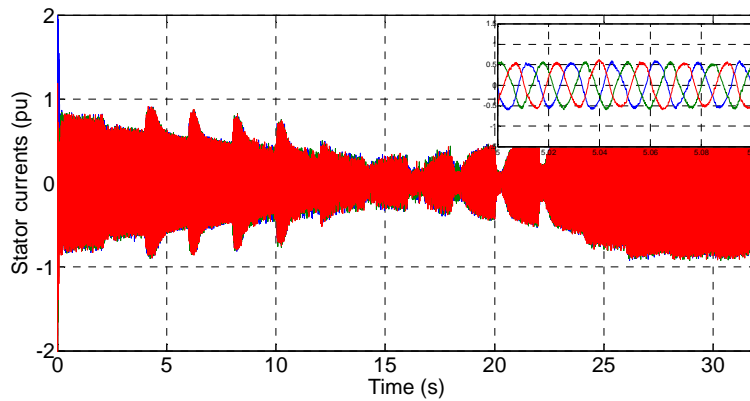
(c) Control of the pitch angle.



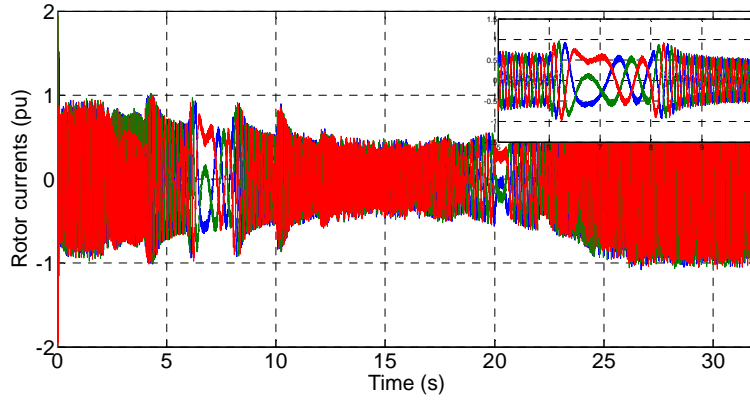
(d) Control of the rotational speed.



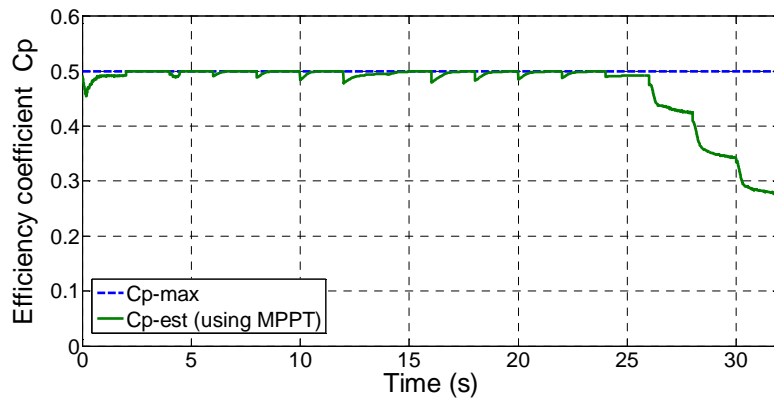
(e) Control of the stator active and reactive power.



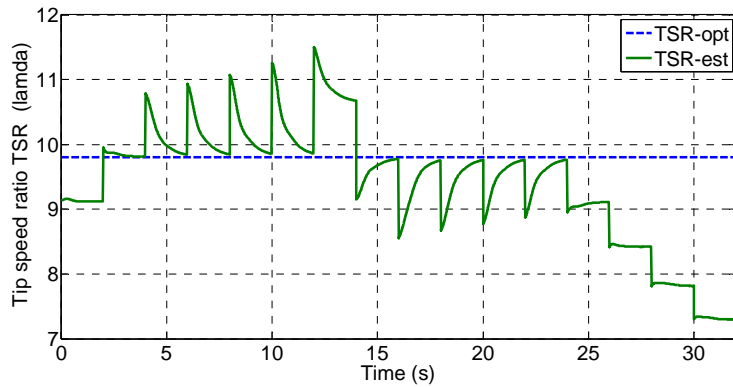
(f) Measured stator windings currents.



(g) Measured rotor windings currents.



(h) Power efficiency coefficient (C_p).



(i) Tip speed ratio.

Figure 2.22 Detailed simulation of different operating modes of the DFIG based WPGS.

Discussion

The initial point of this simulation is the rated wind speed, rated rotor speed and rated output power. The wind speed start to decrease in stairs from the rated wind speed (12m/s) into the 6m/s (Figure 2.22.a), this variation is inside the MPPT operating mode, the rotational speed is changed accordingly in order to maximize the output power as presented in Figure 2.22.d and Figure 2.22.e respectively. After that the wind speed starts to increase in stairs and pass the MPPT zone into the constant power zone (beyond the 12m/s).

The DC-link voltage is regulated to the 1200V using the GSC, Figure 2.22.b presents a good pursuit to the reference without any problems. The pitch angle is controlled to work according to the operating mode, for a wind speed between the cut-in and the rated wind speed ($5\text{m/s} < V_w < 12\text{m/s}$), the pitch angle is maintained zero. Beyond that, pitch control system is activated in order to protect the mechanical construction of the WTS from any risky overload. Also, the Figure 2.22.c presents a good pursuit to the reference without any problems.

The rotational speed of the DFIG is controlled to work only in the permissible zone ($\pm 25\%$ of the synchronous speed), the speed variation possibility allows to track the maximum output power in the moderate wind speed conditions. Figure 2.22.d presents the rotational speed control performance; the optimal rotational speed is given as reference using the TSR maximisation algorithm. Figure 2.22.h presents efficiency coefficient of the WTS, regardless of the intensity or any transient variation in the wind speed, the efficiency coefficient is maintained at its maximum.

Figure 2.22.i presents the TSR variation, in the MPPT zone (before the 26s) the optimal TSR is maintained (almost 10). After the 26s, a constant output power and constant rotor speed operation is activated, the pitch angle is increased to reduce the aerodynamic power of the WTS, the rotor speed and the output power are limited to their rated values. The efficiency coefficient is decreased away from its maximum and likewise the TSR.

The reactive power is maintained zero in order to guarantee a unity power factor in the stator side of the DFIG (Figure 2.22.e). The active power is changing according to the available kinetic power of the wind. The measured stator currents are changing according to the stator active power with constant frequency (Figure 2.22.f), however the rotor currents are changing in magnitude and frequency according to the rotational speed and the stator exchanged power (Figure 2.22.g).

2.6. Conclusion

In this chapter, a detailed modeling and analysis of the WTS driven DFIG is presented, each part of the electromechanical conversion system of the WPGS is discussed and presented, supervision of operating modes, references generation and RSC and GSC control laws demonstration, limitations and protections management of the WPGS are discussed. Finally a detailed simulation test including all the operating modes of the DFIG based WTS is presented. In the next chapter we will discuss the power maximization and power limitation operating modes problems, and we will suggest some improvements based on intelligent ideas.

2.7. References of Chapter 2

- [1] B. T. Ooi and R. A. David. Induction-generator/synchronous-condenser system for wind-turbine power. Institution of Electrical Engineers. Montreal, Canada, pp. 69–74, 1979.
- [2] E. Spahic, J. Morren, G. Balzer and G. Michalke. Mathematical model of the double fed induction generator for wind turbines and its control quality. International Conference on Power Engineering. Setubal, Portugal, pp. 642–649, 2007.
- [3] J. Hu, H. Nian, B. Hu, Y. He and Z.Q. Zhu. Direct active and reactive power regulation of DFIG using sliding-mode control approach, IEEE Trans. on Energy Conversion, Vol. 25, No. 4, 2010.
- [4] T. Burton, D. Sharpe, N. Jenkins, and E. Bossanyi, Wind energy handbook, John Wiley & Sons, Ltd, 2001.
- [5] W. Qiao, W. Zhou, J.M. Aller, and R.G. Harley. Wind speed estimation based sensorless output maximization control for a wind turbine driving a DFIG. IEEE Trans. on Power Electronics, Vol. 23, No. 3, pp. 1156-1169, May 2008.
- [6] P. Sorensen, A D. Hansen, T. Lund and H. Bindner, Reduced models of doubly fed induction generator system for wind turbine simulations, Wind Energy, Vol. 9, pp. 299-311, 2006.
- [7] J. Zafar, Winding short-circuit fault modelling and detection in doubly-fed induction generator based wind turbine systems, PhD Thesis, Free University of Bruxelles, Oct. 13, 2011.
- [8] W. Sadara and B. Neammanee, Implementation of a three phase grid synchronization for doubly-fed induction generators in wind energy system, IEEE International Conference on Electrical Engineering/Electronics Computer Telecommunications and Information Technology (ECTI-CON), 19-21 May 2010
- [9] A. Perdana, Dynamic models of wind turbines, PhD Thesis, Chalmers University of Technology, G oteborg, Sweden 2008.
- [10] E.B. Muhando, T. Senjyu, A. Uehara, T. Funabashi and C-H Kim, LQG design for Megawatt-Class WECS with DFIG based on functional models' fidelity prerequisites, IEEE Trans. on Energy Conversion, Vol. 24, No. 4, pp. 893-904, Dec. 2009.
- [11] E. Koutroulis and K. Kalaitzakis, Design of a maximum power tracking system for wind-energy conversion applications, IEEE Trans. on Industrial Electronics, Vol. 53, No. 2, pp. 486-494, 2006.
- [12] A.A. El-Sattar, N.H. Saad, M.Z. Shams El-Dein. Dynamic response of doubly fed induction generator variable speed wind turbine under fault, Electric Power Systems Research, Elsevier, Vol. 78, pp.1240–1246, 2008.
- [13] I. Poultangari, R. Shahnazi, M. Sheikhan. RBF neural network based PI pitch controller for a class of 5-MW wind turbines using particle swarm optimization algorithm. ISA Trans., Vol. 51, pp. 641–648, 2012.
- [14] Hydraulic control technology for wind turbine generators, Production Catalog, Bosch Rexroth AG Industrial Hydraulics Zum Eisengie er 1 97816 Lohr, Germany, www.boschrexroth.com.
- [15] J.L. Rodriguez, Analisis dinamico y dise odelsistema de control de aeroturbinas de velocidad variable con generadorasincrono de doblealimentacion, doctorate thesis, Carlos III University, Madrid, 2000.
- [16] S. Heier, Grid integration of wind energy conversion systems, Wiley, ISBN 0-471-97143-X.
- [17] H. Camblong, Minimisation de l'impact des perturbations d'origine  olienne dans la g neration d' lectricit  par des a rog nerateurs   vitesse variable, L'Ecole Nationale Sup rieure d'Arts et M tiers, Universit  de Bordeaux, 18 D c. 2003.
- [18] F. Iof, A.D. Hansen, P. Sorensen, F. Blaabjerg. Wind turbine blockset in MATLAB/ simulink, General overview and description of the model. Aalborg University, 2004.
- [19] V. Akhmatov, Modelling of variable-speed wind turbines with doubly-fed induction generators in short term stability investigations, International Workshop on Transmission Networks for Offshore Wind Farms, Stockholm, Sweden. 2002.

- [20] P. Ledesma, J. Usaola, Doubly fed induction generator model for transient stability analysis, *IEEE Trans. on Energy Conversion*. Vol. 20, No. 2, pp. 388–397, 2005.
- [21] B. Boukhezzar, H. Siguerdidjane, Nonlinear control of a variable wind turbine using a two mass model, *IEEE Trans. on Energy Conversion*. Vol. 26, No. 1, pp. 149–162, 2011.
- [22] Y. Zhao, X.D. Zou, Y.N. Xu, Y. Kang & J. Chen, Maximal power point tracking under speed-mode control for wind energy generation system with doubly fed induction generator, 5th International Power Electronics and Motion Control Conference (IPEMC 2006), Shanghai, pp. 1-5, issue date 14-16 Aug. 2006.
- [23] H.Li and Z.Chen, A New current control strategy of maximizing the generated power from a doubly fed induction generator system, 12th International Power Electronics and Motion Control Conference (IPEMC 2006), Portoroz, issue date Aug. 30-Sep. 1 2006, pp. 1557-1562.
- [24] J. Zafar, Winding short-circuit fault modelling and detection in doubly-fed induction generator based wind turbine systems, PhD Thesis, Université Libre de Bruxelles, Oct. 13, 2011.
- [25] S. El Aimani, Modélisation de différentes technologies d'éoliennes intégrées dans un réseau de moyenne tension, Thèse de Doctorat de l'Université Des Sciences Et Technologies De Lille, 06/12/2004.
- [26] F. Poitiers, Etude et commande de génératrices asynchrones pour l'utilisation de l'énergie éolienne, Thèse de Doctorat de l'Université de Nantes, 19 déc. 2003.
- [27] N. Laverdure, Sur l'intégration des générateurs éoliens dans les réseaux faibles ou insulaires, Thèse Doctorat, Institut National Polytechnique de Grenoble, 9 déc. 2005.
- [28] J. Morren and S.W.H. De Haan, Rides through of wind turbines with doubly-fed induction generator during a voltage dip, *IEEE Trans. on Energy Conversion*, Vol. 20, No. 2, pp. 435-441, 2005.
- [29] Wu, Bin. 2006. High-Power Converters and AC drives. Wiley-IEEE Press, 2006, p. 1-15.
- [30] B. Pokharel, Modeling, control and analysis of a doubly fed induction generator based wind turbine system with voltage regulation, Master Thesis of Science in Electrical Engineering, Tennessee University, Dec. 2011.
- [31] W. Qiao, W. Zhou, J.M. Aller and R.G. Harley, Wind speed estimation based sensorless output maximization control for a wind turbine driving a DFIG, *IEEE Trans. on Power Electronics*, Vol. 23, No. 3, pp. 1156-1169, May 2008.
- [32] Hansen, and G. Michalke, Voltage grid support of DFIG wind turbines during grid faults. European Wind Energy Conference and Exhibition, May 2007.
- [33] E. Tremblay, A. Chandra, and P. Lagace, Grid-side converter control of DFIG wind turbines to enhance power quality of distribution network, *IEEE Power Engineering Society General Meeting*, Jun. 2006.
- [34] J. Rodriguez and P. Cortes, Predictive control of power converters and electrical drives, A John Wiley & Sons, Ltd., Publication, 2012.
- [35] N. Mohan. Advanced electric drives – analysis, control and modelling using simulink, MNPERE, Minneapolis. 2001.
- [36] C. Wang, Control, stability analysis and grid integration of wind turbines, PhD Thesis, Imperial College London, March 2008.
- [37] A. Dida and D. Benattous, A Complete Modeling and Simulation of DFIG based Wind Turbine System using Fuzzy Logic Control, *Frontier of energy*. Vol. 10, No. 2, 2016.
- [38] John Fletcher and Jin Yang (2010). Introduction to the doubly-fed induction generator for wind power applications, *Paths to Sustainable Energy*, Dr Artie Ng (Ed.), ISBN: 978-953-307-401-6, InTech, Available from: <http://www.intechopen.com/books/paths-to-sustainable-energy/introduction-to-the-doubly-fed-induction-generator-for-wind-power-applications>
- [39] G. Tapia, G. Santamaria, M. Telleria, and A. Susperregui, Methodology for smooth connection of doubly fed induction generators to the grid, *IEEE Trans. on Energy Conversion*, Vol. 24, No. 4, Dec. 2009.

- [40] J.L. Da Silva, R.G. de Oliveira, S.R. Silva, B. Rabelo and W. Hofmann, A discussion about a start-up procedure of a doubly-fed induction generator system, NORDIC Workshop on Power and Industrial Electronics (NORPIE/2008), Helsinki, Finland, 9-11 June, 2008.
- [41] T. Bouaouiche and M. Machmoum, Control and stability analysis of a doubly fed induction generator, 12th International Power Electronics and Motion Control Conference (EPE-PEMC 2006), Portoroz, pp. 1602-1607, Aug. 30-Sep. 1, 2006.
- [42] A. Dida and D. Benattous, Adaptive hill-climb searching method for MPPT algorithm based DFIG system using fuzzy logic controller, International Journal of Systems Assurance Engineering and management, 25 October, 2015.
- [43] G.U.O. Xiao-Qiang, W.U. Wei-Yang and G.U. He-Rong. Phase locked loop and synchronization methods for grid interfaced converters: a review, Przegląd Elektrotechniczny (Electrical Review), ISSN 0033-2097, R. 87 NR 4/2011.
- [44] G. Ahmed, Abo-Khalil, Synchronization of DFIG output voltage to utility grid in wind power system, Renewable Energy, Vol. 44, pp. 193-198, 2012.
- [45] H.M. Hasanien and E.A. Al-Ammar, Dynamic response improvement of doubly fed induction generator-based wind farm using fuzzy logic controller, Journal of Electrical Engineering, Vol. 63, No. 5, pp. 281–288, 2012.

Chapter 3:

Power Maximization and Pitch Angle Control using Fuzzy and Neuro-Fuzzy Controllers

Chapter 3: Power Maximization and Pitch Angle Control using Fuzzy and Neuro-Fuzzy Controllers

3.1. Introduction

WTs are controlled to operate only in a specified range of wind speeds bounded by cut-in and cut-out speeds. Beyond these limits, the turbine should be stopped to protect both the generator and turbine. Figure 3.1 shows the typical power curve of a WT [1-2]. It can be observed from Figure 3.1 that there are three different operational regions. The first one is the low-speed region, where the WT should be stopped and disconnected from the grid. The second is the moderate-speed region that is bounded by the cut-in speed and the rated speed, at which the turbine produces its rated power. In this region the turbine is controlled to produce the maximum available power from the wind. In the high speed region (region 3), the turbine power is limited so that the turbine and generator are not overloaded [3-4]. When WT is stopped generating power, its operation belongs to region 4.

Two control levels can be distinguished. First the DFIG control level with a fast dynamic response contains the electrical control of the DFIG through the power converters. The system contains two power converters; the RSC controls independently the stator generated active and reactive power. The GSC controls the DC link voltage and guarantees unity power factor in the rotor branch regardless of the magnitude and direction of the rotor power, the detailed scheme of the DFIG control is illustrated in Figure 3.2. Second is the WT control level, with slow dynamic response, provides reference signals to the pitch orientation system and to the DFIG control level [5].

The WT control level contains two controllers; pitch angle controller which has as task to control the generator speed at high wind speeds by changing the pitch angle. At low wind speeds, the pitch angle is kept constant to an optimal value, and the MPPT generates the active power (or the electromagnetic torque) reference signal for the active power control loop [5].

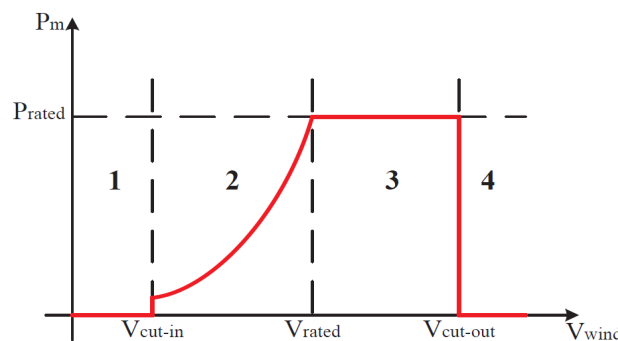


Figure 3.1 Power curve of a variable speed WTS [6].

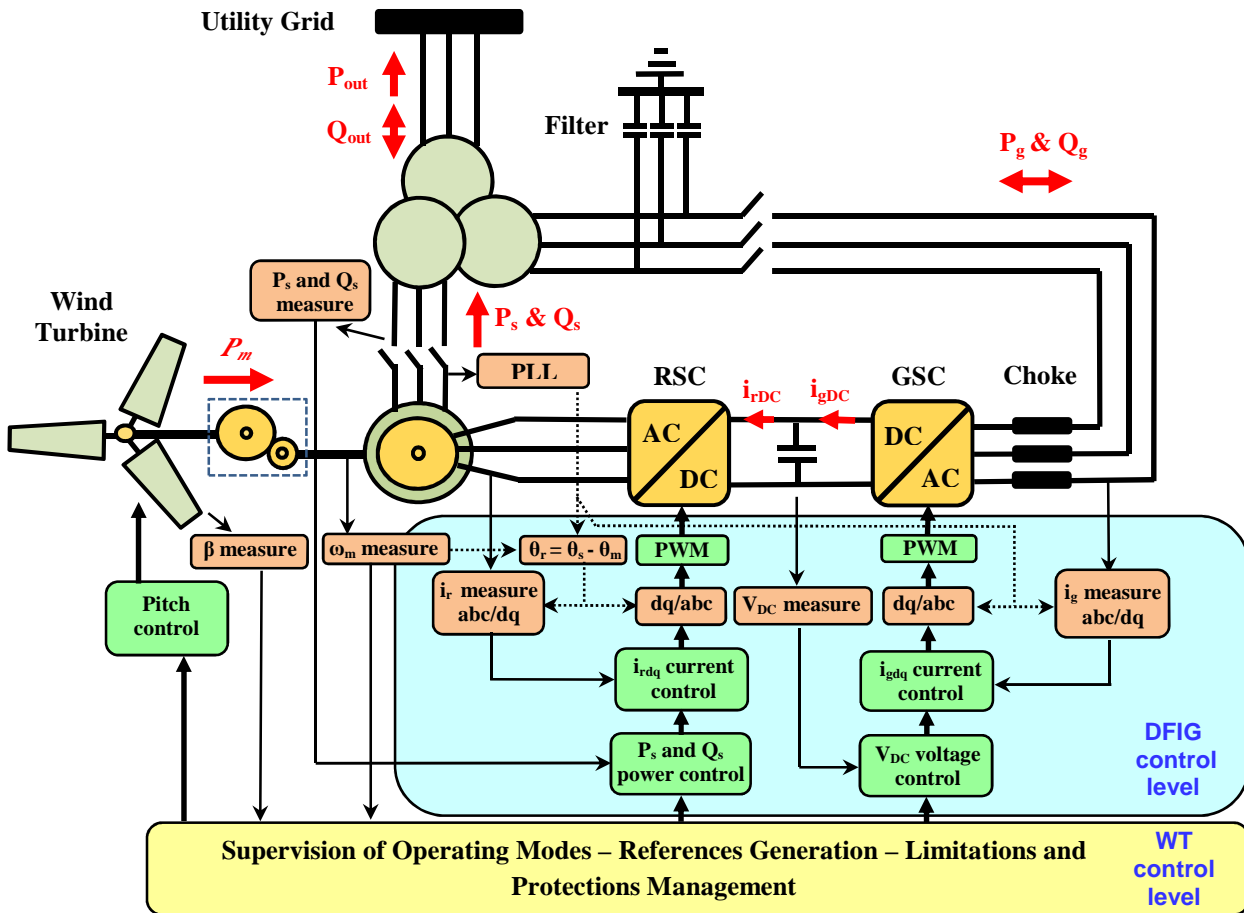


Figure 3.2 Detailed scheme of the DFIG control with back-to-back converters in the rotor circuit.

In this chapter we will try to contribute in the MPPT topic by improving some of the previous methods by using the artificial intelligence techniques.

3.2. Maximum Power Point Tracking Algorithms

In order to get the optimum operating point of the WTS, using a MPPT scheme in the control system is essential [7]. When the wind speed doesn't reach its rated value, the output power cannot reach its rated value, so, capturing the maximum available power from the wind kinetic power becomes the main control task for the under rated wind speed conditions. It is possible to control the DFIG torque so that the rotational speed can be varied with the wind speed in such a way that the maximum efficiency coefficient as well as a maximum output power can be obtained [8]. Many papers have been written on this topic on the literature, it can be classified into five groups [9]:

- The lookup table based (OT, PSF, TSR)
- The state space linearization and nonlinear state space based
- The neural network-fuzzy logic based
- The hill climbing based (HCS or P&O)
- The modified or hybrid HCS/lookup table techniques

3.2.1. Optimal Torque Algorithm

Maybe the lookup table based is the most widely used MPPT method, it need either a pre-programmed 2D lookup table using stored data of optimum generator speed and the corresponding maximum power (or maximum torque) at different wind speeds; or a cubic (or a quadratic) mapping function to offer reference signal for optimum WT power or torque at any operation speed. Therefore they need a generator speed sensor or observer [10].

If the rotor is running at the optimal TSR and the maximum efficiency coefficient, thus, by replacing $\lambda = \lambda_{opt}$ and $C_p = C_{p\max}$ into Equation (2.9), the following expression is obtained:

$$P_{m_max} = \frac{1}{2} \rho \pi R^5 \frac{C_{p\max}}{\lambda_{opt}^3} \omega_t^3 \quad (3.01)$$

If we neglect the gearbox mechanical losses ($P_{loss,GB}$) and neglect the generator friction losses, the following relation can be considered in the steady state: $P_m = T_t \omega_t = T_{hss} \omega_m$ & $\omega_m = N_g \omega_t$

The high-speed shaft output torque (T_{hss}) extracted from the wind that in turn drives the generator is given by:

$$T_{hss_opt} = \frac{1}{2} \rho \pi R^5 \frac{C_{p\max}}{\lambda_{opt}^3} \omega_t^3 \left(\frac{1}{\omega_m} \right) = \frac{1}{2} \rho \pi R^5 \frac{C_{p\max}}{\lambda_{opt}^3 N_g^3} \omega_m^2 = K_{opt} \cdot \omega_m^2 \quad (3.02)$$

In the optimal torque (OT) control based method, the analytical expression of the OT curve represented by Equation (3.02) is given as a reference torque (T_{em}^*) for the controller that is connected to the WT (Figure 3.3). In general, this method is simple, and efficient.

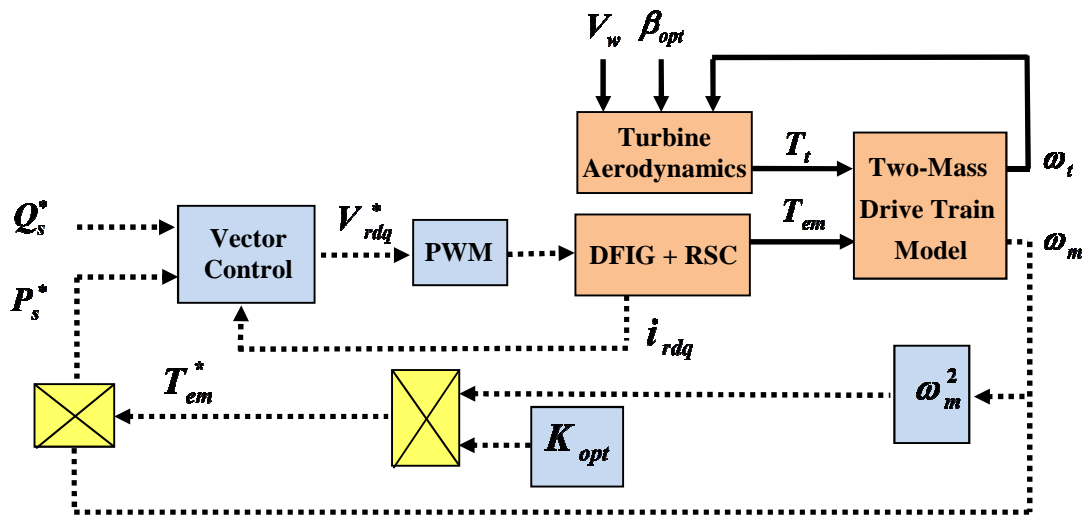
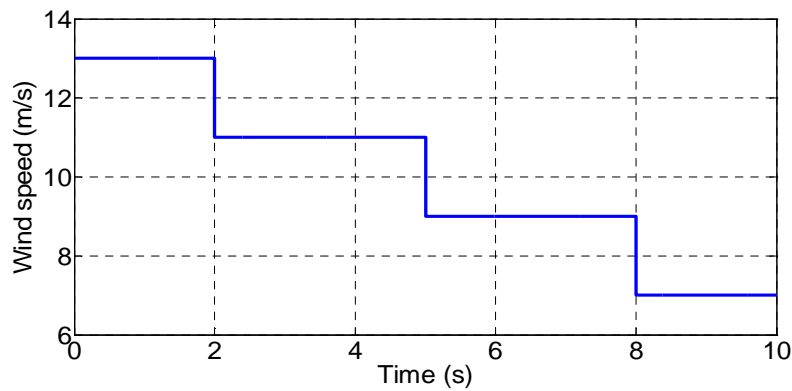


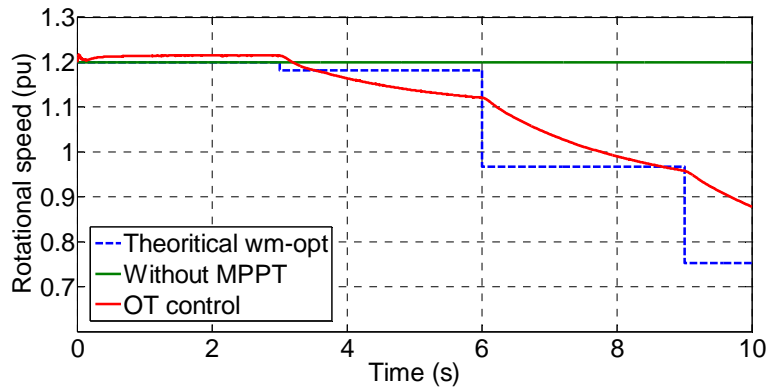
Figure 3.3 Block diagram of OT control based MPPT method [7].

• **Simulation Results :**

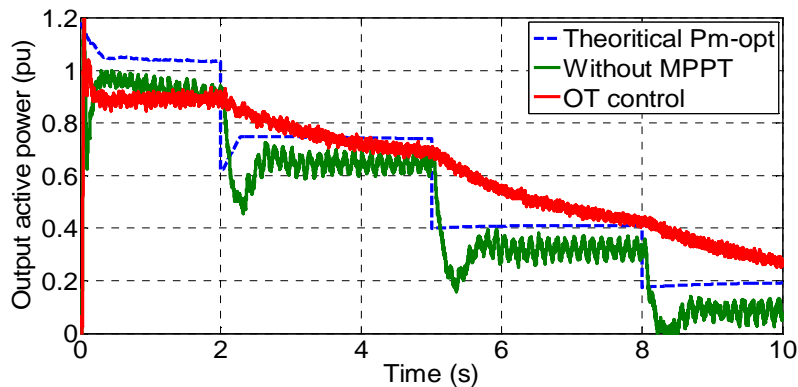
The simulation goal is to apply a moderate wind speed to examine the dynamic response of the WPGS with and without the MPPT algorithm. The wind speed profile is chosen in order to get a VSOM of the DFIG which is between the 0.7 and 1.2pu. Simulation results are presented in Figure 3.4. Also in this chapter, *the simulations have been carried out using the Matlab/SimPowerSystems with motor convention on the rotor side and generator convention on the stator side*, the parameters of the DFIG-WTS are cited in the appendix as Table A.1. A correct initialization of the simulation model is essential in this case, since transients at the beginning of simulation can lead to numerical instabilities.



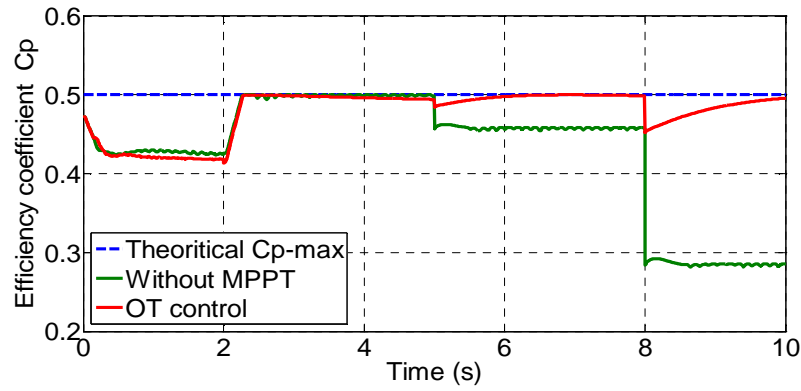
(a) Wind speed profile employed



(b) Measured rotational speed.



(c) Measured output stator active power



(d) Power efficiency coefficient

Figure 3.4 Dynamic responses of WPGS in the VSOM with and without MPPT algorithm.

- **Discussion:**

Figure 3.4a shows a stepped wind speed profile, Figure 3.4b shows the rotational speed response with and without using MPPT algorithm. Without using MPPT, the rotational speed has been fixed in the rated speed, however the OT control changes the rotational speed of the system according to the optimal operation point, but its dynamic is slow. Figure 3.4c shows the output active power of the WPGS, by using a MPPT algorithm, the generated power is always superior then in case without using a MPPT algorithm, Figure 3.4d shows the power efficiency coefficient which confirms the last conclusion. The OT control seems suitable but its dynamic is low because it does not use directly the wind speed data, meaning that wind changes are not reflected instantaneously and significantly on the reference signal [9].

3.2.2. Power Signal Feedback Algorithm

The most common method is the power signal feedback (PSF) method [14-15] it usually uses either a 2D lookup table obtained theoretically with the MPC or a plotting function using the product of the cube of measured rotational speed with the proportionality constant. The data points for MPC and the corresponding rotational speed could be obtained experimentally from the experimental results, and then recorded in a 2D lookup table [16-17]. Because experimental data is needed in this MPPT method, so we pass it. The block diagram of a WTS with PSF control is shown in Figure 3.5.

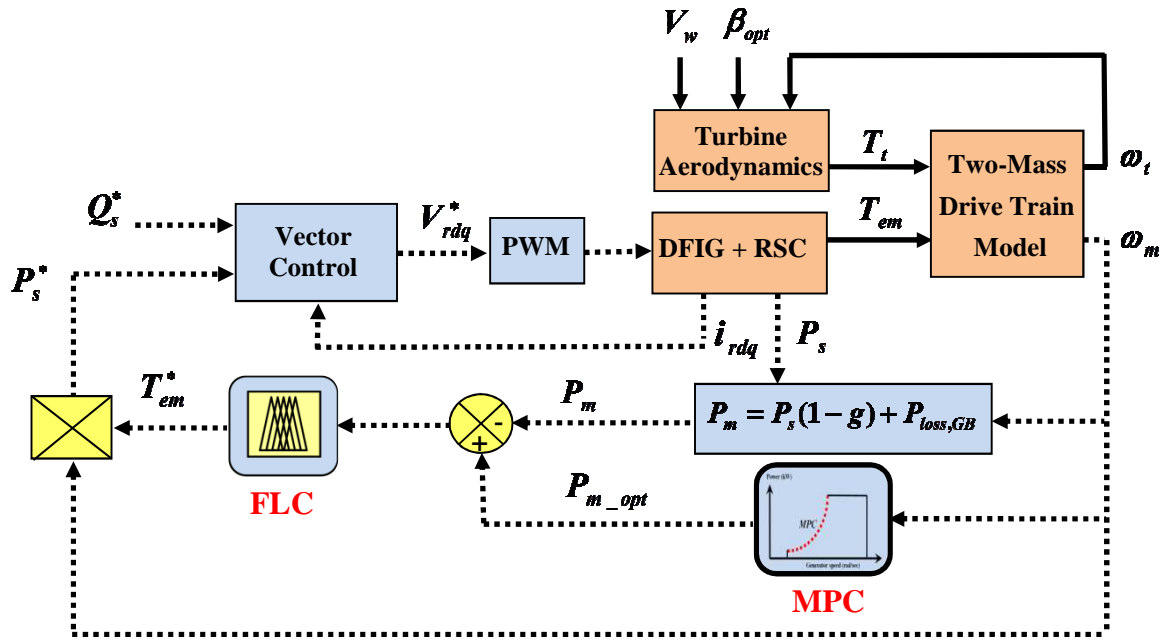


Figure 3.5 Block diagram of PSF control based MPPT method [7].

3.2.3. Optimum TSR Algorithm

The optimal TSR point for a given WT is constant regardless of wind speed. If TSR remains constantly at the optimal value, it is guaranteed that the extracted energy will be maximized. Therefore, this method seeks to force the WTS to remain at this point by comparing it with the actual value and feeding this difference to a controller. That, in turn, changes the speed of the generator to reduce this error. The optimal point of the TSR can be determined experimentally or theoretically and stored as a reference. Although this method seems simple as wind speed is directly and continuously measured, a precise measurement for wind speed is impossible in reality and increases the cost of the system [9-18-19].

We can use a rotational speed control loop to track the optimal TSR, the optimal rotational speed which will be taken as reference is given by:

$$\omega_{m_opt} = N_g \cdot \omega_{t_opt} = N_g \cdot \frac{\lambda_{opt} V_w}{R} \tag{3.03}$$

From the plot shown in Figure 2.7, it can be stated that the optimal point for VSOM of this WTS is: $\beta=0^\circ$ and $\lambda_{opt}=10$ and $C_{pmax}=0.5$.

A. TSR Algorithm using PI or FLC as Rotational Speed Controller

The block diagram of the TSR control method is shown in Figure 3.6. The FLC that used in the rotational speed control loop to replace the PI controller is presented in Figure 3.7 [20].

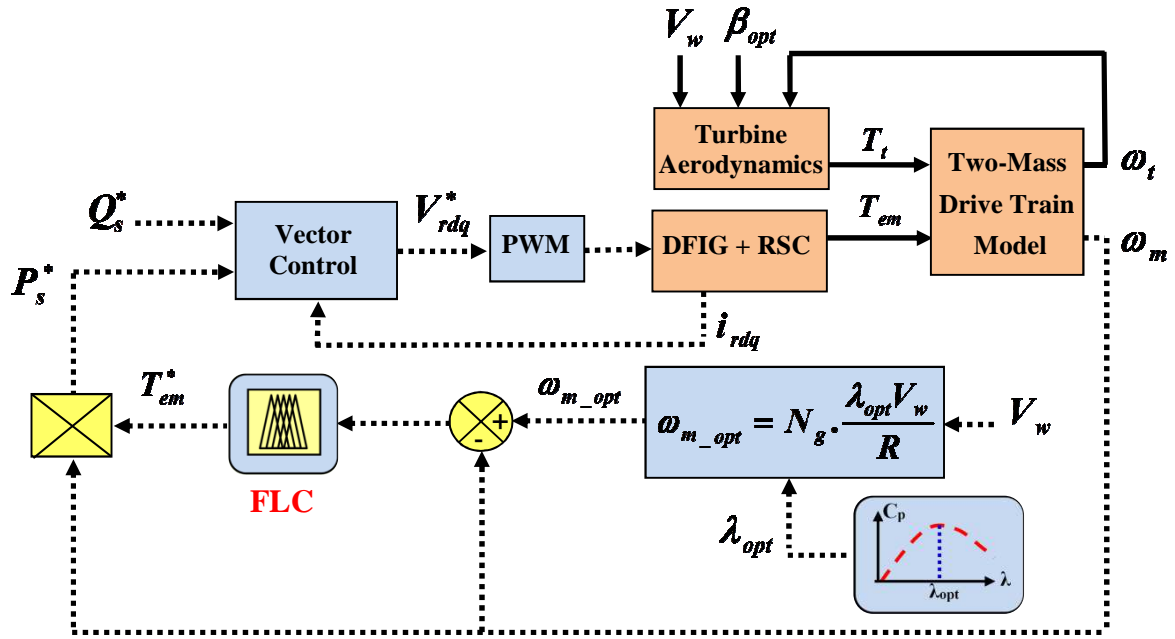


Figure 3.6 Block diagram of the TSR based MPPT control system [7].

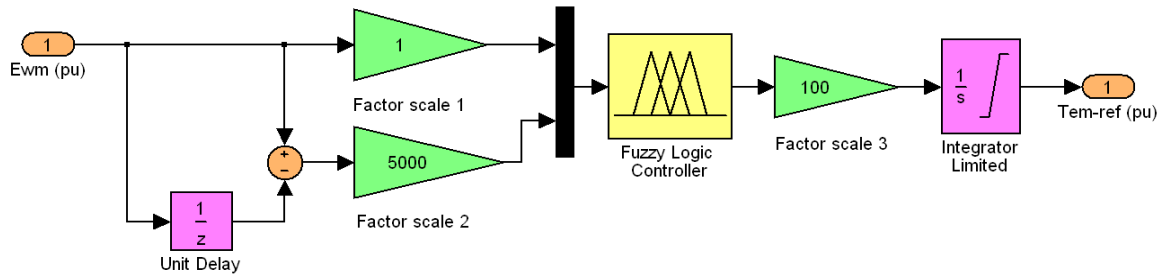


Figure 3.7 FLC structure of the rotational speed control loop.

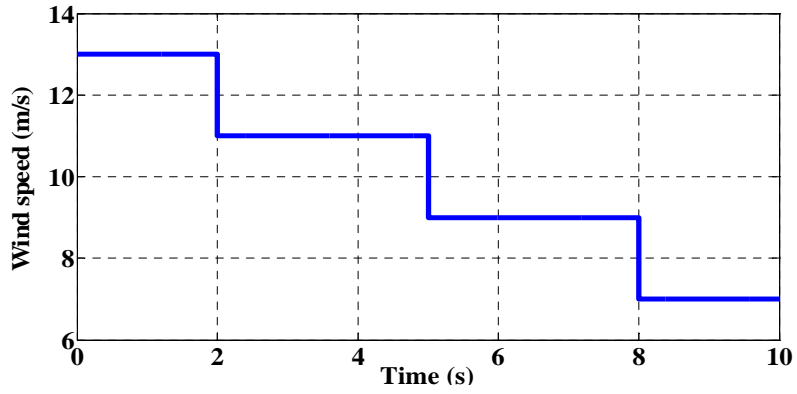
Table 3.1 illustrates the fuzzy inference rules of the rotor speed controller

Table 3.1: Rule table for the fuzzy logic rotor speed controller

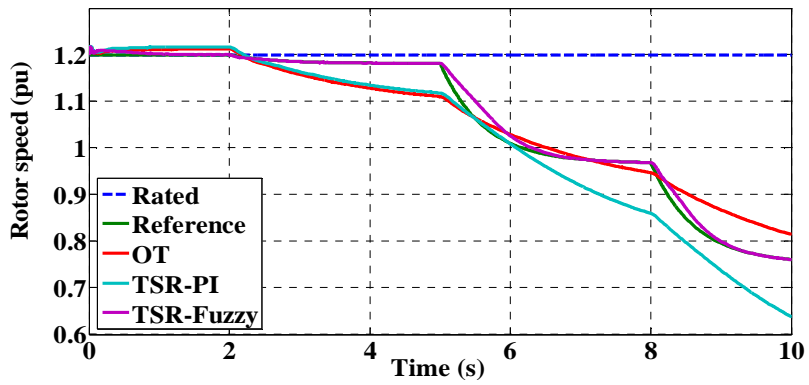
Δe (pu) \ e (pu)	NB	NM	NS	Z	PS	PM	PB
NB	NB	NB	NB	NB	NM	NS	Z
NM	NB	NB	NB	NM	NS	Z	PS
NS	NB	NB	NM	NS	Z	PS	PM
Z	NB	NM	NS	Z	PS	PM	PB
PS	NM	NS	Z	PS	PM	PB	PB
PM	NS	Z	PS	PM	PB	PB	PB
PB	Z	PS	PM	PB	PB	PB	PB

• **Simulation Results :**

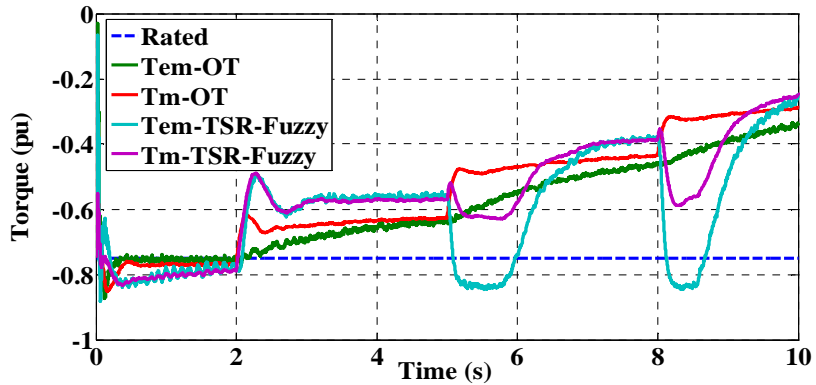
The same previous simulation test is used under the same operating conditions and WT characteristics, the goal is to compare the PI controller and the FLC dynamic responses in the rotational speed control loop and VSOM. The simulation results are presented in Figure 3.8.



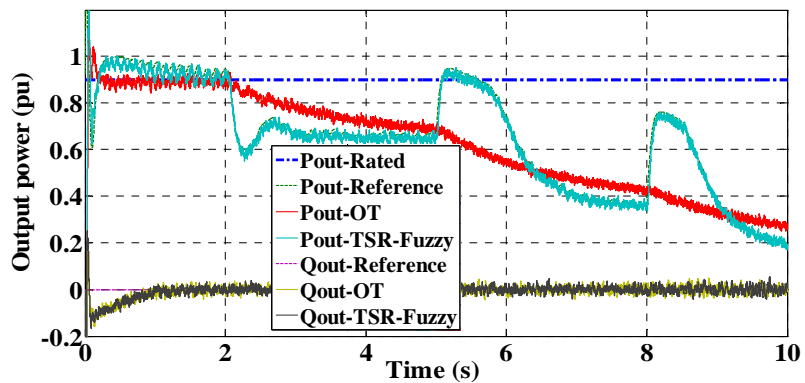
(a) Wind speed profile employed.



(b) Measured rotational speed.



(c) Electromagnetic and mechanical torques in the high speed shaft.



(d) Measured output stator active and reactive power.

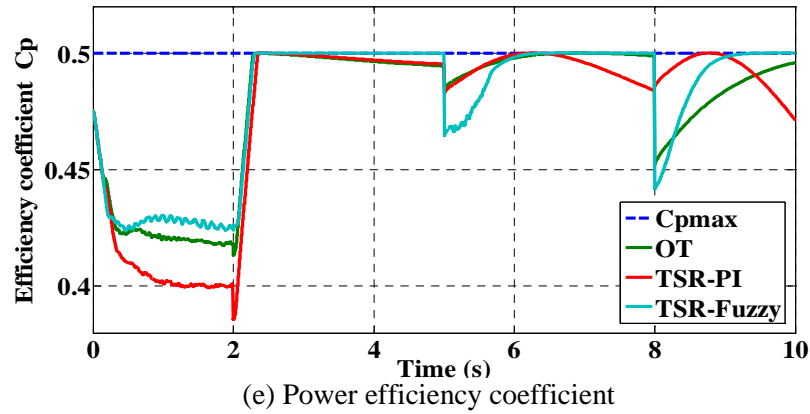


Figure 3.8 Dynamic responses of WPGS in the VSOM using TSR-FLC algorithm [20].

- **Discussion:**

Wind speed decreases in steps from 13m/s into 7m/s as presented in Figure 3.8a. Rotational speed is following wind speed variation with significant time delay as presented in Figure 3.8b, this because of the large turbine inertia, the main difference is in the high wind speed between 0 and 2sec where the pitch system was activated to avoid any overload, and the rotational speed was maintained at its maximum (1.2pu). TSR-fuzzy control is faster and more efficient than the OT and the TSR-PI control because it's directly deal with the wind speed signal by using an intelligent reasoning language. Moreover, the rotational speed passed on the synchronous point at the 6sec, this means that the operating mode was in the super-synchronous mode and became in the sub-synchronous mode, and this shows the advantages and the superiority of the DFIG in the variable speed WTS.

Figure 3.8c illustrates the dynamic response of torques in the turbine HSS, the T_m is inversed in order to compare it with the T_{em} . In the OT strategy, T_{em} and the T_m are reacting slowly by means of the sudden variation of wind speed. However, on the TSR-Fuzzy strategy, T_{em} and the T_m are reacting quickly because of the rotational speed control loop, which makes the T_{em} bigger than the T_m in order to reduce the rotational speed and maximize the efficiency coefficient according to the optimal TSR like in the 5sec and 8sec. TSR-PI strategy is not presented because of the space, but it's quicker than the OT and slower than the TSR-Fuzzy strategy.

Figure 3.8d shows the output stator active and reactive power of the DFIG. Active power in the TSR control follows its reference that brought from the rotational speed control loop, it depends on the turbine aerodynamic power, and the reactive power follows its reference which kept at zero. The TSR-Fuzzy strategy has a faster dynamic, and the measured power follows its reference exactly. However, in the OT control, there is no active power control loop, the active power follows the slow dynamic of the turbine optimal torque. Another remark in the 5sec and the 8sec, there is a rise in the active power, this because of the rapid dynamic of the TSR-Fuzzy control system, in order to

decrease the Rotational speed quickly, the mechanical power of the shaft was converted into electrical power, and the contrary will happen if there is an increase in the wind speed.

Figure 3.8e shows the efficiency coefficient, it is maintained at its maximum after the 2sec, this means that the MPPT algorithm is working perfectly for all the studied MPPT techniques, here also the TSR-fuzzy control is faster and more effective than the OT and TSR-PI based speed control.

B. Sensorless TSR based MPPT Algorithm using a FLC

TSR is the fastest MPPT technique because it uses directly the wind speed signal to compute the optimal Rotational speed of the WT, However, the significant wind speed variations at different points over the blades swept area makes difficult any direct measurement of effective wind speed, our objective is to increase the system's reliability by reducing the cost of both equipment and maintenance by means of a rotor speed observer, and wind speed estimator [10].

• Rotational Speed Estimation

The proposed MRAS (Model Reference Adaptive System) observer consists of using an adaptive model and a reference model in the closed loop scheme. A FLC is used in order to reduce the error between the two models. Figure 3.9 shows the overall scheme of the generator rotor position and speed estimation of the proposed method. From Equations (3.15) and (3.16), the q component of the rotor voltage and the d-axis rotor current can be expressed respectively as [21]:

$$V_{rq} = R_r i_{rq} + L_r \frac{di_{rq}}{dt} + L_m \frac{di_{sq}}{dt} + \omega_r (L_r i_{rd} + L_m i_{sd}) \quad (3.04)$$

From Equation (2.45), the q component of the rotor current can be expressed as a function of the q component of the q-axis stator current as follow:

$$i_{rq} = -\frac{L_s}{L_m} i_{sq} \quad (3.05)$$

From Equation (2.46), (2.04) and (2.05), the estimated q-axis component of the rotor voltage used in the adaptive model can be written as:

$$V_{rq_est} = -\frac{R_r L_s}{L_m} i_{sq} + (L_m - \frac{L_s L_r}{L_m}) \frac{di_{sq}}{dt} + \omega_{r_est} (\frac{L_r}{L_m} \Phi_{sd} + (L_m - \frac{L_s L_r}{L_m}) i_{sd}) \quad (3.06)$$

The FLC is used to reduce the error between the real and the adaptive models. After estimating the rotor electrical angular velocity, the rotational speed of DFIG is estimated using the synchronous frequency throughout a PLL. The FLC includes four parts [22]: fuzzification, fuzzy rule base, inference engine and defuzzification. There are two input signals to the FLC: the speed's error e and the change of the error Δe . These two inputs are converted by scaling factors as presented in Figure 3.10. To obtain the output, the defuzzification used is based on the center of gravity method, and the triangular MFs are used for the inputs and for the output.

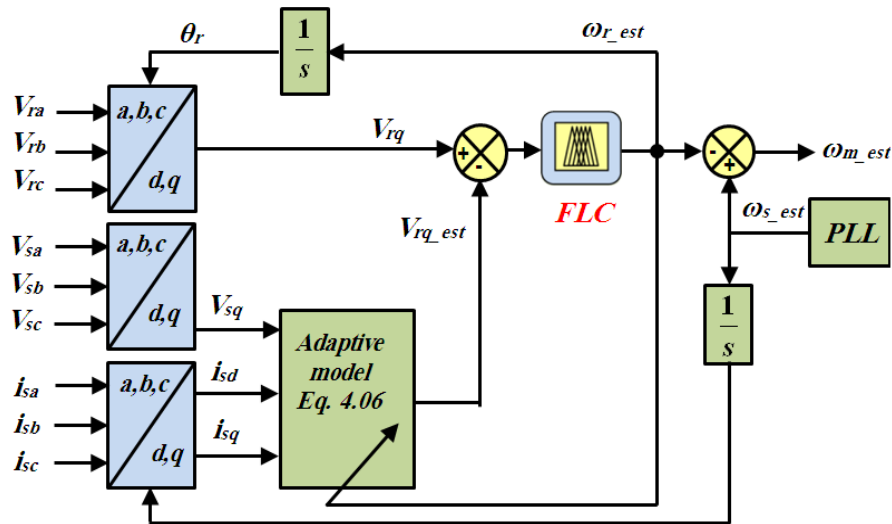


Figure 3.9 Schematic blocks of the MRAS based DFIG rotor speed observer [21].

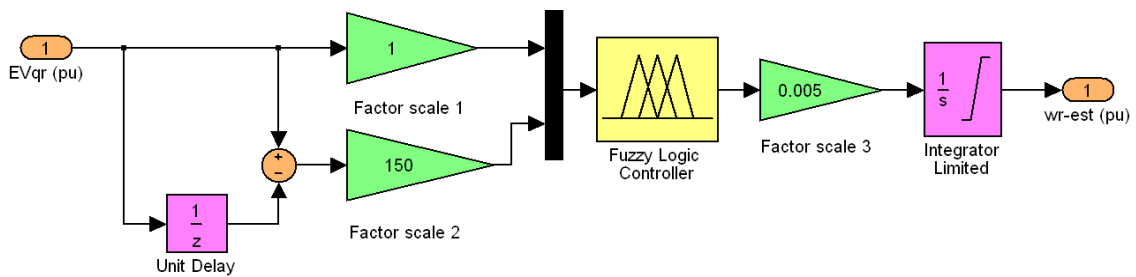


Figure 3.10 Structure of FLC for rotational speed MRAS observer [10].

Table 3.2 illustrates the fuzzy inference rules of the rotor speed estimator. In order to improve the performance of the FLC, an empirical analysis is used to set parameters of the MFs. Figure 3.11 shows the MFs for the inputs and output variables.

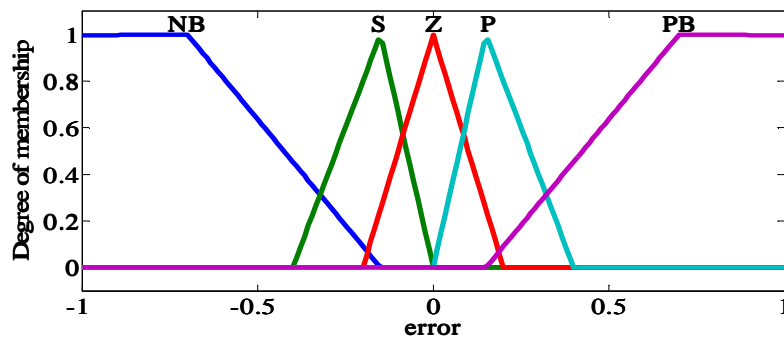
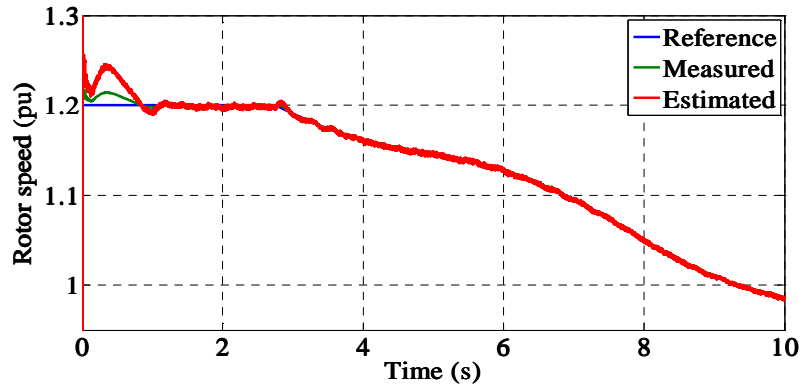


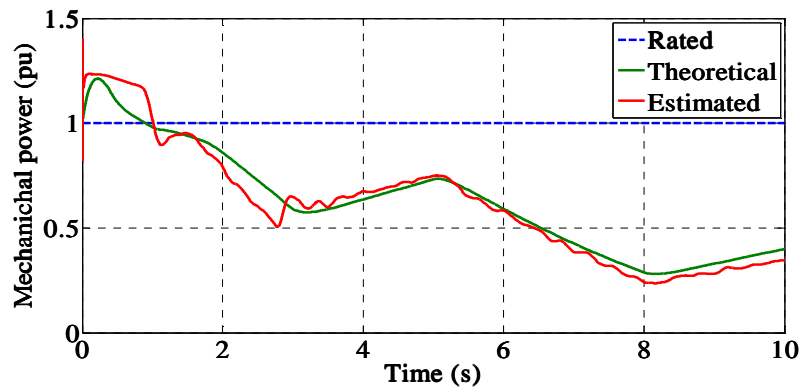
Figure 3.11 Inputs and output MFs of the FLC based MRAS observer.

Table 3.2: Rules table of the FLC used for rotor speed estimator

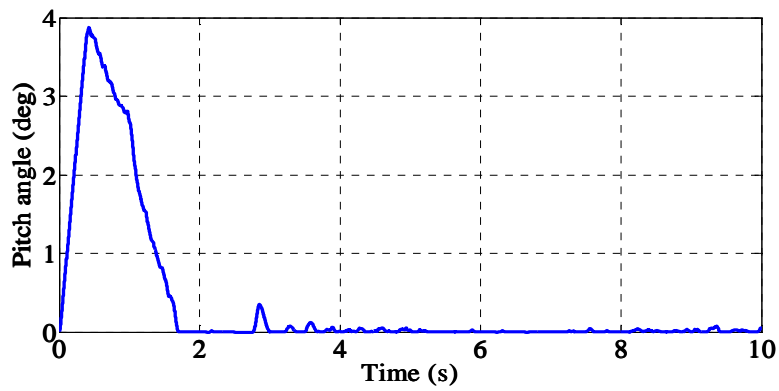
Output		$\Delta e(pu)$				
		BN	N	Z	P	BP
$e(pu)$	BN	BN	Z	BN	Z	Z
	N	Z	Z	N	Z	Z
	Z	BN	N	Z	P	BP
	P	Z	Z	P	P	Z
	BP	Z	Z	BP	Z	BP



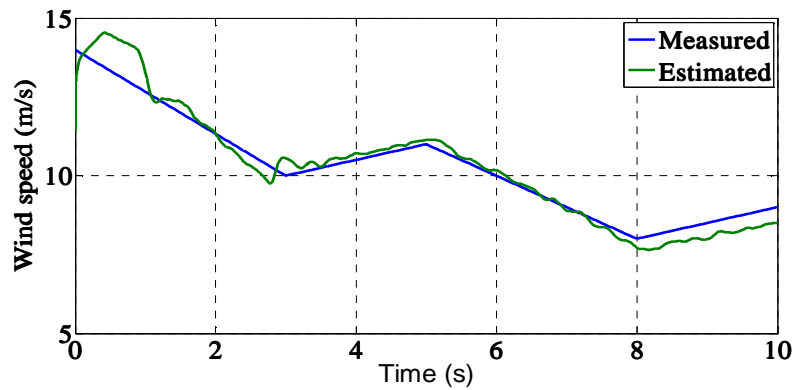
(a) Estimated and measured rotational speed



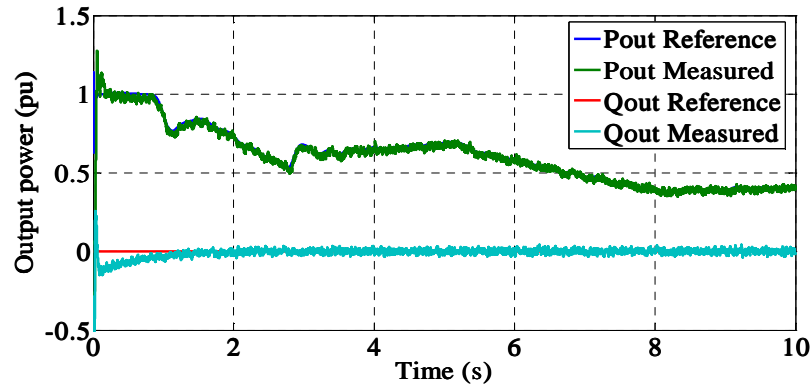
(b) Mechanical power of the wind turbine



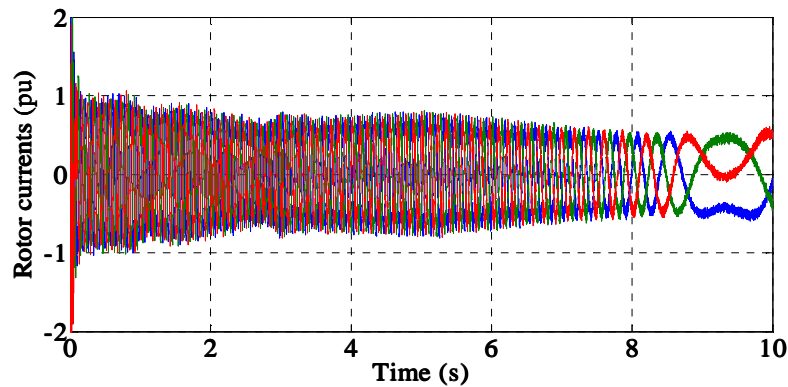
(c) Measured pitch angle



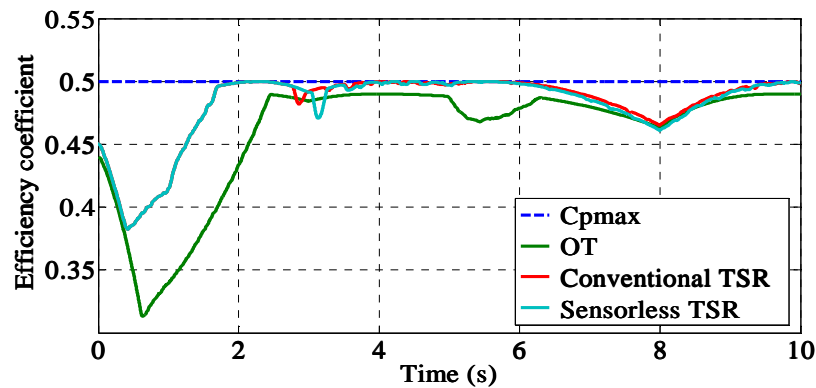
(d) Estimated and measured wind speed



(e) Measured stator output active and reactive power



(f) Rotor windings currents



(g) Power efficiency coefficient

Figure 3.13 Dynamic responses of WTS in the VSOM using sensorless TSR algorithm [10].

- **Discussion:**

Figure 3.13a shows the rotational speed response, the performance the MRAS observer based rotational speed estimator is represented, where the tracking error is less than $\pm 2\%$. Figure 3.13b shows the theoretical and the estimated mechanical power of the WT according to the rated power which is 1 pu or 1.5/0.9 MW, the theoretical mechanical power instantaneously affected by the wind speed variation as denoted in Equation (3.05), but the estimated mechanical power suffers from the large WT inertia which gives slower dynamic response, but we can say that they are nearly similar. Figure 3.13c shows the pitch angle response, the power limitation system has been activated between

0 and 1.5sec, this because of the mechanical overload and after the 1.5sec pitch angle returned to 0 in order to allow the VSOM. Figure 3.13d shows the measured and the estimated wind speed, the tracking error is less than $\pm 6\%$.

Figure 3.13e shows the measured output active and reactive power of the DFIG, the measured powers track their references precisely, between the 0 and 1.5sec the system is in the rated power operating mode, because the output power and the rotor speed are limited to their rated values, after the 1.5sec the wind speed decreased and the system returned to the MPPT operating mode below the rated power.

Figure 3.13f shows the rotor's currents, they vary in magnitude and pulsation according to the operation mode. In the rated power operating mode, the system is in the super-synchronous mode ($\omega_r = -0.2\text{pu}$), in the MPPT mode the rotor pulsation continue to increase until the synchronous point at 9.3sec which became 0, after that the system become in the sub-synchronous operation mode and the rotor pulsation became positive.

Figure 3.13g shows the efficiency coefficient response, the sensorless TSR algorithm keeps its fast response in the transient phase, and its high efficiency and stability in the steady-state phase. Compared to the conventional TSR algorithm, the sensorless TSR algorithm keeps the whole distinguished characteristics of the conventional TSR control, so this leads to a decrease in both cost and maintenance of the overall control system.

3.2.4. Maximum Power Curve Searching Algorithm

Maximum power curve searching (MPCS) method bases on the MPC characteristic of the WTGS, only the mechanical losses in the gearbox are considered. A FLC with its adaptive reasoning is applied to unsure the convergence of the proposed method through variable output step-size signal until the error becomes zero. If the operating point is to the left of the peak point after changing in the wind speed (point A), the controller must move it to the right to be closer to the peak until it gets to the zero error (point B), and vice versa if it is on the other side as shown in Figure 3.14 [24].

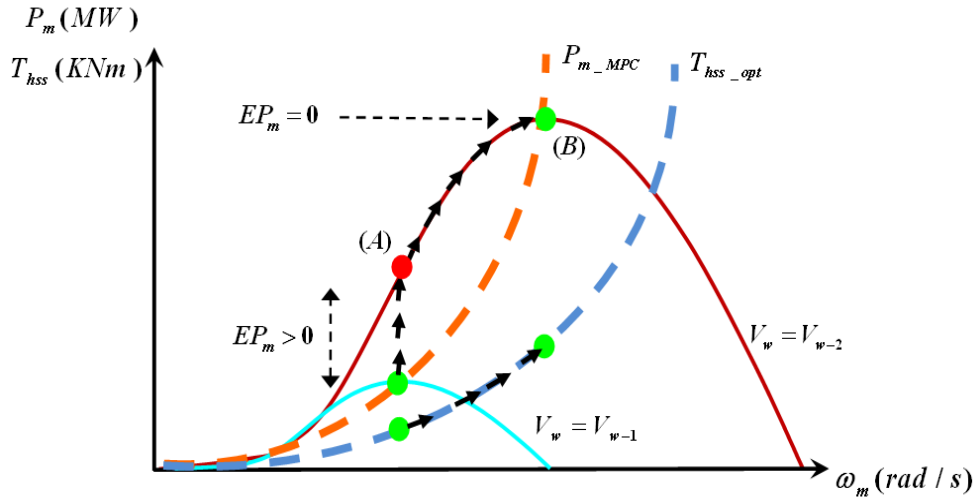


Figure 3.14 Working principle of MPC approach [24].

The general structure of the FLC is shown in Figure 3.15 , the measured rotational speed and stator power will be used as inputs to the MPPT system, the error in estimated mechanical power and its change (EP_m and ΔEP_m) are used as inputs to the FLC, the output is the change on the electromagnetic torque of reference (ΔT_{em}^*). MFs and the surface created by the FLC are shown in Figure 3.16. Triangular symmetrical MFs are suitable for the inputs and output, which give more sensitivity especially as variables approach to zero. Table 3.3 gives the corresponding rules of this Fuzzy-MPCS controller. The FLC is efficient to track the maximum power point, especially in case of frequently changing wind conditions [25]. The overall block diagram of the MPPT control is shown in Figure 3.17. We assume the power converters and the machine windings are lossless and by taking into account the losses in the gearbox and Equations (2.27), the mechanical power is obtained by this relation:

$$P_m = T_{em} \omega_m + P_{loss,GB} = P_s + P_r + P_{loss,GB} = (1 - s)P_s + P_{loss,GB} \tag{3.09}$$

According to the Equations (2.05), if the rotor is running at the optimal TSR, it will also run at the maximum efficiency coefficient. Thus, the MPC expression is obtained:

$$P_{m_MPC} = \frac{1}{2} \rho \pi R^5 \frac{C_{p\max}}{\lambda_{opt}^3} \omega_m^3 = K_{opt} \omega_m^3 \tag{3.10}$$

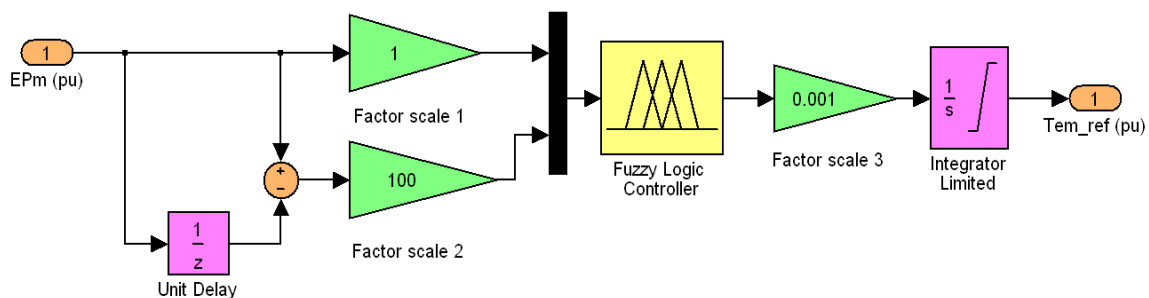
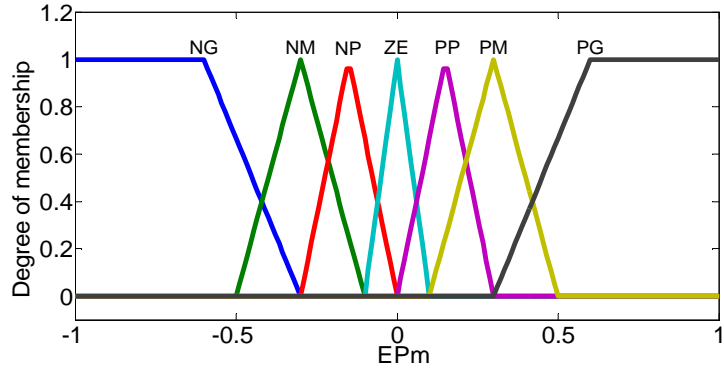
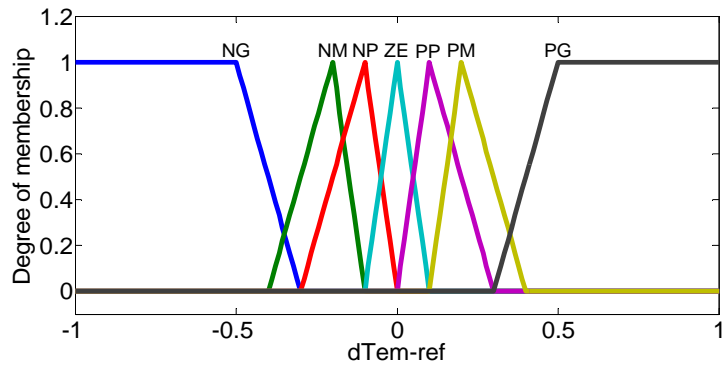


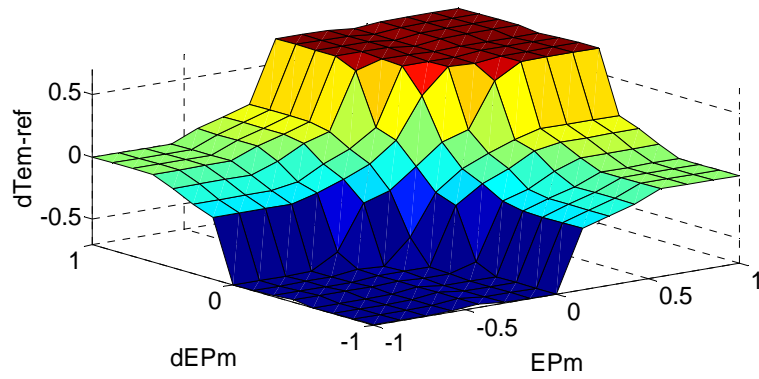
Figure 3.15 Structure of the FLC used for the mechanical power control loop [24].



(a) Input MFs used for EP_m and ΔEP_m



(c) Output MFs used for ΔT_{em-ref}



(d) Surface created by the FLC

Figure 3.16 Membership functions of Fuzzy-MPCS controller [24].

Table 3.3: Rule table of the Fuzzy-MPCS controller

$\Delta EP_m(pu)$	$EP_m(pu)$	<i>NB</i>	<i>NM</i>	<i>NS</i>	<i>Z</i>	<i>PS</i>	<i>PM</i>	<i>PB</i>
<i>NB</i>		<i>NB</i>	<i>NB</i>	<i>NB</i>	<i>NB</i>	<i>NM</i>	<i>NS</i>	<i>Z</i>
<i>NM</i>		<i>NB</i>	<i>NB</i>	<i>NB</i>	<i>NM</i>	<i>NS</i>	<i>Z</i>	<i>PS</i>
<i>NS</i>		<i>NB</i>	<i>NB</i>	<i>NM</i>	<i>NS</i>	<i>Z</i>	<i>PS</i>	<i>PM</i>
<i>Z</i>		<i>NB</i>	<i>NM</i>	<i>NS</i>	<i>Z</i>	<i>PS</i>	<i>PM</i>	<i>PB</i>
<i>PS</i>		<i>NM</i>	<i>NS</i>	<i>Z</i>	<i>PS</i>	<i>PM</i>	<i>PB</i>	<i>PB</i>
<i>PM</i>		<i>NS</i>	<i>Z</i>	<i>PS</i>	<i>PM</i>	<i>PB</i>	<i>PB</i>	<i>PB</i>
<i>PB</i>		<i>Z</i>	<i>PS</i>	<i>PM</i>	<i>PB</i>	<i>PB</i>	<i>PB</i>	<i>PB</i>

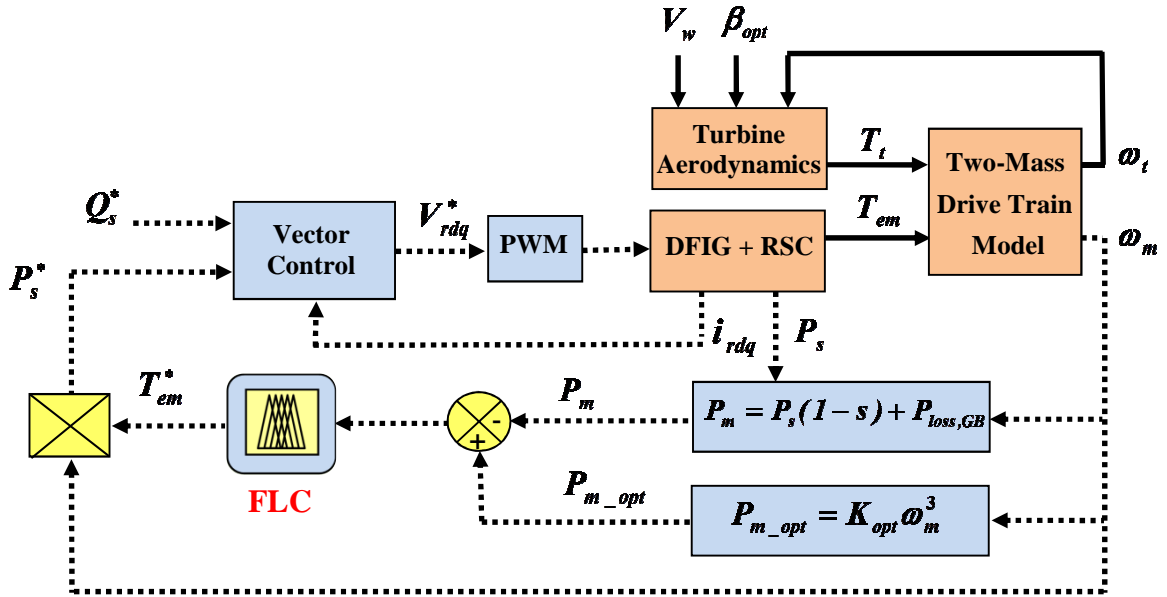
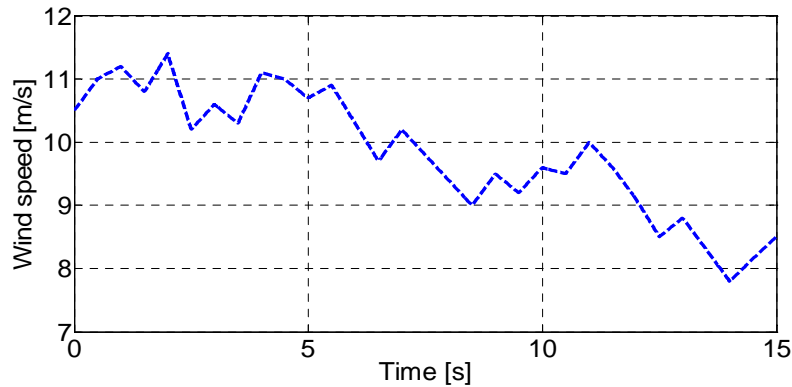


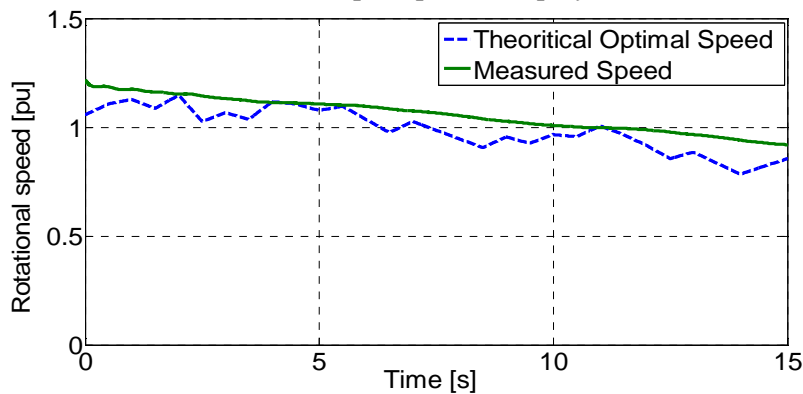
Figure 3.17 Block diagram of the MPC based MPPT control system [24].

• Simulation Results

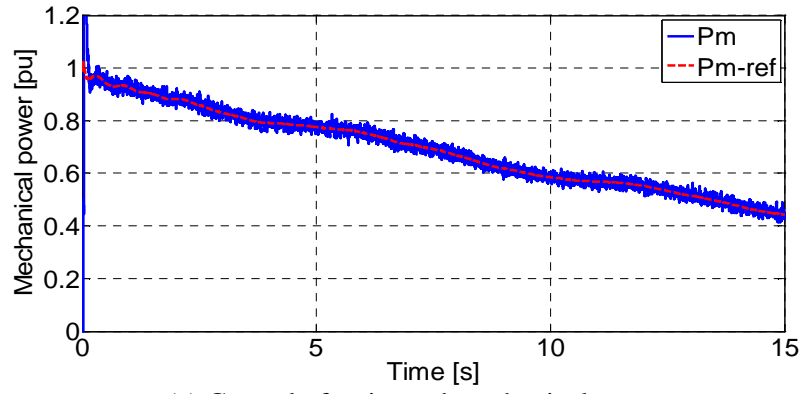
Simulation objective is to apply a random wind speed profile to emulate normal wind turbulence, the wind speed profile is chosen to cover the whole VSOM which is between 0.7 and 1.2pu. The simulation results are presented in Figure 3.18 and Figure 3.19.



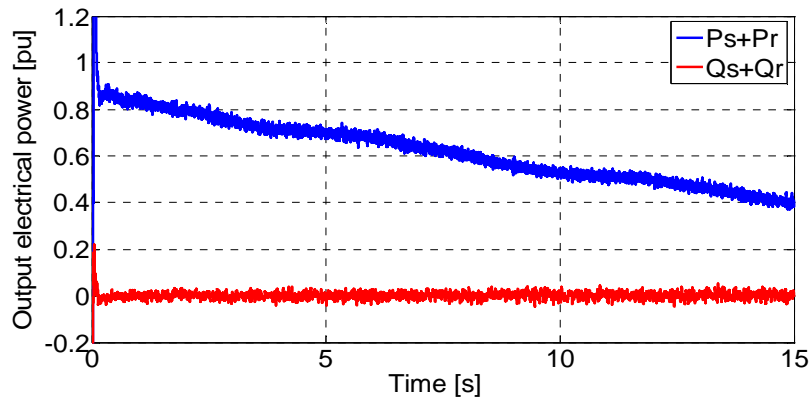
(a) Wind speed profile employed.



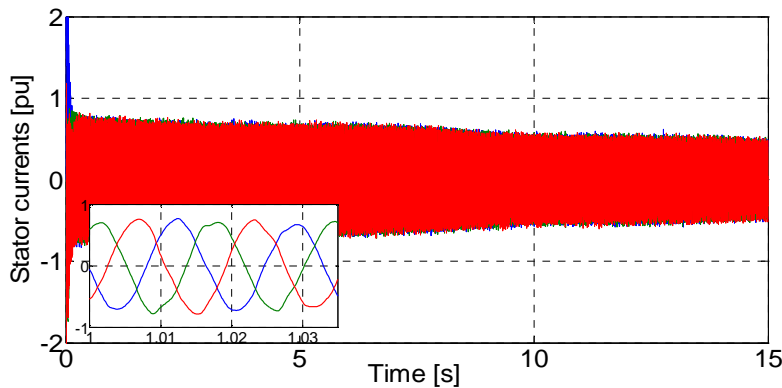
(b) Measured rotational speed.



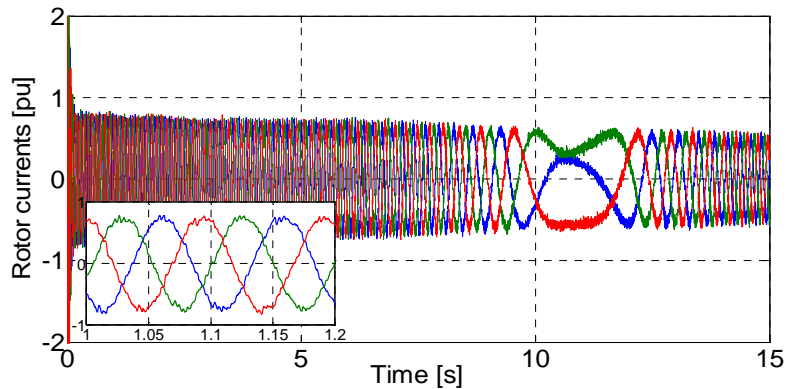
(c) Control of estimated mechanical power.



(d) Measured stator output active and reactive power



(e) Stator *abc* currents.



(f) Rotor *abc* currents.

Figure 3.18 Dynamic responses of the fuzzy-MPCS algorithm in the VSOM.

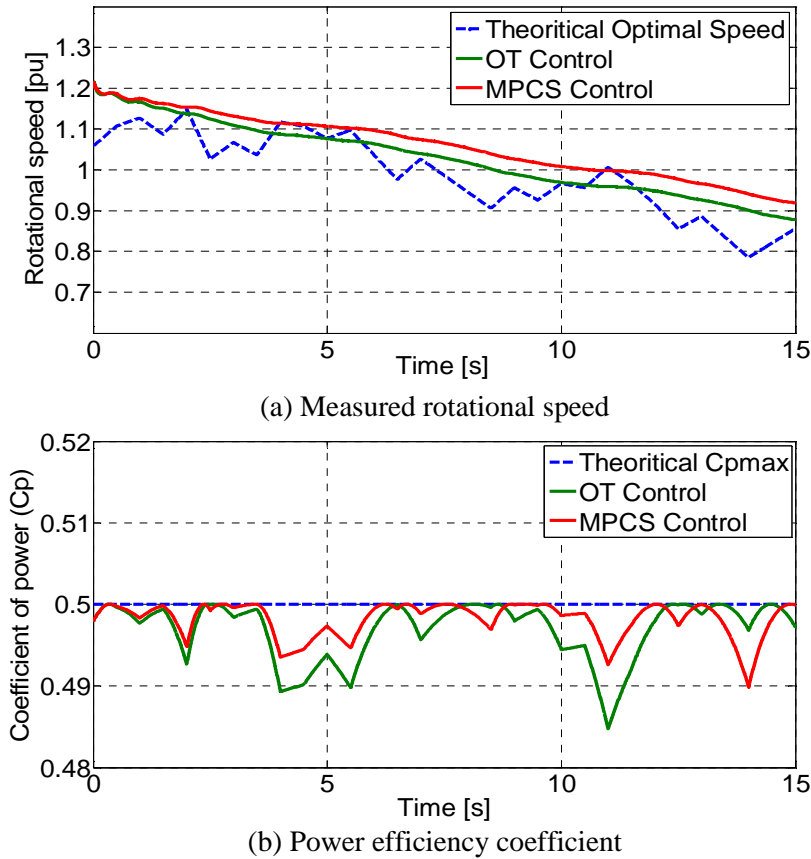


Figure 3.19 Comparison study of dynamic response between OT and MPCS control techniques [24].

- **Discussion:**

Simulation results in Figure 3.18 and 3.19 demonstrated the simplicity and accuracy of the MPCS method. This method obtained the maximum average value of power efficiency coefficient and maintained it at its maximum like in the OT control method even with changes in wind speed. Nevertheless, its dependency on WT characteristics made it inflexible.

3.2.5. *Perturb and observe Algorithm using a FLC*

Perturb and observe (P&O) control or the hill-climb searching (HCS) is a mathematical optimization technique used to search for the local optimum point of a given function. This method is based on perturbing a control variable in small step-size and observing the resulting changes in the target function until the slope becomes zero. If the operating point is to the left of the peak point, the controller must move it to the right to be closer to the peak, and vice versa if it is on the other side [7]. Additionally, choosing an appropriate step-size is not an easy task, though larger step-size means a faster response and more oscillations around the peak point, and hence, less efficiency, a smaller step-size improves efficiency but reduces the convergence speed [26-27-28].

To improve the efficiency and the accuracy of the conventional P&O method, the step-size is automatically updated according to the operating point. If the system is working on a certain point

that is far from the peak, the step-size should be increased to speed up the tracking process. Conversely, the action is reversed to decrease the step-size when the operating point nears the peak, in order to drive the operating point to settle down exactly at the peak point as illustrated in Figure 3.20. This working principle reduces the oscillations that occur in the conventional P&O method, accelerates the speed to reach the maximum, and lowers the time needed for tracking [7].

The employed FLC is shown in Figure 3.21 [29-30], the change in mechanical power and measured Rotational speed are used as inputs (ΔP_m and $\Delta \omega_m$) and the output is the change on rotational speed reference ($\Delta \omega_m^*$).

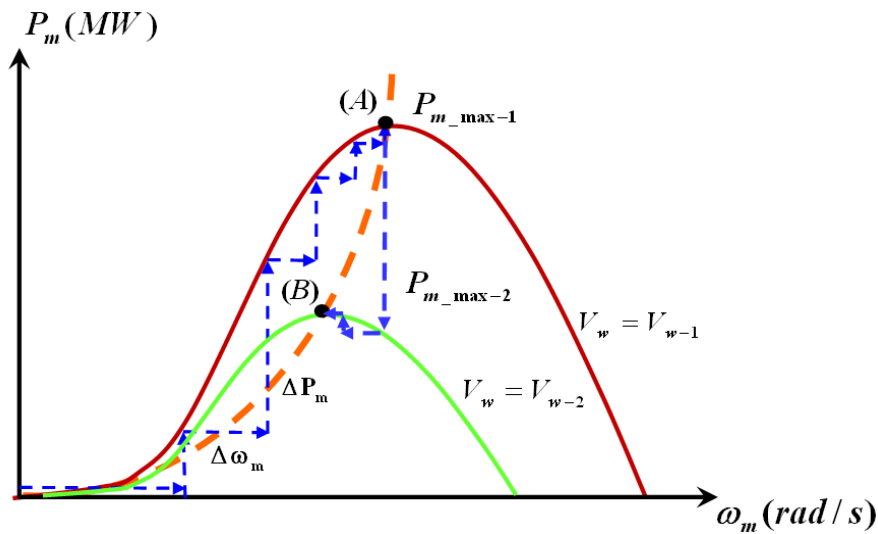


Figure 3.20 Working principle of the adaptive P&O approach [29].

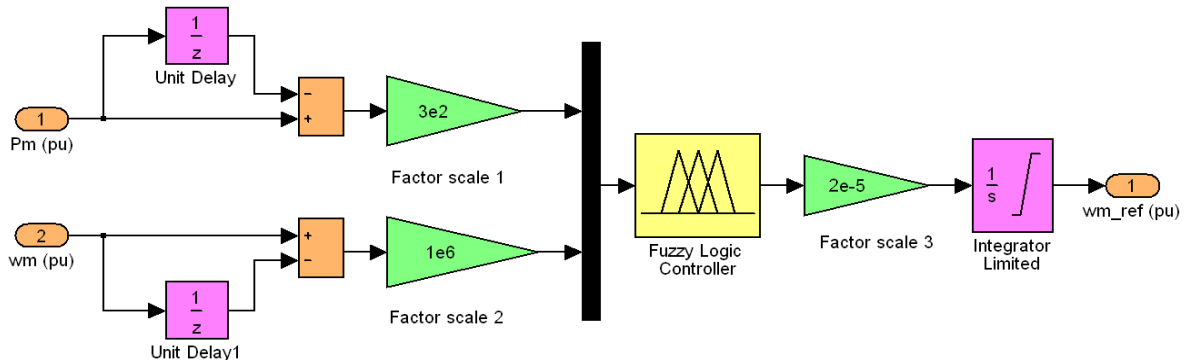


Figure 3.21 Structure of the FLC used for P&O based MPPT algorithm [29].

The role of the FLC is to perturb the reference speed and to observe the corresponding change of output power. If the output power increases with the last speed increment, the searching process continues in the same direction. On the other hand, if the speed increment reduces the output power, the direction of the searching is reversed. FLC is efficient to track the maximum power point, especially in case of frequently changing wind conditions [25]. The overall block diagram of the MPPT control is shown in Figure 3.23 where the Equations (4.01), (4.02) and (4.09) are taken into account to estimate the output power.

MFs and the surface created by the fuzzy controller are shown in Figure 3.22. Because the triangular symmetrical MFs give more sensitivity especially as variables approach to zero, we again use it in the Fuzzy-P&O. Table 3.4 gives the corresponding rule table of this Fuzzy-P&O controller.

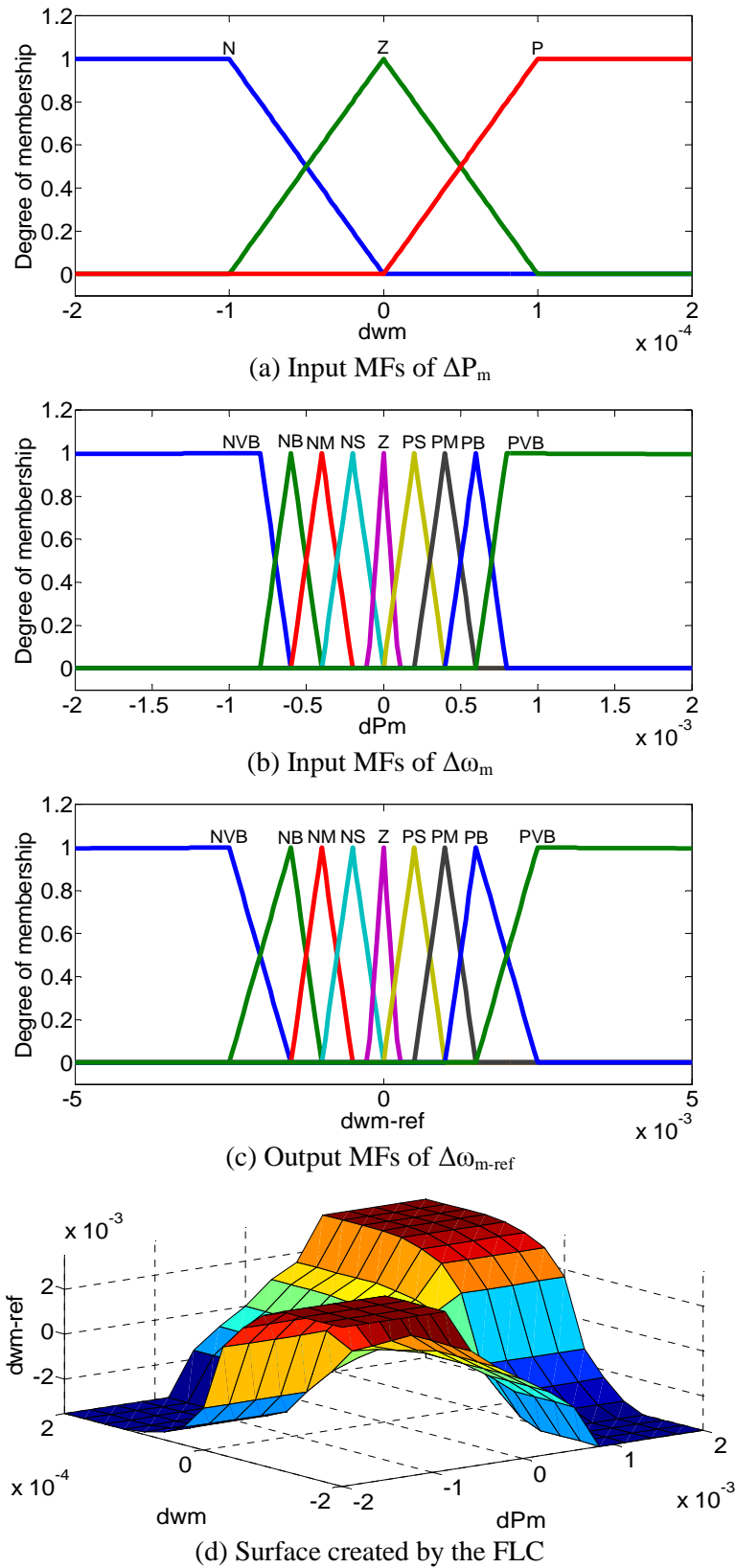


Figure 3.22 Membership functions of Fuzzy-P&O algorithm.

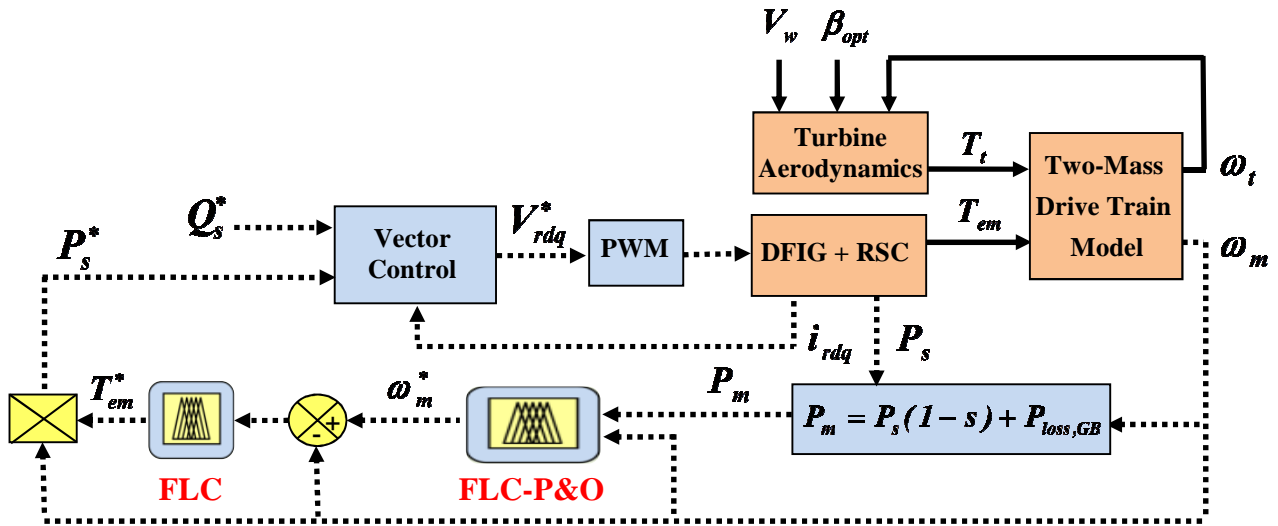


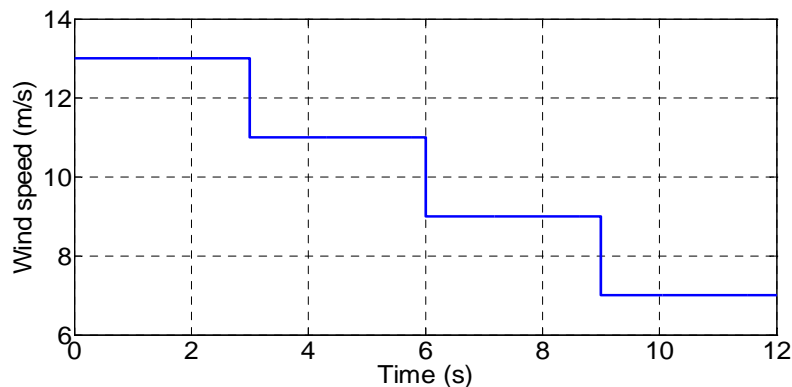
Figure 3.23 Block diagram of P&O based MPPT control system [29].

Table 3.4: Rule table of Fuzzy-P&O controller

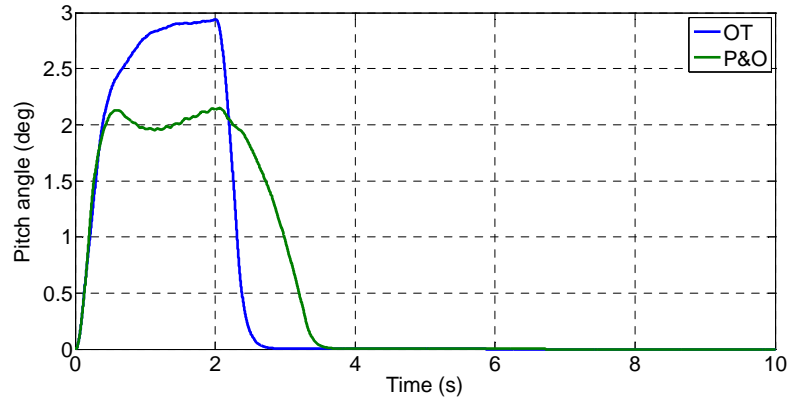
$\Delta\omega_m$	ΔP_m	<i>NVB</i>	<i>NB</i>	<i>NM</i>	<i>NS</i>	<i>Z</i>	<i>PS</i>	<i>PM</i>	<i>PB</i>	<i>PVB</i>
<i>N</i>		<i>PVB</i>	<i>PB</i>	<i>PM</i>	<i>PS</i>	<i>Z</i>	<i>NS</i>	<i>NM</i>	<i>NB</i>	<i>NVB</i>
<i>Z</i>		<i>NB</i>	<i>NM</i>	<i>NS</i>	<i>NS</i>	<i>Z</i>	<i>PS</i>	<i>PM</i>	<i>PM</i>	<i>PB</i>
<i>P</i>		<i>NVB</i>	<i>NB</i>	<i>NM</i>	<i>NS</i>	<i>Z</i>	<i>PM</i>	<i>PM</i>	<i>PB</i>	<i>PVB</i>

• Simulation Results

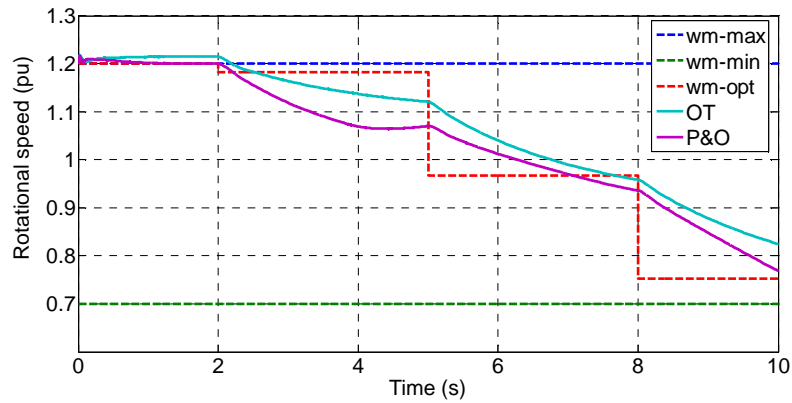
The simulation objective is to apply a stepped wind speed profile to emulate powerful wind turbulence, The wind speed profile is chosen in order to cover the whole VSOM as shown in Figure 3.24.



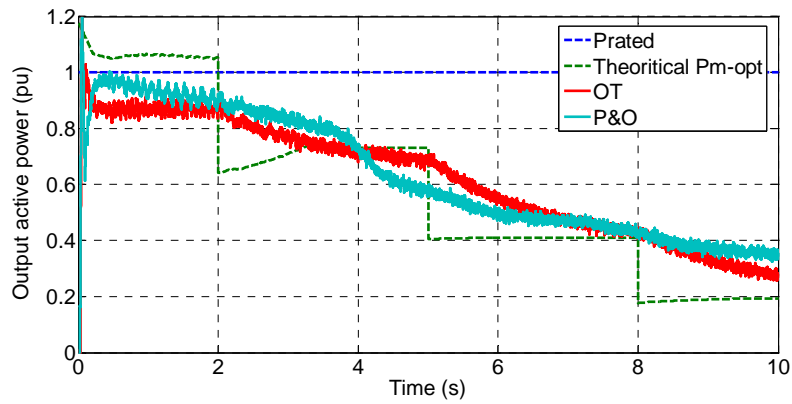
(a) Wind speed profile employed.



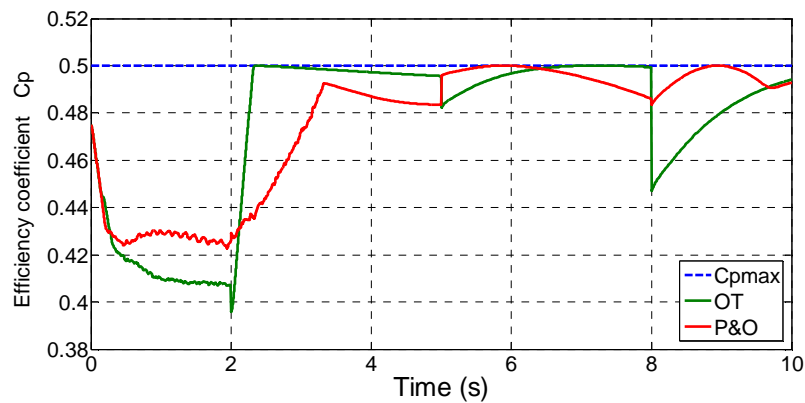
(b) Measured pitch angle.



(c) Measured rotational speed.



(d) Measured stator output active power.



(e) Power efficiency coefficient.

Figure 3.24 Dynamic responses of the Fuzzy-P&O algorithm in VSOM [29].

- **Discussion:**

Figure 3.24a shows a stepped wind speed profile covered almost the entire variable speed operating range of the WTS. Figure 3.24b shows the pitch angle variations according to the operating point of the system, between 0 and 3sec, the pitch orientation system is activated in order to limit the speed and the power to their rated points, but after that the pitch orientation system was deactivated to allow the MPPT system to work freely. The Figure 3.24c shows the rotational speed response and its theoretical optimal speed, it is changing according to the wind speed changes. In term of stability, the Fuzzy-P&O method seems less stable because the measured speed moved away from the optimal speed even in the steady-state phase.

Figure 3.24d shows the measured output power and the rated power of the WTS, the output power decreases for every wind speed reduction; also, it seems equal for the different MPPT method. OT control seems steadier than the P&O because the Fuzzy-P&O is suffering from oscillations.

The power efficiency coefficient response is presented in Figure 3.24e, the OT method is superior in maintaining the highest efficiency especially in the steady state, on the contrary, the Fuzzy-P&O suffers from the optimal step-size searching operation, and this takes time depending on the mechanical characteristics of the WT (this is obvious between the 6s and 8s), but the difference between of them can be acceptable (0.5-0.49).

3.3. Blade Pitch Angle Control

If the wind speed is above the rated value, the pitch control system is activated in order to reduce the aerodynamic power of the WT.

3.3.1. Blade Pitch Angle Control using Neuro-Fuzzy Controllers

Beyond the rated wind speed (12m/s), a pitch angle reference superior than zero have applied to the blade orientation system. We can control the rotational speed of the DFIG to its rated speed 1.2pu, and as a compensation term, we control the mechanical power to its rated value. Some authors use a gain scheduling control [31-5-32], in order to compensate the non-linear characteristics of the blade orientation system and this need a lot of testing operations. The employed NFCs have two inputs (the error and its change) with five *gbellMfs*. The learning data set is collected by extensive simulation tests using classical PI controllers. The overall pitch angle control system is presented in Figure 3.25. The mechanical power is given by the Equation (3.09).

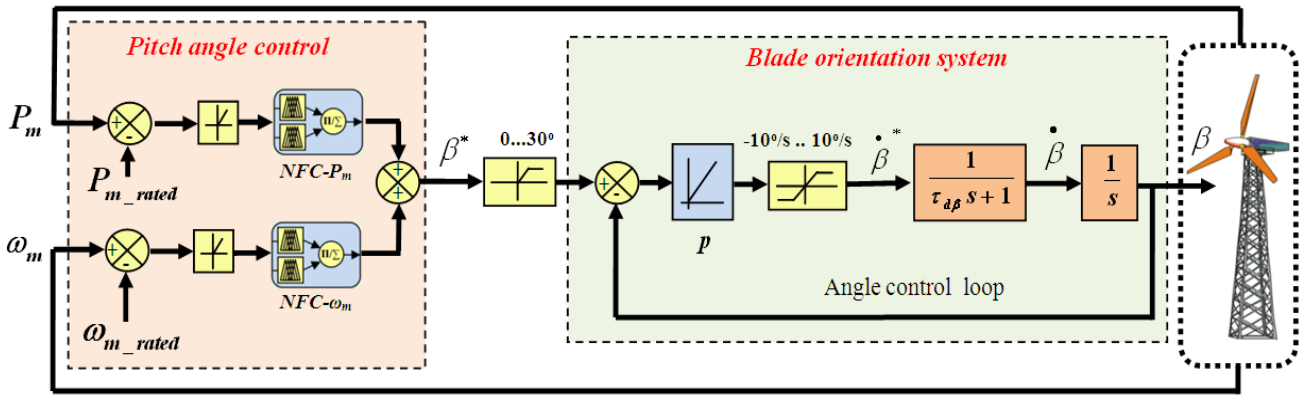
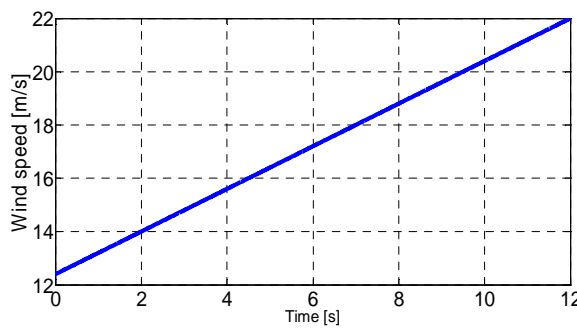


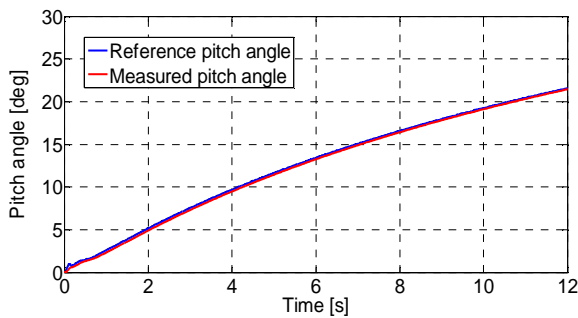
Figure 3.25 Pitch angle control scheme using two NFCs.

• **Simulation Results**

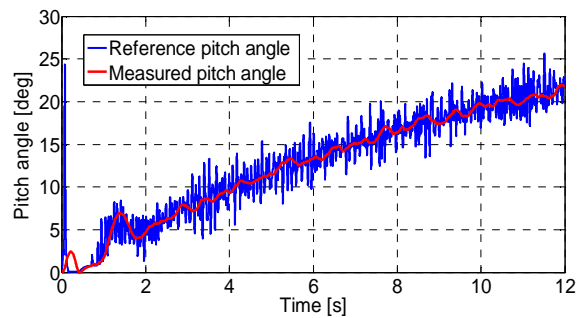
In order to show the effectiveness of the proposed control system in the constant speed and constant power mode, we apply a high wind speed profile vary from 12 to 22(m/s), the simulation results are shown in Figure 3.26.



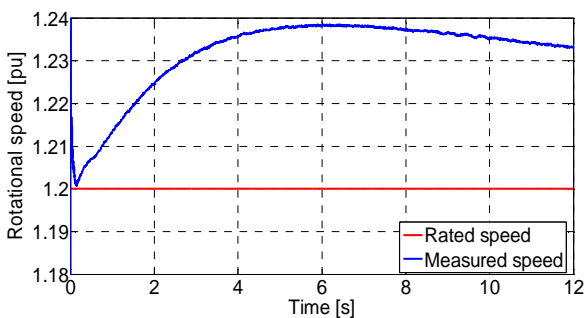
(a) Wind speed profile employed



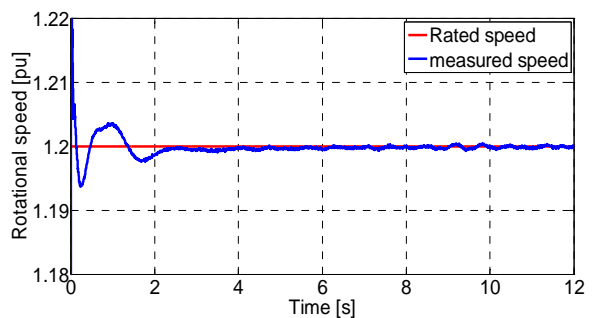
(b) PI control : Pitch angle response



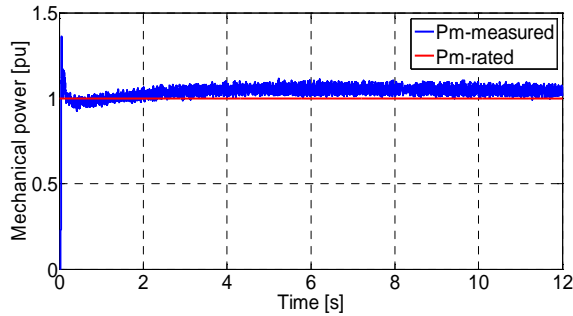
(b) NFC : Pitch angle response



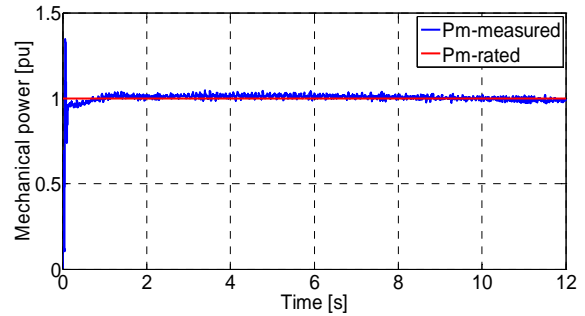
(c) PI control : Rotational speed



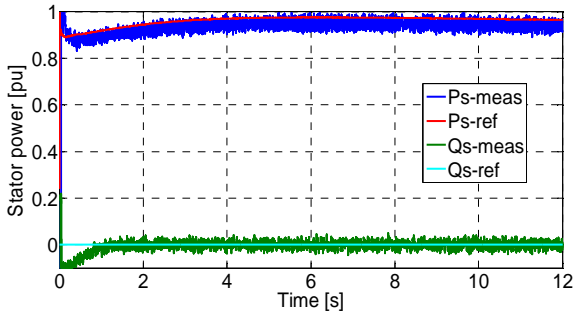
(c) NFC : Rotational speed



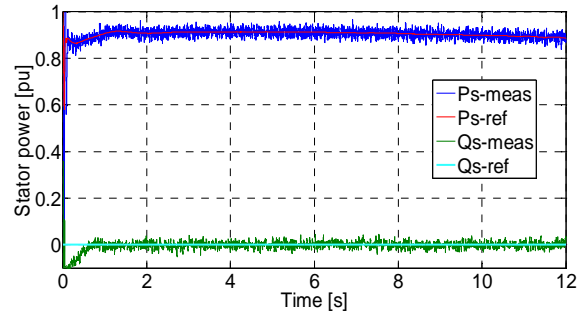
(d) PI control : Estimated mechanical power



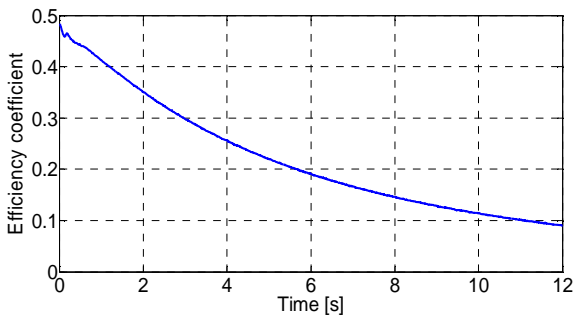
(d) NFC : Estimated mechanical power



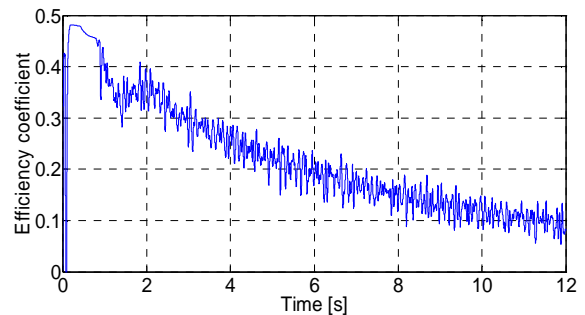
(e) PI control : Stator output power



(e) NFC : Stator output power



(f) PI control : Efficiency coefficient



(f) NFC : Efficiency coefficient

Figure 3.26 Dynamic responses of the WPGS in the constant speed operation mode using ANFIS.

• **Discussion:**

According to Figure 3.26, when the wind speed became higher than the rated wind speed (12m/s), the pitch angle reference became superior than zero in each control method, the main difference in these two reference signals is their nature, which is linear in the PI control, and oscillated and noisy in the NFC case. The NFC is superior in maintaining the Rotational speed and the mechanical power in their rated values regardless of the wind speed intensity; however in the PI control case, the Rotational speed and the mechanical power exceeded their rated values also the mechanical power seems more oscillated than the case of a NFC. The same remark is observed in the output electrical powers, they are more oscillated in the PI control law, and the active power exceeded the rated output power of the DFIG (0.9pu).

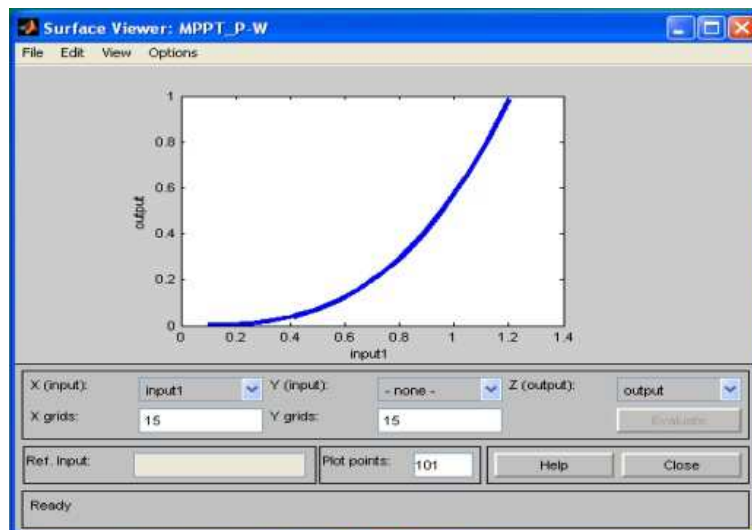
We can say that the NFC with an appropriate data collection of the system is able to maintain the WPGS steady in the rated operating point in case of high wind speed condition, with more output power oscillations damping capability compared to the PI control method.

3.3.2. Blade Pitch Control and MPPT Algorithm using ANFIS

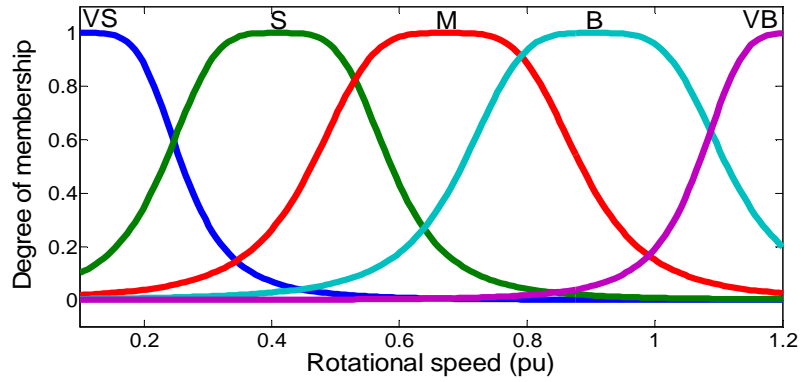
As the case of PSF algorithm, the reference MPC of the WT should be obtained first from the experimental results. Then, the data points for maximum output mechanical power and the corresponding WT rotational speed must be recorded in a lookup table [16-17]. Our idea is to use the ANFIS environment and the WT characteristics to design a TSK fuzzy system to emulate the optimal MPC or $P_m=f(\omega_m)$, the estimated rotational speed is used as input to the fuzzy system. Assume that the power converters are lossless and the windings resistances are neglected, we can get the reference electromagnetic torque from Equation (3.07) as:

$$T_{em}^* = (P_m^* - P_{loss,GB}) / \omega_{m_est} \quad (3.11)$$

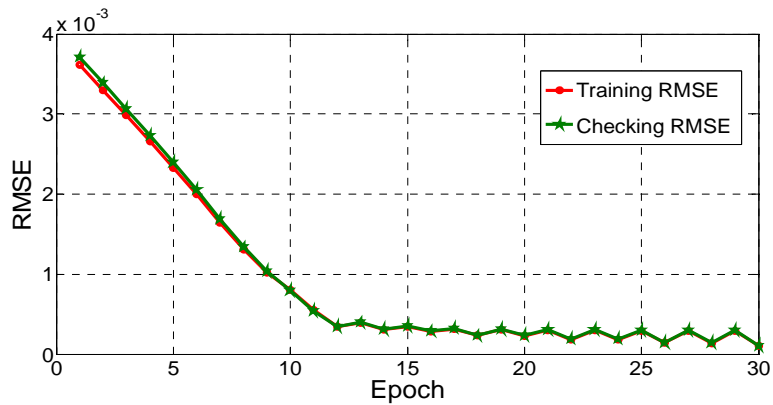
From the WT power curve and by using the ANFIS, we constructed a fuzzy system (Fuzzy_MPPT) performs the MPC versus the generator speed (see Figure 3.27a). The fuzzy system has a single input with five MFs (see Figure 3.27b), the number of the training epochs is set to 30 with an error tolerance of 10^{-6} (see Figure 3.27c). Figure 3.27d compares the ANFIS output with training and checking data sets after training, clearly the ANFIS output presents a good fit to the original data.



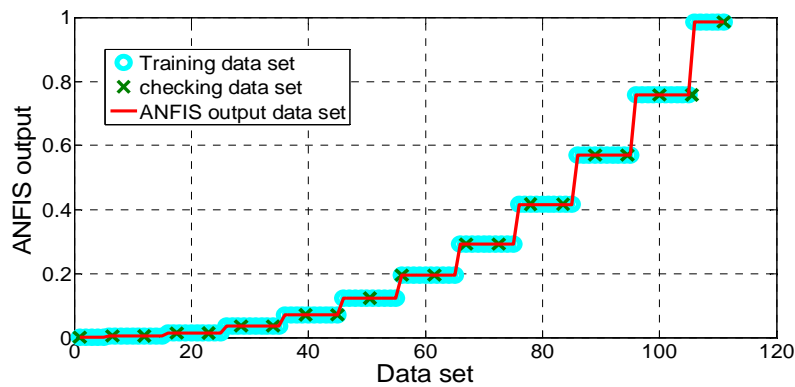
(a) MPC created by ANFIS.



(b) Input MFs of Fuzzy_MPPT.



(c) RMSE during the training process of ANFIS.



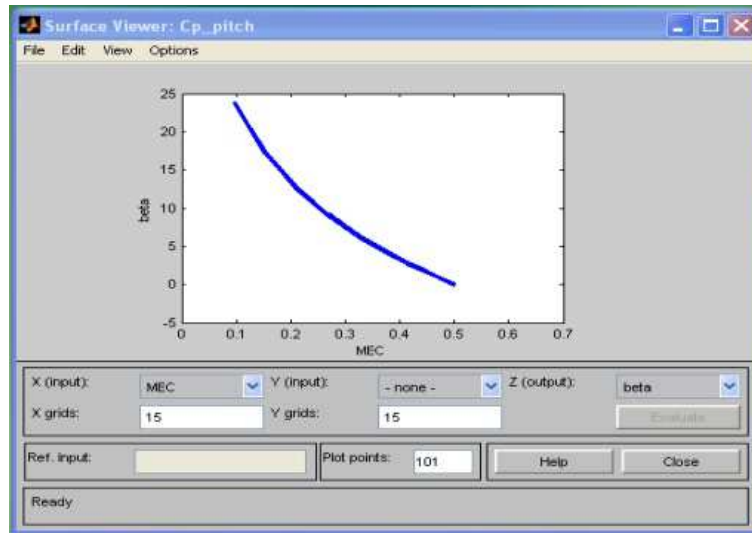
(d) Training and checking data compared to ANFIS output.

Figure 3.27 Training process of the ANFIS based MPPT.

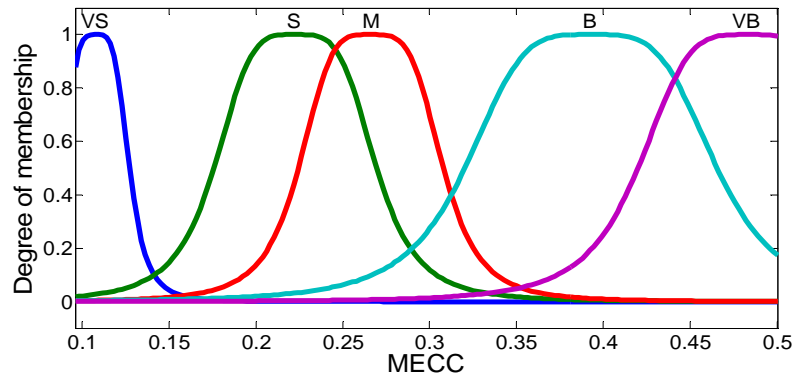
In the pitch angle control, we used a proportional controller in the rotor speed limitation loop, and an ANFIS in the mechanical power limitation loop. The ANFIS is inspired from the efficiency curve ($C_p=f(\beta,\lambda)$), it has one input which is the efficiency coefficient that estimated from Equations. (2.05) and (3.07), and the output is the optimal pitch angle reference, the activating condition is given as:

$$\begin{cases} \beta_p^* = \beta_{p_opt} & \text{while : } P_{m_est} > 1 \\ \beta_p^* = 0 & \text{while : } P_{m_est} < 1 \end{cases} \quad (3.12)$$

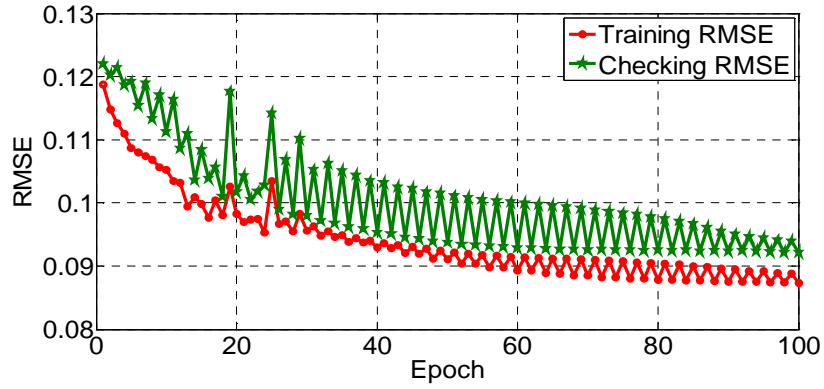
We built a fuzzy system (Fuzzy_pitch) performs the pitch angle versus the MECC presented in Figure 3.28a. The system has a single input with five MFs (Figure 3.28b), the number of training epochs is set to 100 with an error tolerance of 10^{-6} (Figure 3.28c). Figure 3.28d compare the ANFIS output with the training and the checking data sets after training, again the ANFIS output presents a good fit to the original data sets.



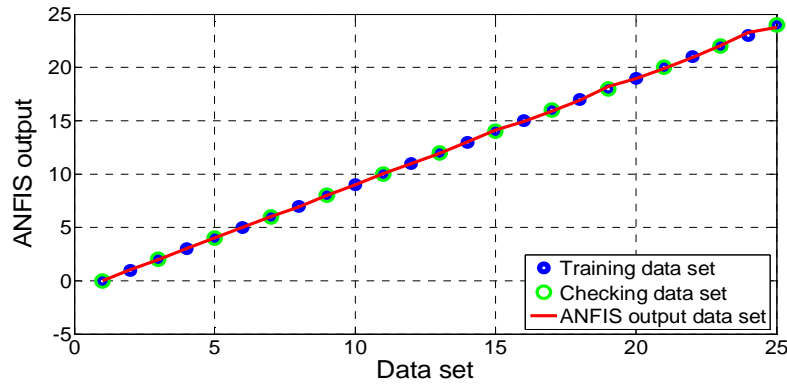
(a) MECC created by ANFIS.



(b) Input MFs of Fuzzy_pitch.



(c) RMSE during the training process of ANFIS.



(d) Training and checking data compared with ANFIS output.

Figure 3.28 Training process of the ANFIS based blade pitch angle control.

The proposed MPPT and pitch angle control are presented with the per unit system in Figure 3.29.

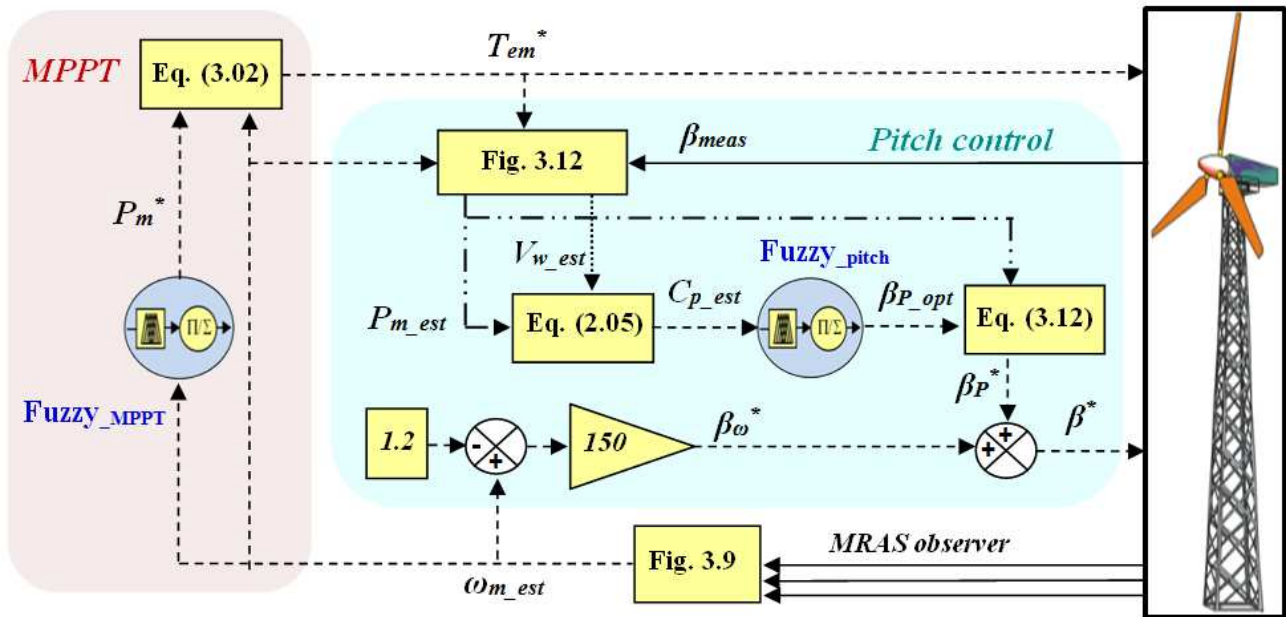
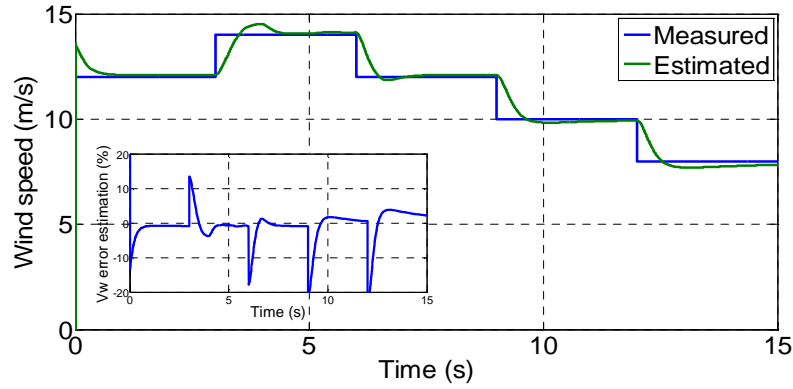


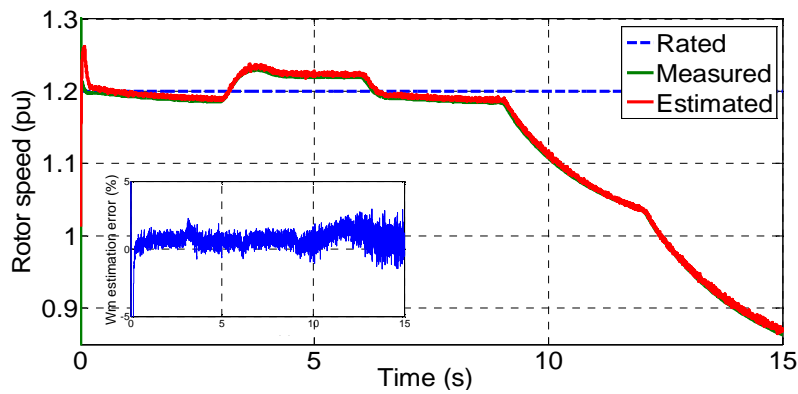
Figure 3.29 MPPT and Pitch angle control scheme of the WPGS using ANFIS.

• **Simulation Results**

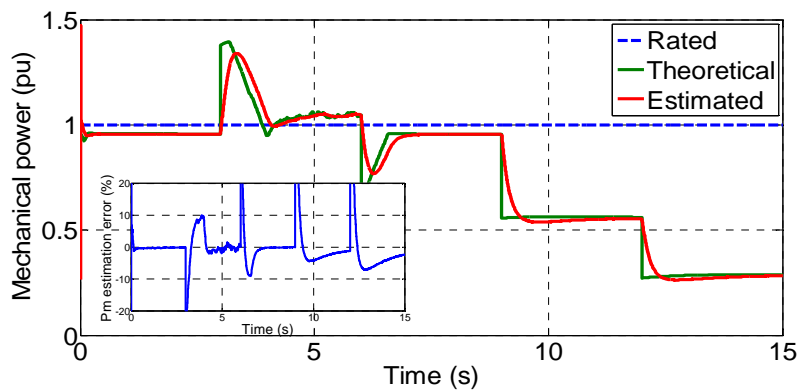
The wind speed profile is chosen in order to get a VSOM of the DFIG system which is between the 0.7 and 1.2pu and in the limited power operating mode for wind speed above 12m/s. The simulation results are represented in Figure 3.30.



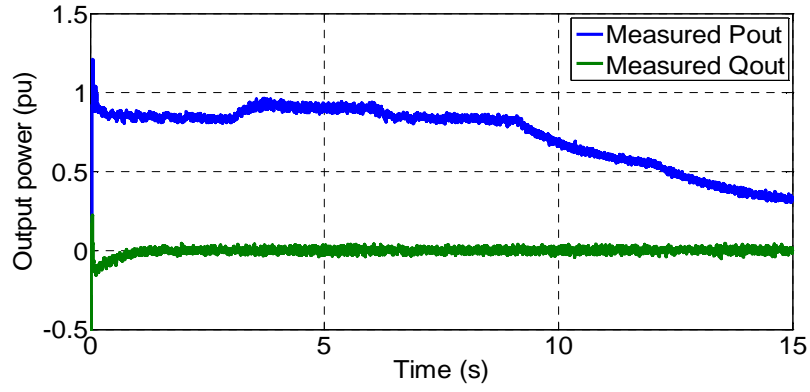
(a) Measured and estimated wind speed



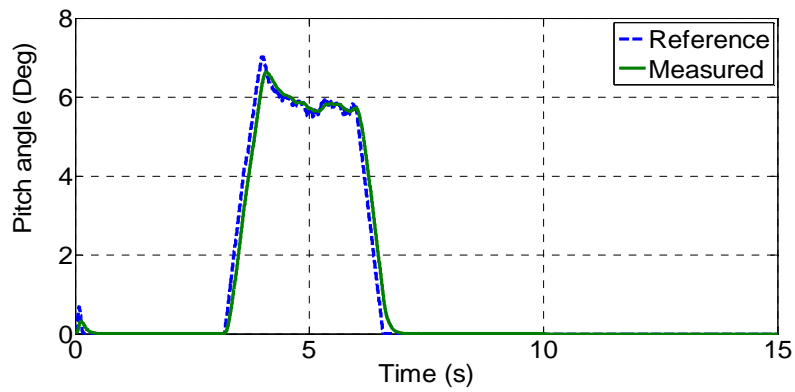
(b) Measured and estimated rotational speed



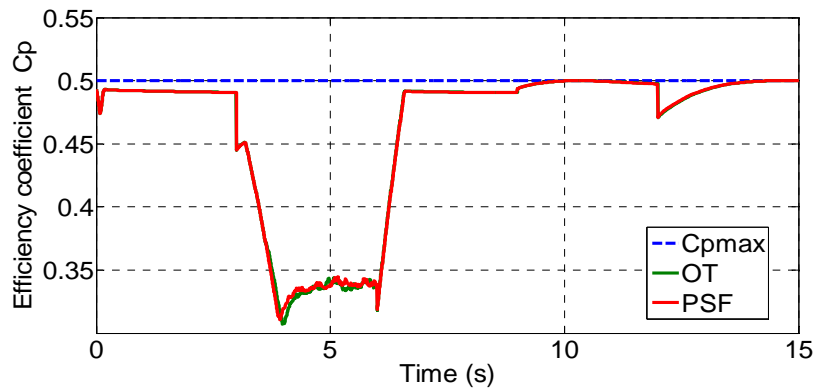
(c) Estimated mechanical power.



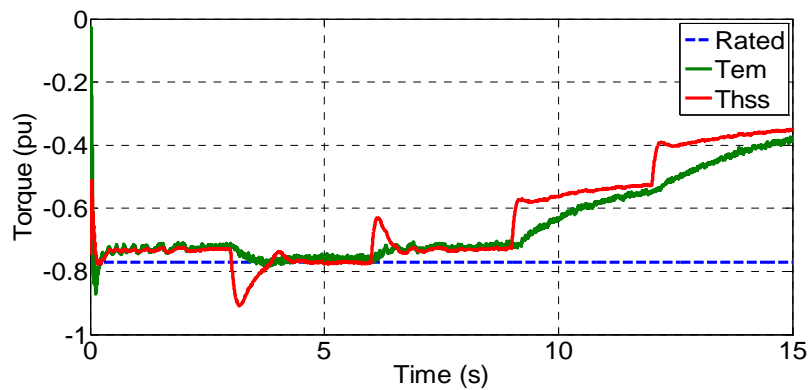
(d) Measured stator output active and reactive power.



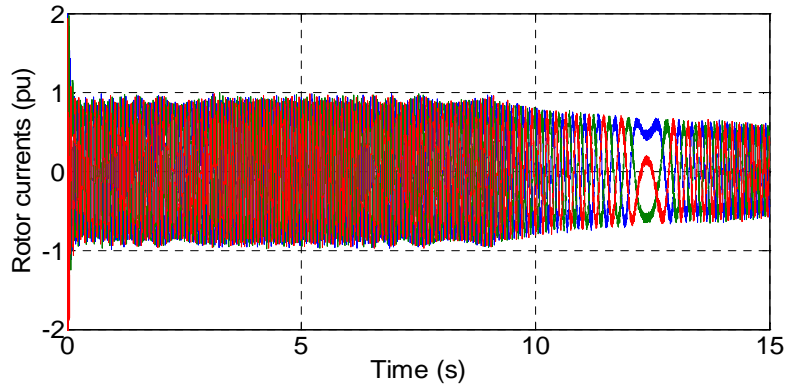
(e) Pitch angle control.



(f) Power efficiency coefficient.



(g) Electromagnetic and mechanical torques in the high speed shaft.

(h) Rotor windings *abc* currents.**Figure 3.30** Dynamic responses of the proposed algorithm in the largely variable wind speed.

- **Discussion :**

Figure 3.30 shows the dynamic response of the WTS in high and moderate wind speed, Figure 3.30a shows the measured and the estimated wind speed where the estimation error is less than $\pm 6\%$ in the steady-state condition as denoted in the estimation error figure added within the Figure 3.30a. Figure 3.30b shows the rotor speed response, where the estimation error is less than $\pm 3\%$ in the steady-state condition as denoted in the estimation error figure added within the Figure 3.30b. Figure 3.30c shows the theoretical and the estimated mechanical power of the WT according to the rated mechanical power which 1.5MW, this estimated power has been used to estimate the wind speed as mentioned earlier. The theoretical power instantaneously affected by the wind speed variation as denoted in Equation. (2.09), however the estimated mechanical power suffers from the large WT inertia which gives slow dynamic response according to the available wind speed. Between 3 and 6sec the mechanical power is limited to its rated value. The estimation error is less than $\pm 7\%$ in the steady-state condition as denoted in estimation error figure within the Figure 3.30c.

The Figure 3.30d shows the measured output active and reactive power of the DFIG, between the 3 and 6sec the system is in the rated power operating mode, because the output power and the rotor speed are limited to their rated values, after the 6sec the wind speed became lower and the system returned to the MPPT operating mode. Figure 3.30e shows the pitch angle control response of the system, the power limitation system has been activated between 3 and 3sec because the mechanical power exceeded the rated value of the WT, and apart this, pitch angle is kept to zero in order to allow the MPPT mode. Figure 3.30f shows the efficiency coefficient response, the PSF is nearly similar to the OT control, and maintained their efficiency and stability in the steady-state phase with maximum reached value of 0.49. Between the 3 and 6sec, the efficiency coefficient is decreased according to the pitch angle.

Figure 3.30g represents the high speed shaft (T_{hss}) and the electromagnetic torques (T_{em}), the T_{hss} changed according to the mechanical power captured by the turbine, the T_{hss} is braked by the controlled T_{em} in order to harvest the maximum power. During steady-state between 3 and 6sec, the rotor speed is constant and T_{hss} and T_{em} are equal to their rated value.

Figure 3.30h presents the rotor's three-phase currents, they vary in magnitude and pulsation according to the operating mode. In the rated power operating mode, the system is in the super-synchronous mode ($\omega_r = -0.2pu$), in the MPPT mode the rotor pulsation continue to increase until the synchronous point at 12.5sec which becomes 0, after that the system enter into the sub-synchronous operating mode and the rotor pulsation becomes positive.

3.4. Conclusion

Based on the simulation results and the analysis, the OT method was found the steadier and superior in maintaining the steady-state, put its dependency on WT characteristics makes it inflexible. Optimal TSR based MPPT algorithm is fast and efficient, nevertheless, its dependency on wind speed measurement and the WT characteristics makes it also inflexible. On the other hand, Fuzzy-P&O algorithm is flexible and simple in implementation if we consider the problematic of defining the optimum step-size, but it is less efficient because of the continually researching of the optimal operating point. With no need to any information about the wind speed or the WT characteristics, P&O seems an interesting idea. MPCs method is hybrid of look-up based and P&O methods, it is more stable and accurate. Using the NFC in the blade pitch control system can be so useful in maintaining the stability and protection of the WPGS even in case of wind speed above the 20m/s.

3.5. References of Chapter 3

- [1] F. Bianchi, H. De Battista and R. Mantz, Wind turbine control systems: principles, modelling and gain-scheduling design advances in industrial control. Lavoisier, 2006.
- [2] X. Feng, Z. Jianzhong and C. Ming, Analysis of double objectives control for wind power generation system with frequency separation. 4th International Conference on Electric Utility Deregulation and Restructuring and Power Technologies (DRPT), pp.1366–1371, 2011.
- [3] J. L  pez, P. Sanchis, X. Roboam and L. Marroyo, Dynamic behavior of the doubly fed induction generator during three-phase voltage dips. IEEE Trans. on Energy Conversion, Vol. 22, No. 3, pp. 709–717, 2007.
- [4] F.D. Bianchi, H. De Battista and R.J. Mantz, Wind turbine control systems: principles, modelling and gain scheduling design. Springer-Verlag, 2007.
- [5] H. Morten. Hansen, Anca Hansen and J. Torben, Control design for a pitch-regulated, variable speed wind turbine. Ris  National Laboratory, Roskilde Denmark, Jan. 2005.
- [6] B. Pokharel, Modeling, control and analysis of a doubly fed induction generator based wind turbine system with voltage regulation, Master Thesis, Tennessee Technological University, Dec. 2011.
- [7] M.A. Abdullah, A.H.M. Yatim, C.W. Tan, and R. Saidur, A review of maximum power point tracking algorithms for wind energy systems, Renewable and Sustainable Energy Reviews, Vol. 16, pp. 3220–3227, 2012.
- [8] A. Dida and D. Benattous, A complete modeling and Simulation of DFIG based wind turbine system using fuzzy logic control, Frontier of energy. Vol. 10, No. 2, 2016.
- [9] S.M. Raza Kazmi, H. Goto, G. Hai-Jiao, and O. Ichinokura, Review and critical analysis of the research papers published till date on maximum power point tracking in wind energy conversion system, IEEE Energy Conversion Congress and Exposition (ECCE), pp. 4075–4082, Sep. 2010.
- [10] A. Dida and D. Benattous, Fuzzy logic based sensorless MPPT Algorithm for wind turbine system driven DFIG, 3rd IEEE International Conference on Control, Engineering & Information Technology (CEIT'2015), Tlemcen, Algeria, May 2015.
- [11] R. Fadaeinedjad, M. Moallem and G. Moschopoulos, Simulation of a wind turbine with doubly fed induction generator by FAST and Simulink, IEEE Trans. on energy conversion, Vol. 23, No. 2, pp. 690–700, 2008.
- [12] Y.Zou, M.Elbuluk and Y. Sozer. A complete modeling and simulation of induction generator wind power systems, IEEE Proceedings of [Industry Applications Society Annual Meeting \(IAS\)](#), pp. 1-8, 2010.
- [13] J. Morren and SWH. De Haan, Ridethrough of wind turbines with doubly-fed induction generator during a voltage dip, IEEE Trans. on Energy Conversion, Vol. 20, No. 2, pp. 435-441, 2005.
- [14] I. K. Buehring and L. L. Freris, Control policies for wind energy conversion systems, IEE Proceedings, Part C - Generation, Transmission and Distribution, Vol. 128, pp. 253-261, Sep. 1981.
- [15] E. Koutroulis and K. Kalaitzakis, Design of a maximum power tracking system for wind energy conversion applications, IEEE Trans. on Industrial Electronics, Vol. 53, N^o. 2, Apr. 2006.
- [16] B. Masoud. Modeling and controller design of a wind energy conversion system including a matrix converter, PhD Thesis, Ontario, Canada: Electrical and Computer Engineering, University of Waterloo; 2008.
- [17] S.M. Barakati, M. Kazerani, J.D. Aplevich. Maximum power tracking control for a wind turbine system including a matrix converter, IEEE Trans. on Energy Conversion, Vol. 24, pp. 705–13, 2009.
- [18] M.R. Patel. Wind and solar power systems, CRC Press; 1999.
- [19] Jogendra Singh Thongam and Mohand Ouhrouche (2011). MPPT Control Methods in Wind Energy Conversion Systems, Fundamental and Advanced Topics in Wind Power, Dr. Rupp Carriveau (Ed.), ISBN: 978-953-307-508-2, InTech, Available from: <http://www.intechopen.com/books/fundamental-and-advancedtopics-in-wind-power/mppt-control-methods-in-wind-energy-conversion-systems>
- [20] A. Dida and D. Benattous, Modeling and control of DFIG via back-to-back multilevel converters using fuzzy logic controller, 3rd IEEE International Conference on Control, Engineering & Information Technology (CEIT'2015), Tlemcen, Algeria, May 2015.

- [21] K. Belmokhtar, M.L. Doumbia and K. Agbossou, Novel fuzzy logic based sensorless maximum power point tracking strategy for wind turbine systems driven DFIG, *Energy*, Vol. 76, pp. 679-693, 2014.
- [22] M. Kalantar and G.S. Mousavi, Dynamic behavior of a stand-alone hybrid power generation system of wind turbine, microturbine, solar array and battery storage, *Applied Energy*, Vol. 87, N^o. 10, pp. 3051-3064, 2010.
- [23] Q. Wei, Z. Wei, J.M. Aller and R.G Harley, Wind speed estimation based sensorless output maximization control for a wind turbine driving a DFIG, *IEEE Trans. on Power Electronics*, Vol. 23, No. 3, pp. 1156-1169, 2008.
- [24] A. Dida and D. Benattous, Doubly-fed induction generator drive system based on maximum power curve searching using fuzzy logic controller, *International Journal of Power Electronics and Drive System*, Vol. 5, No. 4, 2015.
- [25] A.G. Abo-Khalil, D.C. Lee and J.K. Seok, Variable speed wind power generation system based on fuzzy logic control for maximum power output tracking, 35th Annual IEEE Power Electronics Specialists Conference, PESC, Aachen, Germany, Vol. 3, pp. 2039–2043, 2004.
- [26] S.M. Raza Kazmi, H. Goto, G. Hai-Jiao and O. Ichinokura, A novel algorithm for fast and efficient speed-sensorless maximum power point tracking in wind energy conversion systems, *IEEE Trans. on Industrial Electronics*. Vol. 58, pp. 29–36, 2011.
- [27] P. Ching-Tsai and J. Yu-Ling, A novel sensorless MPPT controller for a high-efficiency micro-scale wind power generation system, *IEEE Trans. on Energy Conversion*, Vol. 25, pp. 207-216, 2010.
- [28] M.K. Hong and H.H. Lee, Adaptive maximum power point tracking algorithm for variable speed wind power systems, International conference on life system modeling and intelligent computing, and International conference on Intelligent computing for sustainable energy and environment. Part I. Wuxi, China: pp. 380–388, 2010.
- [29] A. Dida and D. Benattous, Adaptive hill-climb searching method for MPPT algorithm based DFIG system using fuzzy logic controller, *International Journal of Systems Assurance Engineering and management*, 25 October, 2015.
- [30] A. Dida and D. Benattous, Adaptive P&O control for MPPT algorithm in DFIG system using fuzzy logic controller, The 3rd IEEE International Conference on Information Processing and Electrical Engineering, Tebessa, Algeria, Nov. 2014.
- [31] E.B. Muhando, A. Uehara and C.H. Kim, LQG design for megawatt-class WECS with DFIG based on functional models Fidelity Prerequisites, *IEEE Trans. on energy conversion*, Vol. 24, No. 4, pp. 893-904, 2009.
- [32] I. Poultangari, R. Shahnazi and M. Sheikhan, RBF neural network based PI pitch controller for a class of 5-MW wind turbines using particle swarm optimization algorithm, *ISA Transactions*, Vol. 51, No. 5, pp. 641–648, 2012.

Chapter 4:

Direct Power Control of Grid-Connected Doubly-Fed Induction Machine, Review

Chapter 4: Direct Power Control of Grid-Connected Doubly-Fed Induction Machine, Review

4.1. Introduction

This chapter gives an investigation on the decoupled and direct power control strategies of the DFIG and their robustness capabilities against the sudden rotational speed variation and machine parameters uncertainties. The ability to operate in motoring and generating modes, sub- and super-synchronous modes are tested by directly control the stator active and reactive powers for different control laws, firstly the well-known field oriented control (FOC), next the classic direct power control (DPC) using a lookup table, then the nonlinear sliding mode control (SMC) approach, and finally the intelligent fuzzy logic control law. Finally a brief comparison study has been given of the simulation results in order to clarify the straight and weakness points of each control law.

In this chapter, the simulations have been carried out using the Matlab/Simulink with motor convention on both rotor and stator sides of the DFIG,

4.2. Control Strategies of the DFIG

The DFIG is a dynamic system with strong nonlinear coupled characteristics and time varying uncertain inputs. Many control approaches have been proposed for the power electronic converters and drives, the most usually used ones being presented in Figure 4.1 [1].

The basic idea of hysteresis control law is to keep the variable inside the hysteresis band by changing the switching state of the converter each time the variable reaches the boundary. The simplest application is the current control, more complex schemes of hysteresis control law such as direct torque control (DTC) [2] and DPC [3] are proposed using the error between the measured variable and its reference considering a given hysteresis width and a lookup table, the main advantages of the hysteresis control is its robustness and its very fast dynamic response. However, the hysteresis width and the nonlinearity of the system inherently introduce variable switching frequency and a spread spectral content.

Given a modulation stage with fixed switching frequency for the converter and any linear controller such as PI controller can be used for drives. Cascaded structure including PI controllers scheme with modulation stage often needs additional coordinate transformations such as the well-

known field oriented control which firstly mentioned in [4]. Also, using a linear control law to control a nonlinear system can lead to unequal performance all over the dynamic range.

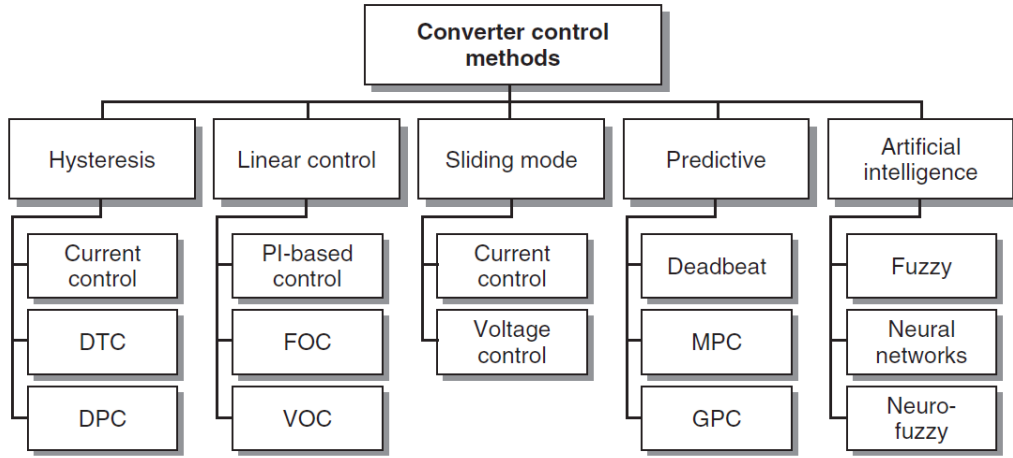


Figure 4.1 Different control schemes for power converters and drives [1].

With the development of more powerful microprocessors, new control schemes have been proposed. Some of the most important ones are FLC, neural networks control (NNC), SMC, and model predictive control (MPC) [1]. Each kind of the previous mentioned control laws has its background, its points of strength and points of weakness. In this chapter, four different control laws have been selected to compare their performances in the directly and independently stator power control of the DFIG,

4.2.1. Field Oriented Control of the DFIG

Direct FOC of the DFIG can be applied with independently control of stator active and reactive power based on the field orientation approach. Figure 4.2 shows the block diagram of the system implemented with PI controller. The quotient B/A represents the transfer function to be controlled, where A and B are presently defined as follows [5]:

$$A = L_s R_r + sL_s (L_r - \frac{L_m^2}{L_s}) \quad \text{and} \quad B = L_m V_s \tag{4.01}$$

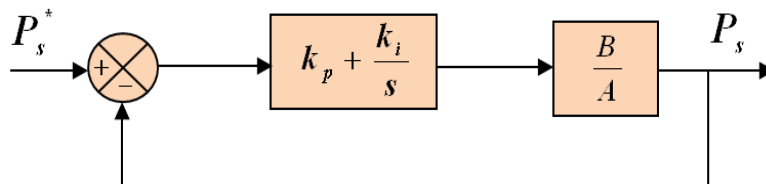


Figure 4.2 Closed loop stator active power control using PI controller.

instantaneous errors variations, the power controllers' hysteresis bandwidth as well as the machine operating speed. The stator and rotor voltage space vector equations are expressed in the rotor reference frame as follows:

$$\begin{cases} V_s^r = R_s i_s^r + \frac{d\Phi_s^r}{dt} + j\omega_e \Phi_s^r \\ V_r^r = R_r i_r^r + \frac{d\Phi_r^r}{dt} \end{cases} \quad (4.03)$$

According to [10], the stator active and reactive powers can be calculated as:

$$\begin{cases} P_s = -\frac{3}{2} \frac{L_m}{\sigma L_s L_r} \omega_s |\Phi_s^r| |\Phi_r^r| \sin \delta \\ Q_s = \frac{3}{2} \frac{\omega_s}{\sigma L_s} |\Phi_s^r| \left(\frac{L_m}{L_r} |\Phi_r^r| \cos \delta - |\Phi_s^r| \right) \end{cases} \quad (4.04)$$

where ω_s and ω_e are the synchronous and rotor angular frequencies, δ angle between the rotor and stator flux linkage vectors. The fact that stator circuit is directly connected to the grid, the stator flux amplitude and the synchronous pulsation can be regarded as constants. The time derivative of Equation (4.04) yields:

$$\begin{cases} \frac{dP_s}{dt} = -\frac{3}{2} \frac{L_m}{\sigma L_s L_r} \omega_s |\Phi_s^r| \frac{d(|\Phi_r^r| \sin \delta)}{dt} \\ \frac{dQ_s}{dt} = \frac{3}{2} \frac{L_m}{\sigma L_s L_r} \omega_s |\Phi_s^r| \frac{d(|\Phi_r^r| \cos \delta)}{dt} \end{cases} \quad (4.05)$$

So, the stator active and reactive powers can be controlled independently by adjusting $|\Phi_r^r| \sin \theta$ and $|\Phi_r^r| \cos \theta$ respectively. Neglecting the rotor resistance in Equation (2.14), the rotor flux variations in the rotor reference frame are approximated as:

$$\frac{d\Phi_r^r}{dt} = V_r^r - R_r i_r^r \approx V_r^r \quad (4.06)$$

According to Equation (4.06), the rotor flux moves in the same direction of the applied rotor voltage vector during a sampling period (T_s), and its speed is proportional to the amplitude of the rotor voltage vector, therefore, $|\Phi_r^r| \sin \delta$ and $|\Phi_r^r| \cos \delta$ can be adjusted independently as shown in Figure 4.4.

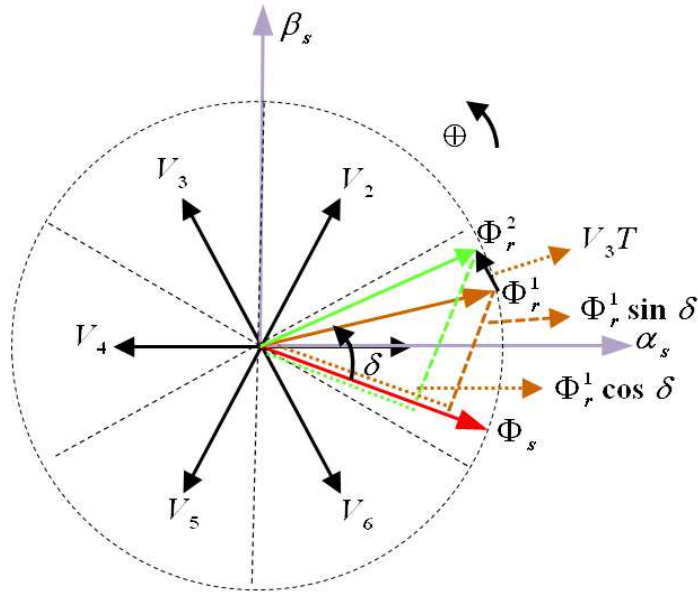


Figure 4.4 Stator and rotor flux vectors in rotor reference frame.

Because the control of DFIG is made on the rotor windings, the voltage vectors applied are rotating with the slip speed related to the stator windings, thus, stator flux must be expressed in the rotor reference frame (D-Q), the Clark transformation matrix is used:

$$\Phi_s^r = \begin{bmatrix} \sin \theta_m & -\cos \theta_m \\ \cos \theta_m & \sin \theta_m \end{bmatrix} \cdot \Phi_s^s \tag{4.07}$$

The module and the phase of the stator flux referred to the rotor reference frame are given by:

$$\begin{cases} |\Phi_s^r| = \sqrt{\Phi_{sD}^2 + \Phi_{sQ}^2} \\ \theta_{\Phi_s^r} = \arctan(\Phi_{sQ} / \Phi_{sD}) \end{cases} \tag{4.08}$$

Considering a two level converter, the (α, β) plane is then divided into six sectors, as given by:

$$(2k - 3) \frac{\pi}{6} \leq N_k \leq (2k - 1) \frac{\pi}{6} \tag{4.09}$$

The variation of sector number according to the stator flux angle is presented in Figure 4.5.

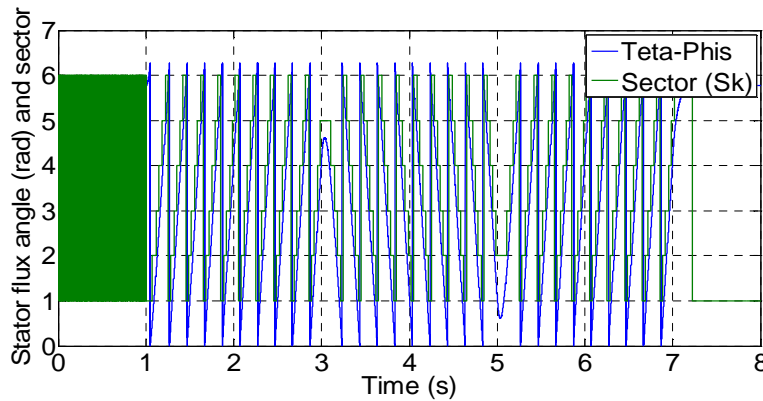


Figure 4.5 Stator flux angle referred to rotor reference frame and correspond sector.

In the proposed control law only active vectors were used for simplicity reason, because using zero vectors gives different behaviors of DFIG operating in super-synchronous or sub-synchronous operating modes. Table 4.1 shows the rotor voltage selection according to the state of the two levels hysteresis controllers and the corresponding sector.

Table 4.1: Optimal lookup table for stator flux based DPC law

S_q	S_p	Sector (S_k)					
		1	2	3	4	5	6
+1	+1	V_5	V_6	V_1	V_2	V_3	V_4
	-1	V_3	V_4	V_5	V_6	V_1	V_2
-1	+1	V_6	V_1	V_2	V_3	V_4	V_5
	-1	V_2	V_3	V_4	V_5	V_6	V_1

where: $V_1 = (1\ 0\ 0)$, $V_2 = (1\ 1\ 0)$, $V_3 = (0\ 1\ 0)$, $V_4 = (0\ 1\ 1)$, $V_5 = (0\ 0\ 1)$, $V_6 = (1\ 0\ 1)$. The bandwidth of the two-level hysteresis controllers of active and reactive powers are chosen in order to get a switching frequency under the 10kHz. The detailed control scheme of the lookup table based DPC of the DFIG is presented in Figure 4.6.

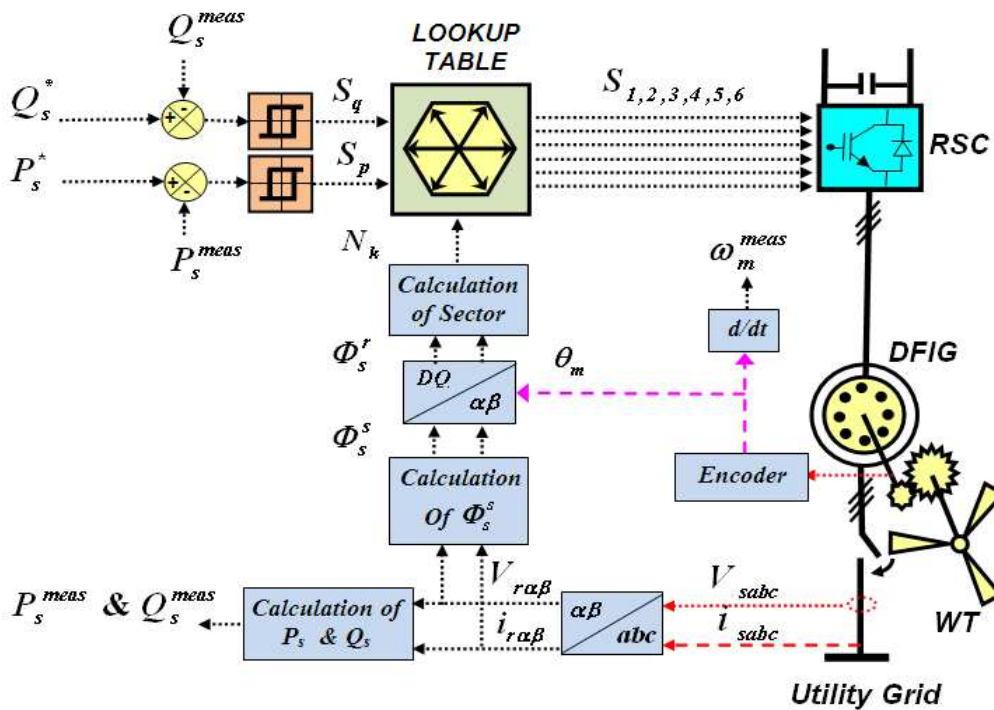


Figure 4.6 Global diagram of the conventional lookup table based DPC strategy for DFIG.

4.2.3. Sliding Mode Control of the DFIG

The design of SMC and its applications on the electrical drive systems were initially presented in [11]. It features are simple in implementation, fast responses, rejection of disturbance, and high robustness, but the controlled state may show undesired chattering phenomenon [12]. The basic idea of traditional SMC algorithms is to enforce the system state to slide along a predefined sliding surface. Once the state of system gets the sliding surface, the structure of the controller is adaptively

changed to slide the state of system along the sliding surface [13]. SMC strategy with its variable control structure is based on the design of discontinuous control signals that drives the system operation states to special manifolds in the state space [11]. In this study, a SMC scheme for directly control the instantaneous stator active and reactive powers of the grid connected DFIG is exploited. The output of the SMC law consists of the sum of the equivalent control and the switching control:

$$\begin{cases} V_{rq} = V_{rq}^{eq} + V_{rq}^s \\ V_{rd} = V_{rd}^{eq} + V_{rd}^s \end{cases} \quad (4.10)$$

The equivalent control is used to control the nominal plant model, and the switching control is added to ensure the desired performance despite parametric uncertainty [13]. The control objectives for the DFIG are to slide along the predefined active and reactive power trajectories. Thus, the chosen sliding surfaces are set as:

$$\begin{cases} S_q = P_s^* - P_s^{meas} \\ S_d = Q_s^* - Q_s^{meas} \end{cases} \quad (4.11)$$

The final expression of the equivalent control law is:

$$\begin{cases} V_{rq}^{eq} = \frac{L_s L_r \sigma}{V_s L_m} \dot{P}_s^* - (R_r i_{rq} + s \omega_s \sigma L_r i_{rd} + s \frac{V_s L_m}{L_s}) \\ V_{rd}^{eq} = \frac{L_s L_r \sigma}{V_s L_m} \dot{Q}_s^* - (R_r i_{rd} + s \omega_s \sigma L_r i_{rq}) \end{cases} \quad (4.12)$$

The famous *Lyapunov* approach is used for driving the state trajectory to the stability manifold. The switching control law must be chosen so that the time derivative of the quadratic *Lyapunov* function ($W_{d,q} = \frac{1}{2} S_{d,q}^2 \geq 0$) is definitely negative. Thus, the following control law is selected [12]:

$$\begin{cases} V_{rq}^s = -k_q \operatorname{sgn}(S_q) \\ V_{rd}^s = -k_d \operatorname{sgn}(S_d) \end{cases} \quad (4.13)$$

where k_q and k_d are positive control gains, $\operatorname{sgn}(S_q)$ and $\operatorname{sgn}(S_d)$ are respective switch functions for stator active and reactive powers. The problem of the chattering phenomenon can be eliminated by introducing a boundary layer. The sign functions are replaced by saturation functions in a small vicinity of the sliding surface [12, 14].

$$\operatorname{sat}(S_j) = \begin{cases} 1 & \text{if } S_j > \lambda_j \\ S_j / \lambda_j & \text{if } |S_j| \leq \lambda_j \\ -1 & \text{if } S_j < -\lambda_j \end{cases} \quad \text{where } j = 1, 2 \quad (4.14)$$

where $\lambda_j > 0$ is the width of the boundary layer. The global SMC of the DFIG is shown in Figure 4.7:

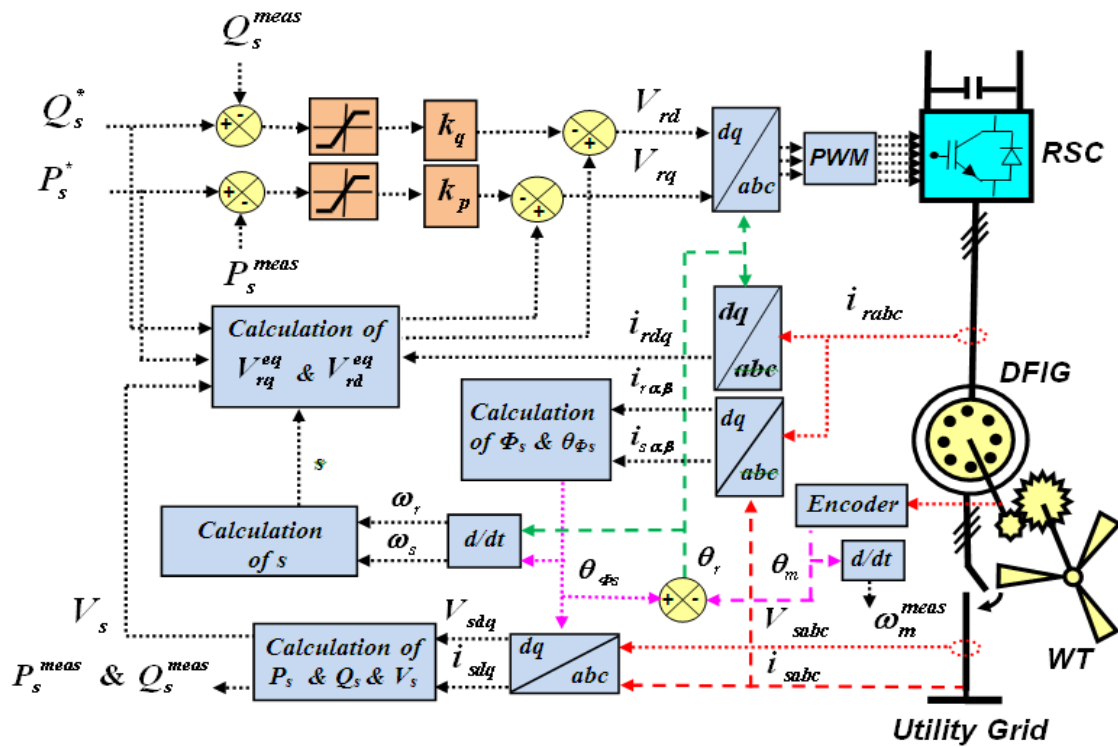


Figure 4.7 Block diagram of the overall SMC scheme of the DFIG.

4.2.4. Fuzzy Logic Control of the DFIG

FLC has the ability to control non-linear, uncertain or adaptive systems, which gives robust performance for parameter variation [15]. FLC doesn't need to any mathematical model of the controlled system, its control law can be expressed based on logic language variation. The structure of FLC applied in the stator power control loops is illustrated in Figure 4.8 where the input signals are the error and its derivative (e and de/dt) and the output signal is the command's derivative (du/dt). Figure 4.9a shows the fuzzy sets and corresponding triangular membership functions description of the inputs and output signals, and Figure 4.9b shows the surface constructed by the seven membership functions. The global control structure is the same one of the Figure 4.3.

Table 4.2 shows the corresponding rule table for the FLC [16]. The determination of the fuzzy rules and the scaling factors (k_e , k_{de} and k_{du}) is based on a qualitative experience and extensive simulation tests using different PI controller and different operating conditions.

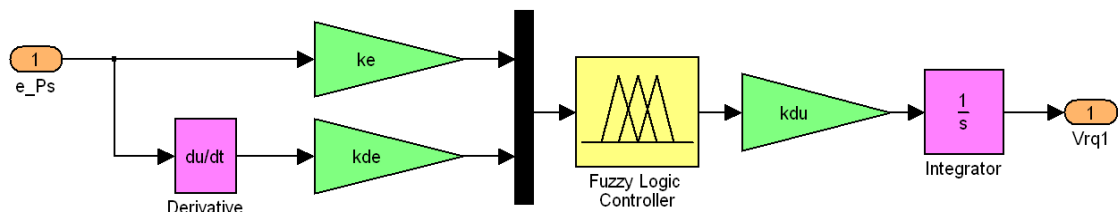
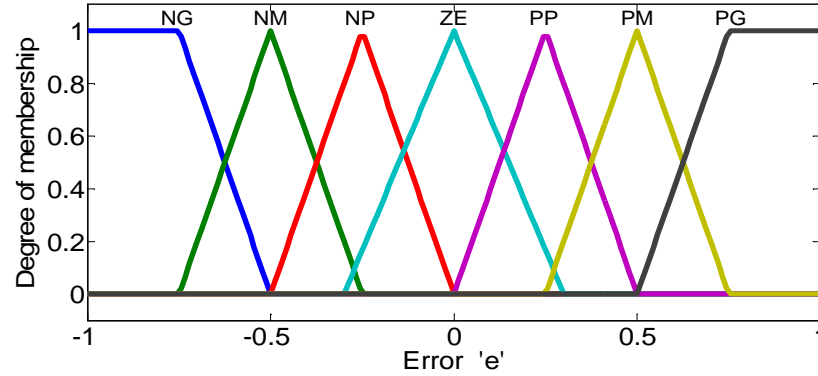
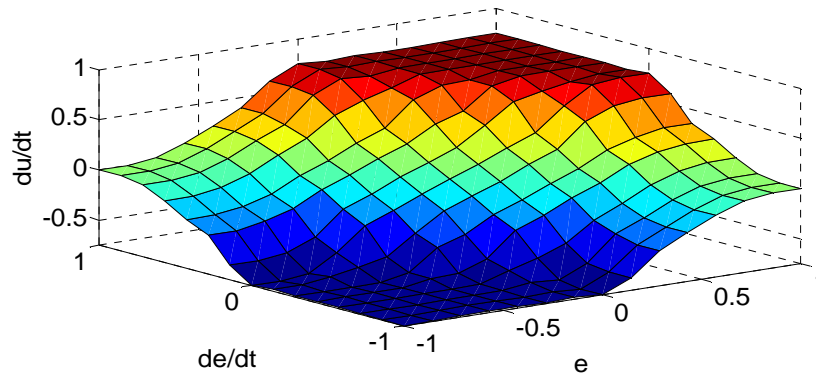


Figure 4.8 Structure of fuzzy logic controller for stator active power control loop.



(a) Inputs and output MFs of the FLC



(b) Surface created by the FLC

Figure 4.9 Membership functions of the adopted FLC**Table 4.2:** Rule table for the fuzzy logic controller

de/dt (pu) \ e (pu)	<i>NB</i>	<i>NM</i>	<i>NS</i>	<i>Z</i>	<i>PS</i>	<i>PM</i>	<i>PB</i>
<i>NB</i>	<i>NB</i>	<i>NB</i>	<i>NB</i>	<i>NB</i>	<i>NM</i>	<i>NS</i>	<i>Z</i>
<i>NM</i>	<i>NB</i>	<i>NB</i>	<i>NB</i>	<i>NM</i>	<i>NS</i>	<i>Z</i>	<i>PS</i>
<i>NS</i>	<i>NB</i>	<i>NB</i>	<i>NM</i>	<i>NS</i>	<i>Z</i>	<i>PS</i>	<i>PM</i>
<i>Z</i>	<i>NB</i>	<i>NM</i>	<i>NS</i>	<i>Z</i>	<i>PS</i>	<i>PM</i>	<i>PB</i>
<i>PS</i>	<i>NM</i>	<i>NS</i>	<i>Z</i>	<i>PS</i>	<i>PM</i>	<i>PB</i>	<i>PB</i>
<i>PM</i>	<i>NS</i>	<i>Z</i>	<i>PS</i>	<i>PM</i>	<i>PB</i>	<i>PB</i>	<i>PB</i>
<i>PB</i>	<i>Z</i>	<i>PS</i>	<i>PM</i>	<i>PB</i>	<i>PB</i>	<i>PB</i>	<i>PB</i>

4.3. Simulation Results

Investigation has been performed on 1.5MW DFIG including the already presented control laws. The parameters of the DFIG are inspired from [17] and cited in the appendix (Table A.3). The simulation goal is to examine the robustness of each control law in the motor and generator operating modes (for example: a pumped storage system) against a suddenly changed rotational speed.

4.3.1. The Normal Operating Conditions Test (Test N⁰1): Because we are not interested with the dynamic of the DFIG, and our concern is only on the power control performance, the rotational speed is introduced as perturbation with extremely hard dynamic as shown in Figure 4.10, which covers the three operation modes of the DFIG (sub-synchronous, synchronous, super-synchronous).

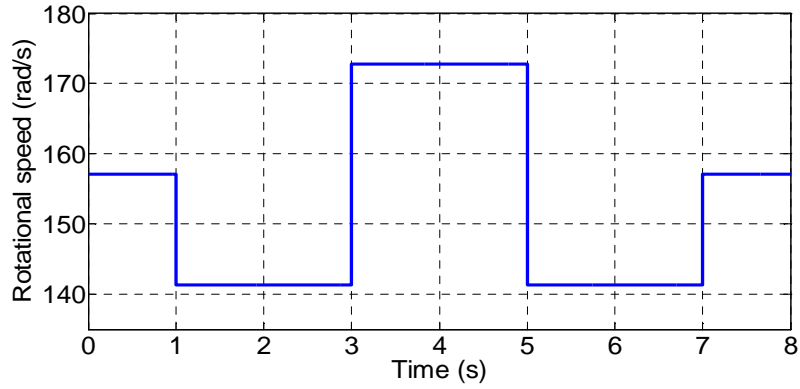


Figure 4.10 Variation of the rotational speed of the DFIG.

4.3.2. The Machine Parameter Variations Test (Test N⁰2): in this test we repeat the same last normal test, also, the machine parameters variation has been introduced as presented in Table 4.3.

Table 4.3: Parameters variation of the 1.5MW DFIG

Parameter	R_s	R_r	L_s	L_r	L_m	J	f
Normal	0.012	0.021	0.0137	0.0136	0.0135	1000	0.0024
Faulty	0.012×2	0.021×2	$0.0137/2$	$0.0136/2$	$0.0135/2$	1000	0.0024

4.3.3. The Faulty Grid Voltage Test (Test N⁰3): the faulty grid voltage is shown in Figure 4.11. The unbalance is created by reducing the a and b grid phases by 15% in the instant $t=4$ sec, the distortion is created by adding 20% of the fifth, 20% of the sixth and 20% of the seventh harmonics of the fundamental for the three phases in the instant $t=4$ sec.

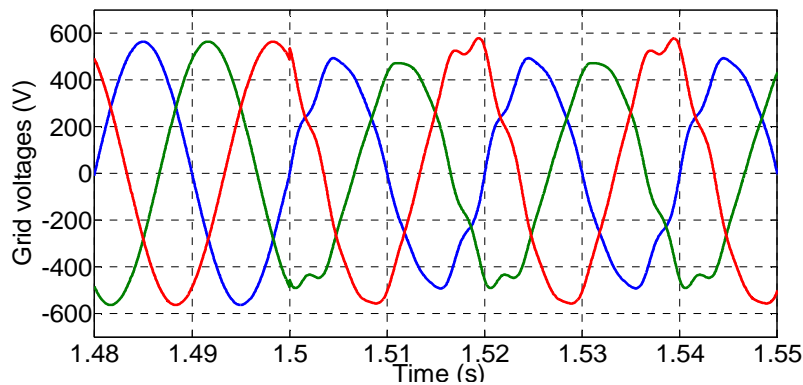
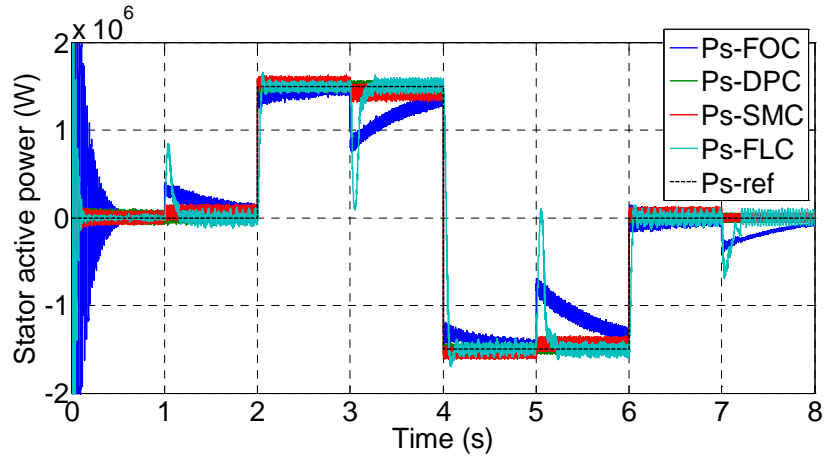
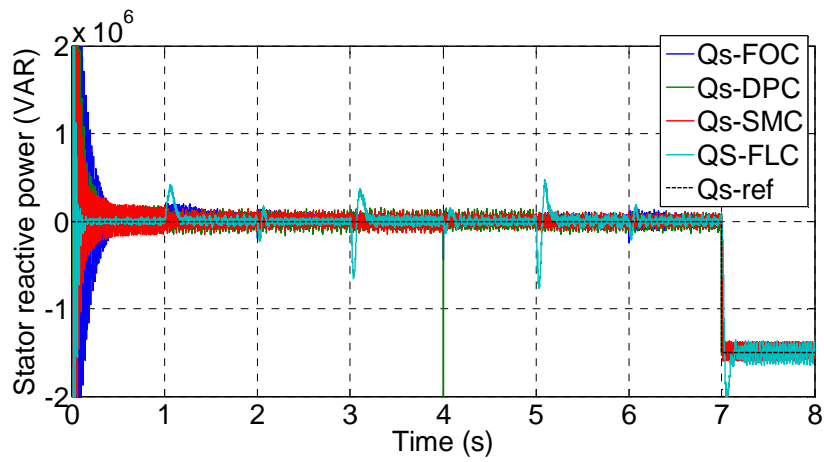


Figure 4.11 Grid line to neuter voltages unbalance and distortion.

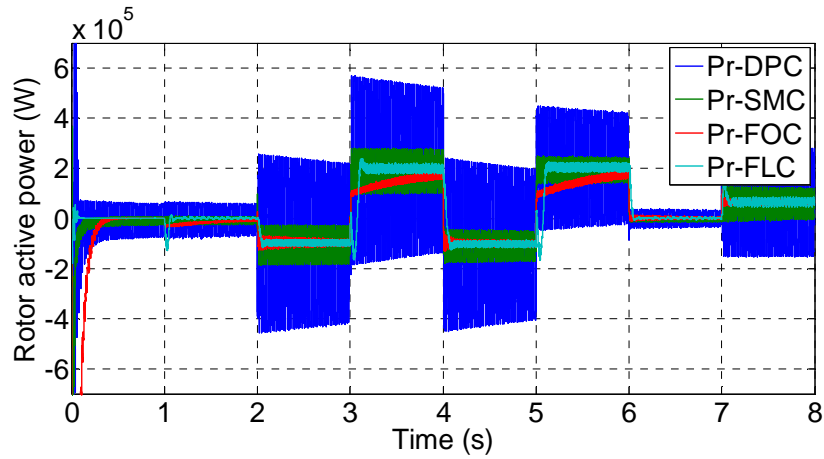
In order to make the comparison process easier, the four control laws (FOC, DPC, SMC, FLC) presented in this study are tested in the same simulation conditions and the same machine and power grid characteristics. Also, the results are grouped in one figure for each variable. The normal operating conditions test is presented in Figure 4.12.



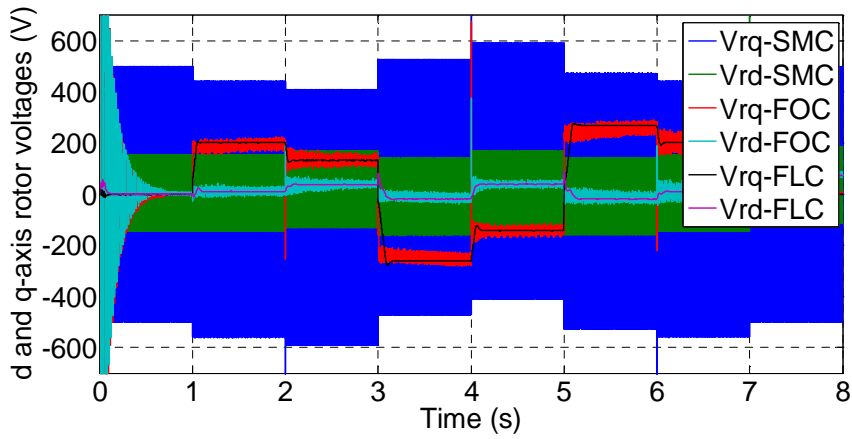
(a) Stator active power control.



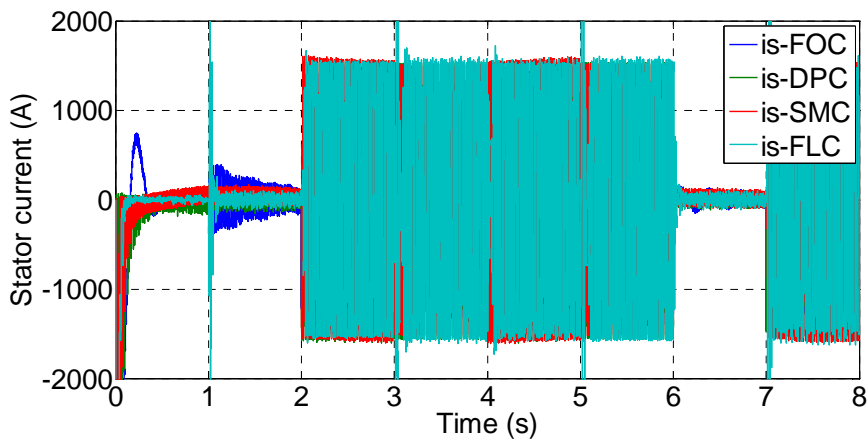
(b) Stator reactive power control.



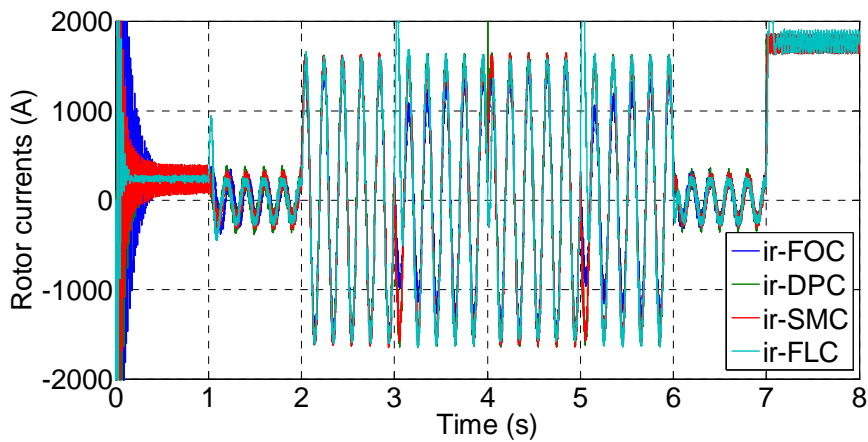
(c) Rotor active power.



(d) d and q axis rotor voltages.



(e) One stator phase current.



(f) One rotor phase current.

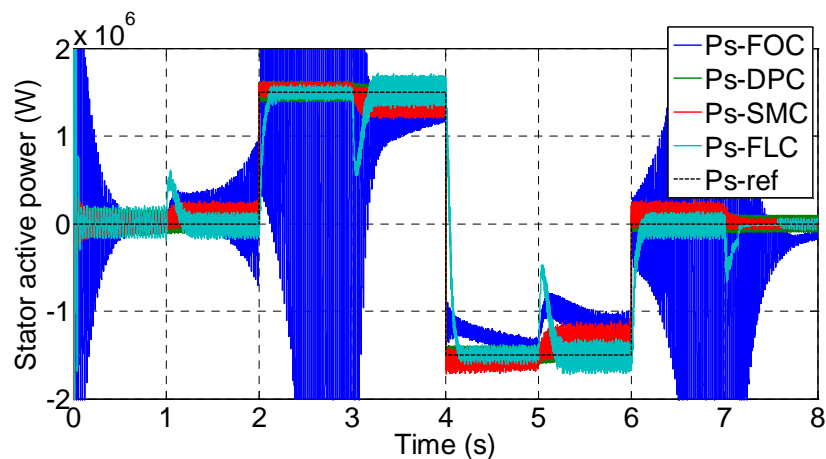
Figure 4.12 Decoupled stator powers control of DFIG under normal operating conditions.

• **Discussion of Normal Operating Conditions :**

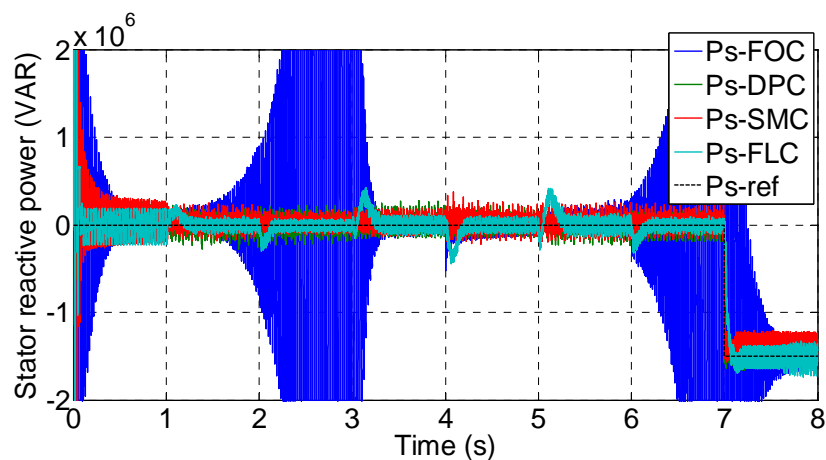
Figure 4.12.a and Figure 4.12.b show the behavior of the stator active and reactive power control of the DFIG in normal operating conditions, each control method achieved a good reference

tracking characteristic, the DPC and SMC law are more insensitive against rotor speed variation than the FOC and FLC, another remark which is the ability of working in the four-quadrants of the stator power/rotor slip for each control law. Figure 4.12.c shows the slip power of the DFIG, the direction of the slip power is changing according to the operating mode and the rotational speed. Figure 4.12.d shows the output of control law applied on the DFIG in each control method; the main remark is nature of the control law which is linear in the FOC and FLC, and discontinuous in the SMC which causes the *chattering* problem, in the DPC the switching order are injected directly without any modulation stage. Figure 4.12.e and Figure 4.12.f show the stator and the rotor currents respectively of the DFIG, they are both sinusoidal with good quality and they are changing according to the stator power and rotor power directions, another difference is the frequency, in the stator current the frequency is enforced by the grid voltage, however in the rotor current the frequency depends on the rotational speed.

Also, robustness against parameters variations has been tested as denoted in Figure 4.13.



(a) Stator active power control.



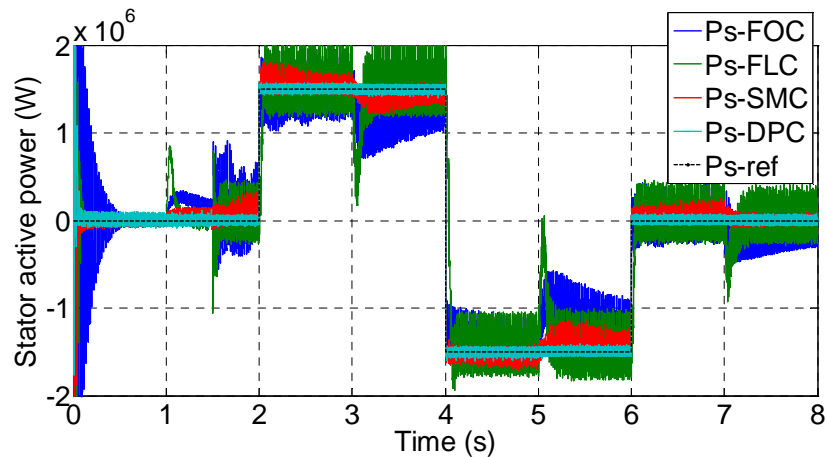
(b) Stator reactive power control.

Figure 4.13 Decoupled power control of DFIG under parameters variations operating conditions.

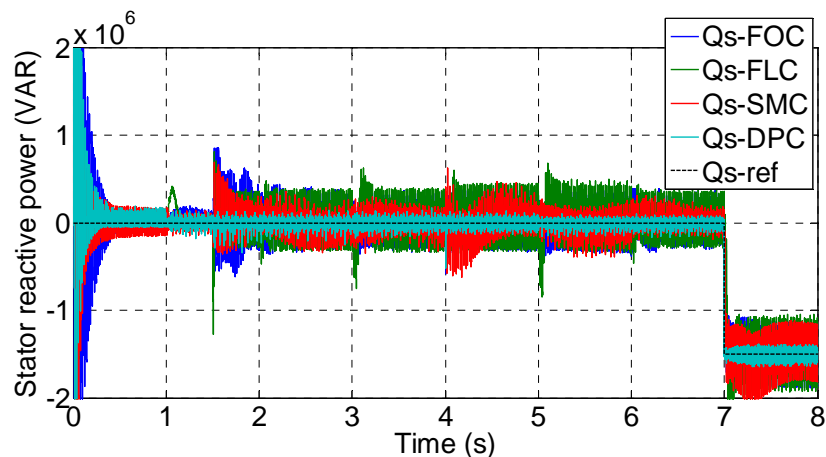
- **Discussion of Parameters Variations Operating Conditions:**

Figure 4.13.a and Figure 4.13.b show the behaviour of stator active and reactive power control of the DFIG in machine parameters variation conditions, DPC, SMC and FLC achieved a good tracking performance with a tiny extra ripple in the SMC and FLC, however FOC failed in this test and a huge oscillation and instability is appeared.

Robustness against grid voltage unbalance and distortion has been tested as denoted in Figure 4.14.



(a) Stator active power control.



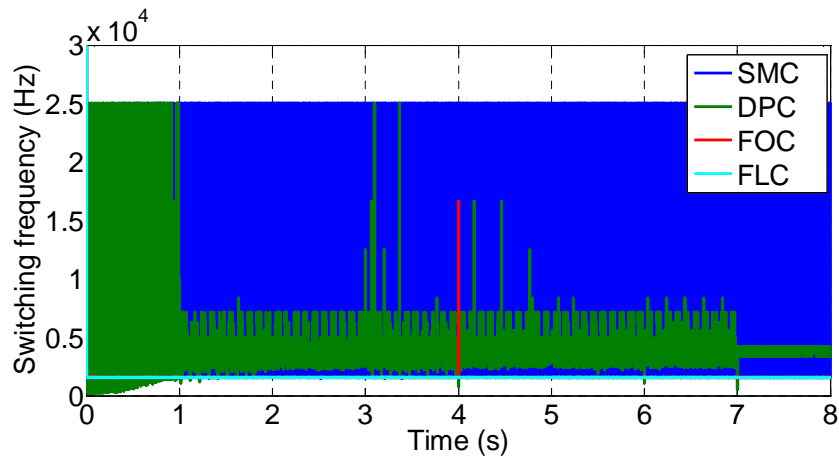
(b) Stator reactive power control.

Figure 4.14 Decoupled stator powers control of DFIG under unbalanced and disturbed utility grid.

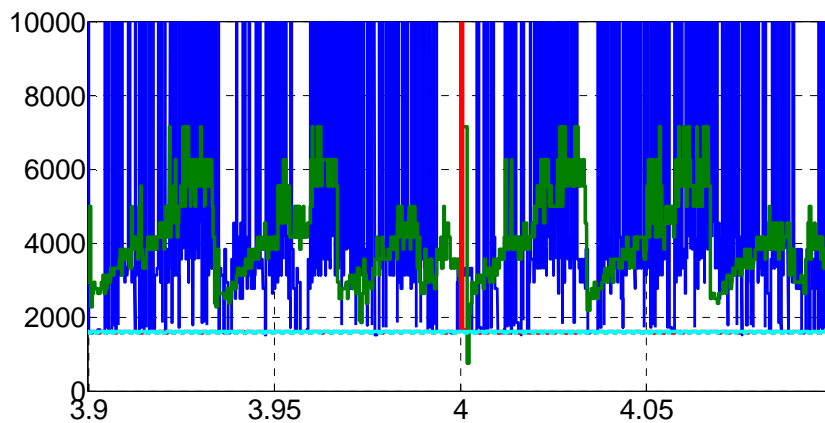
- **Discussion of Unbalanced and Disturbed Utility Grid :**

Figure 4.14.a and Figure 4.14.b show the behavior of the stator active and reactive power control of the DFIG in the grid voltage unbalance and distortion test, DPC gave an excellent reference tracking performance without any disturbance, SMC classified number two in this test with tiny extra ripple, FOC and FLC remained robust for reference tracking characteristic before and after injecting the grid voltage faults with a significant extra ripple in the supplied power response.

The switching frequency is an important factor in the evaluation of control laws in power electronics, it has to be small and constant in order to minimize the switching losses and make the filtering operation easier. Figure 4.15 compares the switching frequency for each control law.



(a) Switching frequency of modulation algorithm.



(b) Zoom

Figure 4.15 Switching frequency of each control law of the DFIG.

- **Discussion of Switching Frequency :**

Figure 4.15.a shows the behavior of the switching frequency of the RSC for each control method, and Figure 4.15.b shows a zoom of Figure 4.15.a, despite of the excellent tracking capability of the DPC and SMC laws, the nonlinear nature of these two control law makes the power electronic system suffers from a high and variable switching behavior. However FOC and FLC laws give a low and constant switching frequency, so they are more adequate for switching losses minimization and harmonic filtering problem. Table 4.4 gives a brief comparison study between the four control laws applied on the DFIG system.

Table 4.4: Brief comparison study of various direct power control laws of DFIG

Control law	FOC	DPC	SMC	FLC
Performance				
Principal	Pole-compensation method and compensation	Direct injection of switching orders in the converter	Variable structure control law	Interpretation of human reasoning and experience
Major complexity	Determination of k_p and k_i gains	Determination of best voltage vectors	Determination of k_d and k_q gains	Determination of fuzzy rules and K_e, k_{de}, k_{du} gains
Speed of response	Fast	Very fast	Very fast	Fast
Accuracy	Precise	Precise	Precise	Precise
Sensitivity to speed variation	Average	So good	So good	Good
THD of i_s	Test N°1: 01.33% Test N°2: 06.19% Test N°3: 10.66%	Test N°1: 01.14% Test N°2: 02.48% Test N°3: 06.22%	Test N°1: 01.29% Test N°2: 01.65% Test N°3: 07.35%	Test N°1: 01.30% Test N°2: 01.77% Test N°3: 11.53%
THD of i_r	Test N°1: 01.69 % Test N°2: 06.35% Test N°3: 13.07%	Test N°1: 04.14% Test N°2: 04.24% Test N°3: 08.70%	Test N°1: 02.44% Test N°2: 02.72% Test N°3: 09.69%	Test N°1: 01.70% Test N°2: 02.48% Test N°3: 13.90%
Robustness against : • parameters variation • grid voltage faults	Very weak Weak	Strong Strong	Strong Strong	Strong Average
Switching frequency	Low and constant	High and variable	High and variable	Low and constant
Major drawbacks	- Mathematical model is needed - No robustness	- Mathematical model is needed - Variable switching frequency	- Mathematical model is needed - Chattering phenomena	- Stability and robustness are not certain - High computational power is needed

4.4. Further Decoupled Direct Power Control Laws of DFIG

Diverse control strategies for WT-driven DFIGs have been proposed by different authors over the last decade, some of which constitute real alternatives to classical vector control schemes based on encoder and PI regulators. Among others, various robust control techniques have been explored. At the same time, other control and estimation schemes, which are commonly applied to electric drives like “sensorless” and DTC, have also been adopted in the particular case of DFIGs [18]. One example of each control law is presented in this section.

4.4.1. Vector Control with RST or LQG Regulators

In [19], the authors present a control method for the RSC in order to regulate the active and reactive power exchanged between the machine and the grid. The presented results show that robust control method as LQG can be a very attractive solution for devices using DFIG such as WPGSSs. Indeed, most of the studied DFIG control schemes use classical PI controllers but the comparison done in this chapter show that the limits of this type of controller can have negative effects on the quality and the quantity of the generated power. Using a polynomial RST can be a solution but its tuning parameters are difficult to adjust and disturbances can be not perfectly rejected. The LQG controller is no more complex than the RST one for a numerical implementation and it is more attractive in terms of tuning parameters and provided results.

4.4.2. Nonlinear Input-Output Feedback Linearization Control

In [20], the authors present an adaptive nonlinear controller has been introduced for DFIM drives. The proposed controller design is based on the adaptive input-output feedback linearization control (IOFLC) approach and is capable of making the system states trajectories follow the torque and flux reference signals in spite of stator and rotor resistance uncertainties and external load torque disturbance. The proposed control approach has been tested for both the motoring and generating modes of operation bellow and above the synchronous speed.

4.4.3. Second-Order Sliding-Mode Control

In [21], the authors present a second-order-SMC both for grid synchronization and power control of a DFIG has been presented. It allows keeping the tracking accuracy and robustness features characteristic of standard SMC, while leading to a fixed switching frequency of the RSC transistors. Experimentation conducted on a 7 kW DFIG test bench proves that high dynamic performance control and superior robustness against DFIG parameter variations are achieved when applying the proposed global second-order-SMC scheme. In addition, bumpless transfer between the grid synchronization and power control operating regimes is guaranteed, which results in smooth connection of the DFIG stator to the grid.

4.4.4. Adaptive Back-Stepping Control

In [22], the authors present a nonlinear Adaptive robust control of active and reactive power by the use of the technique Back-stepping a DFIG system incorporated in a WT. A new control technique for wind systems is presented. This control scheme is based on an adaptive pole placement control strategy integrated to a Back-stepping control scheme. The overall stability of the system is shown using *Lyapunov* technique. The performance and robustness are analyzed and compared by simulation based Matlab/Simulink software, the proposed control system seems robust and stable in case of disturbances like speed and torque variations.

4.4.5. Model-Based Predictive Control

In [23], the authors propose a predictive DPC (PDPC) strategy for DFIGs. A DFIG model that defines the stator active and reactive power flow was presented. Based on such a model, a DFIG's active and reactive power variations with a fixed sampling period were predicted, which was then used to directly calculate the required rotor voltage to eliminate stator power errors at the end of the sampling period. Experimental results from a 1.5kW DFIG test system proved the dynamic performance and power control accuracy of the PDPC method. System performance during parameter variation and with varying reference further illustrated the performance of the PDPC method.

4.4.6. Deadbeat Control

In [24], the authors provide the designing and the modeling of a deadbeat power control scheme for DFIG. In this way, the deadbeat power control aims the stator active and reactive power control using the discretized DFIG equations in synchronous coordinate system and stator flux orientation. The deadbeat controller calculates the rotor voltages required to guarantee that the stator active and reactive power reach their desired references values at each sample period using a rotor current space vector loop. Experimental results using a TMS320F2812 platform are presented to validate the proposed controller.

4.4.7. Model Reference Adaptive Control

In [25], a model reference adaptive controller (MRAC) is implemented to test an optimal indirect control of the active and reactive power amounts exchanged with the grid and based on the rotor currents measurement. The proposed MRAC controller is implemented in a real time via a dSPACE 1104 card. The obtained results provided good tracking of the predefined references regardless the wind speed changing. It is shown that the adaptive control method can be a very attractive solution for systems using the DFIG for wind energy conversion.

4.4.8. Robust H_∞ Control

In [26], the authors presented a comparative study in order to control stator active and reactive powers exchanged between the DFIG and the grid. Simulations results has been carried out using Matlab show interesting performances of the proposed approach in terms of the reference tracking and stability, the robustness against DFIG parameters variations and there are improvements in the dynamic response and stability of the generator system with the H_∞ controller. Settling time in active and reactive power response is 0.1 sec in H_∞ controller, however the settling time is 0.4 sec in case of PI controller.

4.4.9. Adaptive Neural Network Control

In [27], the authors presented the experimental application of DPC of a DFIG under oriented stator flux using a controller based on multilayer perceptron (MLP). The choice of training datasets and the training process itself presented more difficulties when compared with the other tasks of the overall design of the controller; however, these tasks are executed offline and consequently, the application of the MLP controller becomes easier; it exhibits a simpler experimental implementation, requires a lower computational effort. The DPC approach combined with the MLP controller has maintained the features of DPC and has added the inherent MLP's capability to control the coupled and nonlinear system and to generalize the performance for distinct operating conditions. The experimental results have shown the effectiveness of the controller, i.e., it presents fast responses, no overshoot, no steady-state error, and minimal oscillation around the steady-state operating points.

4.4.10. Fuzzy Logic Control

In [28], a vector control strategy has been investigated based on the oriented grid flux intended for the DFIG, which can control the stator active and reactive powers independently with desired performances as stability and robustness of the global structure. The vector control is achieved using an optimized FLC. The controller is designed by taking into account the similarity of the conventional PI controller actions but with some optimization in order to approve and ameliorate its behavior. The obtained results demonstrate that the proposed DFIG system control based on the optimized FLC may be considered as an interesting solution in the wind power generation area.

4.4.11. Adaptive Neuro-fuzzy Control

In [29], the authors presented a direct control of active and reactive powers of a stator flux oriented DFIG without current controllers are proposed. The power controller is based on ANFIS combined to a first order T-S FLC and has the function of determining the required rotor voltage components. The experimental results show zero steady state error, fast response of the active and reactive power, no overshoot and minimal oscillation around the steady-state operating points, confirming the feasibility of the proposed strategy with the additional advantage of eliminating the use of rotor current controllers.

4.5. Conclusion

The simulation results proved that FOC is simple in implementation but it is hard to determine the optimal PI gains, the FOC law gives a good performance in the normal operating conditions, however it degrades in the parameters variations condition. DPC method has a fast dynamic response, excellent reference tracking performance and reduced power ripple in normal and degraded operating mode, its only problem is the traditional problem of any hysteresis control law which is the variable switching frequency which can make the filtering process of the supplied current so difficult. SMC law also has a fast dynamic response and good reference tracking performance except a small extra power ripple in the degraded operating modes, however the SMC law is harder in implementation than the FOC law. FLC law has a little bit slower dynamic response and good reference tracking performance in both normal and degraded operating mode, the implementation of an intelligent FLC is simple, but it depends on the experience of the operator especially how to tune its scaling factors.

Based on the previous results, each nonlinear control law has its points of strength and points of weakness, maybe a hybrid control law can reach a better dynamic performance and robustness capability, for example, DPC based on the sliding mode approach or FIS, recently, hybrid control law became a strong research axis and some of them are gained a remarkable results.

4.6. References of Chapter 4

- [1] J. Rodriguez and P. Cortes. Predictive control of power converters and electrical drives, Universidad Tecnica Federico Santa Maria, Valparaiso, Chile, 2012.
- [2] I. Takahashi and T. Noguchi, A new quick response and high efficiency control strategy for an induction motor, *IEEE Trans. on Industry Applications*, Vol. 22, No. 5, pp. 820–827, Sep. 1986.
- [3] R. Datta and V.T. Ranganathan, Direct power control of grid-connected wound rotor induction machine without rotor position sensors, *IEEE Trans. Power Electronics*. Vol. 16, , No. 3, pp. 390–399, 2001.
- [4] F. Blaschke, The principle of field-orientation applied to transvector closed-loop control system for rotating field machines, *Siemens Review*, Vol. 39, No. 5, pp. 217–219, 1972.
- [5] F. Poitiers, T. Bouaouiche and M. Machmoum, Advanced control of a doubly-fed induction generator for wind energy conversion, *Electric Power Systems Research*, Electric Power Systems Research, Vol. 79, pp. 1085–1096, 2009.
- [6] M. Depenbrock, Direct self-control (DSC) of inverter-fed induction machine, *IEEE Trans. Power Electron.*, Vol. 3, No. 4, pp. 420–429, Oct. 1988.
- [7] J. Bendl, M. Chombt, and L. Schreier, Adjustable-speed operation of doubly fed machines in pumped storage power plants, *Ninth International Conference on Electrical Machines and Drives*, pp. 223–227, Sep., 1–3, 1999.
- [8] G. Abad, M. A. Rodriguez, and J. Poza, Two-level VSC-based predictive direct power control of the doubly fed induction machine with reduced power ripple at low constant switching frequency, *IEEE Trans. Energy Convers.*, Vol. 23, No. 2, pp. 570–580, Jun. 2008.
- [9] Y. S. Lai and J. H. Chen, A new approach to direct torque control of induction motor drives for constant inverter switching frequency and torque ripple reduction, *IEEE Trans. Energy Convers.*, Vol. 16, No. 3, pp. 220– 227, Sep. 2001.
- [10] M. V. Kazemia, M. Moradib and R. V. Kazemic, Minimization of powers ripple of direct power controlled DFIG by fuzzy controller and improved discrete space vector modulation, *Electric Power Systems Research*, Vol. 89, pp. 23-30, 2012.
- [11] V. I. Utkin, Sliding mode control design principles and applications to electric drives, *IEEE Trans. Ind. Electron.*, Vol. 40, No. 1, pp. 23–36, 1993.
- [12] J. Hu, H. Nian, B. Hu, Y. He, Z. Q. Zhu, Direct active and reactive power regulation of DFIG using sliding-mode control approach, *IEEE Trans. Energy Convers.*, Vol. 25, No. 4, 2010.
- [13] S.Z. Chen, N.C. Cheung, K.C. Wong, J. Wu, Integral variable structure direct torque control of doubly fed induction generator, *IET Renew. Power Generation*, Vol. 5, No. 1, pp. 18-25, 2011.
- [14] J.E Slotine, W. Li. *Applied nonlinear control*. Prentice Hall; 1991.
- [15] Y. Ren, H. Li, J. Zhou, Z. An, J. Liu, H. Hu and H. Liu. Dynamic performance analysis of grid-connected DFIG based on fuzzy logic control. *IEEE International Conference on Mechatronics and Automation*, Changchun, China, pp. 719–723, 2009.
- [16] A. Dida, and D. Benattous, Doubly-fed induction generator drive based WECS using fuzzy logic controller, *Frontiers in Energy*, Vol. 9, No. 3, pp. 272-281, 2015.
- [17] S. El Aimani, Practical Identification of a DFIG based wind generator model for grid assessment, *IEEE International Conference on Multimedia Computing and Systems (ICMCS '09)*, pp. 278-285, 2009.
- [18] G. Tapia, G. Santamaria, M. Telleria, and A. Susperregui, Methodology for Smooth Connection of Doubly Fed Induction Generators to the Grid, *IEEE Trans. on Energy Conversion*, Vol. 24, No. 4, Dec. 2009.
- [19] F. Poitiers, T. Bouaouiche, M. Machmoum, Advanced control of a doubly-fed induction generator for wind energy conversion, *Electric Power Systems Research*, Vol. 79, pp. 1085–1096, 2009.
- [20] A. F. Payam, An adaptive input-output feedback linearization controller for doubly-fed induction machine drives, *Serbian Journal of Electrical Engineering*, Vol. 5, No. 1, pp. 139-154, May 2008.

- [21] A. Susperregui, M. I. Martinez, G. Tapia and I. Vechiu, Second-order sliding-mode controller design and tuning for grid synchronisation and power control of a wind turbine-driven doubly fed induction generator, *IET Renew. Power Generation*, Vol. 7, No. 5, pp. 540–551. 2013.
- [22] B. Bossoufi, M. Karim, A. Lagrioui, M. Taoussi and A. Derouich, Adaptive backstepping control of DFIG generators for variable-speed wind turbines system, *Journal of Electrical Systems*, Vol. 10, No. 3, pp. 317-330, 2014.
- [23] D. Zhi, L. Xu, and B. W. Williams. Model-based predictive direct power control of doubly fed induction generators, *IEEE Trans. on Power Electronics*, Vol. 25, No. 2, February 2010.
- [24] Alfeu J. Sguarezi Filho and Ernesto Ruppert (2011). Modeling and Designing a Deadbeat Power Control for Doubly-Fed Induction Generator, *Wind Energy Management*, Dr Paritosh Bhattacharya (Ed.), ISBN: 978-953-307-336-1, InTech, Available from: <http://www.intechopen.com/books/wind-energy-management/modelingand-designing-a-deadbeat-power-control-for-doubly-fed-induction-generator>
- [25] S. Abdeddaim, A. Betka, S. Drid and M. Becherif, Implementation of MRAC controller of a DFIG based variable speed grid connected wind turbine, *Energy Conversion and Management*, Vol. 79, pp. 281–288, 2014.
- [26] S. Abdelmalek, H. Belmili, L. Barazane and L. Abdelkader, A New Robust H_∞ Control Power, *International Conference on Control, Engineering & Information Technology (CEIT'14)*, pp.123-128. 2014.
- [27] R. V. Jacomini and E. Bim, Implementation of the Direct Power Control of a Doubly Fed Induction Generator by using a Takagi-Sugeno Neuro-Fuzzy Inference System, the 39th IEEE Annual Conference Industrial Electronics Society (IECON 2013), 2013.
- [28] R. Cheikh, A. Menacer, S. Drid and M. Tiar, Application of fuzzy logic control algorithm as stator power controller of a grid-connected doubly-fed induction generator, *Frontiers in Energy*, Vol. 7, No. 1, pp. 49–55. 2013.
- [29] R. Andreoli de Marchi, P. Sergio Dainez, F. J. Von Zuben, and E. Bim, A Multilayer Perceptron Controller Applied to the Direct Power Control of a Doubly Fed Induction Generator, *IEEE Trans. On Sustainable Energy*. Vol. 5, No. 2, 2014.

Chapter 5:

Modeling and Control of Back-to-Back Multilevel Converters based DFIG using Neuro-Fuzzy Controllers

Chapter 5: Modeling and Control of Back-to-Back Multilevel Converters based DFIG using Neuro-Fuzzy Controllers

5.1. Introduction

This chapter deals with the WPGS equipped with a DFIG and two back-to-back five-level (5L) neutral point clamped (NPC) converters in the rotor circuit. The modeling and the control of the 5L converter is presented. A new method of controlling the DC-link voltage through the 5L rectifier is presented, the proposed control algorithms consist of two loops, the fundamental loop controls the average value of the DC-link voltage, whereas the supplementary loop controls the difference between the two voltages in each half-arm of the DC-bus using a clamping bridge circuit.

In this chapter, the simulations have been carried out using the Matlab/Simulink with motor convention on both rotor and stator sides of the DFIG,

5.2. Multilevel converters

Nowadays, multilevel converters have attracted increasing attention in medium-voltage and high-power applications such as static VAR compensators and renewable energy sources [1-2]. The term multilevel starts with the three-level inverter introduced by *Nabae et al.* [3]. By increasing the number of levels in the inverter, the output voltages have more steps generating a staircase waveform, which has a reduced harmonic distortion. However, a high number of levels increases the control complexity and introduces voltage imbalance problems [4]. Three different topologies have been proposed for multilevel inverters: diode-clamped (NPC) [5-6]; capacitor-clamped (flying-capacitors (FC)) [7-8]; and cascaded multi-cell (H-bridge) with separate DC sources [9-10]. In addition, several modulation and control strategies have been developed for multilevel inverters including the following: multilevel sinusoidal PWM, multilevel selective harmonic elimination, and Space-Vector Modulation (SVM) [3]. Figure 5.1 shows four examples of the three previously mentioned multilevel converters.

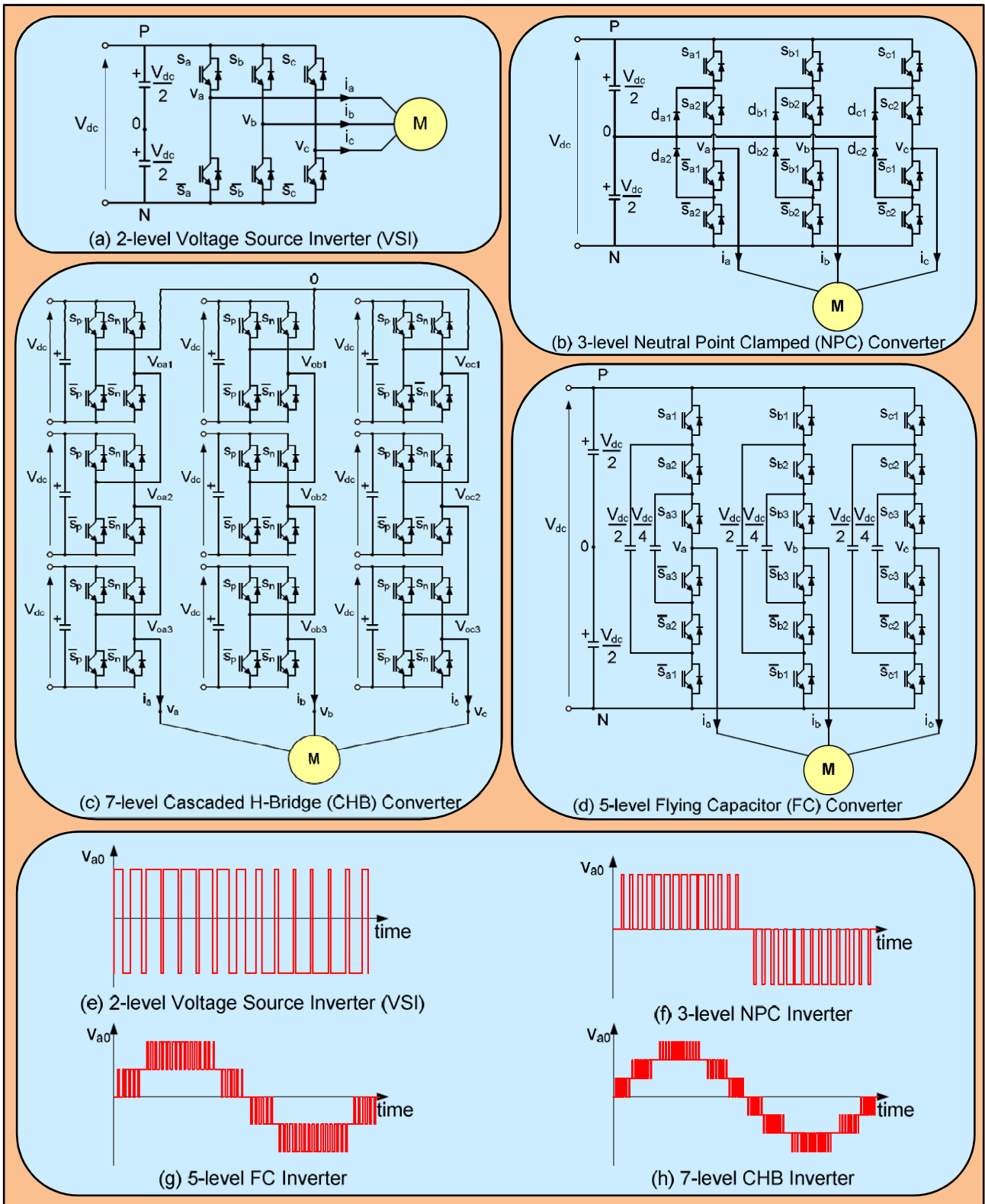


Figure 5.1 Topologies and phase voltages of the conventional two-level and multilevel VSIs [13].

5.3. Five-Level NPC Converter Model

The topology of the 5L NPC converter is shown in Figure 5.2. For the operation of this converter, seven possible configurations are used for each arm [11]. Table 6.1 presents the electrical

magnitudes that characterize each configuration (with M as the origin of the potentials and V_{KM} ($K = A, B$ or C) as the potential of node K of arm k ($k = 1, 2$ or 3)), the various configurations are shown in Figure 5.3. The continuous voltage U_{c1} , U_{c2} , U_{c3} , and U_{c4} are provided by controlling the GSC, which is also a 5L NPC rectifier.

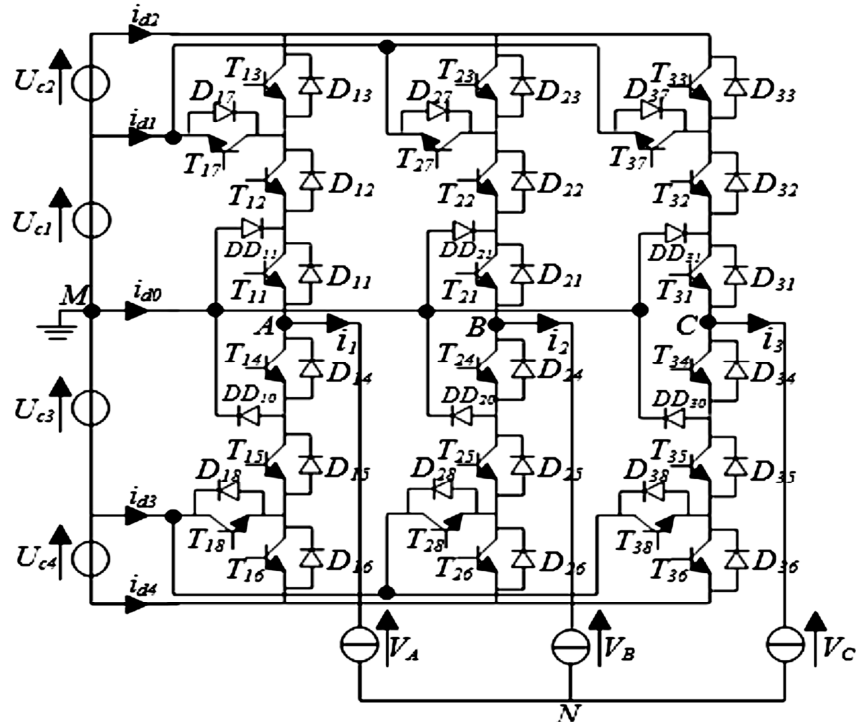


Figure 5.2 Topology of the 5L NPC converter [5].

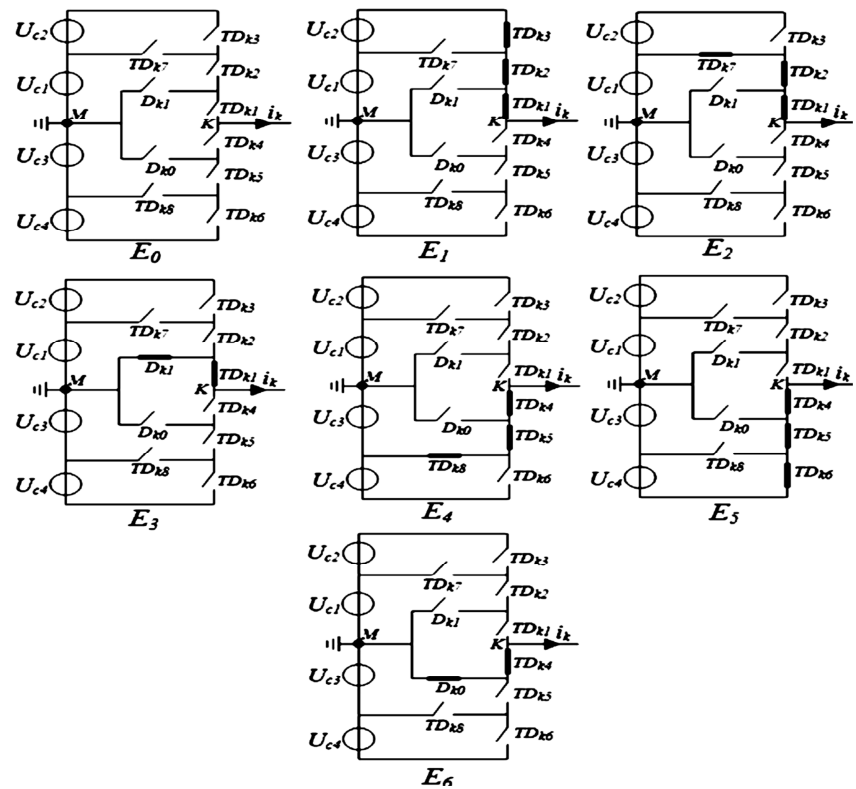


Figure 5.3 Different configurations of the 5L NPC converter [5].

Table 5.1: Electrical magnitude of each configuration of arm k.

<i>Configurations</i>	<i>Electric grandeur</i>
E_0	$i_k = 0$
E_1	$V_{KM} = U_{c1} + U_{c2}$
E_2	$V_{KM} = U_{c1}$
E_3	$V_{KM} = 0$
E_4	$V_{KM} = -U_{c3}$
E_5	$V_{KM} = -U_{c3} - U_{c4}$
E_6	$V_{KM} = 0$

- **Connection Functions**

Each switch TD_{ks} introduces a connection function F_{ks} that describes its state, such as the following: $F_{ks} = 1$ if the switch is closed, $F_{ks} = 0$ if the switch is open ($s = 1, 2, \dots, 8$) [5].

- **Complementary Control**

To avoid short circuit of the voltage sources and the converter become completely controlled, several complementary controls are possible for arm k of the converter. For an optimal operation, the connection functions of the switches on the arm are given by the following system of equations [12]:

$$\begin{cases} F_{k4} = 1 - F_{k2} \\ F_{k5} = 1 - F_{k1} \\ F_{k6} = 1 - F_{k3} \\ F_{k7} = F_{k1} F_{k2} (1 - F_{k3}) \\ F_{k8} = F_{k4} F_{k5} (1 - F_{k6}) \end{cases} \quad (5.01)$$

For the arm k, the connection functions of the half-arm are expressed by the switch connection functions as follows:

$$\begin{cases} F_{k1}^b = F_{k1} F_{k2} F_{k3} \\ F_{k0}^b = F_{k4} F_{k5} F_{k6} \end{cases} \quad (5.02)$$

The voltages across the load are given by the following system:

$$\begin{bmatrix} V_a \\ V_b \\ V_c \end{bmatrix} = \frac{1}{3} \begin{bmatrix} 2 & -1 & -1 \\ -1 & 2 & -1 \\ -1 & -1 & 2 \end{bmatrix} \left\{ \begin{bmatrix} F_{17} + F_{11}^b \\ F_{27} + F_{21}^b \\ F_{37} + F_{31}^b \end{bmatrix} U_{c1} + \begin{bmatrix} F_{11}^b \\ F_{21}^b \\ F_{31}^b \end{bmatrix} U_{c2} - \begin{bmatrix} F_{18} + F_{10}^b \\ F_{28} + F_{20}^b \\ F_{38} + F_{30}^b \end{bmatrix} U_{c3} - \begin{bmatrix} F_{10}^b \\ F_{20}^b \\ F_{30}^b \end{bmatrix} U_{c4} \right\} \quad (5.03)$$

The Matlab/Simulink code of the later equation is presented in Figure A.8 in the appendix.

Using the connection functions of the half-arm yields the inverter input currents according to load currents i_1 , i_2 , and i_3 as follows:

$$\begin{cases} i_{dc1} = F_{17}i_1 + F_{27}i_2 + F_{37}i_3 \\ i_{dc2} = F_{11}^b i_1 + F_{21}^b i_2 + F_{31}^b i_3 \\ i_{dc3} = F_{18}i_1 + F_{28}i_2 + F_{38}i_3 \\ i_{dc4} = F_{10}^b i_1 + F_{20}^b i_2 + F_{30}^b i_3 \end{cases} \quad (5.04)$$

i_{d0} is expressed according to the load currents by the relation:

$$i_{d0} = (i_1 + i_2 + i_3) - (F_{17} + F_{18} + F_{11}^b + F_{10}^b)i_1 - (F_{27} + F_{28} + F_{21}^b + F_{20}^b)i_2 - (F_{37} + F_{38} + F_{31}^b + F_{30}^b)i_3 \quad (5.05)$$

5.4. Modulation Strategy for Five-Level NPC Converter

The fundamental objective of a modulation technique is to obtain the best waveforms (voltages and currents) with minimum losses. Other secondary control objectives can be dealt with the proper modulation technique such as common-mode voltage reduction, dc voltage balancing, input current harmonics minimization, low dv/dt's, among others. To achieve simultaneously all the control targets is impossible, so a trade-off is needed [13]. A classification of the modulation techniques for power converters is shown in Figure 5.4. In this classification, the modulation techniques are divided in four main groups: PWM, SVM, harmonic control modulation and other variable switching frequency methods.

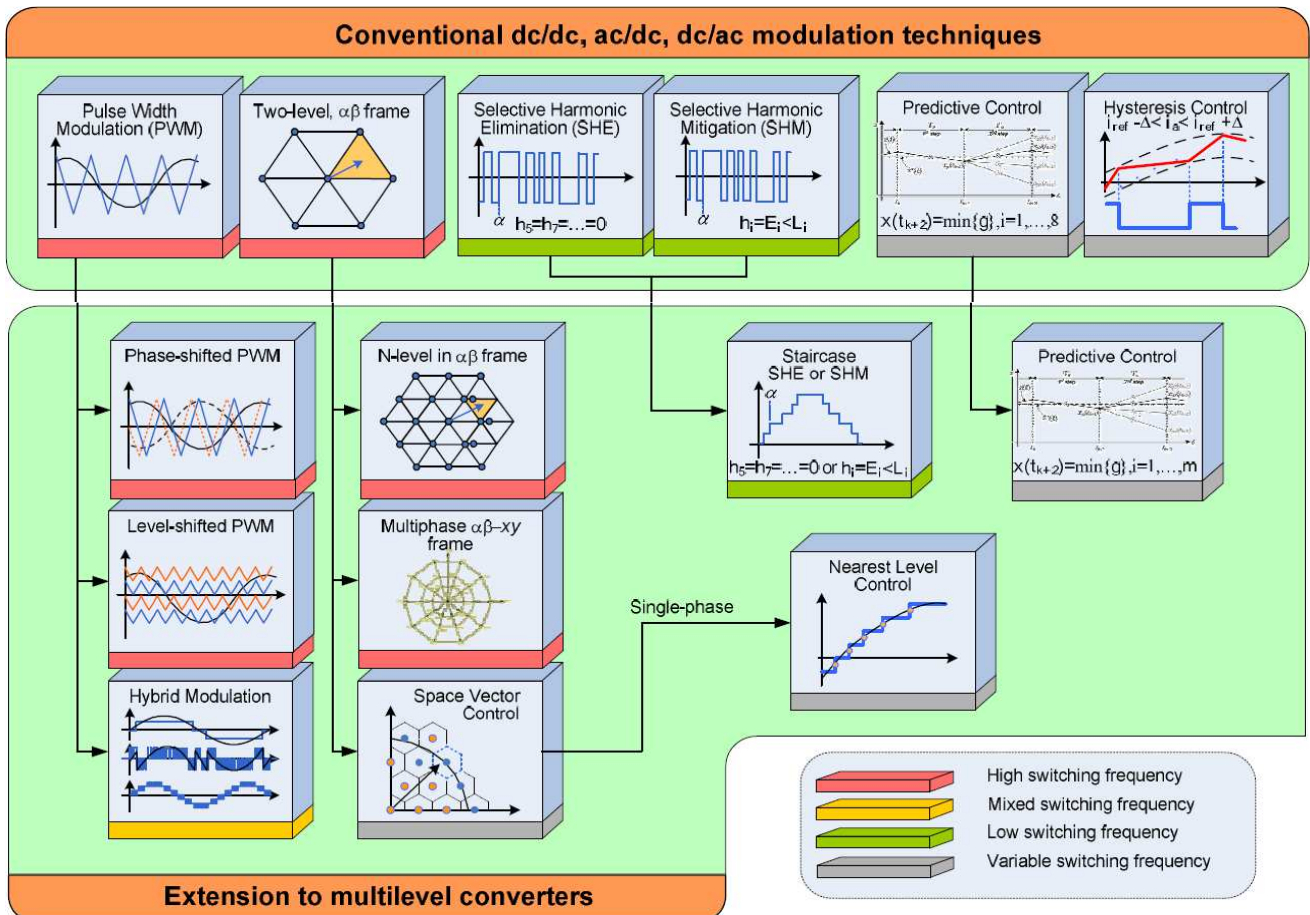


Figure 5.4 Classification of the most common modulation techniques for power converters [13].

In this study, the level-shifted PWM with four triangular bipolar carriers is employed and presented in Figure A.6. Modulation index “m” and modulation rate “r” are two parameters that must be taken into consideration in the sinusoidal PWM technique [12-14]. After we have chosen the control strategy and the three voltage references, two stages characterize the control algorithm, where:

$$U_c = U_{c1} = U_{c2} = U_{c3} = U_{c4} \tag{5.06}$$

- *Intermediate voltage determination*

$$\begin{cases} U_{refk} \geq U_{car-4} \Rightarrow V_{k4} = 2U_c \\ U_{refk} < U_{car-4} \Rightarrow V_{k4} = U_c \end{cases} \quad \& \quad \begin{cases} U_{refk} \geq U_{car-3} \Rightarrow V_{k3} = U_c \\ U_{refk} < U_{car-3} \Rightarrow V_{k3} = 0 \end{cases} \quad \& \quad \begin{cases} U_{refk} \geq U_{car-2} \Rightarrow V_{k2} = 0 \\ U_{refk} < U_{car-2} \Rightarrow V_{k2} = -U_c \end{cases} \quad \& \quad \begin{cases} U_{refk} \geq U_{car-1} \Rightarrow V_{k1} = -U_c \\ U_{refk} < U_{car-1} \Rightarrow V_{k1} = -2U_c \end{cases} \tag{5.07}$$

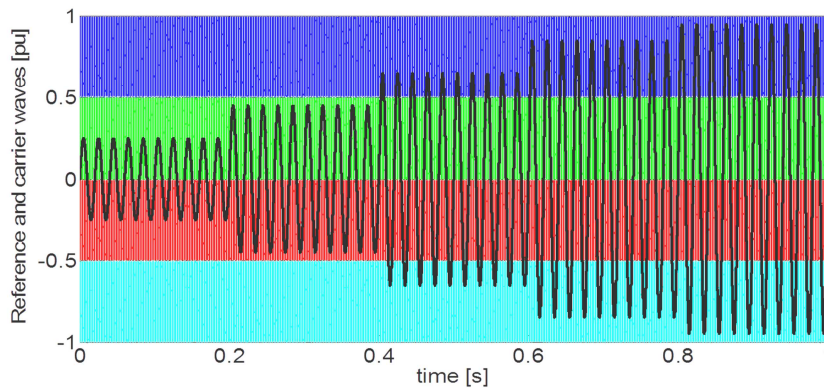
- *Determination of V_{KM} and switch order control B_{ks} .*

$$V_k = V_{k1} + V_{k2} + V_{k3} + V_{k4} \tag{5.08}$$

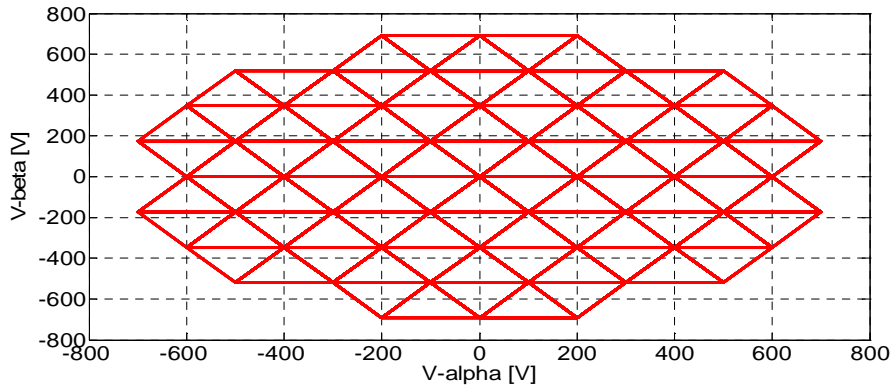
V_{KM} and switch order control B_{ks} are given in Table 5.2. The PWM of the 5L NPC converter is presented in Figure 5.5. Figure 5.5a shows the comparison between the reference waves and the triangular carrier ($m=60$ and $r= 0.25 \rightarrow 0.95$). Figure 5.5b shows the output voltage in the $\alpha\beta$ plan, which occupies all the possible cases, Figure 5.5c shows the increased fundamental of the output voltage, Figure 5.5d shows the total harmonic distortion of the output voltages which seem falling down depending of the modulation ratio.

Table 5.2: V_{KM} and switch order control B_{ks}

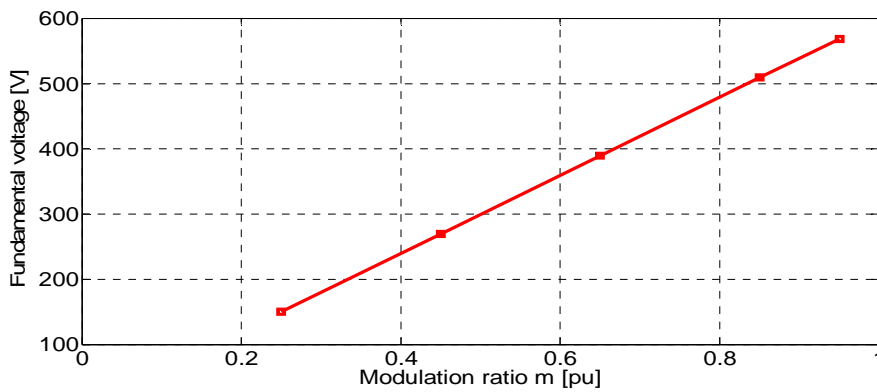
V_{KM}	Switch order
$2U_c$	$B_{k1}=1, B_{k2}=1, B_{k3}=1$
U_c	$B_{k1}=1, B_{k2}=1, B_{k3}=0$
0	$B_{k1}=1, B_{k2}=0, B_{k3}=0$
$-U_c$	$B_{k1}=0, B_{k2}=0, B_{k3}=1$
$-2U_c$	$B_{k1}=0, B_{k2}=0, B_{k3}=0$



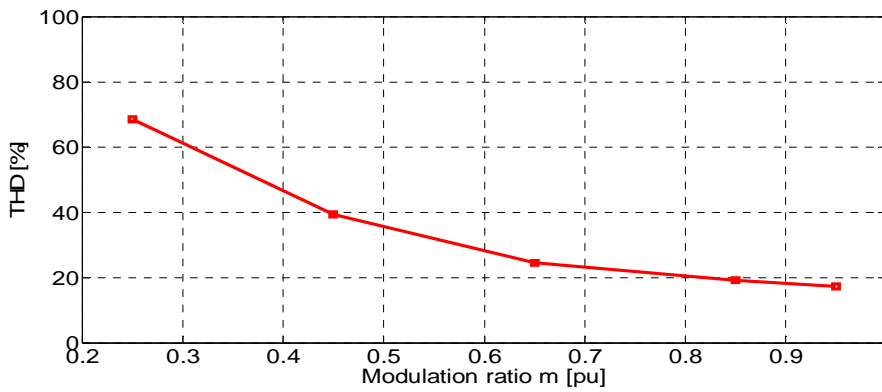
(a) Reference and carrier waves



(b) Output voltage components V_β (V_α)



(c) Fundamental of output voltage



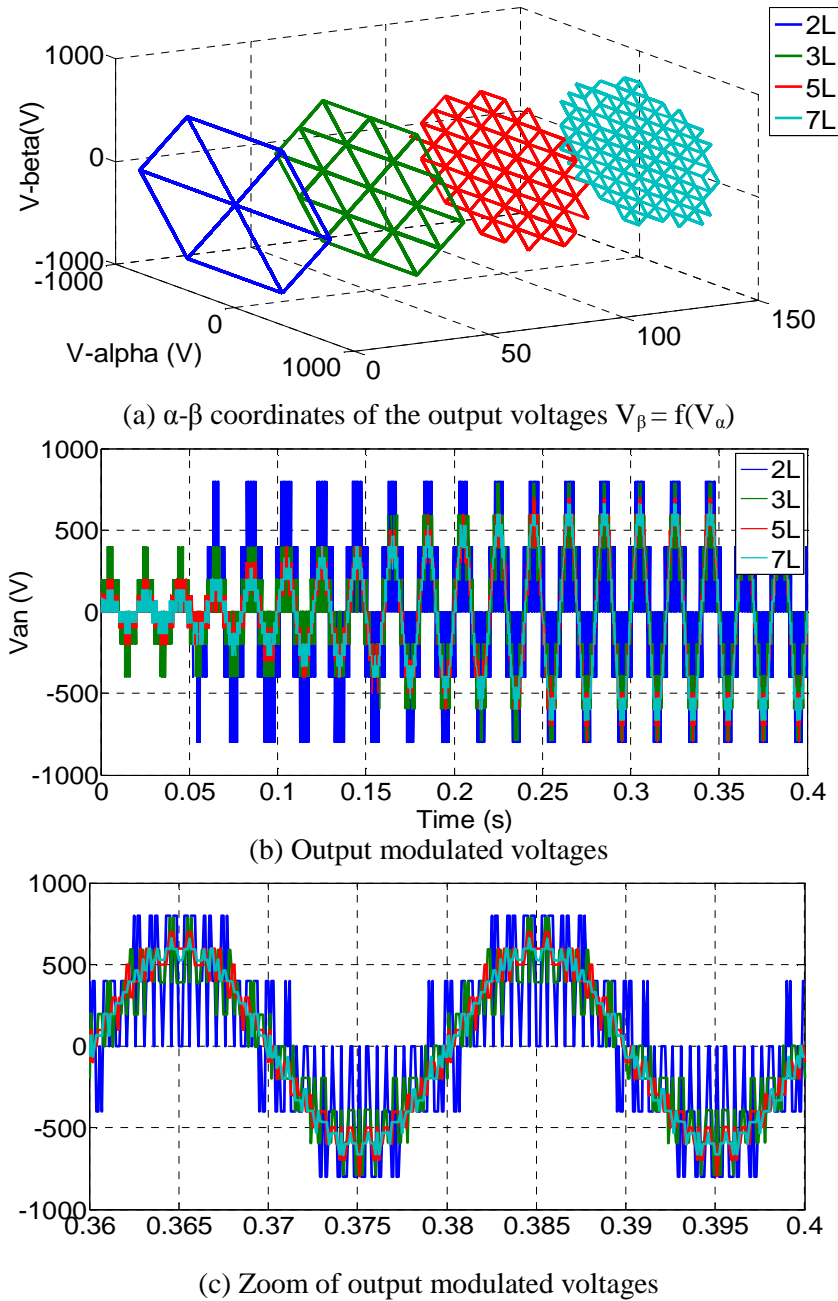
(d) THD of output voltage

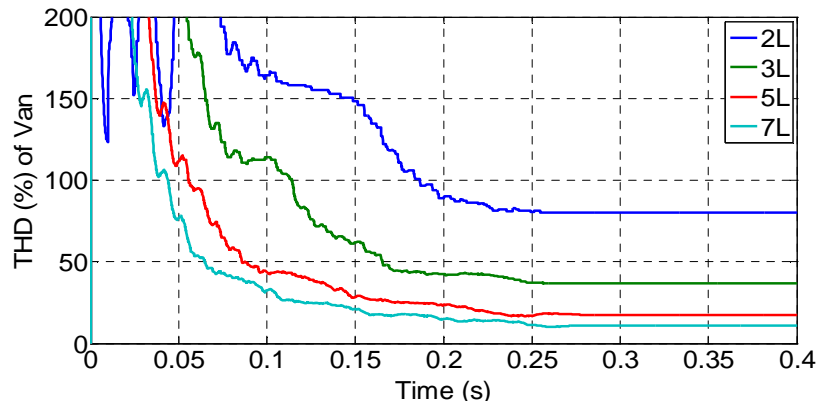
Figure 5.5 Proposed PWM strategy for the 5L NPC converter.

5.5. Comparison between 3L, 5L and 7L NPC Converter

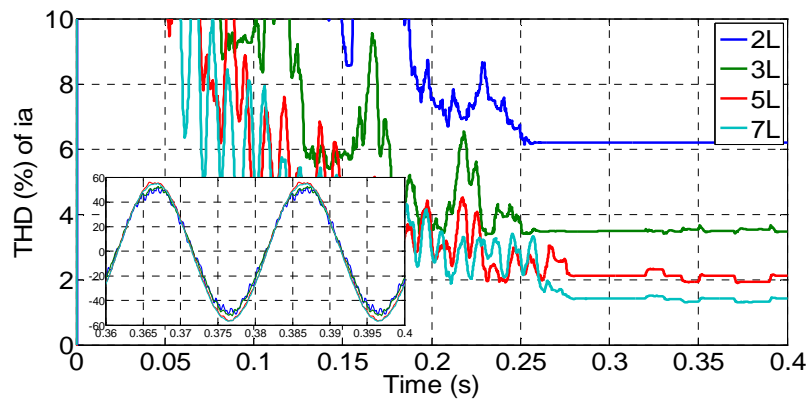
In order to show the reason behind choosing the 5L converter, a comparative study is carried out between the 5L converter and the 2L, 3L, and the 7L NPC converters. In the last decades, 3L and 7L NPC converters modeling and control strategies were a strange researching axis, and they are massively available in the literature as research papers or PhD thesis, we take for example [15-16-17-18-19].

The same level-shifted PWM strategy with N-1 (N: number of levels) triangular bipolar carriers is also employed in the 3L and 7L NPC converters (Figure A.3 and Figure A.10), this strategy is characterized by modulation index $m = 20$ and modulation rate changes from $r = 0$ until 1. Figure 5.6 presents the output currents and voltages and their THD for a PF=0.9, the Table 6.3 gathers some statistics about the NPC multilevel converters according to the levels number.





(d) THD of phase-to-ground voltage



(e) THD of line current

Figure 5.6 PWM strategy for 2L, 3L, 5L, and 7L converters

Table 5.3: Comparison between 2L, 3L, 5L and 7L NPC converters

Number of levels	Number of switches	Number of diodes	Number of capacitors	Total number	Capacitor voltage (V)	THD (%) of Van	THD (%) of ia
2Levels	6	6	1	13	1200	80.3	6.2
3Levels	12	18	2	32	600	36.8	3.6
5Levels	24	30	4	58	300	17.4	2.2
7Levels	36	42	6	84	200	11	1.5

After this information, we can say that the 5L converter represents a good combination between less complexity and less harmonic distortion performance.

5.6. DC-Bus Balancing using a Clamping Bridge Circuit in the 5L

The differences $(U_{c1} - U_{c2})$ and $(U_{c3} - U_{c4})$ continue to increase as shown in Figure 5.7a, the continuous voltages reach the values that ensure the DC bus balance then they start to dispartate, this can reverberate negatively on the behavior of the global system by introducing higher voltage stresses on the semiconductor and prevents the stabilization of the continuous voltages [5].

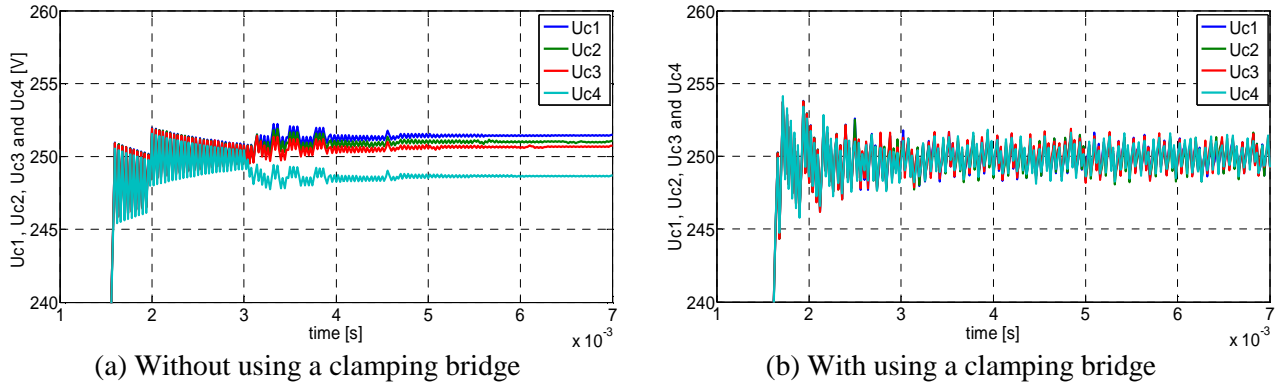


Figure 5.7 Imbalance minimization between the DC-link voltages.

To minimize the imbalance between the input voltages U_{c1} , U_{c2} , U_{c3} , and U_{c4} , we suggest the insertion of a clamping bridge circuit as shown in Figure 5.8 [5]. The new DC-bus model is defined by the following system:

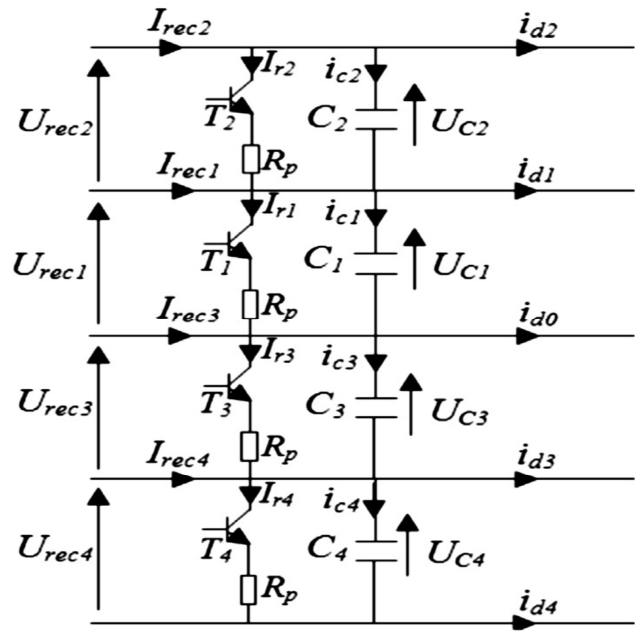


Figure 5.8 Clamping bridge structure.

$$\left\{ \begin{array}{l} c_1 \frac{dU_{c1}}{dt} = i_{rec1} + i_{rec2} - i_{dc1} - i_{dc2} - i_{r1} \\ c_2 \frac{dU_{c2}}{dt} = i_{rec2} - i_{dc2} - i_{r3} \\ c_3 \frac{dU_{c3}}{dt} = -i_{r3} - i_{rec3} - i_{rec4} + i_{dc3} + i_{dc4} \\ c_4 \frac{dU_{c4}}{dt} = -i_{r4} - i_{rec4} + i_{dc4} \end{array} \right. \quad \text{where } i_{r1:4} = \frac{U_{c1:4}}{R_p} \text{ if } T_{1:4} \text{ is on,}$$

$$\text{otherwise } i_{r1:4} = 0 \quad (5.09)$$

The algorithm that controls the clamping bridge is applied separately in the upper and the lower stages. If the difference is not zero, the excess energy will be dissipated through the resistance. The control algorithm of the clamping bridge is given as follows:

The input signals are the error and its derivative of the DC-link voltage. The adopted FGT controller is shown in Figure 5.11 and the rule tables are given in Table 5.4 and Table 5.5 [21]. The input/output MFs used in these two FGTs are like the FLC presented in Figure 5.9a.

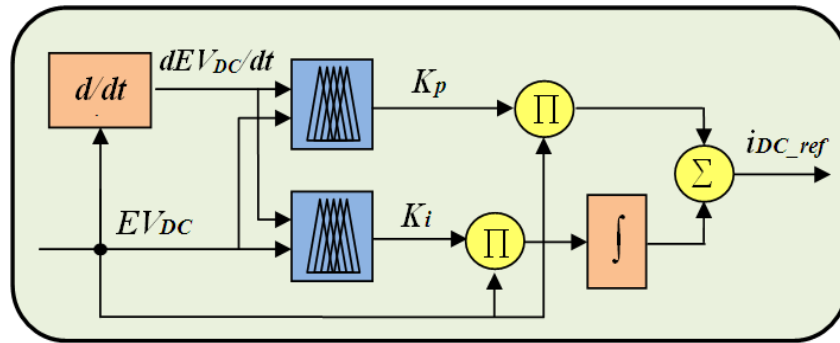


Figure 5.11 FGT of the DC-link voltage controller.

Table 5.4: Rule table for DC-link voltage fuzzy \$K_p\$ tuner

$e(pu)$	NB	NM	NS	Z	PS	PM	PB
$de/dt(pu)$							
NB	PB	PB	PM	PM	PS	Z	Z
NM	PB	PB	PM	PS	PS	Z	NS
NS	PM	PM	PM	PS	Z	NS	NS
Z	PM	PM	PS	Z	NS	NM	NM
PS	PS	PS	Z	NS	NS	NM	NM
PM	PS	Z	NS	NM	NM	NM	NB
PB	Z	Z	NM	NM	NM	NB	NB

Table 5.5: Rule table for DC-link voltage fuzzy \$K_i\$ tuner

$e(pu)$	NB	NM	NS	Z	PS	PM	PB
$de/dt(pu)$							
NB	PB	PB	PM	PM	PS	Z	Z
NM	PB	PB	PM	PS	PS	Z	NS
NS	PM	PM	PM	PS	Z	NS	NS
Z	PM	PM	PS	Z	NS	NM	NM
PS	PS	PS	Z	NS	NS	NM	NM
PM	PS	Z	NS	NM	NM	NM	NB
PB	Z	Z	NM	NM	NM	NB	NB

5.8. Adaptive Neuro-Fuzzy Inference System

The design and choice of the MFs parameters in fuzzy system (number, shape and location) require an extensive knowledge and experience of the control system designer. In such cases, a set of input/output data can be used. In the NFS, a learning method similar to that of neural networks is used to train and adjust the parameters of the MFs. Neuro-adaptive learning techniques provide a method for the fuzzy modeling procedure to learn information from a data set [22]. Currently, several neuro-fuzzy networks exist in the literature. Most notable are ANFIS developed by Jang [23].

The idea is to learn the shape of MFs for the fuzzy system efficiently by taking the advantage of adaptive property of the neural methods. Takagi, Sugeno and Kang [24-25] are known as the first to utilize this approach.

The developed NFC is a first-order TSK type which has two inputs and one output, with seven gbellmf (*generalized bell MF*). It has 49 rules. A simple structure of the developed NFS is shown in Figure 5.12 where the inputs are the normalized error signal and its normalized change ($e, \Delta e$) of the controlled active and reactive power, the output is the normalized change of the command signals which are the q and d-axis rotor current components respectively. The scaling factors ($K_{EPs}, K_{\Delta EPs}, K_{\Delta irq}$) are deduced after several tests. A typical "if-and-then" rule can be expressed as:

Rule 1: If x is A_1 and y is B_1 , then $z_1 = p_1 x + q_1 y + r_1 \dots\dots\dots$

Rule 49: If x is A_7 and y is B_7 , then $z_{49} = p_{49} x + q_{49} y + r_{49}$

As indicated in Figure 5.12, the ANFIS system has a total of five layers. The functioning of each layer is described as in [23].

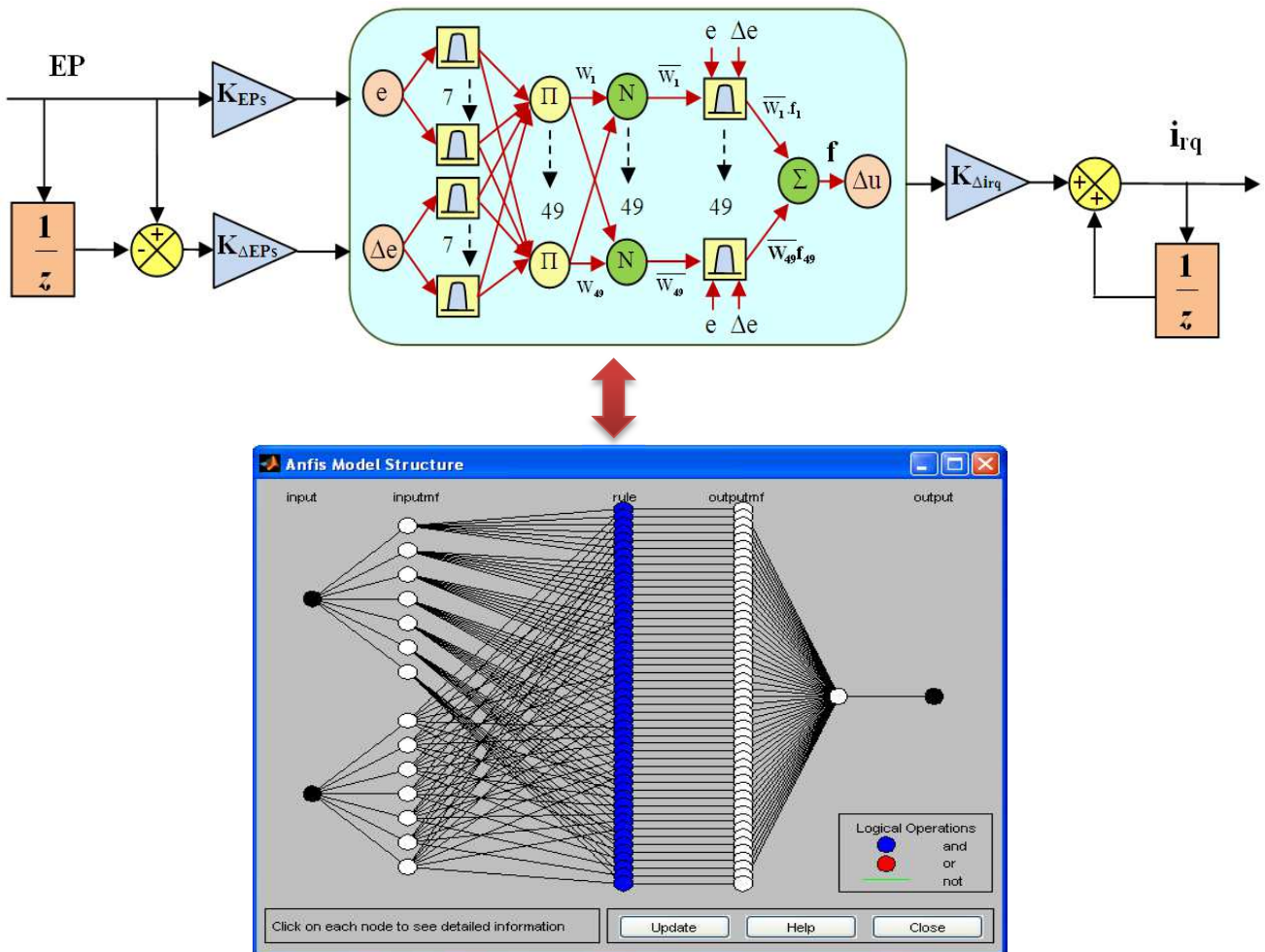


Figure 5.12 NFC structure for the stator active power control loop.

- **Input Node (Layer 1):** Nodes in this layer contains MFs. Parameters in this layer are referred to as premise parameters, and every node i is a square and adaptive node with a node function:

$$O_i^1 = \mu_{A_i}(x) \quad \text{for } i = 1, \dots, 7 \quad (5.11)$$

Where x is the input to node i , and A_i is the linguistic label (small, big, etc.) associated with this node function. In other words, O_i^1 is the MF of A_i and it specifies the degree to which the given x satisfies the quantifier A_i .

- **Rule Nodes (Layer 2):** Every node in this layer is a circle node labeled II, whose output represents the firing strength of a rule. This layer chooses the minimum value of two input weights. In this layer, the OR operator is applied to get one output that represents the result of the antecedent, that is the firing strength. It means the degrees by which the antecedent part of the rule is satisfied and it indicates the shape of the output function for that rule. The node generates the output by cross multiplying all the incoming signals:

$$O_i^2 = w_i = \mu_{A_i}(x) \cdot \mu_{B_i}(y) \quad \text{for } i = 1, \dots, 49 \quad (5.12)$$

- **Average Nodes (Layer 3):** Every node in this layer is a circle node labeled N. The i^{th} node calculates the ratio between the i^{th} rule's firing strength to the sum of all rules' firing strengths. Every node of these layers calculates the normalized weight. The outputs of this layer are called normalized firing strengths.

$$\bar{w}_i = \frac{w_i}{w_1 + \dots + w_{49}} \quad \text{for } i = 1, \dots, 49 \quad (5.13)$$

- **Consequent Nodes (Layer 4):** This layer includes linear functions, which are functions of the input signals. This means that the contribution of i^{th} rule's towards the total output. Every node i in this layer is a square node with a node function:

$$O_i^4 = \bar{w}_i f_i = \bar{w}_i (p_i x + q_i y + r_i) \quad \text{for } i = 1, \dots, 49 \quad (5.14)$$

Where \bar{w}_i is the output of layer 3, and (p_i, q_i, r_i) are the parameter set of the i^{th} node. These parameters are referred to as consequent parameters.

- **Output Node (Layer 5):** The single node in this layer is a fixed node labeled Σ , which computes the overall output by summing all the incoming signals:

$$O^5 = \sum_i \bar{w}_i f_i = \frac{\sum_i w_i f_i}{\sum_i w_i} \quad \text{for } i = 1, \dots, 49 \quad (5.15)$$

Four NFCs are used to control the DFIG, two for the stator active and reactive power control loops and two for the d and q rotor currents components control loops as denoted in Figure 5.13.

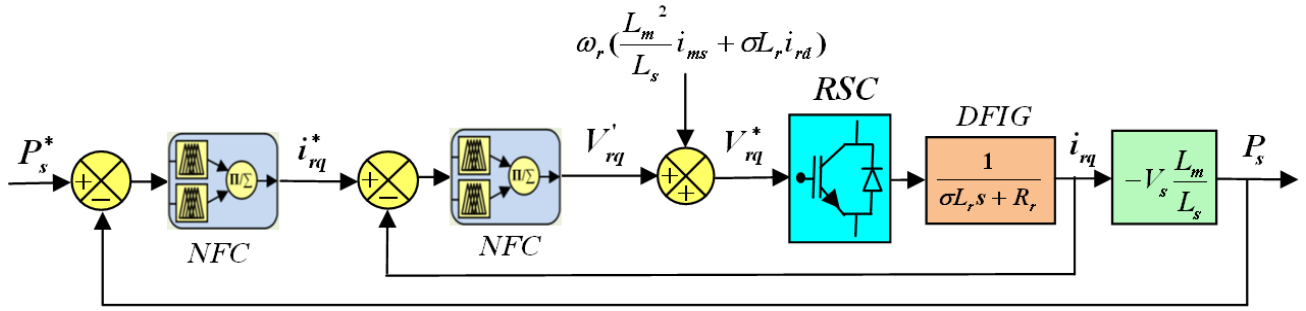


Figure 5.13 Indirect vector control of the DFIG using the RSC.

5.9. Training process of the NFCs of stator power and rotor currents

Training is performed using the hybrid back-propagation algorithm. The training data set used is collected from extensive simulations of the controlled system with different PI controllers in various operating conditions. The number of training epochs is set to 80 with an error tolerance of 10^{-6} . The number of epochs is chosen to be the highest number after which there is no significant reduction in the training error. The inputs MFs of the active power NFC after the training process are shown in Figure 5.14b and Figure 5.14d, and the output MFs are chosen to be linear [26-27].

Figure 5.15 shows the training and the checking errors (RMSE: root mean squared error) while training at each epoch for the NFC. The trained TS-fuzzy system output is compared with the training and checking data and the results are presented in Figure 5.16. The NFCs of the rotor currents have the same structure as the power controllers, and the same training process of the power controllers has been used.

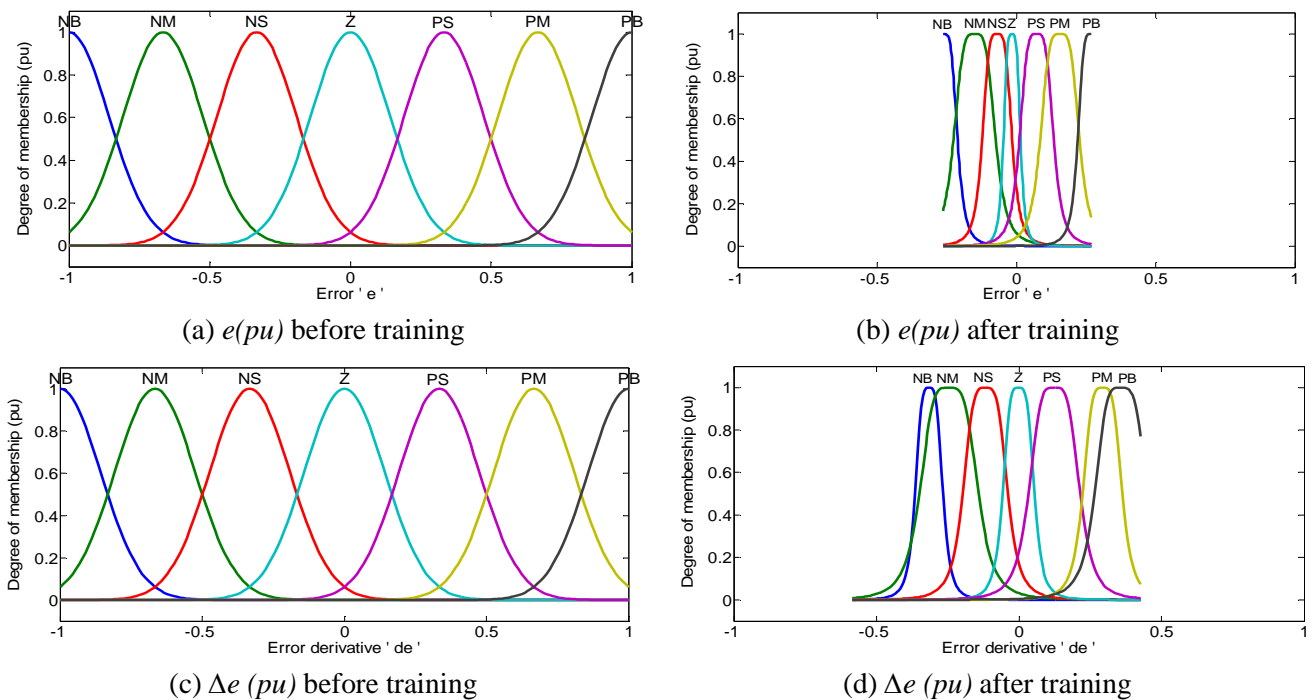
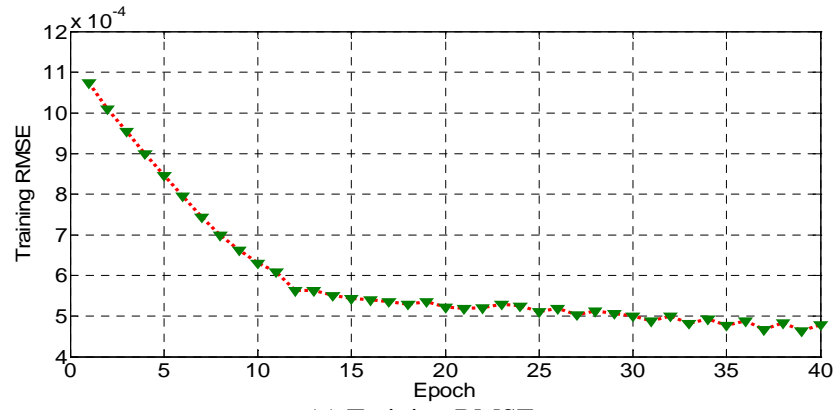
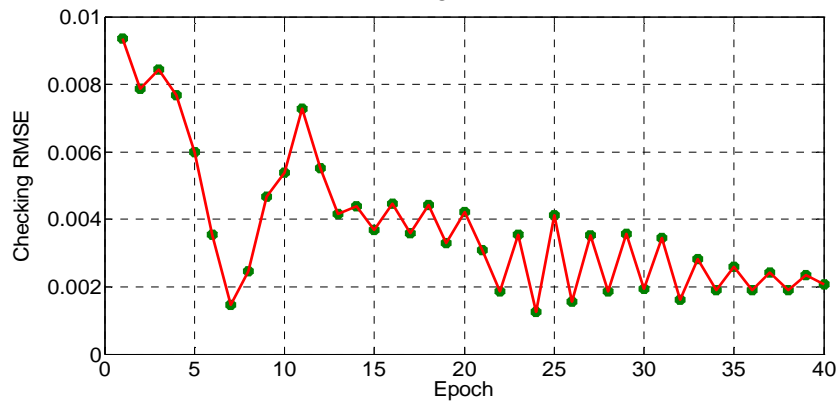


Figure 5.14 Membership Functions of the TS-FLC inputs.

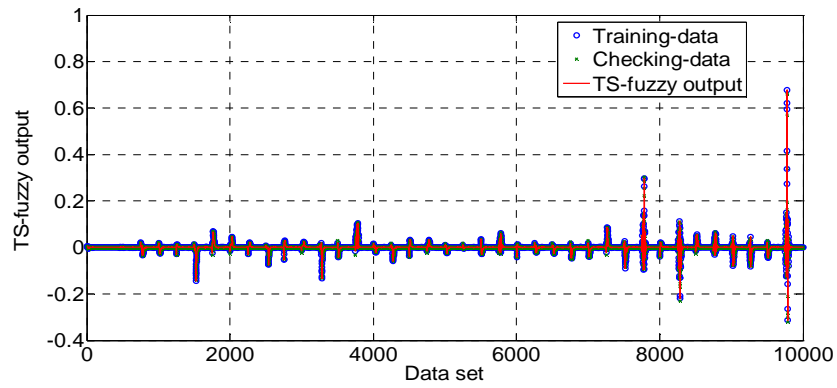


(a) Training RMSE

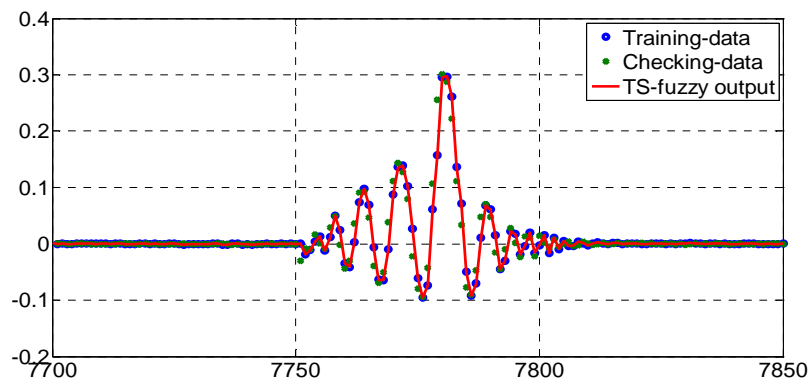


(b) Checking RMSE

Figure 5.15 RMSE of the active power NFC



(a) Normal



(b) Zoom

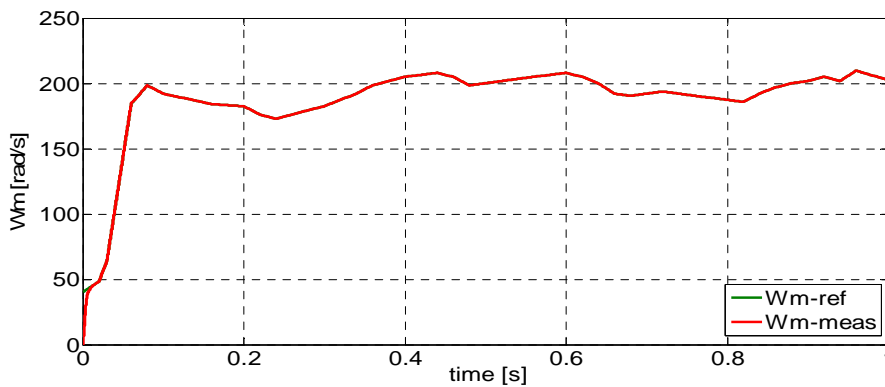
Figure 5.16 NFC test with training and checking data sets.

5.10. Simulation Results

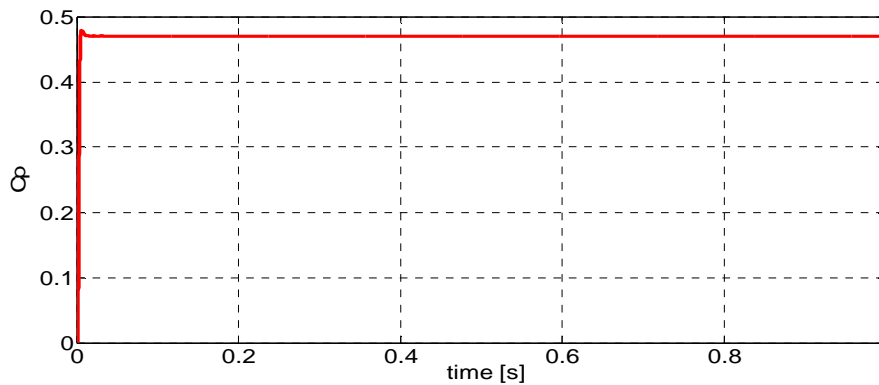
Simulations have been performed on the 1.5MW DFIG-WPGS system incorporating the proposed TS-FLCs. The parameters of the DFIG system are inspired from [28] and cited in the appendix as Table A.3. The simulation objectives is to apply a random wind speed with average value about 12m/s, the MPPT strategy has to gives the optimal rotational speed of the system, and the induction machine vector control has to track the stator active and reactive power reference, the operating is performed in the super-synchronous mode, Reference tracking and disturbance rejection performance of the speed, stator active and reactive power have been presented in Figure 5.17.

To insure the robustness of the proposed NFC against the usual faults, parameters variations of the induction machine and the grid voltage disturbances, these different faults are introduced separately in the system by using the simple *Mamdani* type FLC and the trained TS-FLC (ANFIS), and the results are compared with the response of the conventional PI controller as shown in Figure 5.18 and Figure 5.19.

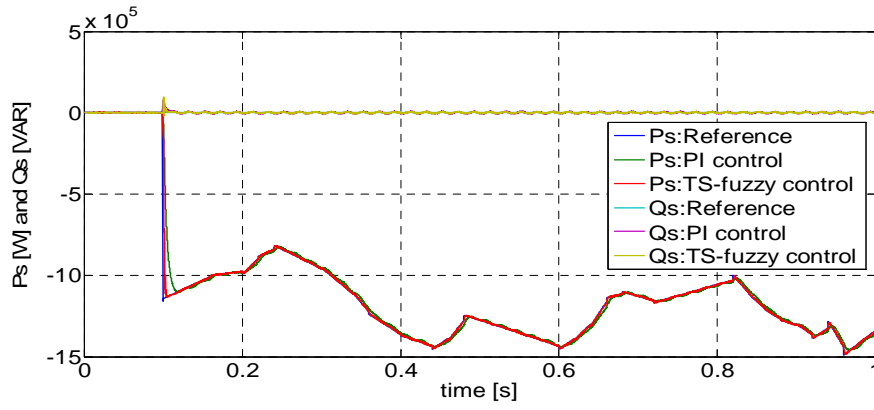
5.10.1. Normal Operation of the WPGS-DFIG



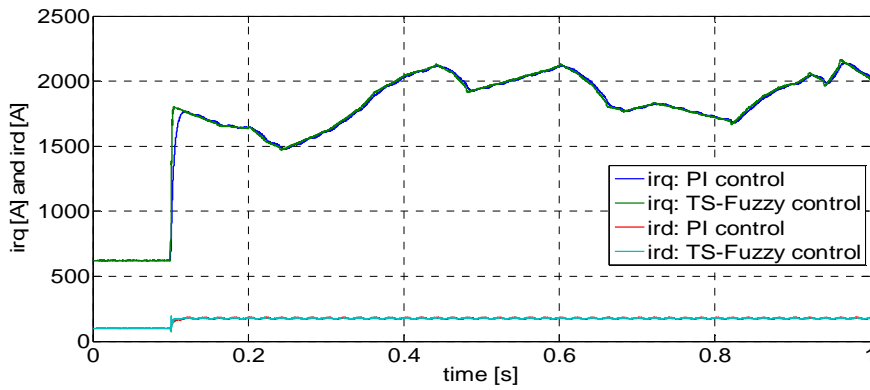
(a) Generator rotational speed



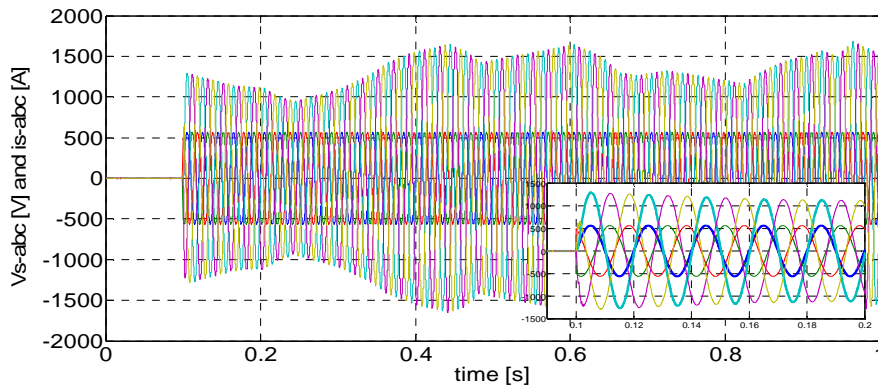
(b) Power efficiency coefficient



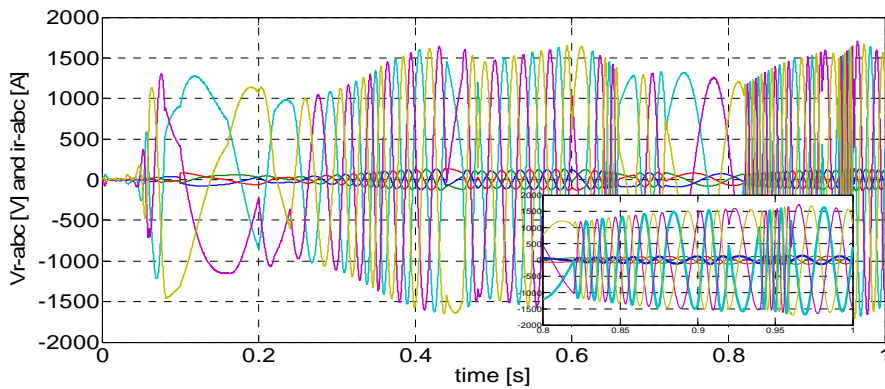
(c) Stator active and reactive power



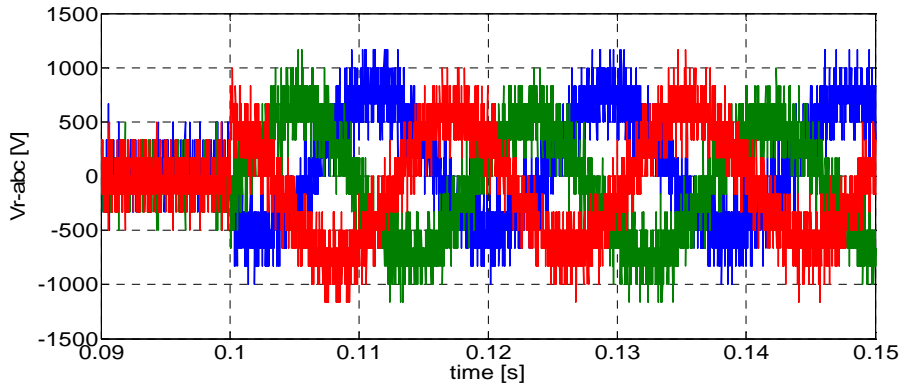
(d) d and q-axis rotor current components



(e) Stator voltages and currents

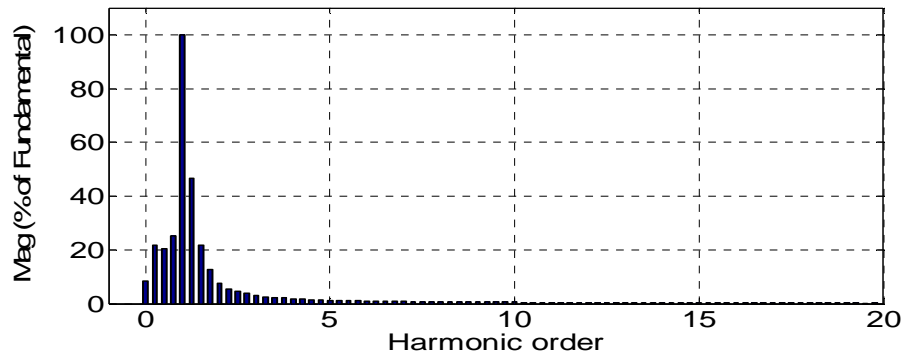


(f) Rotor currents and estimated voltages

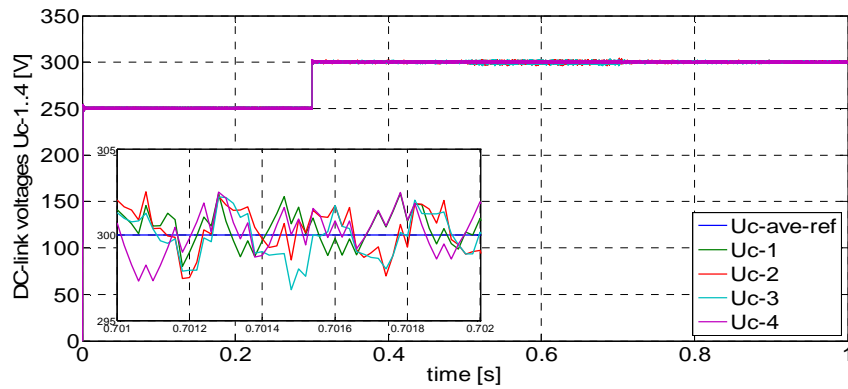


(g) Output voltages of RSC

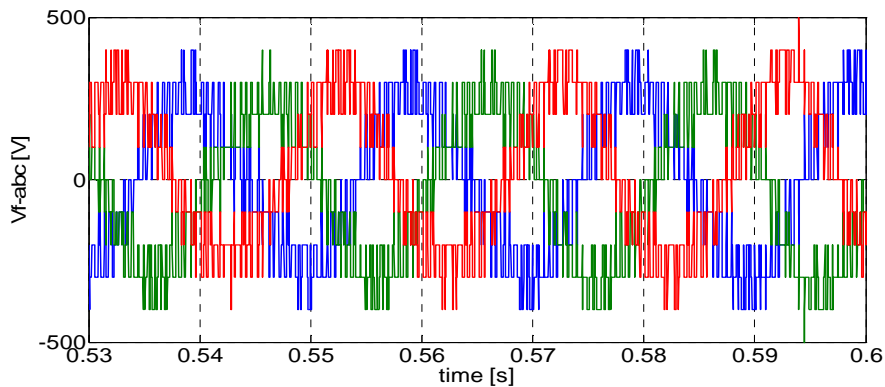
Fundamental = 545.1V , THD= 23.89%



(h) Spectrum of output voltage of RSC



(i) DC-link voltages



(j) Output voltages of GSC

Figure 5.17 Reference tracking characteristics of the DFIG based WPGS.

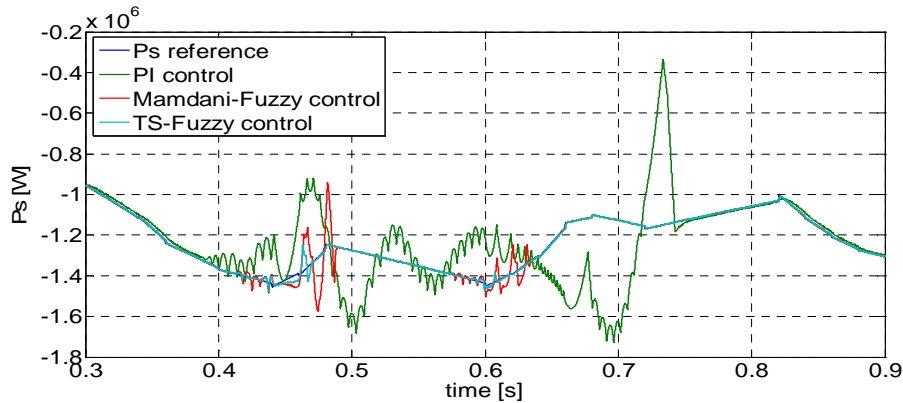
In the variable speed, constant frequency operation of the DFIG-WPGS, the grid connection is applied before the 0.1s.

- Wind speed changes randomly, the generator speed has the same image of the wind speed as presented in Figure 5.17a, this because of the constant tip speed ratio. The TS-fuzzy speed control is fast and efficient; the measured rotating speed is conformable to the reference speed.
- Figure 5.17b shows the efficiency coefficient, it is maintained at its maximum, this means that the MPPT algorithm is working perfectly.
- Figure 5.17c shows the measured stator active and reactive power, the active power follows its reference brought from the speed control loop, it depends on the turbine mechanical power, the stator reactive power follows its reference that kept at zero. In the normal operating condition, the proposed TS-FLC response is almost similar to the PI controller's one.
- Figure 5.17d shows the d and q-axis component of the rotor current, they have the same image of the stator reactive and active power respectively.
- Figure 5.17e shows the sinusoidal waveform of the stator currents and voltages, the stator currents frequency is 50Hz and undergoes the same variation as the wind speed, which is random.
- Figure 5.17f shows sinusoidal waveform of the currents and the estimated voltages in the rotor circuit, their magnitude and frequency change according to the slip or the generator speed.
- Figure 5.17g shows the modulated output voltages of the RSC, their frequency and magnitude change according to the generator speed, the number of levels vary according to the RMS value of the rotor voltage reference.
- Figure 5.17h shows the spectrum of output voltage of RSC, by using a multi-level converter and an adequate PWM strategy, a low THD is obtained.
- Figure 5.17i shows a good response achieved in the measured DC-link voltages U_{c1} , U_{c2} , U_{c3} and U_{c4} through the fuzzy gain tuner control strategy of the 5L rectifier, no overshoot, no steady-state error and tiny settling time.
- Figure 5.17j shows the modulated output voltages of the GSC, their frequency is maintained equal to the grid voltage frequency which is 50Hz, and its value changes according to the active power exchanged between the GSC and the grid, the number of levels is vary according to the RMS value of the reference signals of V_{f-abc} .

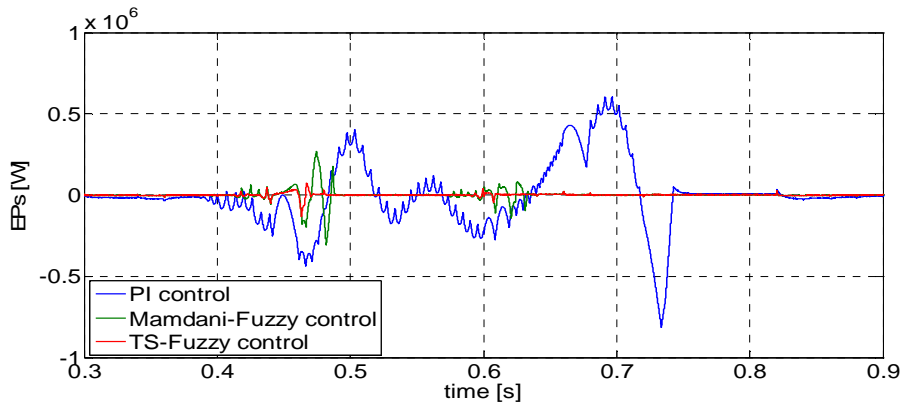
5.10.2. Robustness of the NFC against the Parameters Variations

After long time of exploiting, the induction machine can lose its electrical characteristics like the winding resistances and inductances; we attempted to verify our proposed NFC controller against

these faults, an increase by 500% in the stator and the rotor resistances and a decrease by 50% in the mutual inductance are introduced simultaneously, the results are shown in Figure 5.18.



(a). Stator active power



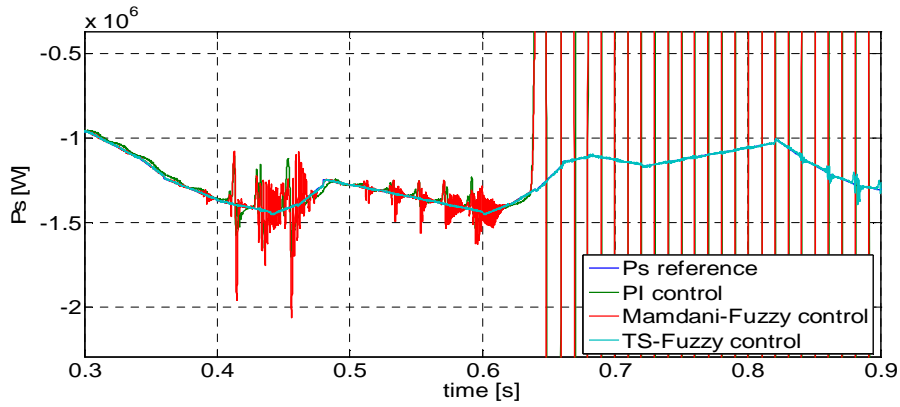
(b). Stator active power error

Figure 5.18 Parameters variation rejection by using the NFC

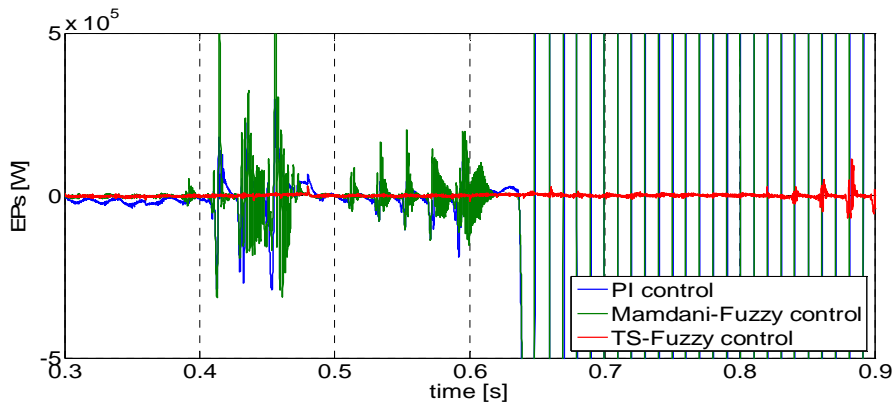
According to Figure 5.18, degradation in the performance appears in the PI control, a huge error is appeared, and the system became unstable, also with *Mamdani* type FLC, the system presents significant disturbance. On the contrary, by using a NFC trained with data set contain information about the parameters variations problem (different input/output MFs arrangements with *Mamdani* type FLC), the system shows a good performance without any affection by the parameters variation.

5.10.3. Robustness of the NFC against the Grid Disturbances

We added the seventh harmonics to the fundamentals of the three phases grid voltage at 0.4sec, and we introduce an unbalance in one phase of grid voltage by -10% at 0.6sec, the usual time taken from any transient disturbance is too short, thus we took the 30msec as fault time, the results are shown in Figure 5.19.



(a) Stator active power control



(b) Stator active power error

Figure 5.19 Grid voltage disturbance rejection by using NFC.

Figure 5.19 shows the stator active power response in the grid voltage fault operation, both the classic PI and the *Mamdani* type FLC are affected with the grid voltage faults and shows instable operating condition. On the contrary, by using a NFC after training with data set contain information about the grid disturbances presented by the input/output of the *Mamdani* type FLC in different arrangements, The system shows some disturbances but after a while it returns to the normal operating condition.

Figure 5.20 shows a good response achieved in the measured DC-link average voltage through the 5L GSC using the FGT control, no overshoot, no steady-state error, less settling time and the oscillations are damped out faster compared to the conventional PI controller during the grid fault. The reference DC-link average voltage was changed between 250V and 300V in order to show the performance of the control system, finally the global DC-link voltage became 1200V.

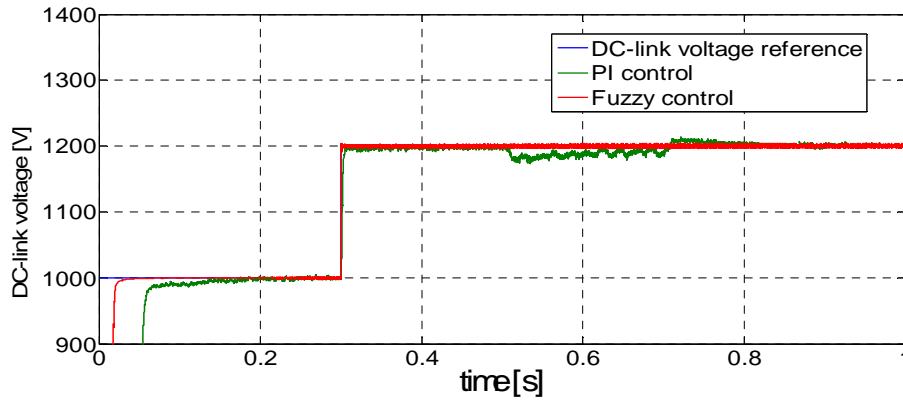


Figure 5.20 Average DC-link voltage response using PI and FGT.

5.11. Conclusion

This chapter performed a study on the decoupled d-q vector control techniques of DFIG through back-to-back 5L-NPC converters. Vector control of the DFIG has been embedded in an optimal tracking controller for maximum energy capture in a wind energy system. An intelligent TS-fuzzy system has been used to control the DFIG. A random wind speed is applied to the system and a triangulo-sinusoidal PWM is used to control the 5L-NPC converters. A NFC is adopted to control the speed, stator active and reactive power, and compared to the PI and the *Mamdani* type fuzzy control responses. To improve the robustness of the TS-FLC against the parameters variation and the grid voltage disturbances, an adequate data set has been collected and used for training, and the results show the superiority of the trained NFC controllers against the different faults. The FGT allows the adaptation of the proportional and integral gains of the PI controller in the vector control scheme of the GSC. Fuzzy logic together with the well-known PI controller provides an excellent adaptive controller. We can conclude that by combining the NFC and an extensive human knowledge and experience represented by a good collection of data set from the controlled system in one operating conditions, we can build an adaptive and robust controller which can be useful for the studied operating condition.

5.12. References of Chapter 5

- [1] A.V. Santiago and I.V. Maria, Direct connection of WECS system to the MV grid with multilevel converters, *Renewable Energy*, Vol. 41, pp. 336-344, 2012.
- [2] J.B. Emilio, C. Santiago, F.J. Rodriguez, A. Hernandez and F. Espinosa, Design of a back-to-back NPC converter interface for wind turbines with squirrel-cage induction generator, *IEEE Trans. on Energy Conversion*, Vol. 23, pp. 932-945, 2008.
- [3] J. Rodríguez, J. S. Lai and F.Z. Peng, Multilevel Inverters: A survey of topologies, controls, and applications, *IEEE Trans. on Industrial Electronics*, Vol. 49, No. 4, 2002.
- [4] M.H. Rashid, *Power Electronic Handbook*, Second Edition, University of West Florida Pensacola, Florida, Elsevier, 2007.
- [5] F. Merahi and E.M. Berkouk, Back-to-back five-level converters for wind energy conversion system with DC-bus imbalance minimization, *Renewable Energy*, Vol. 60, pp. 137-149, 2013.
- [6] R. Guedouani, B. Faila, E.M Berkouk, M.S. Bouchrit, New control strategy of three-phase five-level NPC rectifier - inverter system for induction machine drive, *Energy Procedia*, Vol. 18, pp. 1382-1391, 2012.
- [7] B.R. Lin and C.H. Huang, Single-phase AC/DC/AC converter based on capacitor clamped topology, *IEE Proc.-Electric Power Applications*, Vol. 152, No. 3, pp. 464-472, 2005.
- [8] J. Rodríguez, S. Bernet, B. Wu, J. O. Pontt and S. Kouro, Multilevel voltage-source-converter topologies for industrial medium-voltage drives, *IEEE Trans. on Industrial Electronics*, Vol. 54, No. 6, pp. 2930-2945, 2007.
- [9] X. Xia, F. Zhang, G. Zhang and X. Jing, Simulation and study on cascaded nineteen-level dynamic voltage restorer, *IEEE Power and Energy Engineering Conference (APPEEC)*, pp. 1-4, 2012.
- [10] G. Preethi, J.G. Monika and V. Jamuna, Digital simulation of multicarrier PWM strategy for multi-level inverter, *IEEE International Conference on Computing, Electronics and Electrical Technologies (ICCEET)*, pp. 509-514, 2012.
- [11] P. N. Tekwani, R.S. Kanchan and K. Gopakumark, Five-level inverter scheme for an induction motor drive with simultaneous elimination of common-mode voltage and DC-link capacitor voltage imbalance, *IEE Electric Power Applications*, Vol. 152, pp. 1539-1555, 2005.
- [12] A. Talha, M.O. Mahmoudi, D. Beriber and E.M. Berkouk, Study and control of two two-level PWM rectifiers-clamping bridge-two three-level NPC VSI cascade, Application to double stator induction machine. *IEEE power electronics specialists conference (PESC'04)*, pp. 3894-3899, 2004.
- [13] M. P. Kazmierkowski, L. G. Franquelo, J. Rodriguez, M. Perez and J. I. Leon, High-performance motor drives, *IEEE Industrial Electronics Magazine*, pp. 1932-4529, Sept. 2011.
- [14] F. Merahi and E.M Berkouk, Five level converters cascade integrated in wind chain, *12th international conference on science and techniques of automatic control & computer engineering (STA'11)*, pp. 1-6, 2011.
- [15] A. Talhal, E.M. Berkouk, B. François and M.S. Boucherit, Modeling and Control of a power electronic cascade for the multi DC bus supply of a seven-level NPC voltage source inverter, *12th International on Power Electronics and Motion Control Conference (EPE-PEMC 2006)*. Portoro2, Slovenia. pp. 200-205, Aug. 30-Sept. 1 2006.
- [16] S. Barkati, L. Baghli, E.M. Berkouk and M.S. Boucherit, Harmonic elimination in diode-clamped multilevel inverter using evolutionary algorithms, *Electric Power Systems Research*, Vol. 78, pp. 1736-1746, 2008.
- [17] B. François and E. Semail, Modeling and control of a three-phase neutral-point-clamped inverter by means of a direct space vector control of line to line voltages, *EPE-PEMC 2002 Dubrovnik & Cavtat*.
- [18] D.M. Lee, J.W. Jung, and S.S. Kwak, Simple space vector PWM Scheme for 3-level NPC inverters including the over modulation region, *Journal of Power Electronics*, Vol. 11, No. 5, Sep. 2011.
- [19] S. Mekhilef, H.I. Khudhur and H. Belkamel, DC link capacitor voltage balancing in three level neutral point clamped inverter, *IEEE 13th Workshop on Control and Modeling for Power Electronics (COMPEL)*, pp. 1-4 June 2012.

- [20] H.M. Jabr, C.N. Kar, Fuzzy gain Tuner for vector control of doubly-fed wind driven induction generator, IEEE Canadian Conference on Electric and Computer Engineering, Ottawa, pp. 2266–2269, May 2006.
- [21] Q. Duan, F. Hao and S. Feng. Adaptive fuzzy control used in DFIG VSCF wind power generator system. IEEE 7th World Congress on Intelligent Control and Automation, Chongqing, China, pp. 29–32, June 25-27, 2008.
- [22] H.M. Jabr and C.N. Kar, Neuro-Fuzzy vector control for doubly-fed wind driven induction generator, IEEE Electrical Power Conference, Canada (EPC), pp. 236-241, 2007.
- [23] J.S. Jang, ANFIS: Adaptive-network-based fuzzy inference system, IEEE Trans. on Systems, Man, and Cybernetics, Vol. 23, No. 3, pp. 665-684, 1993.
- [24] T. Takagi and M. Sugeno, Fuzzy identification of systems and its applications to modeling and control, IEEE Transactions on Systems, Man, and Cybernetics, Vol. 15, pp. 116-132, 1985.
- [25] M. Sugeno and G.T. Kang, Structure identification of fuzzy model, Journal of Fuzzy Sets and Systems, Vol. 28, pp. 15-33, 1988.
- [26] A. Dida and D. Benattous. Modeling and control of DFIG through back-to-back five levels converters based on Neuro-Fuzzy controller, Journal of Control, Automation and Electrical Systems. Vol. 26, pp. 506–520, 2015.
- [27] A. Dida and D. Benattous. Neuro-Fuzzy control of grid connected DFIG via five-level NPC converter for WECS, 2nd International Conference on Electrical Energy and Systems, Annaba, Algeria, Oct. 28-30, 2014.
- [28] S. El Aimani, Practical Identification of a DFIG based wind generator model for grid assessment, IEEE International Conference on Multimedia Computing and Systems (ICMCS '09), pp. 278-285, 2009.

General Conclusion and Suggestions

General Conclusion and Suggestions

Wind power, as one of the clean and alternative energy sources. It is expected to become the largest renewable energy source in Europe in the near future. Researches on maximizing the power coefficient and improving the power quality are essential. In this thesis, intelligent control strategies of DFIG based variable speed WT have been investigated and developed.

The power rating of modern offshore WTs has increased up to 10MW in order to harvest more energy, thus reduce the cost per megawatt of capacity. The construction and installation costs of these multi-megawatts turbines are really high and critical in offshore areas. The weight and volume reduction of the power generation system might be a solution to this issue.

Simulation model of a DFIG-based WTS with variable-speed and pitch control scheme for WT control and generator output control power is systematically developed for grid-connected operating condition. Detailed models of all components of the DFIG-based WTGS have been derived and their operation is explained clearly. This thesis reviewed and discussed the MPPT algorithms usually applied in WPGSSs. In addition, the authors analyzed a simulation and comparison of three selected control methods in terms of efficiency and time of response. Simulation results demonstrated the superiority of the OT control method in terms of simplicity and accuracy, nevertheless, its dependency on WT characteristics made it inflexible. TSR control has the same simplicity and accuracy of the OT control, and has a faster dynamic response than OT control; however it still has the wind speed measurement problem. FLC plays an important role to improve the robustness of the classical PI control in the rotational speed closed loop control.

Standard FOC schemes usually used to control WT-driven DFIGs comprise PI controlled cascaded current and power loops, which require the use of an incremental encoder. Although, the stator-side active and reactive powers can be independently controlled by adopting those control schemes. The system transient performance degrades as the actual values of the DFIG resistances and inductances deviate from those based on which the control system tuning was carried out during commissioning. In this framework, the alternative high dynamic performance power control schemes for DFIGs are being proposed by different authors over the last decade. Four DPC strategies of the DFIG have been chosen in this thesis to investigate the robustness capabilities against the rotational speed and machine parameters variations. The PI based control is useless in the uncertain operation

condition, however each one of the investigated robust or intelligent based control schemes has a better robustness and each nonlinear control scheme has its straight and weakness points.

This thesis reviewed and discussed a WPGS equipped with a DFIG and two back-to-back five-level NPC converters in the rotor side. The modeling and the control of the five-level converter is presented with a new method of controlling the DC-link voltage through the five-level rectifier. A NFC is adopted to control the rotational speed, stator active and reactive power, and compared to the PI and *Mamdani* fuzzy controllers to improve performance against the parameters variation and the grid voltage disturbances. We can conclude that by combining the NFC and an extensive human knowledge and experience represented by a good collection of data set from the controlled system, we can build an adaptive controller with high robustness for the studied operating condition. The operator experience plays a huge role in this field of intelligent computing systems.

This thesis has unlocked many gates for the future researchers to work further on the variable-speed pitch-regulated DFIG-based WTS. The following points are identified as potential future work based on the results of the present thesis:

- In the MPPT purpose, using ANN, FLC and NFC in the subject maximum power extraction control of WTSs may be useful, either for wind speed estimation, identification of the WT characteristics or improve the efficiency of one classical MPPT strategy.
- In the subject of independently DPC of grid-connected DFIG, maybe an experimental comparison study between the most famous DPC strategies (FOC, DPC, IOFLC, SMC, FLC and MPC) will be a good contribution to investigate the robustness against speed variation and machine parameters uncertainty.
- The potential of the NFS can be useful in the WPGS in different subjects, such as control of currents, powers, speed, voltages, frequency.., and identification of WT characteristics and optimization of other controller. Moreover, using the on-line training instead of the off-line training of the ANFIS may be a better contribution.
- Using meta-heuristic methods to improve performance.
- An experimental test bench emulating a variable speed WT has to be developed to test the behavior of a WPGS in the grid-connected operating condition.

Appendices

Appendix A

Table A.1: Parameters of the DFIG-WTS in the per-unit system used in chapters N^o: 2 and 3

Parameter	Denomination	Value
Rated wind speed	V_w	12 m/s
Rated mechanical power of the WT	P_{mec}	1,5 MW
Number of blade		3
Rotor radius	R	35.25 m
Air density	ρ	1.225 kg/m ³
Gearbox ratio	N_g	91
Generator inertia constant	$H_g = J_g/2$	0.685 s
Wind turbine inertia constant	$H_t = J_t/2$	4.32 s
Generator friction factor	b	0.01 pu
Equivalent torsional stiffness coefficient	K_{stiff}	1.11 pu
Equivalent damping coefficient	D_{damp}	1.5 pu
Rated grid voltage (line to line)	V_g	575 V
Rated apparent power of the generator	S_{out}	1,5/0.9 MVA
Rated active power of the generator	P_{out}	1,5 MW
Rated apparent power of the transformer	P_{tr}	1,75 MVA
Rated DC-link voltage	V_{DC}	1200 V
Rated Grid frequency	f	60 Hz
Number of pole pairs	p	3
Stator winding resistance	R_s	0.023 pu
Rotor winding resistance	R_r	0.016 pu
Stator winding leakage inductance	L_s	0.18 pu
Rotor winding leakage inductance	L_r	0.16 pu
Magnetizing inductance	L_m	2.9 pu
DC-link capacitor	C_{DC}	0.01 F
Resistance of grid-side coupling inductor	R_g	0.003 pu
Inductance of grid-side coupling inductor	L_g	0.3 pu

Table A.2: K_p , K_i gains of the PI controllers used in chapters N^o: 2 and 3

Parameter	Denomination	Value
DC bus voltage regulator gains	$[K_p, K_i]$	[8 400]
GSC current regulator gains	$[K_p, K_i]$	[0.83 5]
Rotational speed regulator gains	$[K_p, K_i]$	[3 0.6]
RSC current regulator gains	$[K_p, K_i]$	[0.6 8]
Stator active power regulator gains	$[K_p, K_i]$	[0.1 50]
Stator reactive power regulator gains	$[K_p, K_i]$	[0.001 50]
Pitch controller gain of rotational speed	K_p	150
Pitch controller gains of mechanical power	$[K_p, K_i]$	[3 30]
PWM frequency of the RSC		27×60
PWM frequency of the GSC		45×60
Maximum pitch angle		30 deg
Maximum rate of change of pitch angle		10 deg/s
Cut-in/cut-out wind speed		4/30 m/s
Fixed step size		1e-4 s

Table A.3: Parameters of DFIG and the WTS used in chapters N^o: 4 and 5

Parameter	Denomination	Value
Rated apparent power	S_{out}	1,5/0.9 MVA
Rated mechanical power	P_{mec}	1,5 MW
Rated grid voltage (line to line)	V_g	690 V
Rated DC-link voltage	V_{DC}	1200 V
Number of pole pairs	p	2
Grid frequency	f	50 Hz
Stator resistance	R_s	0,012 Ω
Rotor resistance	R_r	0,021 Ω
Stator leakage inductance	L_s	0,0137 H
Rotor leakage inductance	L_r	0,0136 H
Magnetizing inductance	L_m	0,0135 H
DC-link capacitor	C_{DC}	0,0044 F
Grid-side coupling inductor resistance	R_f	0,012 Ω
Grid-side coupling inductor inductance	L_f	0,005 H
Rated wind speed	V_w	12 m/s
Air density	ρ	1.225 kg/m ³
Number of blade		3
Radius of blade	R	35,25 m
Gear-box gain	N_g	90
Global inertia coefficient	J_{eq}	1000 kg.m ²
Global viscous friction	f_{eq}	0,0042 N.m.s/rad

Table A.4: K_p , K_i gains of the PI controllers used in chapters N^o: 5 and 6

Parameter	Denomination	Value
DC bus voltage regulator gains	$[K_p, K_i]$	[20 16]
GSC current regulator gains	$[K_p, K_i]$	[1 100]
Rotational speed regulator gains	$[K_p, K_i]$	[3 0.6]
RSC current regulator gains	$[K_p, K_i]$	[1.1296e4 63]
Stator active power regulator gains	$[K_p, K_i]$	[0.0001 -0.2121]
Stator reactive power regulator gains	$[K_p, K_i]$	[0.0001 -0.2121]
PWM frequency of the RSC		60×50 Hz
PWM frequency of the GSC		60×50 Hz
Fixed step size		2e-5 s

Table A.5: Parameters of DPC methods of the DFIG used in chapter N^o: 4

Parameter	Denomination	Value
FOC: Gain	k_p	0.0175
FOC: Gain	k_i	1.2354
DPC: hysteresis band	$\Delta P = \Delta Q$	4000
SMC: Gain	k_q	500
SMC: Gain	k_d	150
SMC: Saturation	λ	± 100
FLC : Input-1 Gain	k_e	$1/1.5 \cdot 10^6$
FLC : Input-2 Gain	k_{de}	$1/3 \cdot 10^{10}$
FLC : Output Gain	k_{du}	10^8
Fixed step size		2e-5 s

Appendix B

The Per Unit System

The per-unit system is a common method used for expressing true values as normalized values. It is convenient to express values using the per-unit system, as this simplifies representations of power systems with several voltage levels and transformers, and allows generators to be compared more easily. Also having numbers of the same magnitude allows for higher accuracy in numerical calculations. The definition of a per-unit value of a quantity is:

$$\text{Per unit value} = \text{True value} / \text{Base value}$$

Table A.6: Base value definition

Base value	Denomination	Definition
Base power	S_{base}	1,5/0.9 MVA
Base voltage	V_{base}	575 V
Base current	I_{base}	$S_{base} / \sqrt{3} V_{base}$
Base impedance	Z_{base}	V_{base} / I_{base}
Base angular frequency	ω_{base}	$2\pi \cdot 60$
Base torque	T_{base}	$S_{base} / (\omega_{base} / p)$
Base flux	Φ_{base}	V_{base} / ω_{base}

Appendix C

Calculation of PI Controller Gains using the Pole-Compensation Method

In this thesis, the conception of the PI controller is based on the compensation of its time constant with the one of the process of the variable to be controlled. The bloc diagram of the PI control is presented in [Figure A.1](#).

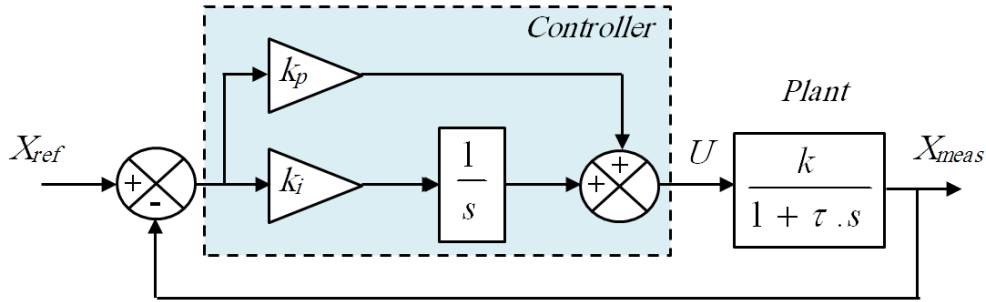


Figure A.1 Basic feedback system block diagram with PI controller.

The form of the PI controller is: $C(s) = k_p + \frac{k_i}{s}$

$$C(s) = k_p + \frac{k_i}{s}$$

The transfer function of the plant controlled by this PI controller is: $H(s) = \frac{k}{1 + \tau \cdot s}$

The open loop transfer function of the global system is given by:

$$H_{OL}(s) = \frac{k(k_p + \frac{k_i}{s})}{1 + \tau \cdot s} = \frac{k(k_p \cdot s + k_i)}{s \cdot (1 + \tau \cdot s)} = k \cdot k_i \cdot \frac{(1 + \frac{k_p}{k_i} \cdot s)}{s \cdot (1 + \tau \cdot s)}$$

If we put: $\frac{k_p}{k_i} = \tau$ then: $H_{OL}(s) = \frac{k \cdot k_i}{s}$

The closed loop transfer function of the global system is given by:

$$H_{CL}(s) = \frac{k \cdot k_i}{k \cdot k_i + s} = \frac{1}{1 + \frac{1}{k \cdot k_i} \cdot s}$$

The time response for a feedback system to get a 95% of the reference is given by: $T_r = 3 \cdot \frac{1}{k \cdot k_i}$

Because: $\frac{k_p}{k_i} = \tau$, Then: $T_r = 3 \cdot \frac{\tau}{k \cdot k_p}$

From which it can be deduced that: $k_p = 3 \cdot \frac{\tau}{k \cdot T_r}$ and $k_i = 3 \cdot \frac{1}{k \cdot T_r}$

Appendix D

Level-Shifted PWM Strategy for 3L NPC Converters using Matlab/SimPowerSystems

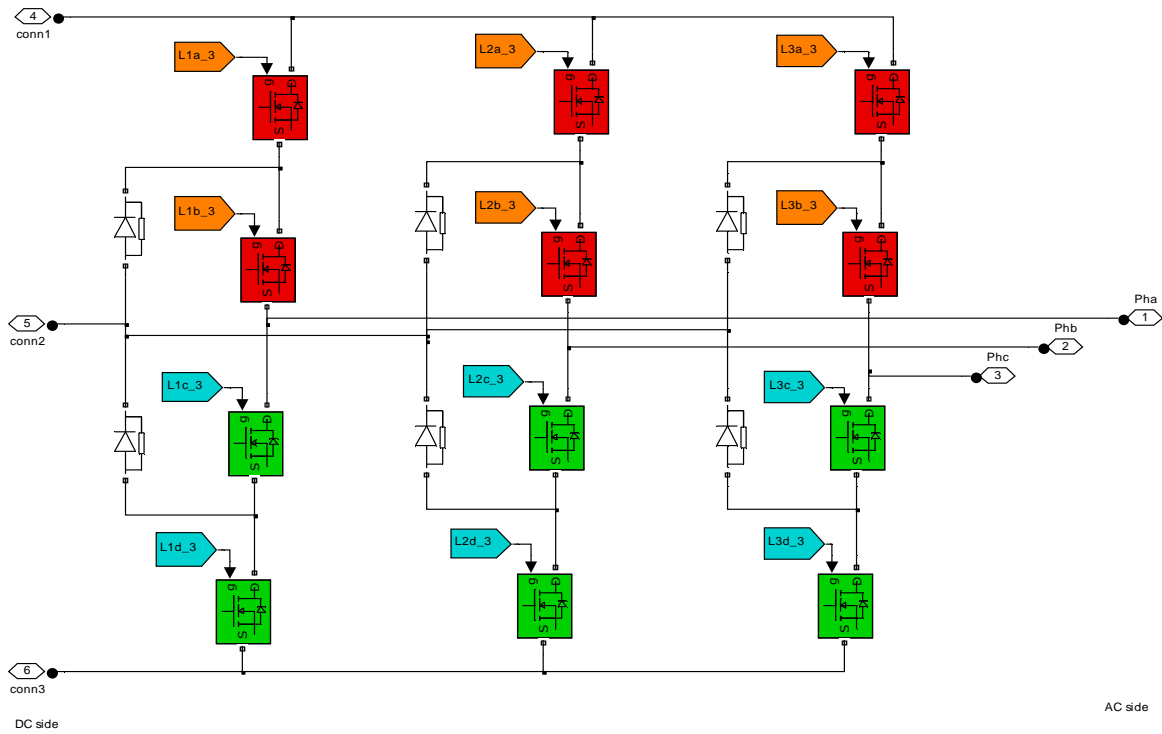


Figure A.2 Topology of the three phase 3L NPC converter.

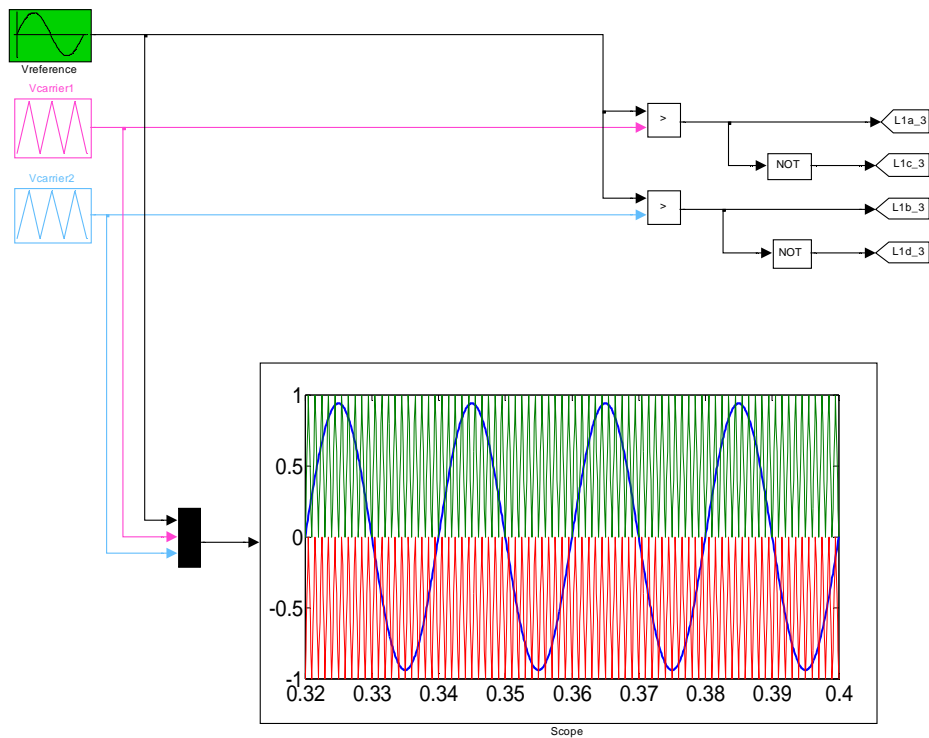


Figure A.3 One phase Level-Shifted PWM strategy for the 3L NPC converter.

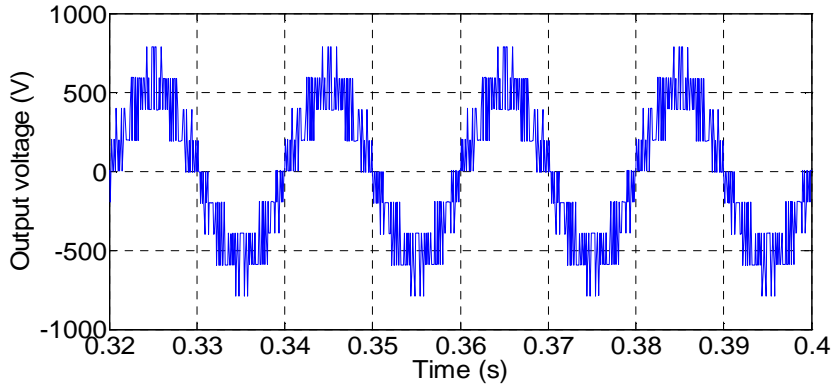


Figure A.4 One phase output voltage of the 3L NPC converter.

Level-Shifted PWM Strategy for 5L NPC Converters using Matlab/SimPowerSystems

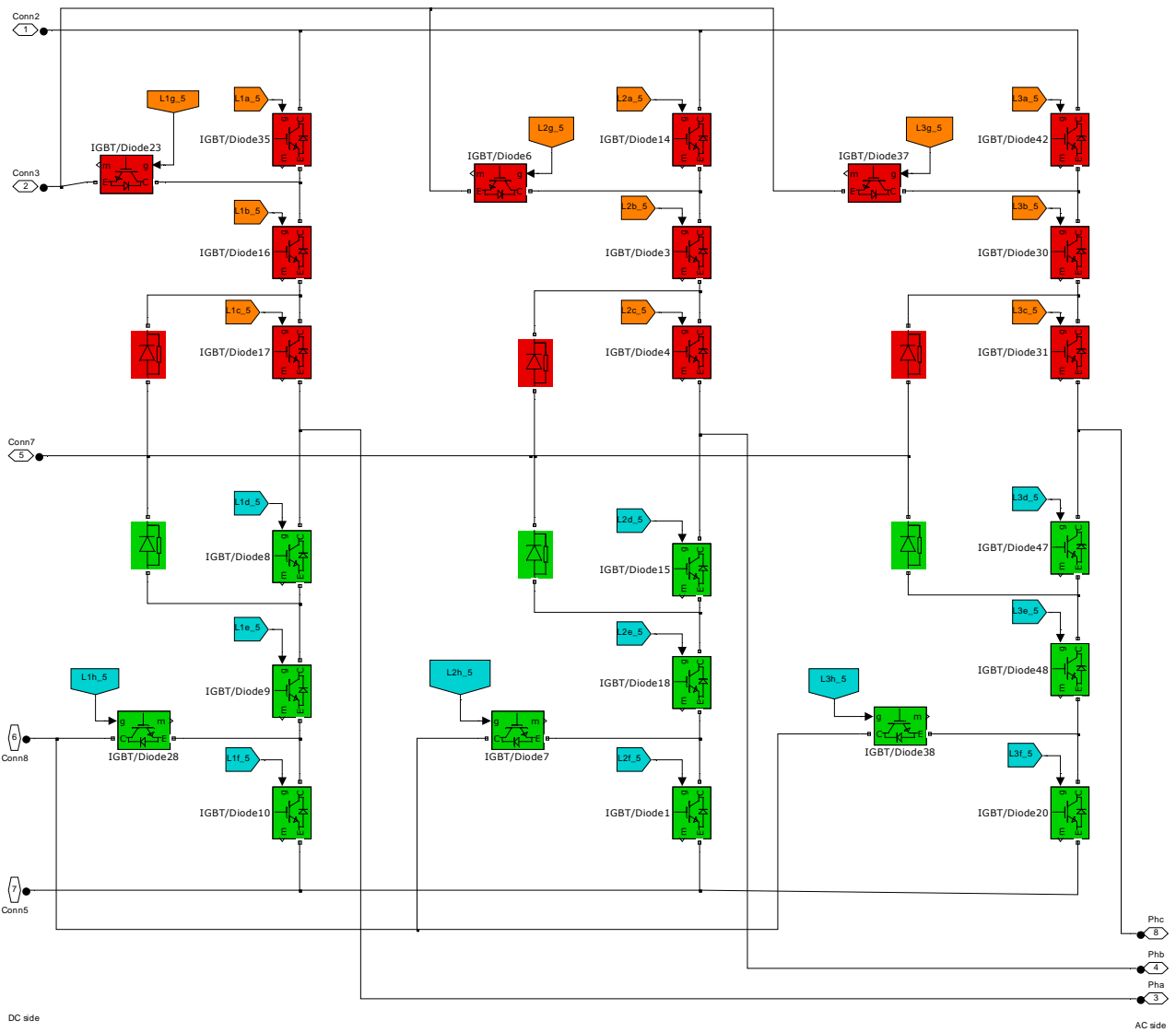


Figure A.5 Topology of the three phase 5L NPC converter.

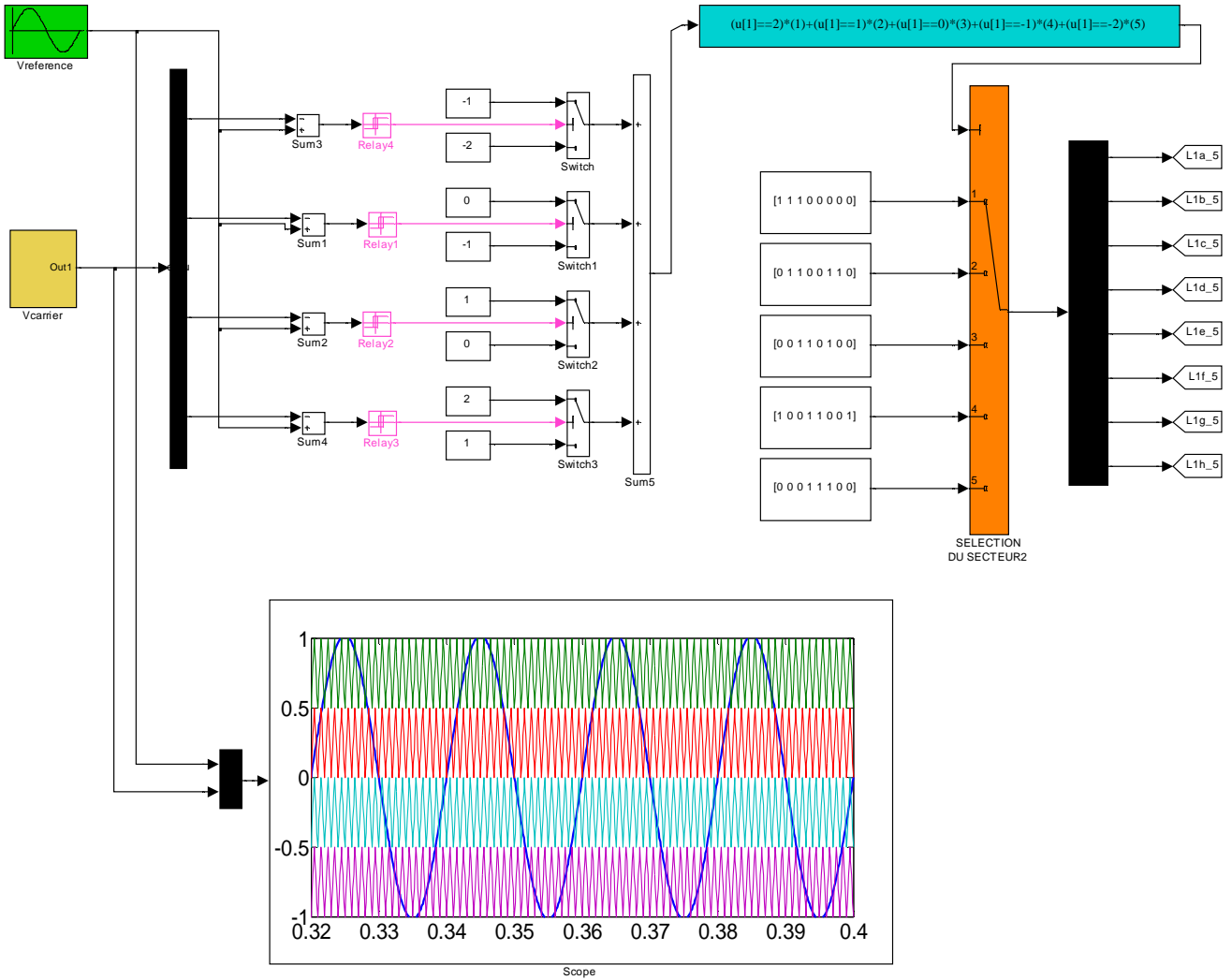


Figure A.6 One phase Level-Shifted PWM strategy for the 5L NPC converter.

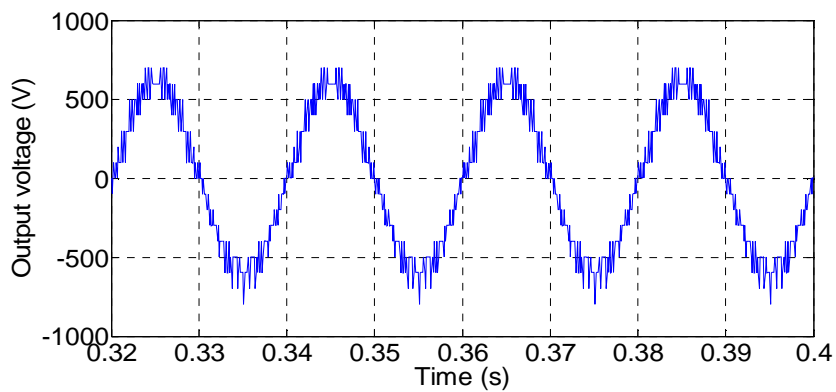


Figure A.7 One phase output voltage of the 5L NPC converter.

Level-Shifted PWM Strategy for 5L NPC Converters using Matlab/Simulink (Equation 5.03)

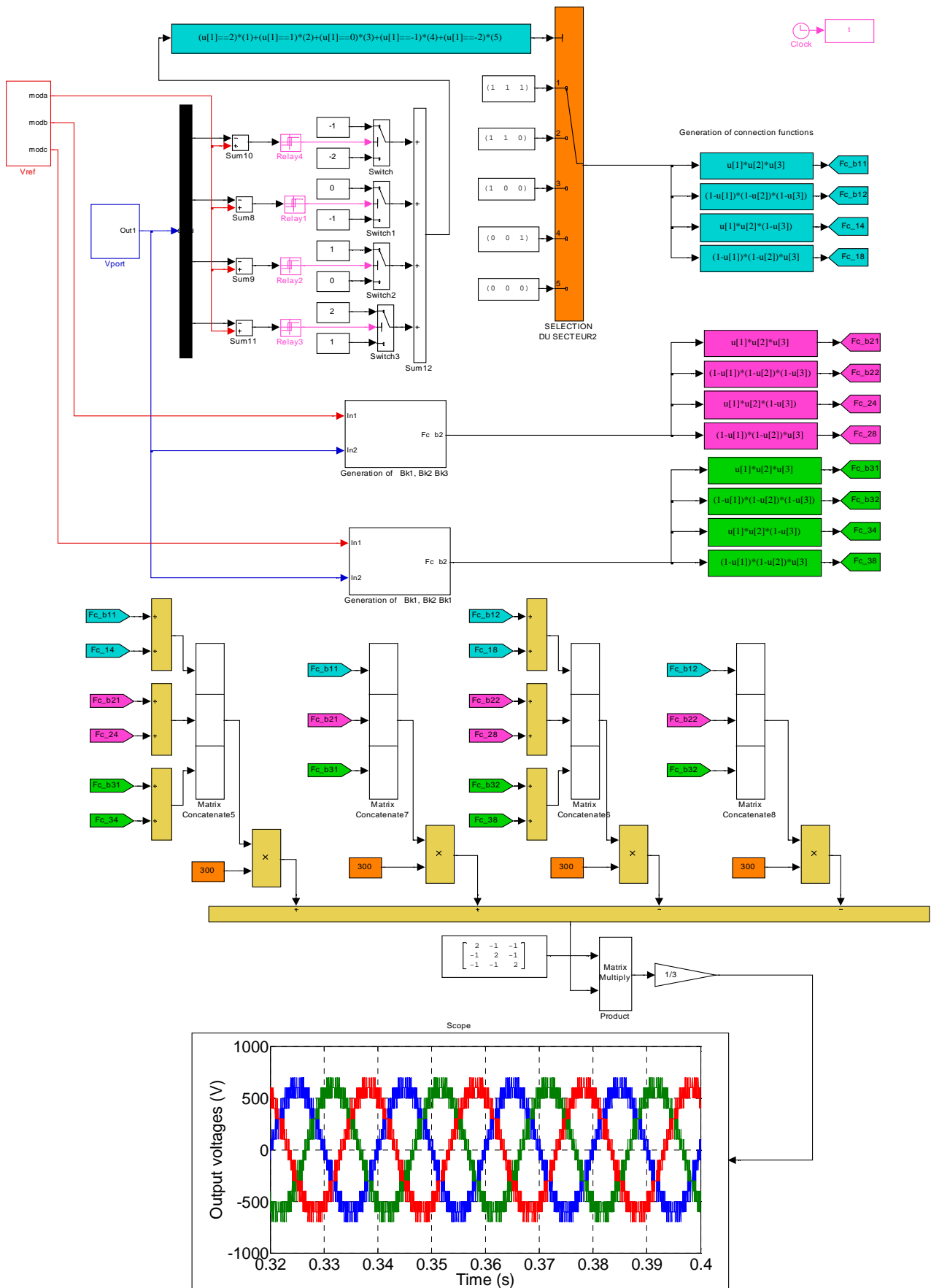


Figure A.8 Three phases PWM of the 5L NPC converter and its model.

Level-Shifted PWM Strategy for 7L NPC Converters using Matlab/SimPowerSystems

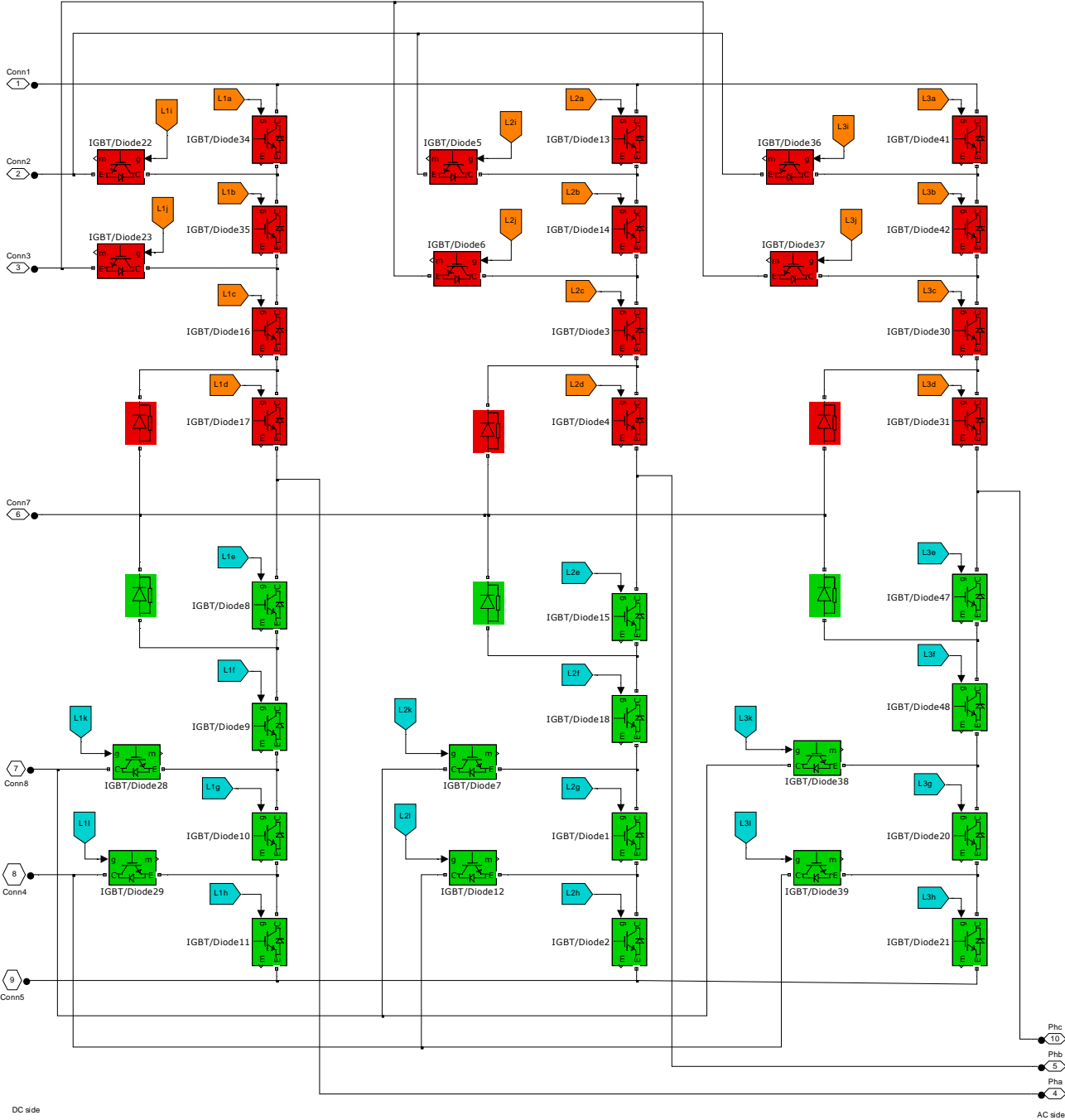


Figure A.9 Topology of the three phase 7L NPC converter.

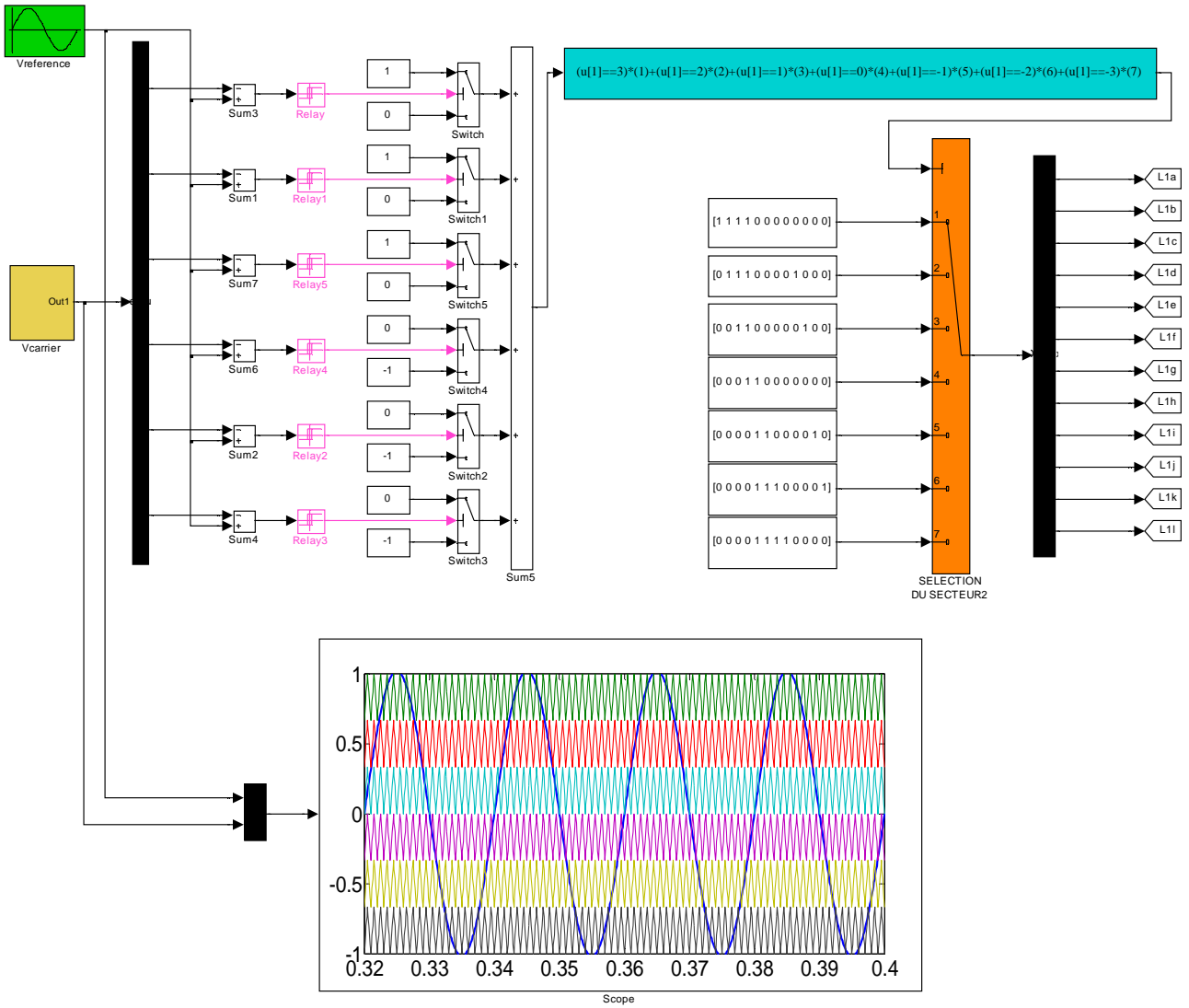


Figure A.10 One phase Level-Shifted PWM strategy for the 7L NPC converter.

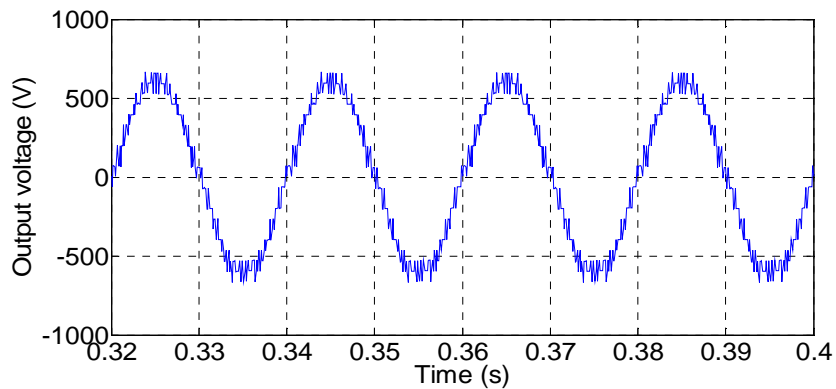


Figure A.11 One phase output voltage of the 7L NPC converter.

Vita

Abdelhak DIDA was born on January 23, 1981 in El Oued, Algeria; he gained his Baccalaureate degree in naturel science in 1999, from Mofdi Zakaria high school of Bayadha, El Oued. He received his Engineering degree in electrical machines from Biskra University, Algeria in 2004. He got his Magister degree in electrical machines and their drives from Ferhat Abbas University, Setif-1, Algeria in 2008. Now he got his Doctorate degree in control and power system engineering from Biskra University. Since 2010, he is lecturer at Ferhat Abbas, Setif-1 University and his research area includes:

- Modeling and simulation using MATLAB/SIMULINK.
- Nonlinear and robust control of electrical machines and drives.
- Power electronics and multilevel converters.
- Automation of renewable energy systems.
- Artificial intelligence control systems and metaheuristic optimization algorithms.

The official corresponding address is the E-mail: abdelhakdida@yahoo.fr

Biskra, Mars 16, 2016

Abdelhak DIDA



إسهام في التحكم بواسطة الشبكات العصبية-الغامضة في الماكينة الامتزازنة مزدوجة التغذية المستعملة في نظام التوليد بالعمفة الهوائية

كلمات مفتاحية:

- ماكينة لامتزازنة مزدوجة التغذية - نظام العمفة الهوائية - التحكم بالحقل الموجه - التحكم المباشر في الطاقة - التحكم اللاخطي - التحكم بالمنطق الغامض - التحكم بالشبكات العصبية-الغامضة - المحولات متعددة المستويات

ملخص:

تنطرق هذه الأطروحة لدراسة التحكم في الماكينة اللامتزازنة مزدوجة التغذية بواسطة تقنيات الذكاء الصناعي. بعد ما قدمنا نبذة حول الماكينة اللامتزازنة مزدوجة التغذية وطرق استعمالها كمولد للطاقة الكهربائية. قمنا بإيجاد الصيغة الرياضية للماكينة وذلك لتسهيل تطبيق التحكم بالحقل الموجه الذي يرتكز أساسا على ضابط كلاسيكي بمبدأ تناسبي وتكاملي. وقد قمنا أيضا بمراجعة للطرق المتبعة للتحكم المباشر اللاخطي في الطاقة و طرق تتبع نقطة الطاقة القصوى المنتجة للعمفة الهوائية. وبعد استعمالنا للضابط التناسبي التكاملي لاحظنا عدم كفاءته على المستوى الديناميكي وكذلك في حال وجود تغيرات في خصائص الماكينة. ولذلك لجأنا إلى استخدام طرق أخرى تعتمد على تقنيات الذكاء الصناعي ونذكر منها المنطق الغامض والشبكات العصبية-الغامضة. هذه التقنيات الأخيرة قدمت تحسينات معتبرة في التحكم في هذه الماكينة وقد عرضنا النتائج المفصلة لكل تقنية لمقارنتها بالتقنيات الأخرى.

Contribution à la Commande Neuro-Floue de la Machine Asynchrone à Double Alimentation Utilisée dans un Système Eolien

Mots Clés :

- Machine asynchrone à double alimentation - Turbine éolienne - Commande à flux orienté, Commande directe de puissance - commande non linéaire - Commande floue - Commande neuro-floue - Convertisseur multiniveaux.

Résumé :

Cette thèse présente la commande d'une machine asynchrone à double alimentation (MADA) par des techniques d'intelligence artificielle. Après avoir présenté l'état de l'art des différents systèmes de génération éoliens, nous avons abordé la modélisation mathématique de la MADA pour élaborer la commande vectorielle à flux orienté avec un régulateur classique proportionnel-intégral (PI). Nous avons révisé aussi les techniques de commande directe non linéaire de puissance générée, et les différentes techniques de maximisation de puissance produite. Après avoir utilisé le régulateur PI, on a remarqué leur inefficacité au niveau de la réponse dynamique et dans les cas des variations paramétriques de la machine. Pour cela, nous avons opté à l'utilisation des techniques de l'intelligence artificielle tels que les régulateurs flous et neuro-flous, lesquelles surpassent les limites des techniques classiques et améliorent la robustesse. Des résultats de simulations par Matlab/Simulink et des tests de robustesse sont présentés pour comparer avec les autres techniques.
